MIOCENE TO RECENT TECTONIC AND SEDIMENTARY EVOLUTION OF THE ANAXIMANDER SEAMOUNTS; EASTERN MEDITERRANEAN SEA

JENNIFER CRANSHAW

MIOCENE TO RECENT TECTONIC AND SEDIMENTARY EVOLUTION OF THE ANAXIMANDER SEAMOUNTS; EASTERN MEDITERRANEAN SEA

by

©Jennifer Cranshaw

A thesis submitted to the
School of Graduate Studies
in partial fulfillment of the
requirements for the degree of

Master of Science

Department of Earth Sciences

Memorial University of Newfoundland and Labrador

May, 2010

St. John's Newfoundland and Labrador

Acknowledgements

I would like to take this opportunity to extend my appreciation to those people who supported me during my masters. Without you this thesis would not be possible.

First, I would like to thank you my thesis supervisors Ali E. Aksu and Jeremy Hall for giving me the opportunity to be part of the this exciting project. Ali, you saw a light in me at a very early age and have never stopped believing in my infinite potential. Jeremy, your constant direction and leadership are unrivaled. Thank you for introducing me to the world of geophysics. You have both provided me with the tools and knowledge necessary to become a well rounded geoscientist. I am ready to move forward.

My sincere appreciation goes out to the faculty, staff and my fellow graduate students of the Earth Sciences Department at Memorial University of Newfoundland. In particular, Tom Colon for help with structural interpretations. Also, Jeremy Hall, Sharron Deemer and Adam Gogaz for help with data processing and Peter and Clyde for there technical support.

I would also like to thank my examiners for taking the time to review this thesis, especially Dr. Ings for his insightful comments on salt tectonics.

Thank to the School of Graduate Studies and the dean of science of Memorial University of Newfoundland, PanAtlantic Petroleum Systems Consortium (PPSC), and NSERC discovery grants for the financial support required for this thesis. Landmark Graphics Corporation for donating the seismic processing software used for data processing

To the Officers and crew of the research vessel *K. Piri Reis* and our Turkish colleagues without you the field work would not have been possible and I have learned so much from you all. I will cherish my summers in Turkey with you for the rest of my life.

Finally I would like to say thank you to all my family and friends. I am extremely grateful for your help and support and am incredibly fortunate to have you all in my life. This has been an incredible journey and I am more than excited to see what comes next!

Abstract

This thesis is focused on the Messinian to Recent tectonic and sedimentary evolution of the Anaximander Mountains and surrounding environs in the eastern Mediterranean Sea. It is based on processing of high-resolution seismic reflection data and the interpretation and mapping of seismic reflection profiles collected from this area during the 2001 and 2007 research cruises. The data show that the greater Anaximander Mountains region experienced a short interval of tectonic quiescence during the Messinian when a thin evaporite unit was deposited across a major erosional surface. This phase of limited tectonic activity ended in the latest Miocene and was replaced by an erosional phase. Major unconformities in the area are interpreted to develop during the desiccation of the eastern Mediterranean associated with the so-called Messinian salinity crisis. During the early Pliocene, the region experienced an increase in tectonic activity, dominated by transpression. Small amounts of growth observed in Pliocene-Quaternary sediments suggested that the tectonic activity remained low during the early Pliocene-Quaternary. However, the extensive growth strata wedges developed in older sediments indicate a period of accelerated tectonic activity during the mid-late Pliocene-Quaternary.

This study suggests that the Anaximander Mountain (*sensu stricto*) and the Anaximenes Mountain developed during the Pliocene-Quaternary as the result of a crustal-scale thick-skinned linked imbricate thrust fan. The development of back thrusts in both mountains heightened the seafloor morphology of these submarine mountains and brought Eocene-Oligocene sediments into the core of these mountains.

The Sırrı Erinç Plateau represents a 30-40 km wide transpressional fault zone developed during the Pliocene-Quaternary. In this region the corrugated seafloor morphology observed in the multibeam bathymetry map is the reflection of high-angle faults. It is speculated that this transpressional fault zone extends from the southern portion of the Rhodes Basin across the greater Anaximander Mountains into the western segment of the Antalya Basin, defining a major present-day tectonic element in the eastern Mediterranean Sea.

The abrupt termination of the crustal-scale south verging thrust that carries the Anaximander Mountain at the large west-verging thrust that defines the boundary between the Anaximander Mountain and the western Sırrı Erinç Plateau is interpreted as a major transfer fault. This thrust displays notable contractional overlap and may have considerable strike-slip component.

Morphological similarities between the Isparta Angle of southwestern Turkey and the greater Anaximander Mountains are used to suggest similarities in the tectonic evolution of these two areas. Therefore, it is speculated that the Anaximander Mountains may be the offshore replication of the Isparta Angle trends, caused by similar mechanisms, but of younger age. If correct, during the Pliocene-Quaternary, the Anaximander and Anaximenes Mountains must have experienced a progressive counterclockwise rotation, while the Anaxagoras Mountain and the Florence Rise must have experienced a clockwise rotation. Thus, the present day arrow-head shaped morphology of the Anaximander Mountains (*sensu lato*) may be viewed as the new phase of the Isparta Angle.

List of figures

CHAPTER 1

CHAPTER 2

CHAPTER 3

CHAPTER 4

CHAPTER 5

List of tables

CHAPTER 1. Introduction

1.1 Background

The tectonic history of the eastern Mediterranean Sea and surrounding area (Fig. 1.1) is extremely complex and has been called a "geological jigsaw puzzle". Today, the region is used as a natural laboratory to investigate a number of plate tectonic processes, such as; (i) convergence and associated subduction, (ii) orogenesis and ophiolite obduction, and (iii) rifting and passive margin development (Robertson, 1998; Aksu et al. 2005). The area is also a world class example of extensive Salt deposition. Numerous authors have documented the ubiquitous presence of a thick evaporite sequence covering the eastern Mediterranean region (e.g., Hsü et al., 1973; Cita et al., 1978; Unit 2 of Hall et al., 2005 and Işler et al., 2005). The evaporites were deposited during the desiccation of the Mediterranean associated with the "Messinian Salinity Crises" (e.g., Cita et al., 1978). However, no study to date has documented evaporite seposition in the Anaximander Mountains or the Rhodes Basin.

The Mediterranean Sea is the remnant of a once much larger Tethys Ocean that evolved during the Mesozoic (Moores et al., 1984; Robertson, 1998). The plate tectonic environment of the eastern Mediterranean Sea is associated with the collision of the African and Arabian Plates (moving north) with the Eurasian Plate and the Aegean-Anatolian Microplate (moving west) in-between (Figure 1.2). All plate motions are made with reference to a fixed Eurasian Plate (McClusky et al., 2000). In the Late Miocene, the collision between the Arabian Plate and the Eurasian Plate initiated the westward

movement of the Aegean-Anatolian Microplate in the Pliocene (Fig. 1.2) and its counter-clockwise rotation in the western most segment of the microplate (Şengör et al., 1981). These continental blocks are converging through subduction and squeezing of the microplates sandwiched between (Fig. 1; Aksu et al., 2005). Today, the tectonic framework of the eastern Mediterranean is characterized by the last phase of convergence between the African and Eurasian Plates and the displacement of the smaller Arabian and Aegean-Anatolian Microplates (Figs. 1.1 and 1.2). The boundary between the African Plate and the Aegean-Anatolian Microplate is delineated by the Hellenic Arc and the Pliny-Strabo Trenches in the west and the Florence Rise, and Cyprus Arc in the east (Fig. 1.2). Numerous studies have taken place in the region, regarding the style and timing of deformation in the Anaximander Mountains. However significant controversy still exists regarding the Miocene-recent tectonic and sedimentary evolution of the area, such as (i) the linkage and role of the Anaximander Mountains in the tectonic evolution of the Southwest Aegean Anatolian Microplate and (ii) the linkage of the Anaximander Mountains with the Hellenic Arc and Plino Strabo Trench in the west and the Cyprus Arc and Florence Rise in the east. Supervisors Ali E. Aksu and Jeremy Hall of the Memorial University of Newfoundland (MUN) initiated the **Eastern Mediterranean Sea Project** in 1991. Currently, they lead an international team of researchers, who are actively investigating the tectonic evolution of the eastern Mediterranean Sea.

Since the project began five marine seismic cruises have taken place in 1991, 1992, 2001, 2007 and 2008 collecting over 14500 km of multi-channel seismic reflection data (Fig. 1.3). The author participated in the summer-fall 2007 cruise, and assisted in the

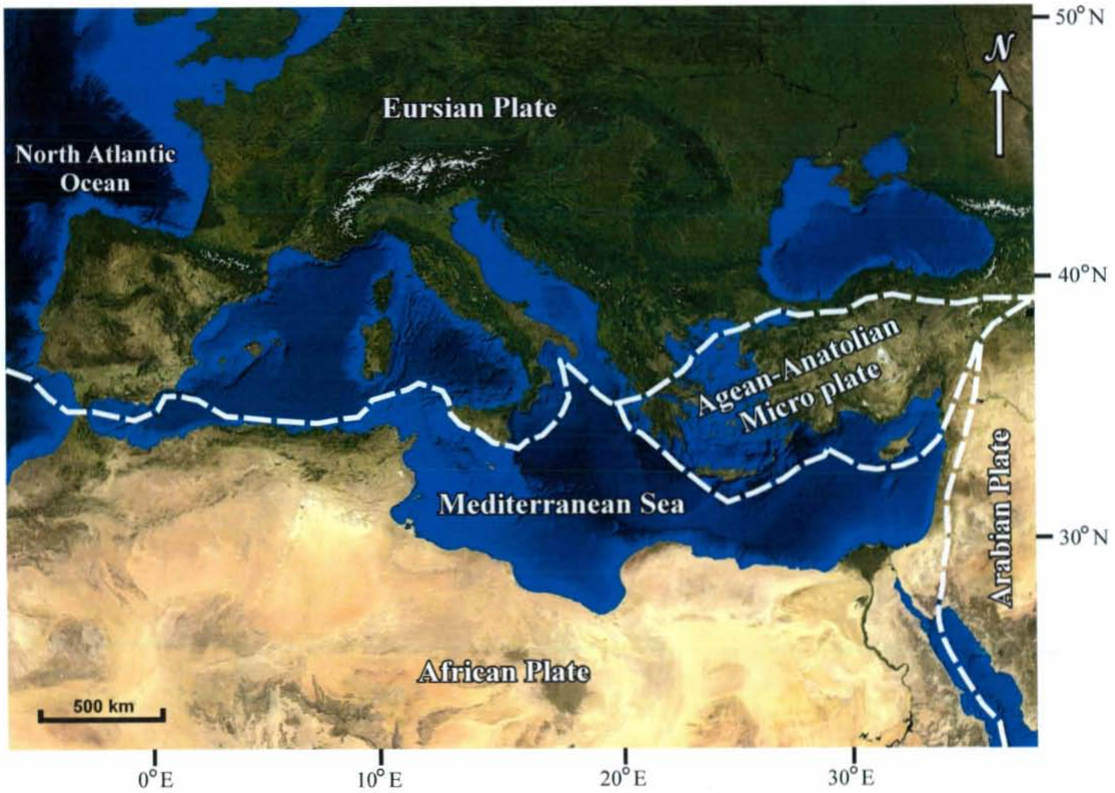

Figure 1.1 Schematic showing the location of the eastern Mediterranean Sea and the surrounding tectonic plate boundaries

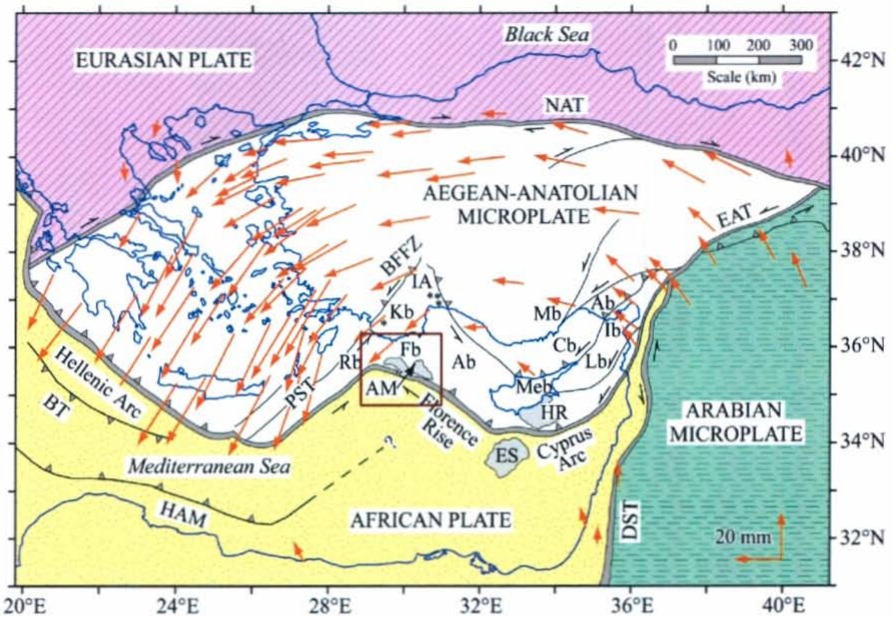

Fig. 1.2 Tectonic map of the eastern Mediterranean Sea and surrounding regions, with the study area highlighted by the red box. Ab = Antalya Basin, AKMb = Aksu, Köprü, Manavgat Basins, AM = Anaximander Mountains (*sensu lato*), BFFZ = Burdur–Fethiye Fault zone, BT = backstop thrust, DST = Dead Sea Transform Fault, EAT = East Anatolian Transform Fault, ES = Eratosthenes Seamount, HAM = Hellenic active margin, HR = Hecateus Ridge, IA = Isparta Angle, Kb = Kasaba Basin, Mb = Mesaoria Basin, NAT = North Anatolian Transform Fault, PST = Pliny–Strabo Trenches, Rb = Rhodes Basin. Large arrows indicate the rate of plate movement and the sense of plate motion relative to a fixed Eurasian plate; half arrows indicate transform/strike-slip faults (modified from Aksu et al., 2009)

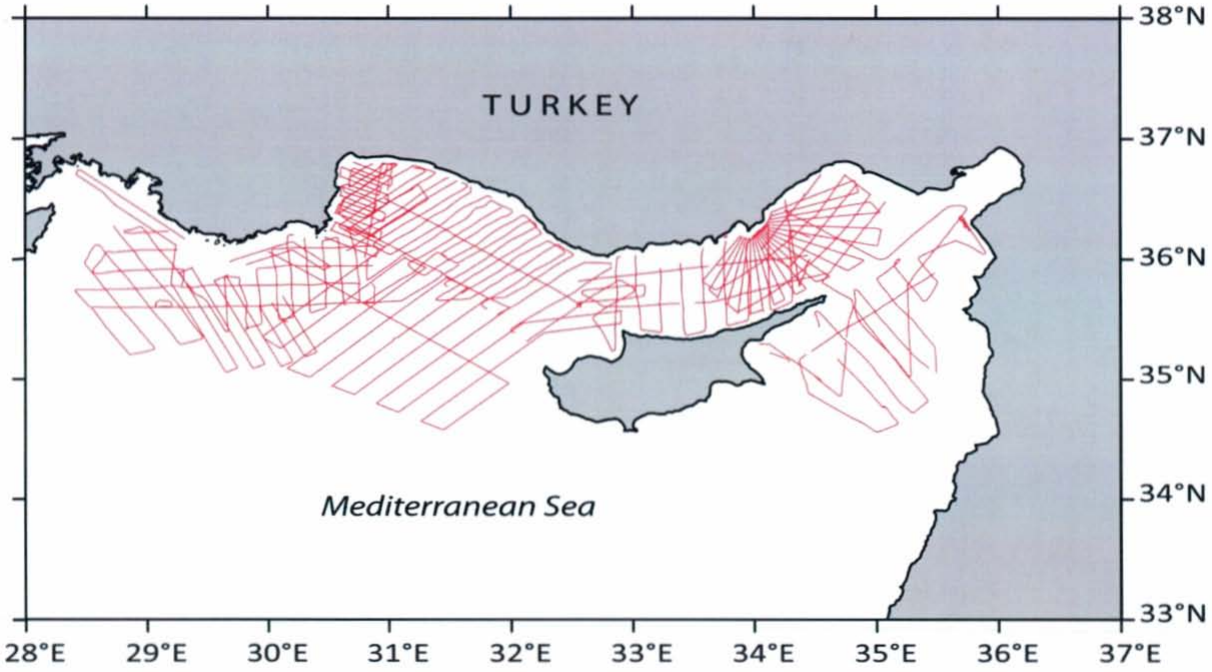

Fig. 1.3 Map of the eastern Mediterranean Sea showing the location of all lines collected during the Eastern Mediterranean Sea Project

collection of ~3000 km of high-resolution seismic reflection profiles from the eastern Mediterranean Sea. Considerable progress has been made by the Memorial group in the eastern Mediterranean as shown by numerous publications (e.g., Aksu et al., 2005a,b, 2009, Hall et al., 2005a,b, 2009, Calon et al., 2005a,b, Bridge et al., 2005, Burton-Ferguson et al., 2005, Işler et al., 2005). This thesis provides considerable new data and new interpretation to the evolution of the Anaximander and Anaximenes Mountains. Please note that all data and interpretations presented in this thesis that are not referenced to the above work are contributed by the author. The main contributions from this thesis are highlighted in the following chapters and are further summarized in the conclusions.

1.2 Thesis Study Area and Geological Setting

The study area is situated over the morphologically and structurally complicated triple junction between the Hellenic and Cyprus Arcs in the eastern Mediterranean Sea (Fig. 1.2). The Anaximander Mountains (*sensu lato*) are located at the junction between these two arcs. They are bounded to the west by the deep Rhodes Basin, to the east by the outer portion of the Antalya Basin and to the south by the Mediterranean Ridge (Figs. 1.2 and 1.4). In detail, these underwater mountains emerge as three prominent morphological highs: the Anaximander Mountain (*sensu stricto*) in the west and northwest, the Anaxagoras Mountain in the east, and the Anaximenes Mountain in the middle (Fig. 1.4).

The 3-dimensional nature of the geology in the Anaximander Mountains requires a dense grid of high-resolution seismic reflection profiles. Therefore, ~2000 km

of multi-channel seismic reflection data from 2007 and 2001 are used in this thesis to create a seismic grid with a 10 km line spacing (Fig. 1.5). The 2007 seismic profiles provide further coverage over the southern segment of the Anaximander Mountain *(Sensu lato)*. In this thesis examples of the 2007 profiles (Figs. 4-8) are presented to provide new lines for a more detailed interpretation of the study area.

The 2007 profiles indicate that the structural architecture of the three mountains is very different. The Anaximander Mountain is a large, E-W trending and N-dipping asymmetric structure, the southern flank of which is bounded by a very steep S-dipping escarpment, where the seafloor is sharply offset by 700-900 m. The northern slope of the mountain gently dips towards the North, and the structure progressively merges with the Finike Basin at the southern limit of the Turkish continental slope (Aksu et al. 2008).

The Anaximenes Mountain is a steep-sided structure south and southeast of the Anaximander Mountain (Fig. 1.4). It is concave to the northwest and trends NE-SW at its northeast end but gradually assumes an ENE-WSW trend towards the southwest. The crest of the Anaximenes Mountain is elevated ~400 m above a 20-30 km-wide flat-bottomed valley between the Anaximander and Anaximenes Mountains, referred to as the Şırrı Erinç Plateau, and is ~500-700 m above the Mediterranean Ridge at the northern flank of the Heredotus Basin to the south.

The Anaxagoras mountain trends NW-SE is the most easterly high. Anaxagoras is situated to the south of the Antalya Basin and merges with the Anaximenes Mountain and Florence Rise at its SW and SE ends respectively. In the NW the mountain exhibits

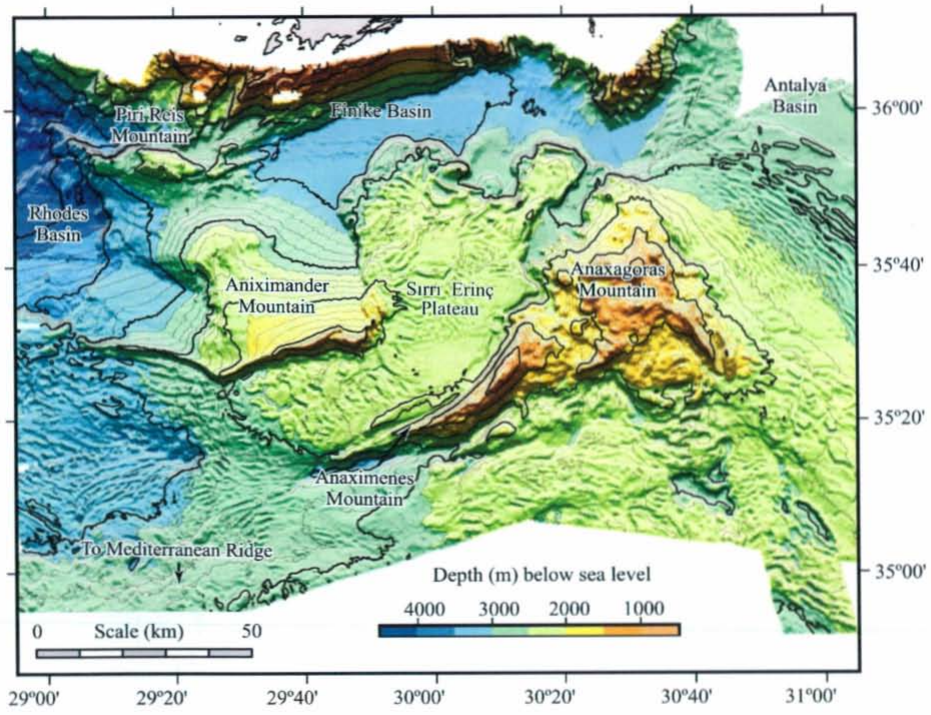

Fig. 1.4 Detailed multibeam bathymetry map of the eastern Mediterranean Sea showing the position of the Anaximander Mountains (*sensu lato*), Sırrı Erinç Plateau, and surrounding environs (Modified from Aksu et al. 2009).

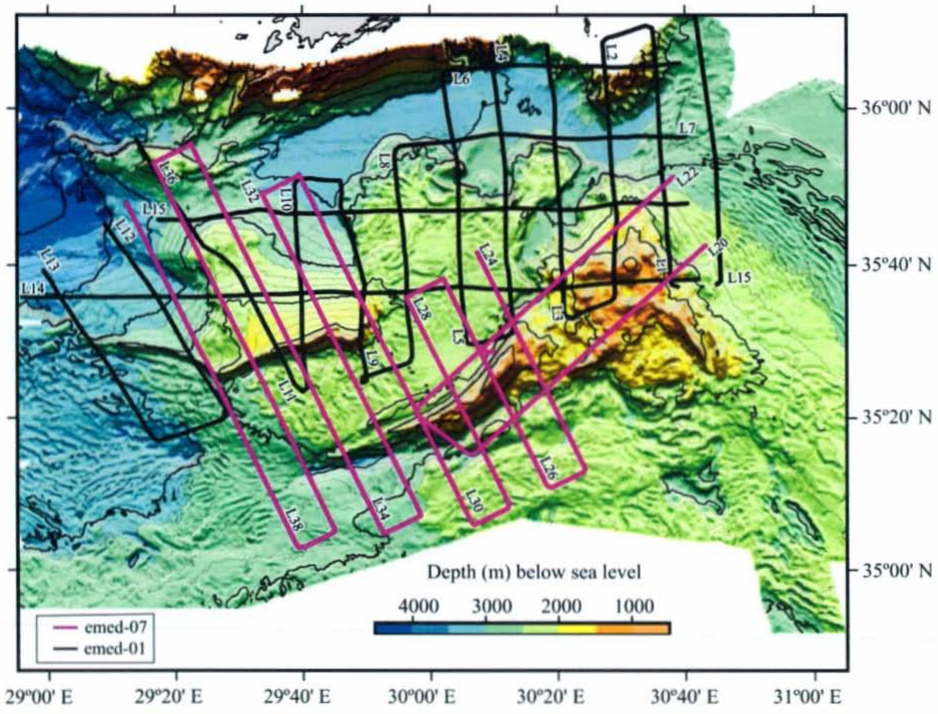

Figure 1.5 Multi-beam bathymetry map of the eastern Mediterranean Sea showing all lines used for this thesis. The 2007 lines (900 km) are highlighted in pink and the 2001 lines (1100 km) are highlighted in black. L9, L38 etc are line numbers.

an arcuate NW-dipping escarpment that is elevated ~700 m above the Sırrı Erinç Plateau to the NW. In the east the mountain is less steep but is cut by a system of faults and canyons and mud volcanism has been documented in the area (Technical report, 1996).

1.3 Tectonic Framework of the eastern Mediterranean Sea

Recent studies suggest that the Anaximander Mountains and Isparta Angle (Poisson et al., 2003) are genetically linked structures which evolved at different times (Zitter et al., 2003; Aksu et al., 2009). Thrusts bounding the northeast margin of the Isparta Angle are similar to the two prominent thrusts that bound the northeast limb the Anaxagoras Mountain (Aksu et al. 2009). The Sırrı Erinç Plateau represents a 30-40 km wide sinistral transpressional belt extending through the Anaximander Mountains. It is similar in orientation and width to the 40-50 km wide sinistral Burdur-Fethiye Fault Zone (BFFZ) that delineates the western margin of the Isparta Angle (Fig. 1.6). In marine areas, the contractional deformation associated with the plate conversion happened at the same time as deformation occurred in the western Tauride Mountains. However, the deformation associated with the block rotation and northward buckling of the western Tauride fold-thrust belt to form the Isparta Angle preceded the block rotation in the Anaximander Mountains. Aksu et al. (2009) and Cranshaw et al. (2010) speculate that the westward propagation of the North Anatolian Fault Zone and the progressive counterclockwise rotation of the western segment of the Aegean-Anatolian Microplate during the Pliocene-Quaternary must have initiated a new tectonic phase dominated by transpression and block rotation in the study area (Fig. 1.7).

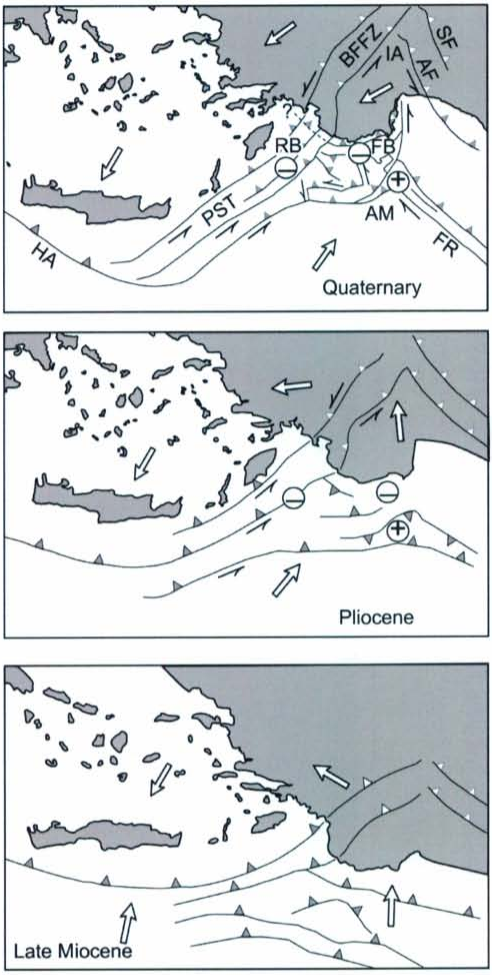

Fig. 1.6 A schematic model showing Miocene, Pliocene and Quaternary stages in the tectonic evolution of the Anaximander Mountains (*sensu lato*) and the surrounding environs. + and − indicate areas of uplift and subsidence, respectively. AF = Aksu Fault; AM = Anaximander Mountain; BFFZ = Burdur-Fethiye Fault Zone; FB = Finike Basin; FR = Florence Rise; HA = Hellenic Arc; IA = Isparta Angle; PST = Pliny-Strabo Trenches; RB = Rhodes Basin; SF = Sultan Dağ Fault. White arrows show relative motion of blocks at different times (From Aksu et al., 2009).

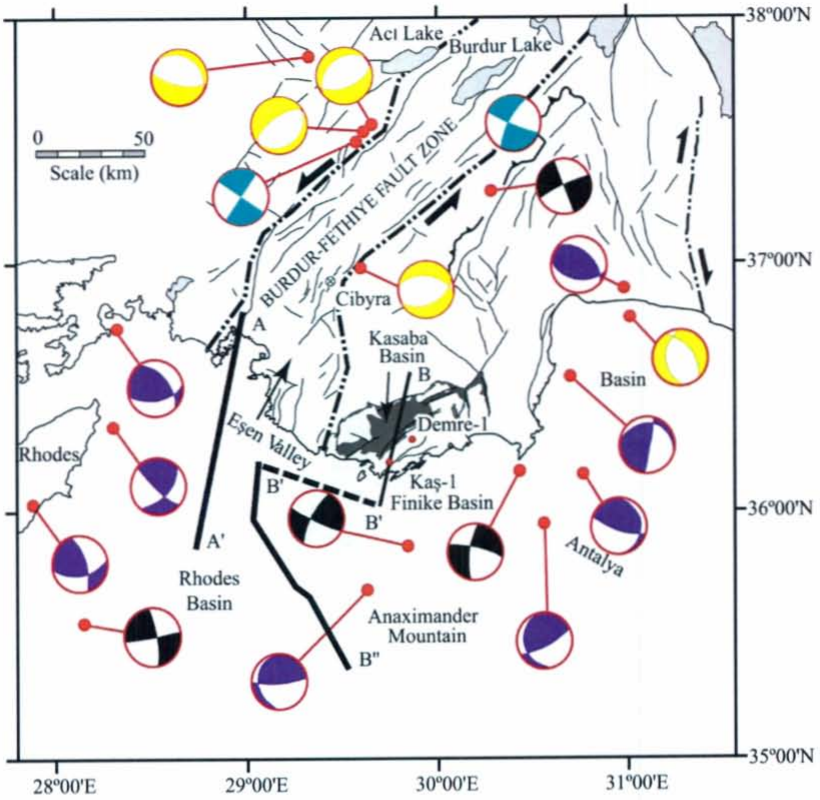

Fig. 1.7 Simplified tectonic map of southwestern Anatolia, showing the Burdur–Fethiye Fault zone, the onland Kasaba Basin, and the locations of the exploration wells Demre-1 and Kaş-1. Also shown are lower hemisphere projections of fault plane solutions associated with earthquake shocks in the region: quadrants with compressional first motion are shaded. Focal mechanisms given by (1)Westaway, (1993), (2)Taymaz and Prize, (1992), (3) Yılmazturk and Burton (1999), (4) Benetatos et al., (2004), (5) Harvard CMT Catalogue (Modified from Hall et al., 2009)

1.4 Scientific Objectives

The primary objectives of this thesis are to image and map the Structures associated with the Neogene tectonic and sedimentary evolution of the Anaximander Mountains in the eastern Mediterranean Sea. This will be accomplished by completing the following geophysical and geological objectives;

1.4.1 Geophysical Objectives

1. to determine the parameters required to process the high resolution multi channel reflection data from the Anaximander Mountains,
2. to establish an optimal processing flow for the data set by testing various steps of the flow using the trial-and-error method
3. to process the data from the shot-domain to final migration

1.4.2 Geological Objectives

1. to produce detailed maps of the structures that make up the Anaximander Mountains using interpretations of high-resolution seismic reflection profiles
2. to understand the structural and tectonic linkages between the Anaximander, Anaximenes and Anaxagoras Mountains

3. to determine why these structures (i.e., Anaximander Mountains) are significantly elevated above the adjacent seafloor?

4. to describe the structural architecture of the Anaximander Mountains, and their relationship with the Sırrı Erinç Plateau in between and

5. to understand why the Messinian evaporite succession is absent in the Anaximander Mountains, when it omnipresent in most areas of the eastern Mediterranean Sea, such as the Antalya Basin to the North East and Mediterranean Ridge to the south.

CHAPTER 2: Methods

2.1 Reflection Seismology

The seismic reflection method is an important geophysical technique that uses echo-sounding to investigate the properties of large volumes of rock beneath the Earth's surface (Yılmaz, 2001). This method requires (i) a controlled source (e.g., air gun, water gun, sparker, vibrator, etc.) to emit a pulse of energy into the ground/water, (ii) a receiver that captures the sound energy reflected back from the interfaces (e.g., hydrophone array, geophone array, etc.) and (iii) a seismograph to record the time it takes for the echos to travel from source to receiver (Fig. 2.1).

The simplest case of seismic reflection is the zero offset/normal incidence reflection experiment, where a source and receiver are positioned at the same location (Fig. 2.2). There is little information that can be derived from zero-offset data, so seismic data are usually recorded as common shot gathers (Fig. 2.3). Here a single shot produces the time-space seismogram and the resulting function is hyperbolic (Fig. 2.3).

The seismic reflection occurs when there is a distinct contrast in acoustic impedance between two layers. Acoustic impedance (Z) is a product of velocity and density of the medium in which propagation takes place (Equation 2.1; see below). Thus, a significant change in velocity (υ) and/or density (ρ) will produce a strong reflection, such as seen across the water – seabed or the sandstone – limestone interfaces. The

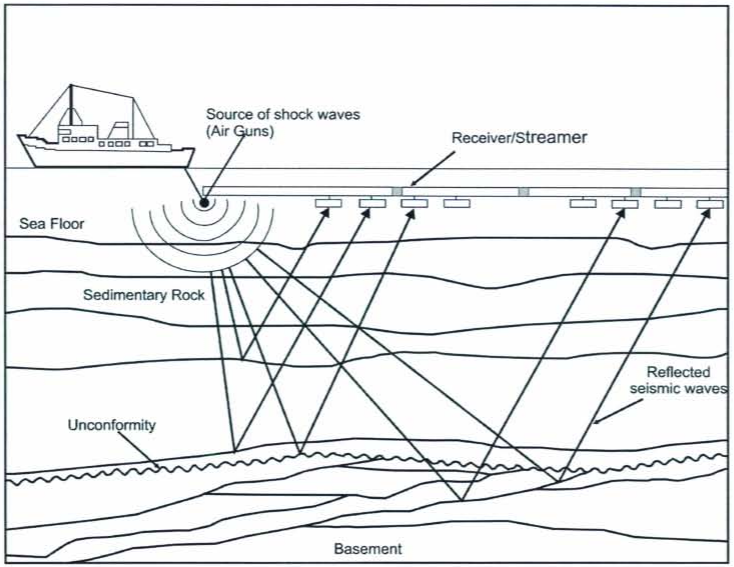

Figure 2.1 General configuration of a seismic reflection survey showing the location of the source (air gun) and receiver/streamer (hydrophones). The seismograph is located onboard ship.

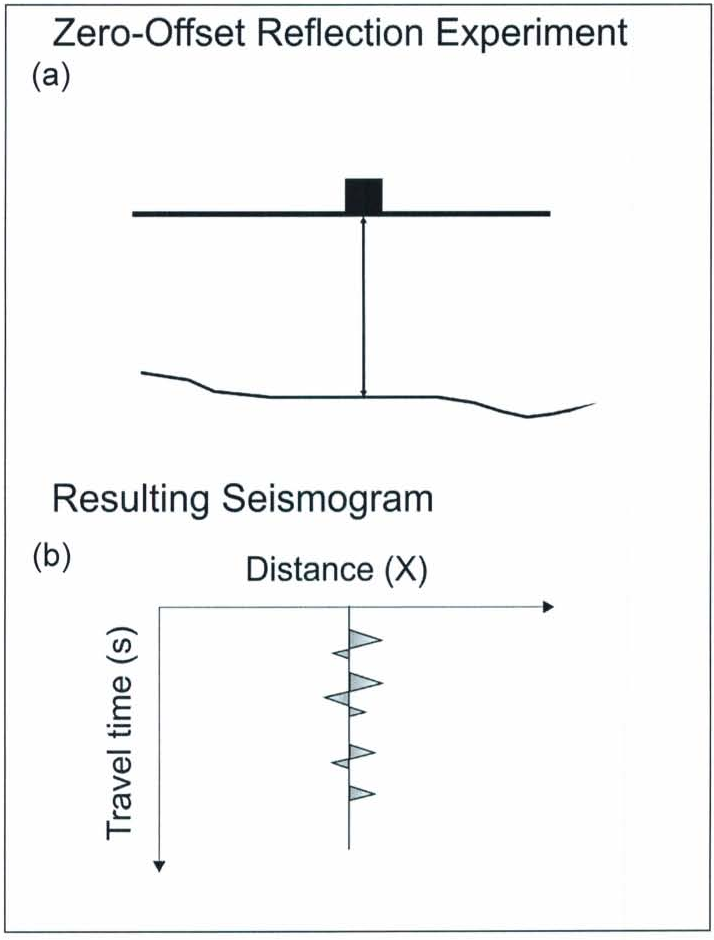

Figure 2.2 Seismic reflection experiment using the zero-offset method, where the source and receiver share a common location. S= Source and R= Receiver.

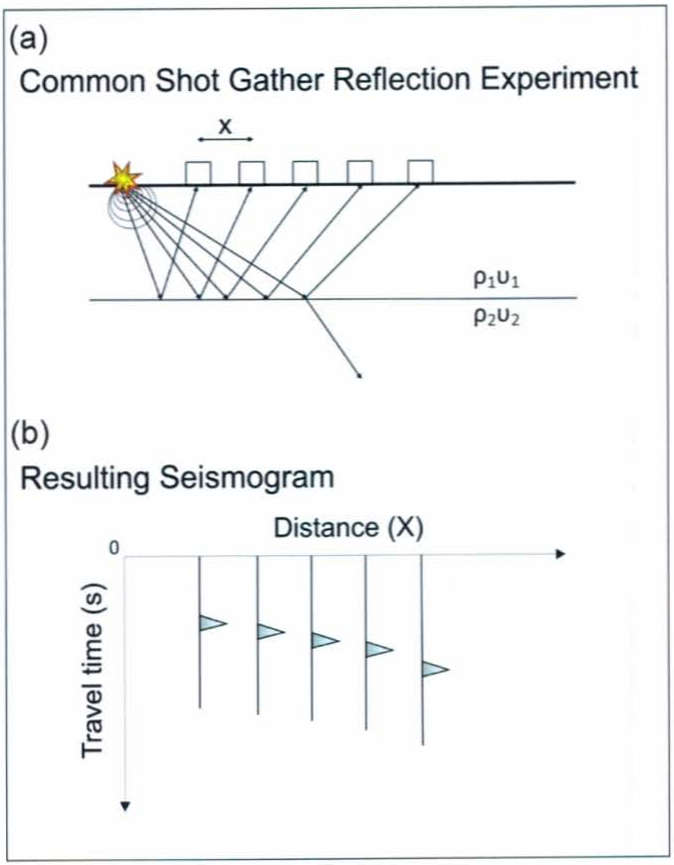

Figure 2.3 Seismic reflection experiment using the common shot gather method with a single source and a number of receivers placed a different distances (x) away from the source. ρ=density and υ= velocity.

amplitude and polarity of the reflected energy is proportional to the acoustic impedance contrast (Z) across the boundary (Yılmaz, 2001).

$$Z = \upsilon\rho \tag{2.1}$$

When a P-wave encounters a boundary where there is a significant change in acoustic impedance, some energy is reflected back to the surface, while some is transmitted into the next layer. The strength of a reflection (at normal incidence) is defined by the reflection coefficient between two layers (R_{12}), which is a function of the acoustic impedance across the interface, and it is described by equation 2.2 where $\rho_1\upsilon_1$ and $\rho_2\upsilon_2$ are the acoustic impedance of layers 1 and 2, respectively.

$$R_{12} = (\rho_1\upsilon_1 - \rho_2\upsilon_2) / (\rho_1\upsilon_1 + \rho_1\upsilon_1) \tag{2.2}$$

The seismic reflection method is a robust procedure. It is assumed that seismic waves travel through homogeneous, isotropic media (Krebes, 1985, 1989, Yılmaz, 2001). Energy is lost as depth increases due to spherical divergence, absorption, scattering and anelastic attenuation of higher frequencies with depth. This affects the choice of the source bandwidth appropriate for a particular target depth.

2.2 Marine Seismic Reflection Survey

2.2.1 Acquisition Parameters

During the 2007 eastern Mediterranean cruise, ~1000 km of high-resolution seismic reflection data were acquired over the Anaximander Mountains (*sensu lato*) using

the RV *Koca Piri Reis* of the Institute of marine Sciences and Technology, Dokuz Eylül University. The locations of the 2007 reflection profiles were chosen carefully with lines running northwest-southeast, broadly perpendicular to the general trend of the prominent structures in the area (Fig. 2.4). The 2001 seismic reflection profiles running N-S and E-W were used as tie lines for interpretation. The flow chart describing the cruise set-up for the 2007 multi-channel seismic survey is shown in Figure 2.5. During the 2007 cruise seismic reflection data were collected with shots fired to time, approximately every 9-10 seconds, corresponding to ~25 m distance. The trigger pulses were generated from the ships Global Positioning System (GPS). The NavPac receives the orientation and coordinates from the vessels Gyro and the vessel's navigation system (i.e., GPS) and sends a TTL (transistor-transistor logic) signal to the trigger box. Next, the interim trigger box which sends a signal to the delay box. The delay box in turn, sends a TTL signal to Macha (i.e., the source controller), and a user-defined delayed TTL to the SeaMUX NTRS-2 seismograph (Fig. 2.5). Finally, the Macha, sends a 5V TTL signal to each air-gun to fire the guns. By setting a specific time delay, the operator can delay the onset of recording according to the variations of the water depth, thus, maximizing data storage space. This was particularly important in the study area because the bathymetry varied from 4000 m to >1000 m over relatively short distances.

The source used was a broad-band, high-frequency sleeve gun array belonging to the Memorial University of Newfoundland (Fig 2.6). The array consisted of seven sleeve guns: 4 x 40 in^3 guns (4 x 655 cm^3), 1 x 20 in^3 gun (1 x 328 cm^3), and 2 x 10 in^3

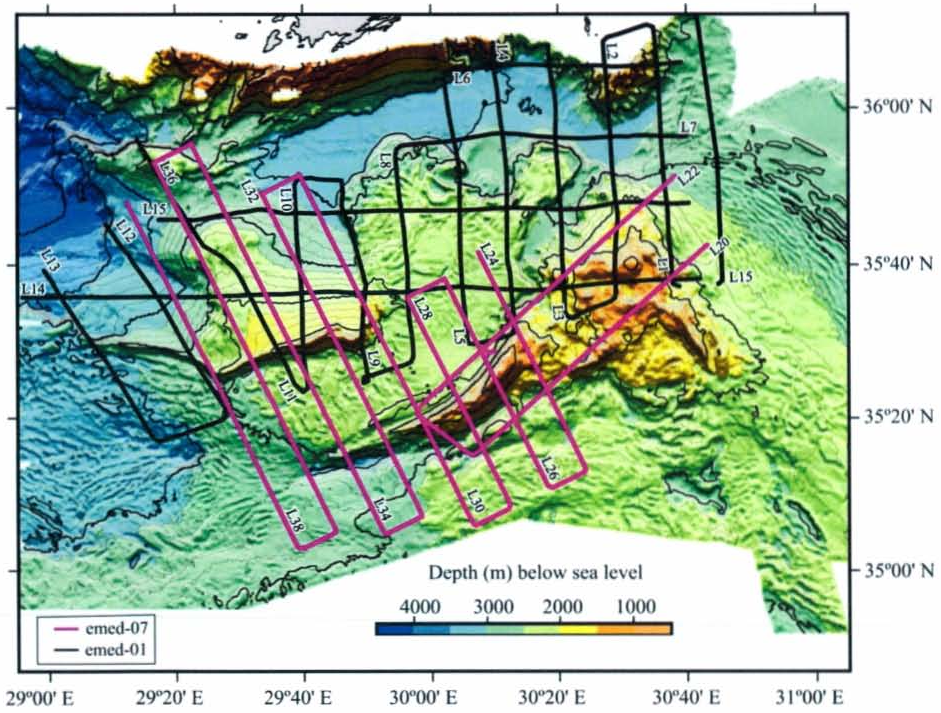

Figure 2.4 Multi-beam bathymetry map of the eastern Mediterranean Sea showing all lines used for this thesis. The 2007 lines (900 km) are highlighted in pink and the 2001 lines (1100 km) are highlighted in black. L9, L38 etc are line numbers.

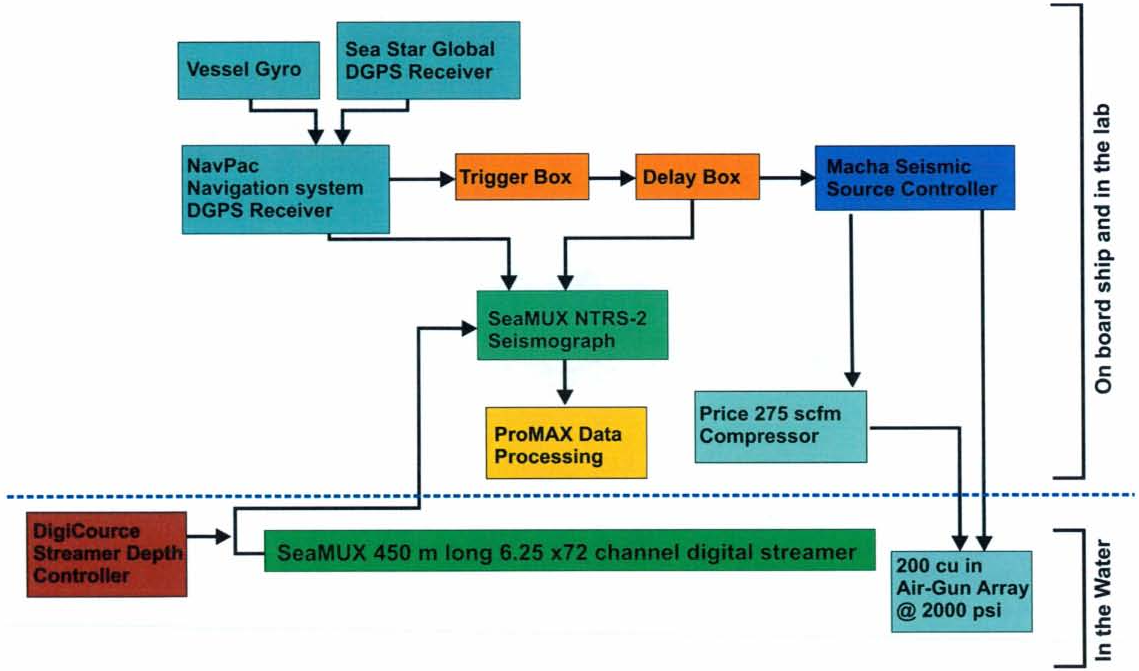

Figure 2.5 Flow chart illustrating the cruise set up for the 2007 eastern Mediterranean seismic survey.

Figure 2.6 Memorial University of Newfoundland's broad-band, high-frequency array consisting of seven sleeve guns

guns (2 x 164 cm^3), with a total volume of 200 in^3 (3277 cm^3). Two of the 40 in^3 guns were placed in close proximity to one another, so that when they fire, their bubbles would coalesce to emulate an 80 in^3 gun. Seismic reflections were recorded using a 72-channel, 450 m-long high-resolution Hydroscience Technologies Inc. streamer array, with a group interval of 6.25 m (72 x 6.25 = 450 m), producing a nominal fold of 9 (Equation 2.3; see below). The streamer was towed at a constant depth (~3 m below the surface of the water) using eight Digi-Course streamer depth controllers, also known as streamer birds. The data were recorded digitally (using the NTRS-2 seismograph) for five seconds below the sea bed with a 1 millisecond sample rate. The delay was altered onboard ship, according to the change in water depth. All incoming data was stored on data DVDs and an external hard drive.

$$\text{fold} = \tfrac{1}{2} [\text{number of channels (group interval/shot interval)}] \qquad (2.3)$$

So in this case,

$$\text{fold} = \tfrac{1}{2} [72\ (6.25/25)\ ] = 9$$

The acquisition parameters for the 2001 survey were similar to those used for 2007 survey, with the following variations. For the 2001 survey, the same sleeve gun array was used as the source, with a total volume of 200 in^3 (3277 cm^3) and shots were fired to time every 9-10 seconds using the vessel's internal clock to trigger the pulse. In contrast, the 2001 data were recorded using a 48 x 12.5 m Teledyne streamer, with a total length of 600 m. The added streamer length produces a greater fold of 12 for the 2001

data. The data were recorded three seconds below the sea floor with a 1 ms sample rate and stored on DAT (digital audio tapes) tapes using a 48 channel OYO DAS-1 seismograph. An initial gain of 36 dB and a slight filter with low-cut frequency of 8 Hz and dB/OCT slope were also applied.

2.2.2 Geometry of the Survey

The geometry of the 2007 eastern Mediterranean cruise is provided in Figure 2.7 and details of the acquisition geometry are given in Table 2.1.

2.3 Post Cruise Procedures

2.3.1 Data Processing Methods

A marine seismic reflection processing flow generally includes: analysis of shot records, frequency filtering, gain control, application of geometry and common mid point (CMP) sorting, CMP gather (CMP is used interchangeably as common depth point - CDP), velocity analysis, normal move out (NMO) correction, deconvolution, stack and migration (Fig. 2.8). These processes are further discussed with specific reference to 2007 data in Chapter 3. It is important to note that each step is dependent on the success of the process that came before it, confirming that seismic processing is an iterative and incremental procedure and many steps are repeated in order to determine the optimal processing parameters. The ultimate goal of processing seismic data is to increase the signal to noise ratio and produce the best possible image of the subsurface geology. This is accomplished through the following steps: (i) to determine the appropriate parameters

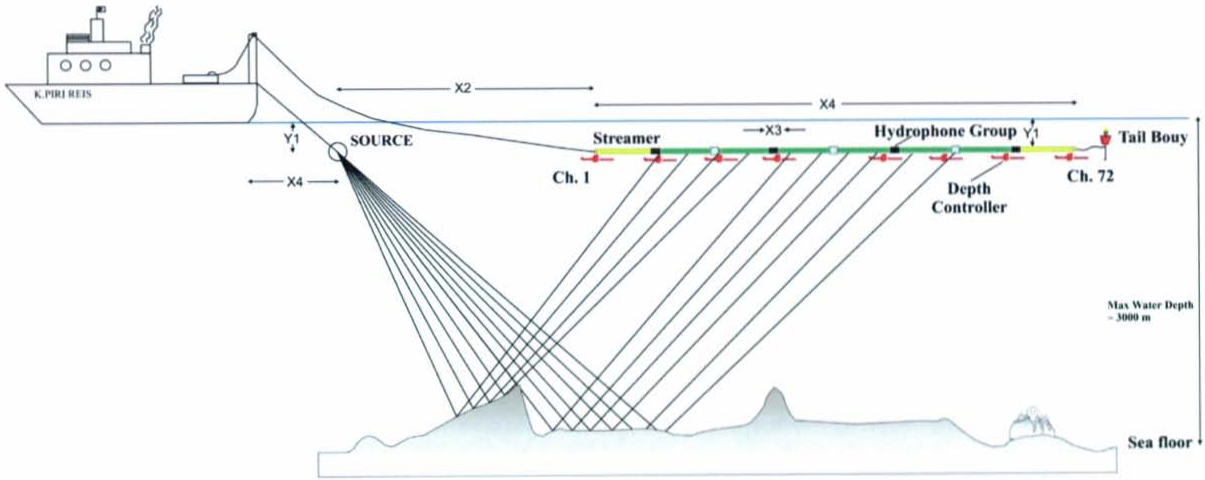

Figure 2.7 The survey geometry for the 2001 and 2007 eastern Mediterranean seismic cruises; the sea bed is not drawn to scale (Modified from Işler, 2003). A summary of the information illustrated in this figure is provided in Table 2.1.

Table 2.1 Survey Geometry

	emed_2001	emed_2007
Stern to Source (X1)	37 m	50 m
Source to centre of first hydrophone group (X2)	95 m	80 m
Hydrophone group interval (X3)	12.5 m	6.25 m
Active streamer length (X4)	600 m	450 m
Source and streamer depth (Y1)	3 m	3m
Shot interval	25 m	25 m
Fold	12	9

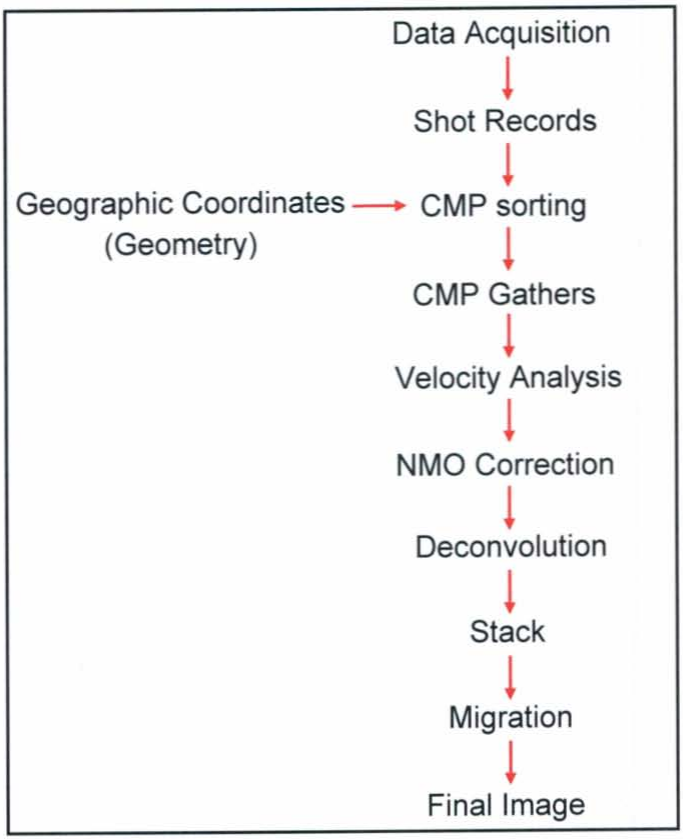

Figure 2.8 Generic data processing flow.

for each process, (ii) to evaluate the output and (iii) to adjust any processing artifacts left from incorrect parameters (Yılmaz, 2001).

A shot record contains both signal, which produces the seismic image, and noise which distorts the image. Primary energy occurs as seismic reflections and noise can be both coherent (e.g., multiple reflections) and random (e.g., noise from the ships propeller, the recording equipment, stormy weather, etc.).

Analysis of Shot Records

The analysis of the shot records involves the examination of the raw data using all channels, paying attention to the frequency content, amplitude variations in the data. The first step is to examine the trace display of the raw data along with the corresponding amplitude spectrum, which involves running of a spectral analysis. This process allows an initial determination of the signal to noise ratio for the data set. The data is then often displayed as a near trace gather, which provides, for the first time, the nature of the subsurface geology.

Frequency Filtering

Following the inspection of the raw data, a bandpass filter within the frequency range of the data set is applied. Frequency filtering increases the signal to noise ratio, giving the operator a clearer image of the data and its frequency content. The above steps provide the operator the necessary information to determine if further trace editing is required, such as the removal of noisy and/or dead traces, and time delay corrections. It

is important to remember that applying a permanent filter at this early stage of processing can lead to removal of frequency content which can adversely affect the quality of the final image. Detailed examples for these steps are provided in Chapter 3.

Gain control

As P-waves travel through the Earth, the amplitude of the wavelet decreases with time due to geometrical spreading (spherical divergence) of the energy, reflection, transmission, and the anelastic attenuation with increasing depth (Yılmaz, 2001). Therefore, the maximum amplitudes are concentrated at shallower depths, and the amplitude of a given event decreases with increasing depth (Fig. 2.9a).

A gain function is used during processing to balance amplitudes down the seismic section (i.e., increasing depth) by scaling up and down the low and high amplitude events, respectively (Fig. 2.9b). It is important to note that applying a gain function permanently alters the true amplitude information, thus caution must be exercised when using a gain function.

CMP Sorting and CMP Gather

It is possible to produce a seismic reflection image with a single source and a number of receivers. However, in this case, each reflection point in the subsurface is only sampled once. Sorting the data using the CMP method provides multiple coverage of each point sampled in the subsurface (i.e., every point is sampled >1). Thus, sorting the data using the CMP method creates redundancy of the sampled points, increases the

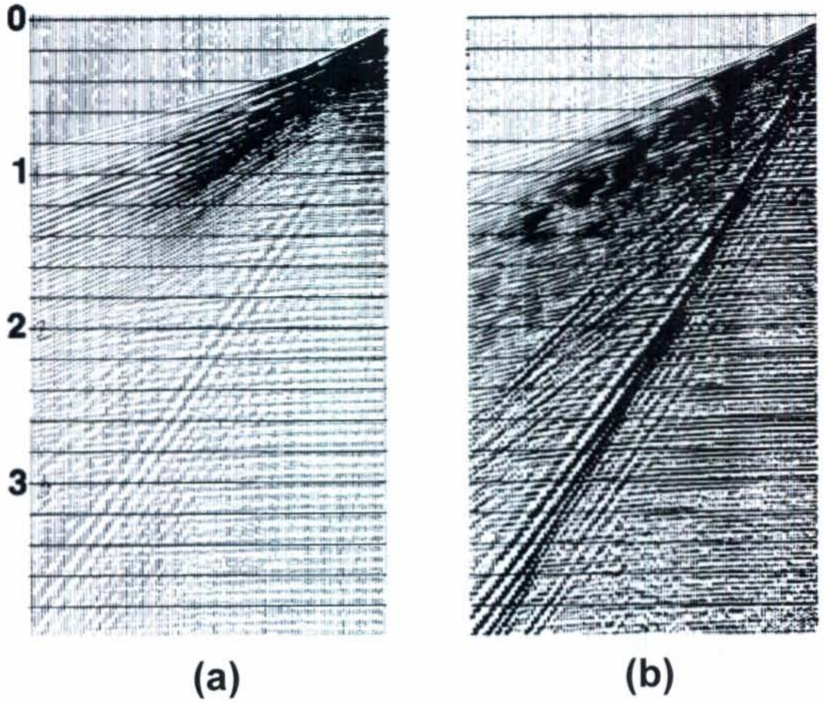

Figure 2.9 **(a)** Raw shot record before the application of a gain function and correction of geometrical spreading. Notice, Amplitudes rapidly decay at later times and **(b)** the same shot record after the gain function has been applied. The amplitudes have been restored to later times (Yılmaz, 2001).

signal to noise ratio and ultimately enhances the quality of the seismic image (Fig. 2.10). This process is called CMP sorting where each trace is assigned a midpoint for a source receiver pair and all traces that correspond to a given midpoint create a CMP gather (Figs. 2.11a, 2.12a). The number of traces in a CMP gather represents the redundancy of each sampled point and defines the fold of the dataset (Equation 2.3).

Velocity Analysis and NMO Correction

There are a number of different tools that can be used for the velocity analysis (Yılmaz, 2001, proMAX Users Manual), such as the semblance spectra, constant velocity stack, and the constant velocity gathers. The semblance spectra represents a range of velocity hyperbolas for a given t_0 and calculates the coherence and semblance, measures of similarity that compare one trace to the next (Fig. 2.13a). The point in the spectra with the maximum coherence or semblance is the best NMO velocity provided that the event is a primary reflection (Yılmaz, 2001). The CMP gather displays the common offset stacked supergather (described in Chapter 3) for the specified CMPs (Fig. 2.13b). By applying the interactive NMO application to the CMP gather it was possible to see if each pick was under- or over-corrected for the NMO velocity. The NMO correction is described below, but this is an iterative process because the NMO correction requires accurate velocity information. When the velocity pick is too low and over-corrected for NMO the event will curve up. If the pick is too high and is undercorrected for NMO the event will curve down. When the NMO velocity is correct the given reflection in the gather will appear flat in time. These three cases are further illustrated using examples

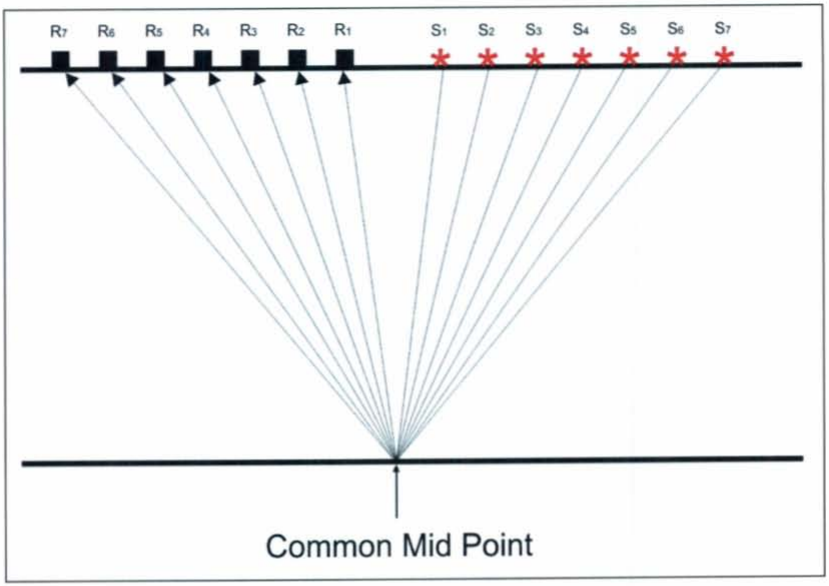

Figure 2.10 Reflection experiment using the common mid point (CMP) method showing a 7-fold CMP gather.

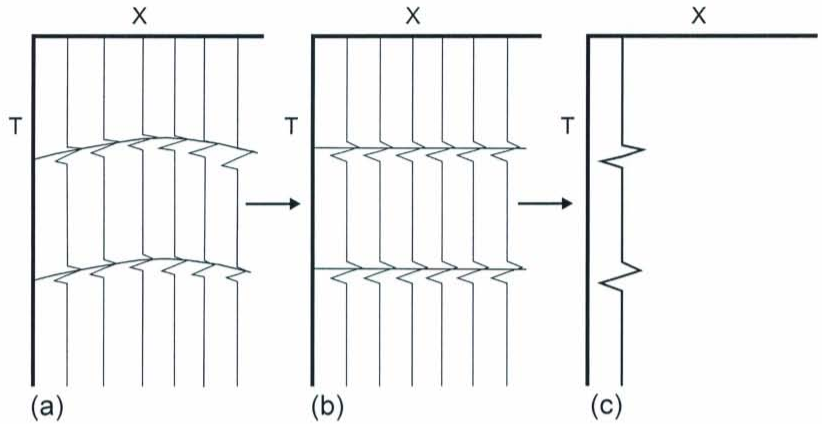

Figure 2.11 A series of seismographs showing CMP gathers with **(a)** hyperbolic NMO response, **(b)** events that have been corrected for NMO and (c) a stacked seismic trace.

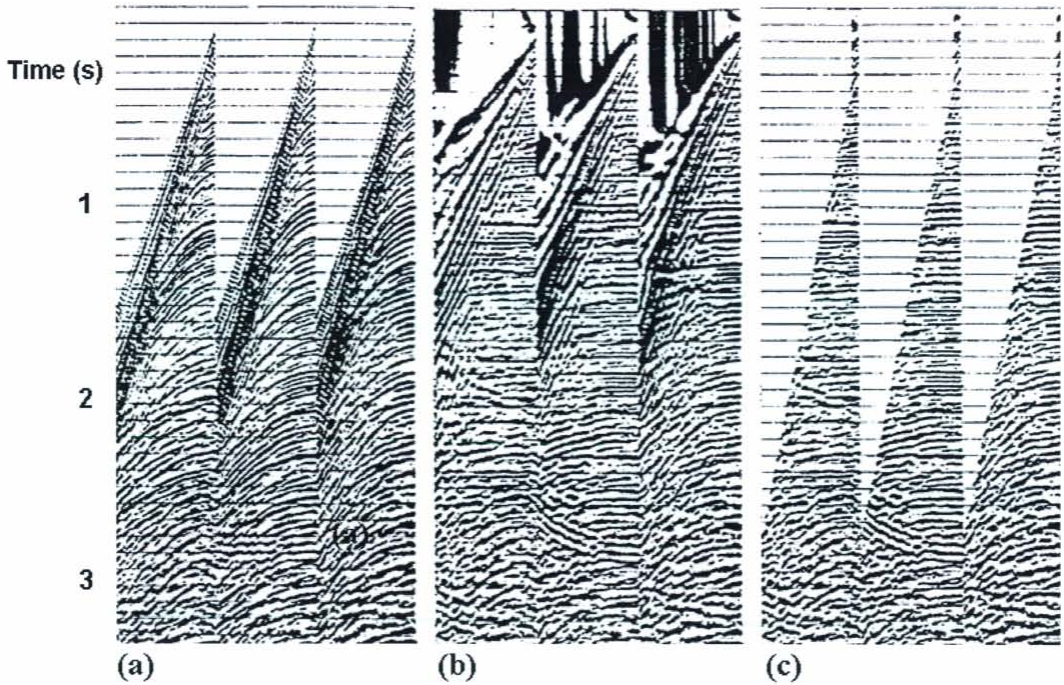

Figure 2.12 From left to right **(a)** CMP gather that has not been corrected for NMO, **(b)** NMO corrected showing the NMO stretch factor and **(c)** NMO corrected gathers with the application of a top mute (Modified from Yılmaz, 2001)

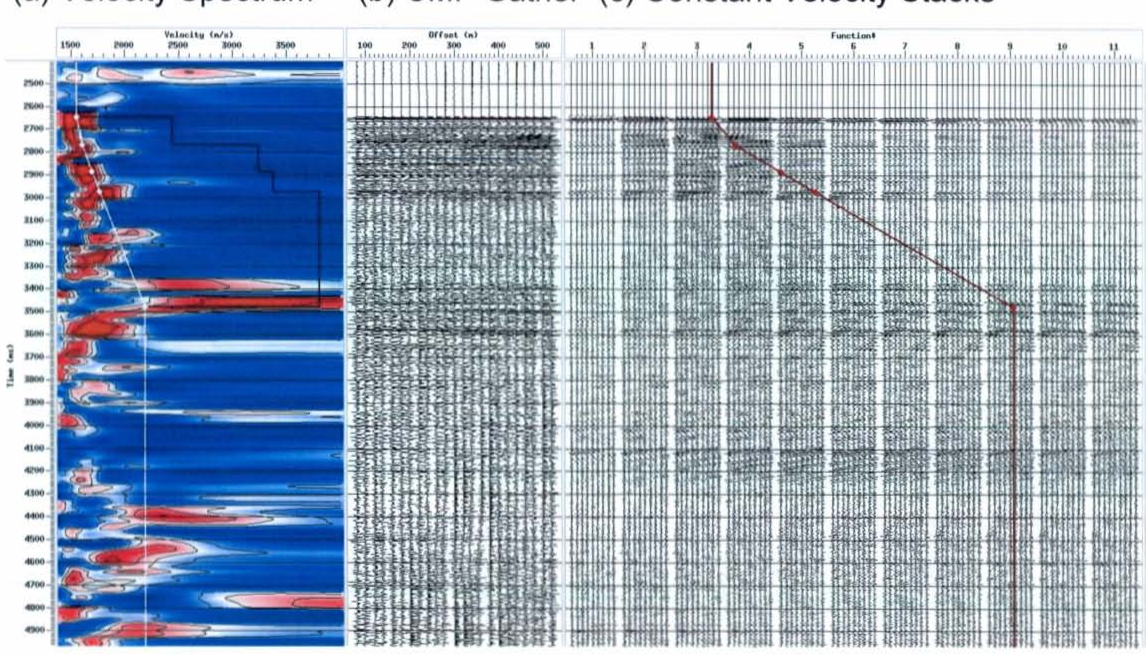

Figure 2.13 Velocity analysis showing from left to right **(a)** the velocity color spectrum, **(b)** common mid point (CMP) gather and **(c)** constant velocity stacks used to determine stacking velocities.

from the 2007 data in Chapter 3. The constant velocity stacks are a series of side-by-side stacked traces for a given supergather (Fig. 2.13c). Each trace is at constant velocity and is corrected for NMO (see below).

NMO Correction

Normal-move-out (NMO) is the effect of the separation between a source and a receiver on the arrival time of a reflection from a horizontal surface. A reflection will arrive at the closest receiver first and the offset between the source and the subsequent receivers will produce a delay in the arrival times, thus the resulting seismograph is a hyperbolic function (Fig 2.11a). The NMO correction is applied to the data to flatten the reflection hyperbolae by shifting the arrival time of each reflection to an equal arrival time for all reflections, the normal incidence travel time (Fig. 2.11b). Before the stacking process can be carried out, the data must be corrected for NMO. Equation (2.4) for the NMO correction requires velocity information and because we use the data to determine the velocities, the success of the velocity analysis is ultimately a function of the data quality (Yılmaz, 2001).

$$T_N = (X^2) / 2V^2 t_o \qquad (2.4)$$

where T_N = normal moveout corrected travel time, X = distance between source and receiver, V = average velocity to the depth corresponding to t_o, and t_o = normal incidence travel time.

One problem with the NMO correction is that the equation is not linear and its application distorts the shallow portion of the data (Fig. 2.12b). This is known as the NMO stretch factor. A stretch factor of 10-20% is acceptable, but anything greater must be removed or zeroed by applying a top mute to the data (Fig. 2.12c).

Deconvolution

The recorded seismic event is the response from a given reflector and is a combination of the source signature, the receiver response, the instrument response and the geology (Krebes, 1985, 1989, Yılmaz, 2001). The goal of wavelet processing is to attenuate the response from the first three variables (i.e., the source signature, the receiver response, the instrument response) and extract the information on geology.

Spiking deconvolution (also called spectral whitening) increases the temporal resolution of the data by collapsing the seismic wavelet to a spike, which is closer to the true geological response. Strictly speaking, the spiking deconvolution operator is the inverse of the wavelet. The process is carried out using both the inverse and the least-squares statistical filters and is dependent on the length of the filter and whether the seismic wavelet is minimum phase or not (Yılmaz, 2001, proMAX Users Manual). The unwanted response of the source, receiver and instruments are treated as linear filters and inverse filters are designed to attenuate these effects. The success of the deconvolution rests on the assumption that (i) the seismic wavelet is minimum phase, and (ii) the information on the original form of the wavelet is known, or can be estimated from the recorded trace. Examples of the deconvolution are given in Chapter 3.

Stack

The stacking process involves summing together each trace in the NMO corrected CMP gather and dividing the product by the total number of traces in the gather to produce a single stacked trace (see Equation 2.5).

$$\text{Stack} = S_0^t \left({}^{1/n} S_1^n S(t) \right) \qquad 2.5$$

where Σ = sum of all traces normal, t = , n = , S = average velocity to the depth corresponding to t_o, and t_o = normal incidence travel time.

The stacked trace (Fig. 2.11c) is an average of the total energy of each trace in a given CMP gather. The stacked CMP gathers are NMO corrected, meaning the arrival time of each event is shifted to the normal incidence travel time (at X=0). Therefore, the staked seismic section is an estimate of the normal incidence travel time (Yılmaz, 2001). CMP stacking enhances reflections and attenuates unwanted noise and multiples (Krebes 1985, 1989). In general, multiple reflections have lower stacking velocities than primaries, therefore they require a greater NMO correction. During velocity picking it is possible to pick the correct NMO velocity for the primary reflections and the multiples will stack-out.

In the text above, only the reflection experiments with respect to horizontal layers are described. However, Earth is complex and most strata in it have a component of geological dip. When an interface is dipping several issues arise including CMP smear

and mispositioning of the CMP (Fig. 2.14). Source receiver pairs with the same theoretical midpoint (assuming dip =0) do not have the same actual midpoint. In such cases, the actual midpoint will be projected up dip, resulting in a smear of the sampled points (e.g., Yılmaz, 2001). Also, the projection of actual mid point to the surface does not fall at the same location of the theoretical midpoint and the seismic section will be miss-plotted (Fig. 2.14).

Migration

After stacking diffraction hyperbolae are still visible, making the geological interpretation difficult. The process of migration collapses these diffractions, moves dipping reflections to their correct locations, increasing the spatial resolution of the data. In nature, reflectors are rarely horizontal and almost always have some component of dip. Dipping reflectors cause mispositioning of the common midpoint (e.g., Fig. 2.14) and the final image can be distorted. The migration process restores this image by moving the theoretical reflection points up-dip to their true locations in the subsurface and the migrated segment is steeper and shorter than the stacked segment (Fig. 2.15). The goal of the migration process is to collapse diffractions that are visible in the stacked section to a single point to produce an image that is the best representation of the true subsurface geology. Thus, the migration process focuses the final seismic image, making detailed structural and stratigraphic interpretations possible. After the data is migrated, complex structures such as steep flanks and fault plains can be imaged more precisely (Yılmaz, 2001).

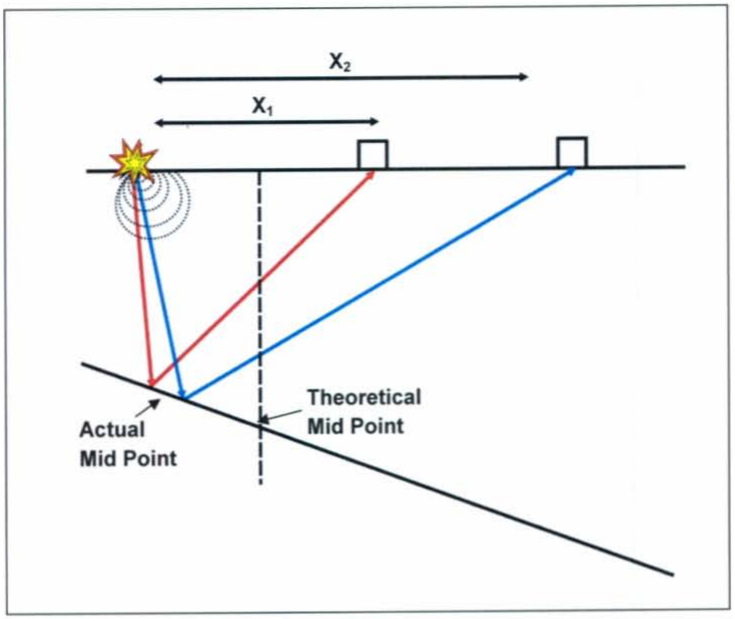

Figure 2.14 Seismic ray path diagram from a dipping interface. Dipping reflector can lead to mis-positioning of the mid point, also known as common midpoint smearing. Mis-positioned midpoints are corrected up dip to their true positions by the migration process

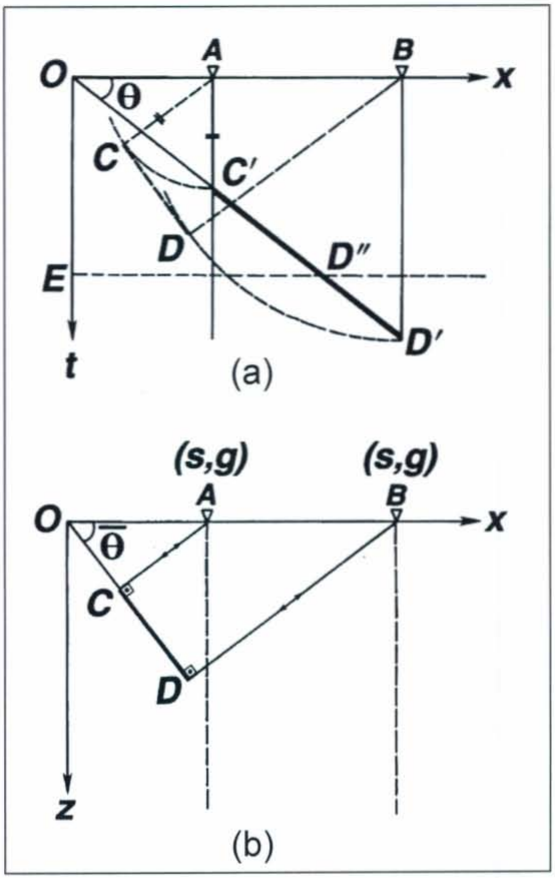

Figure 2.15 Migration principles: The reflection segment C′D′ in the time section as in **(a)** when migrated, is moved up-dip, steepened, shortened, and mapped onto its true subsurface location CD as in **(b)**, the depth migrated (from Yılmaz, 2001)

The process of migration makes the stacked sections look like a true geological cross sections. However, the vertical axis of a cross section is recorded in depth (Z), thus, the t-x section (fig. 2.15) must be converted from the time domain into the migrated depth domain, a process called depth migration. Depth migration requires accurate interval velocity information and therefore, time migration is commonly used for interpretation purposes, especially in deep water surveys like the present study, where velocity control is not well constrained.

2.3.2 Approach to Structural Interpretation

Detailed interpretations of the seismic profiles are carried out by tracing prominent reflections and major unconformities. Thickness maps (in two-way travel time) are made of (i) the upper unit above the major regional unconformity, referred to as the M Reflector and (ii) the middle unit between the M-reflector and the N-reflector, another major regional unconformity (described later). The sedimentary and structural evolution of the Anaximander Mountains and environs since the Late Miocene is delineated by detailed interpretation of the high resolution seismic reflection profiles. Reflectors are correlated using crossover points between the 2001 and 2007 seismic reflection profiles. The level of confidence is found to decrease as one moves farther away from cross over points between the 2001 and 2007 profiles.

Sequence stratigraphy is a geological approach to the stratigraphic interpretation of seismic data: it is theoretical, interpretative and descriptive (e.g., Mitchum et al., 1977, Myers and Milton, 1996). During seismic analyses, the seismic reflection profiles are

divided into distinct packages, known as depositional sequences, which are composed of relatively conformable reflections from genetically related strata bounded at their tops and bases by unconformities or their correlative conformities (e.g., Mitchum et al., 1977, Myers and Milton, 1996). The first step in the seismic interpretation is to print paper copies of the original seismic reflection profiles from the 2001 and 2007 eastern Mediterranean surveys from digital data files. Next, the seismic reflections are divided into discrete seismic stratigraphic packages. This is accomplished by identifying and marking reflection terminations on seismic reflection profiles. Next, distinctive seismic reflections, in particular those defining regional unconformities, are highlighted using colored pencils. Later, the unconformities are re-traced as precisely as possible and correlated throughout the seismic grid to ensure agreement at cross-over points. Mitchum et al. (1977) describes reflection terminations using the terms lapout, truncation, baselap, onlap, downlap and toplap which are used to delineate geometric relationships that define structural architecture along discontinuities in the seismic reflection profiles (Fig. 2.16). These terms are readily used during seismic stratigraphic interpretation and mapping.

Truncation is the termination of a reflector that has been eroded and/or cut from its original size, but is not formed as the consequence of non-deposition. Truncation termination types include: erosional and fault truncations (Mitchum et al. 1977). Baselap is the lapout of reflections against an underlying seismic surface and can be further subdivided into two types: downlap occurs when the younger surfaces dip more steeply than the underlying strata (Fig. 2.16). An onlap occurs when the older surface is dipping

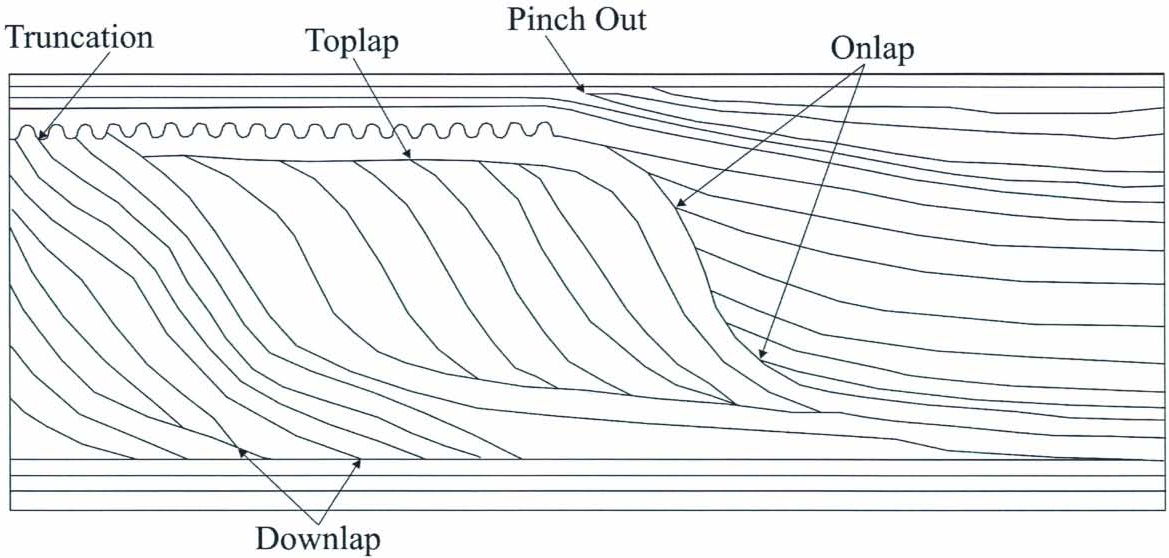

Figure 2.16 Schematic cross section showing onlap, lapout, downlap, toplap and truncation reflector terminations observed in seismic reflection profiles (modified from Işler, 2005).

more steeply. The up-dip termination of an inclined reflector against an overlying near horizontal surface in seismic reflection profiles is identified as toplap (Fig. 2.16). Unconformities are delineated by truncations and/or at downlap, onlap, and toplap reflection terminations against widespread reflections. During this thesis all seismic reflection profiles collected from the Anaximander Mountains (*sensu lato)* are interpreted by the author. Structural interpretation of seismic reflection profiles is based on identification of folds and faults at locations where they directly offset adjacent strata, with further recognition from associated secondary structures when primary offsets are not visible. A schematic of the different geological structures used for structural interpretation is provided in Figure 2.17. The results are described in Chapters 4 and 5.

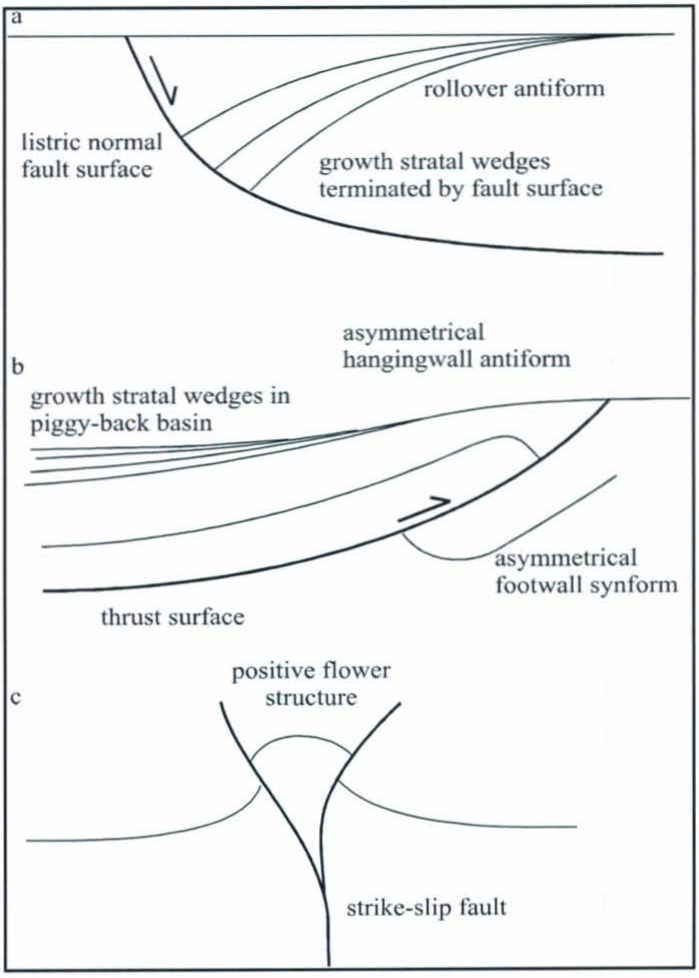

Figure 2.17 show secondary structures associated with **(a)** listric normal faults, **(b)** thrust faults, and **(c)** strike-slip faults, (From Aksu et al., 2009)

CHAPTER 3. Seismic Data Processing

The seismic reflection data processed for this thesis were collected during the summer-fall 2007 eastern Mediterranean research cruise using the RV *Koca Piri Reis*. The data processed for this thesis include eight lines (~700 km) running northwest-southeast over the greater Anaximander Mountains area (Fig 3.1). The other lines used for interpretation were acquired during the 2001 survey (described in Chapter 2) and were previously processed at Memorial University of Newfoundland by graduate and undergraduate students. All seismic data processing was completed at Memorial University of Newfoundland using the Landmark proMAX© software, running on SUN SunFire servers.

The processing flow that was used to process all lines from the shot domain to final migration is provided in Figure 3.2. Processes applied to the data include, trace editing, frequency filtering, gain control, velocity analysis, normal move out correction, deconvolution, common midpoint, migration and multiple attenuationö sımılar to the generic flow described in Chapter 2. These processes are described in greater detail in this chapter with specific references to the 2007 seismic reflection profiles, processed by the author.

3.1 Display

The display application in proMAX© is an extremely useful tool. It is used to display the data on the screen for visual inspection during processing. By analysing the

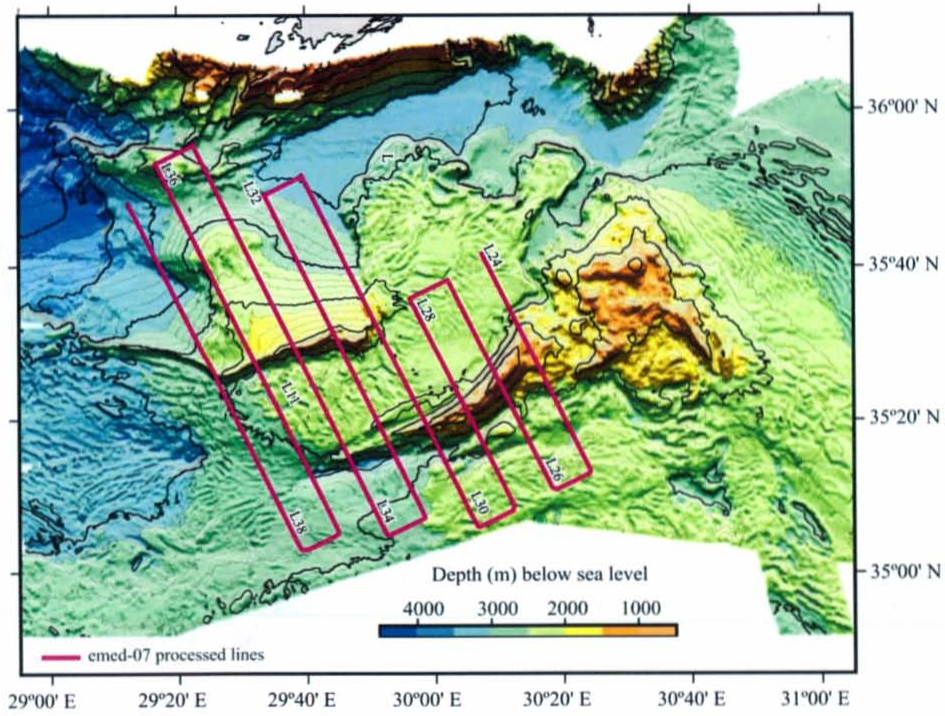

Figure 3.1 Detailed multi-beam bathymetry map of the eastern Mediterranean Sea. The lines processed for this thesis are pink (L24-L38).

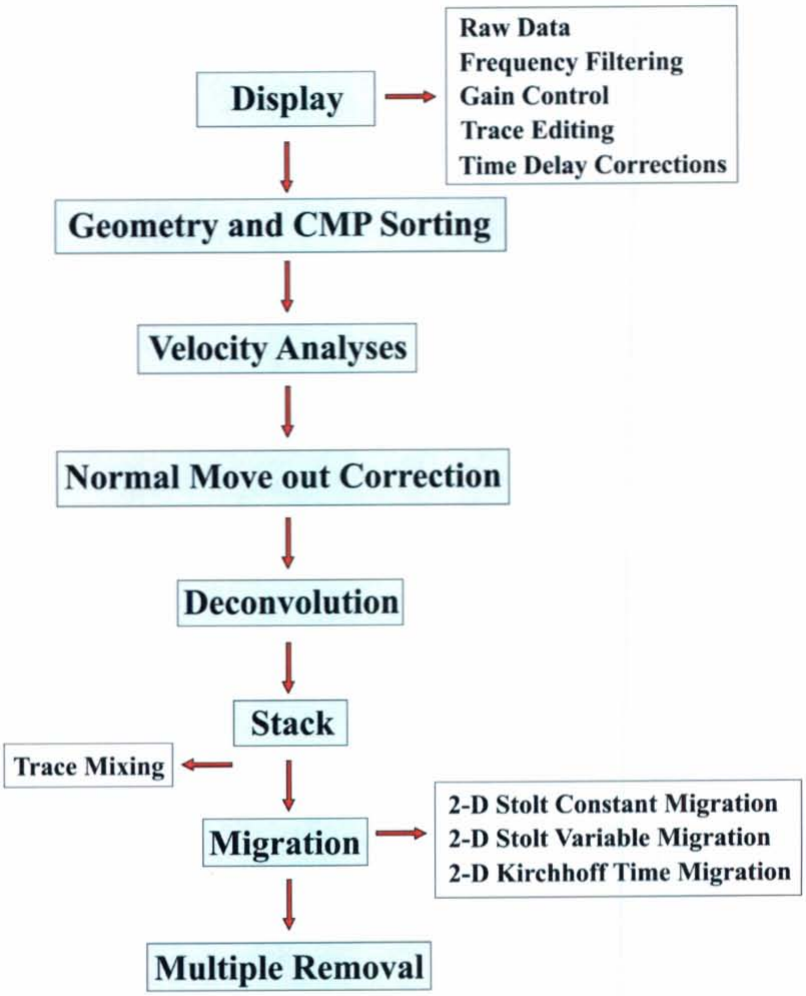

Figure 3.2 Marine seismic data processing flow used to process the 2007 data used for this thesis.

trace display for each line it is possible (i) to determine optimal filter parameters, (ii) to perform trace editing, (iii) to correct time delays if necessary, and (iv) to apply an appropriate gain control. The display flow is also used to create paper-plots that are printed at various steps during processing for data quality control and to produce the final bitmap images. These display applications are described in greater detail in the following sections.

3.1.1 The Raw Data

First, the raw-data is loaded into proMAX© work space using the SEG-Y input application. Next, shots are displayed using all channels (Fig. 3.3a) and as a single channel/near trace gather (Fig. 3.4). First inspection of the raw data shows that the signal to noise ratio of the 2007 data is very low and it is hard to distinguish primary reflections. The seabed reflection can be distinguished at ~500 ms, but it is strongly masked by high levels of noise (Fig. 3.3a). The amplitude spectrum of the raw data graphically represents the amplitudes of the various frequencies of the seismic signal and it is a direct indicator of the low signal to noise ratio for this dataset (Fig. 3.3b). The frequency band of the signal lies around 50-200Hz and is barely visible in the spectra, while a strong low-frequency noise dominates the spectra at ~10 Hz.

3.1.2 Frequency Filtering and Spectral Shaping

It is impossible to produce an interpretable seismic image when the primary energy is significantly masked by high levels of noise. Therefore, it is necessary to

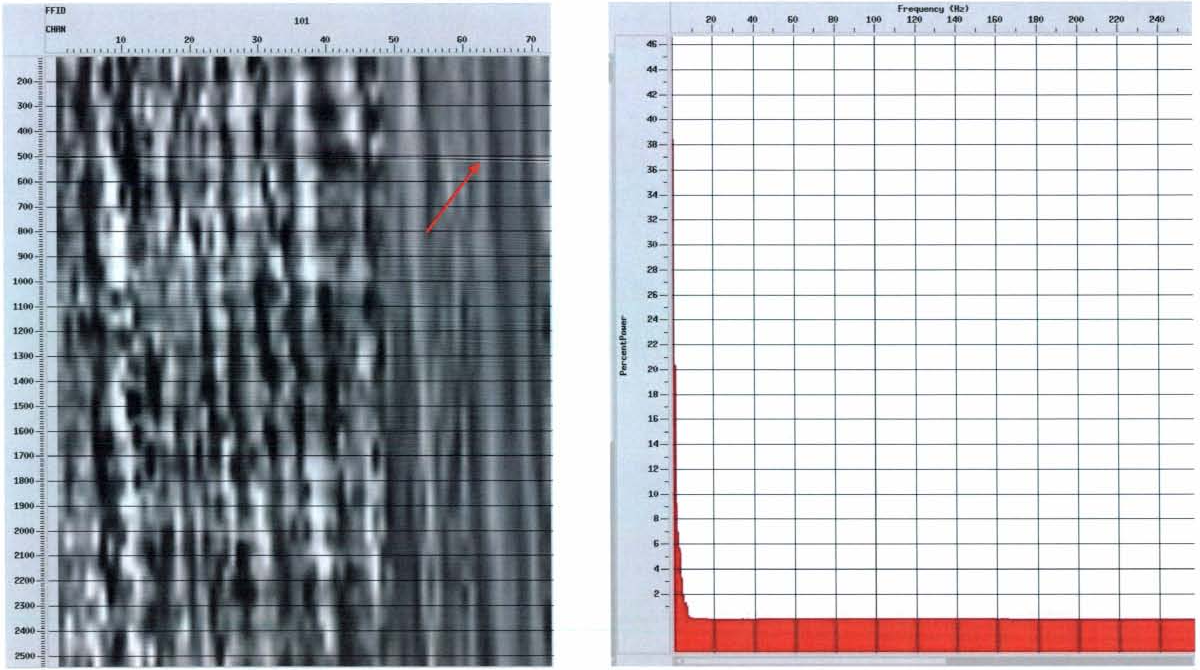

(a) **(b)**

Figure 3.3 **(a)** Trace display of the raw data using all channels. The red arrow highlights the seabed reflection at ~500 ms and **(b)** the amplitude spectrum of the raw data. Notice that the primary signal is dominated by noise and that there is a significant low frequency peak ≤10 Hz

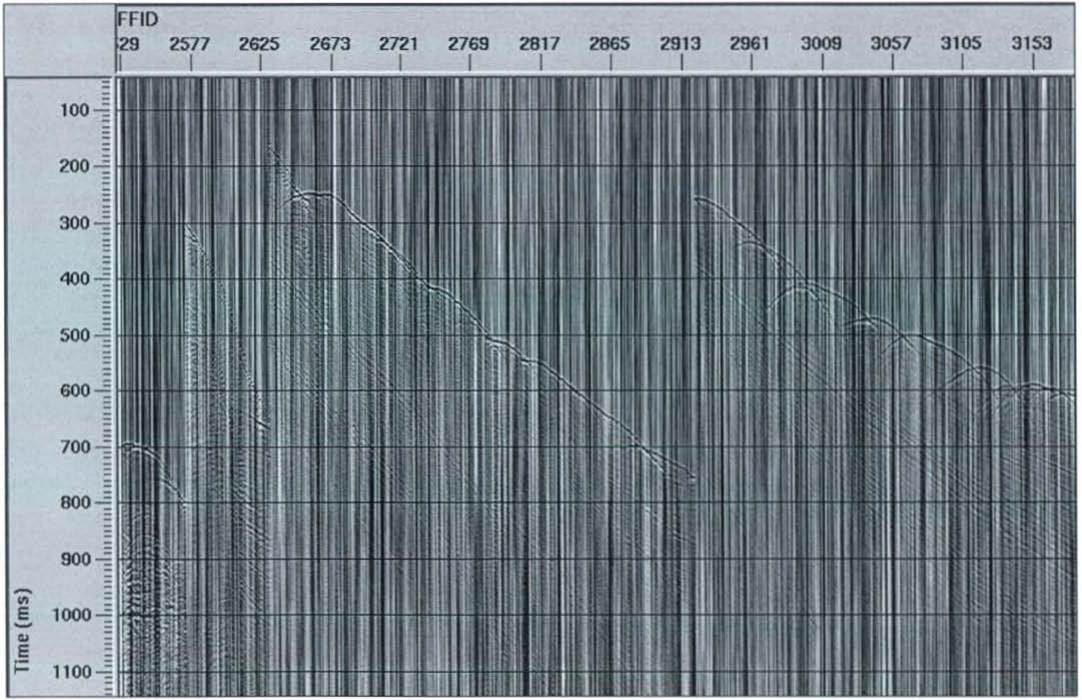

Figure 3.4 Raw data displayed using a single channel/near trace gather.

develop a filter that will suppress the unwanted noise, enhancing the primary energy. Both Ormsby and Butterworth filters were tested using the trial and error method, by altering the filter and phase values to develop the best possible filter. In the end, the most favourable filter is determined to be a minimum-phase Butterworth filter with a typical bandpass around 40-220 Hz (Fig. 3.5). The filtered data show significant improvements in the signal to noise ratio; however, the large peak of low frequency noise at ~10 Hz continues to dominate the spectrum, reaching values >95% power (Fig. 3.5b). Figure 3.6 shows a near trace gather of the data after the application of the 40-220 Hz Butterworth bandpass filter. It is noteworthy that the low frequency noise is clearly visible though the profile. The low frequency noise illustrated above affected every seismic reflection profile in this study, and therefore required additional applications before further processing could take place.

Many filters were tested to remove the low frequency noise from the spectra: unfortunately, none were successful. Therefore, other processing techniques were necessary to eliminate the low frequency spike. The most favourable application was a process called spectral shaping. This process balances frequency filtering by applying a spectral shaping algorithm to all input traces (proMAX© Users Manual). Spectral shaping in the frequency domain scales and multiplies all frequency components by a specified contour with no effect on the original phase of the data. The shaping contour is defined by a series of frequency-amplitude pairs, where amplitudes are given as a percentage of the maximum amplitude. Several shaping contours were tested, but the best shaping contours for the data set were found to be 10-40 Hz, 40-100 Hz, 250-100

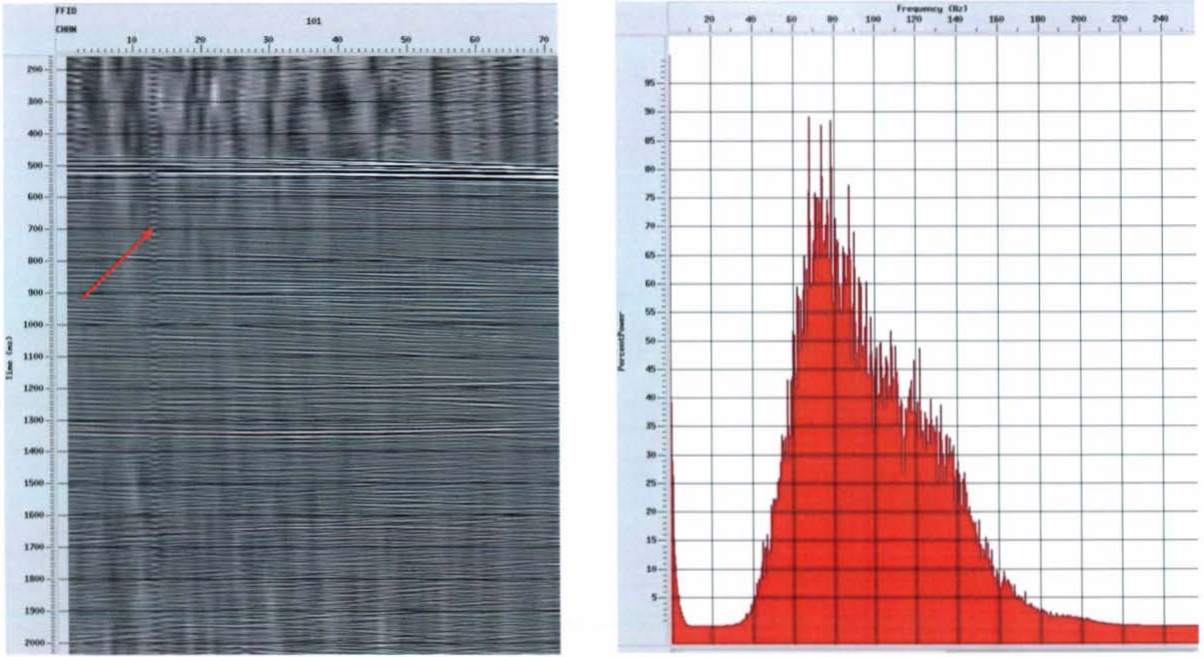

(a) **(b)**

Figure 3.5 **(a)** Trace display after the application of a bandpass filter. The red arrow points out that channel 13 is a noisy or dead trace that must be removed and **(b)** amplitude spectrum after a bandpass filter was applied. Although the signal has been amplified the large peak of low frequency noise has not been eliminated by the filter.

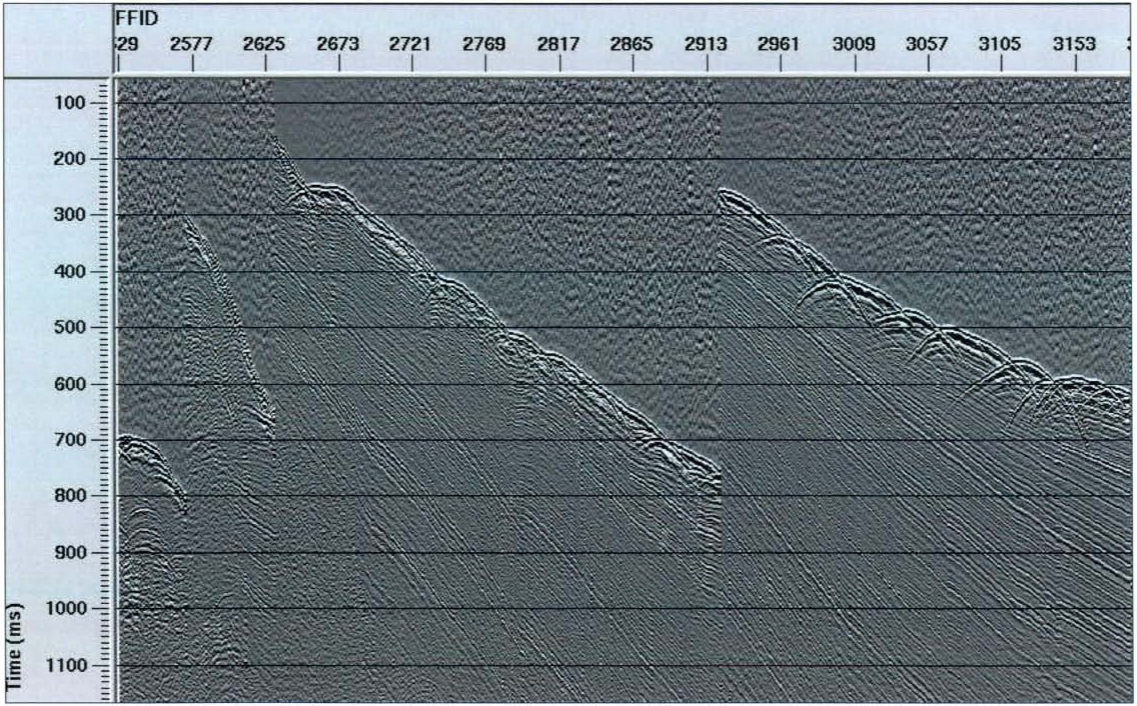

Figure 3.6 Single channel/near trace gather after the application of a butterworth bandpass filter. Notice that although some noise is still visible, the signal to noise ratio has increased and individual reflectors can now be identified.

Hz, 500 Hz. After spectral shaping is applied, the low frequency spike is completely eliminated from the amplitude spectrum (Fig. 3.7). Both Butterworth bandpass filter and spectral shaping are used for display purposes only and are never applied permanently to the data.

3.1.3 Trace Editing

The stacking process involves taking the average amplitude of a given number of traces (i.e., summing together a number of traces and dividing by the total number of traces). An inspection of the trace display (e.g., Fig. 3.5a) confirms that all channels, except channel thirteen are very good. Channel thirteen is consistently either extremely noisy or dead in the 2007 data. Including a bad trace in the stacking process would have negative effects on the final stacked section. Therefore, it is killed/zeroed (Fig. 3.7a) for each line before further processing was carried out. Killing a single channel/trace did not have any adverse effects on further processes.

3.1.4 Time Delay Corrections

The bathymetry of the greater Anaximander Mountains and surrounding areas is extremely complex and there are significant variations in seafloor depth over relatively short distances (e.g., Fig. 3.1). Because of the short shot cycle time, and the time required to write the data to the storage device, it was necessary to use delayed recording to maximize the recorded information from the seabed and below. Therefore, time delays of ±500 ms were manually applied during data acquisition when necessary, to insure the

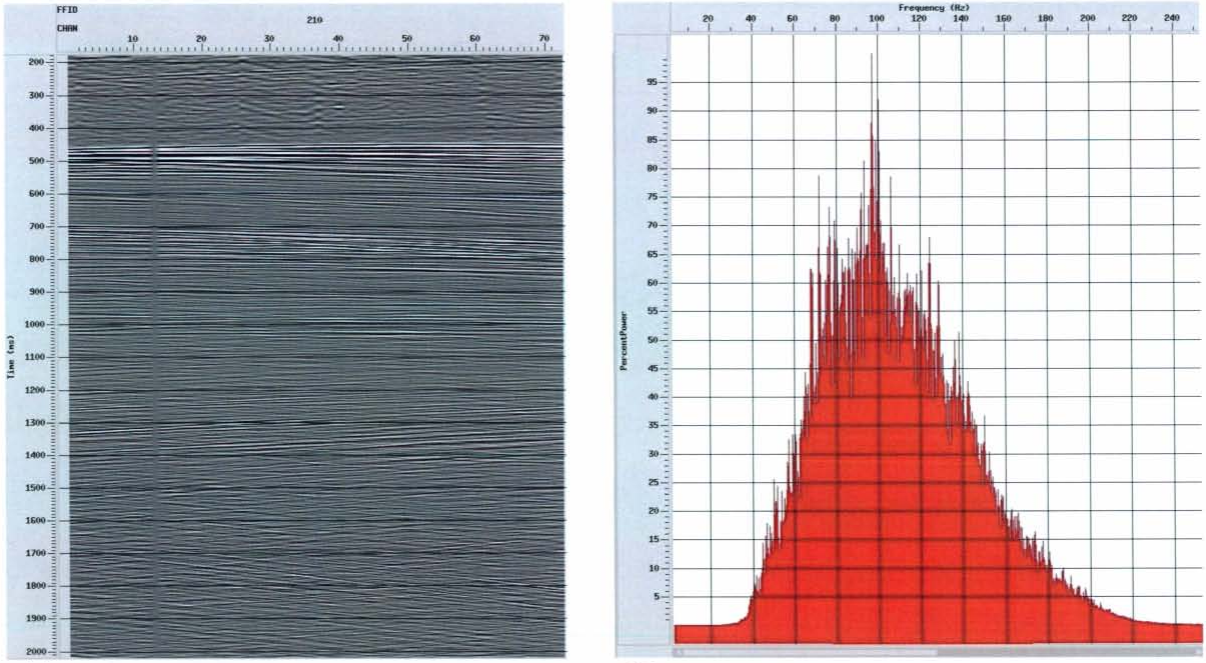

(a) **(b)**

Figure 3.7 **(a)** Trace display and **(b)** amplitude spectrum after the application of a Butterworth band pass filter and spectral shaping. Notice that after spectral shaping was applied the low frequency peak was eliminated from the amplitude spectrum.

maximum amount of data was recorded at all times (Fig. 3.8). During data collection each delay change was recorded by the scientific crew in the cruise-log-book and was later used as a reference during processing in the laboratory.

Although, each delay change was recorded in the cruise-log-book a significant amount of time was spent during data processing, checking each trace of the near trace gather individually to ensure the correct field file identification (FFID) number is determined for each delay change. In order to determine the exact FFID where the delay was applied it was necessary to zoom in and inspect each trace individually (Fig. 3.9). A proMAX© process – hand-statics – is used to shift the time-delayed data back to its original position (Fig. 3.10).

3.1.5 Gain Control

Because the amplitudes of the data decrease with increasing depth, a gain function is required to balance the amplitudes of the seismic data. There are a variety of gain functions available for data processing (e.g., proMAX© Users Manual). The automatic gain control (AGC) is one of these gain functions, which is commonly used in seismic data processing, and is chosen as the gain function to process the 2007 data. AGC involves amplitude scaling in inverse proportion to the average signal level in a sliding a window. The scaling factor was chosen by adjusting the scaling parameters and the size of the AGC window. Figures 3.11 and 3.12 illustrate the data before and after the application of AGC. Notice that the amplitudes are balanced down section, making deeper reflections more visible. It is important to remember that when a gain is applied

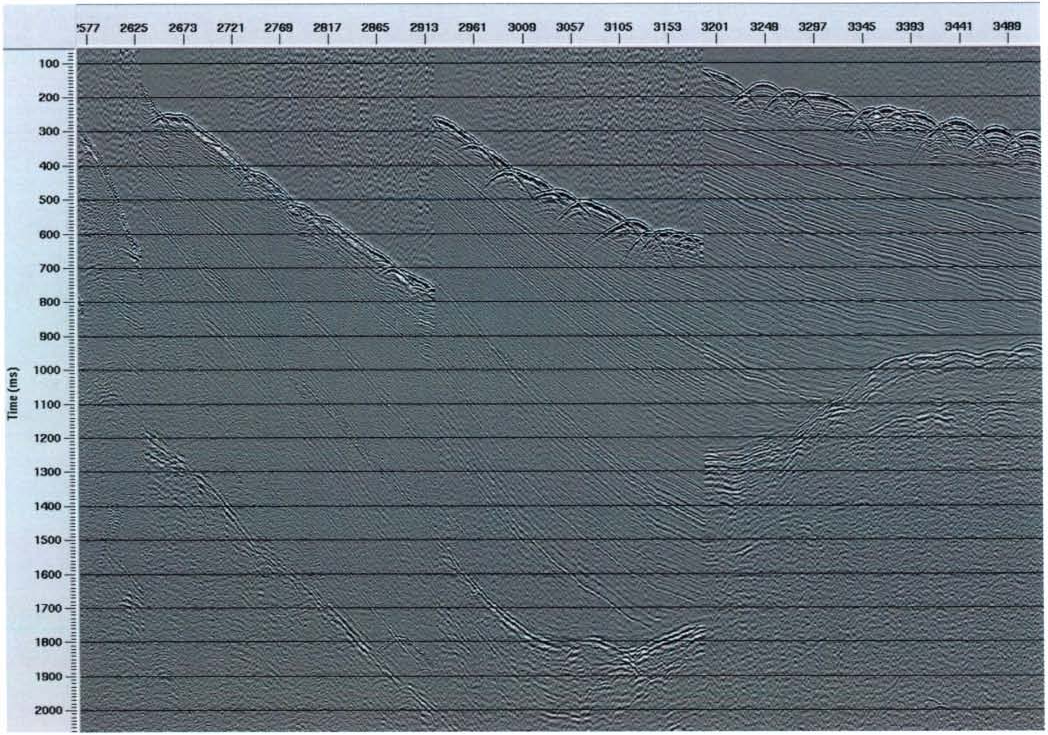

Figure 3.8 Trace display showing a number of delay changes.

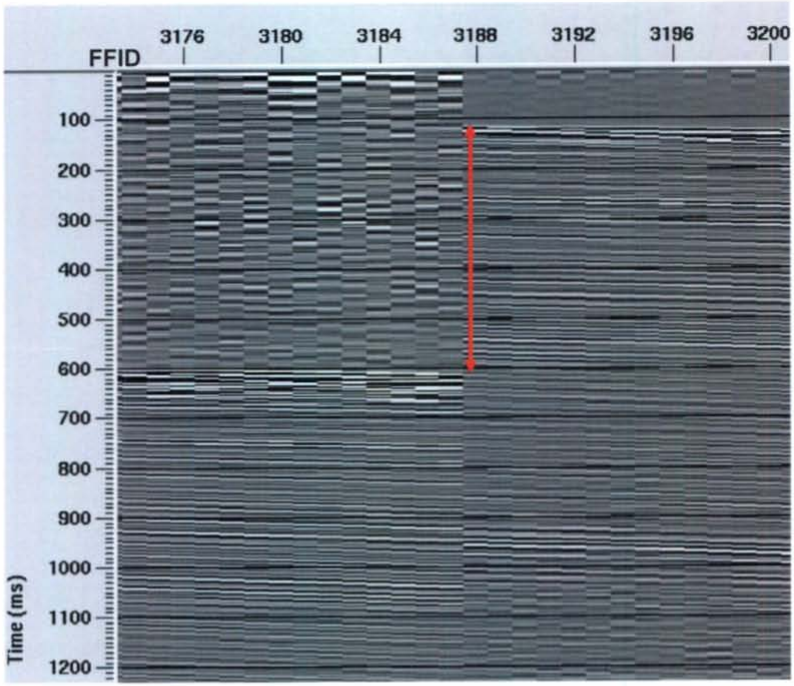

Figure 3.9 Close up of 500 ms delay change.

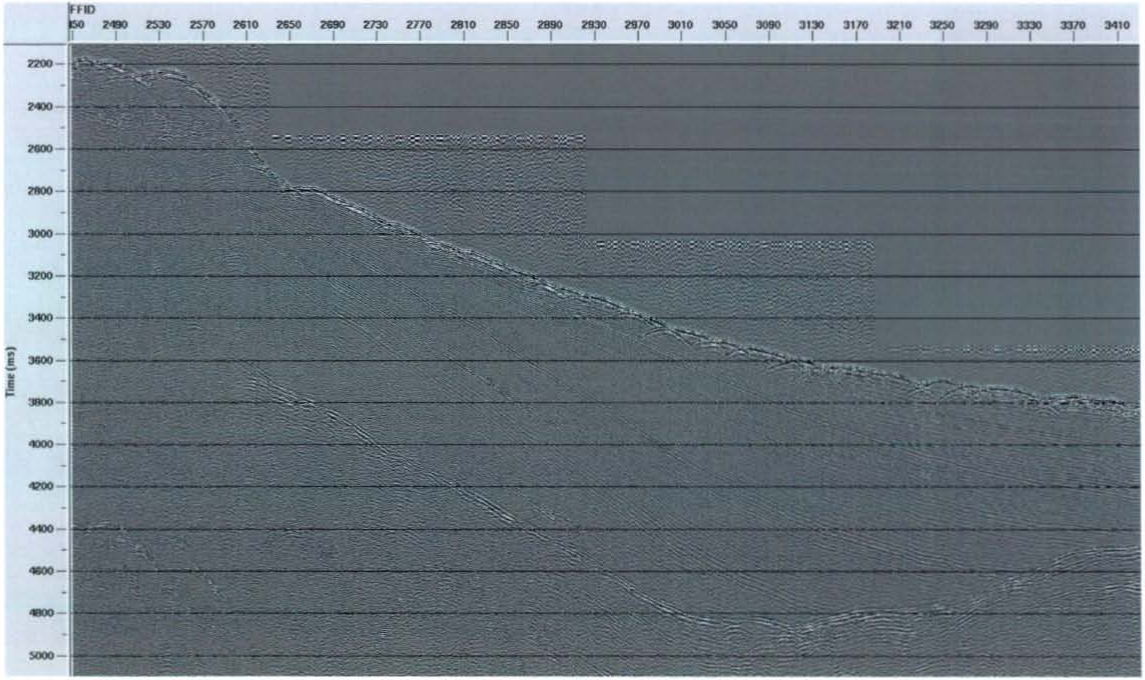

Figure 3.10 Trace display after hand statics was applied. The delays are now corrected and the sea bed is shifted to the correct. Position.

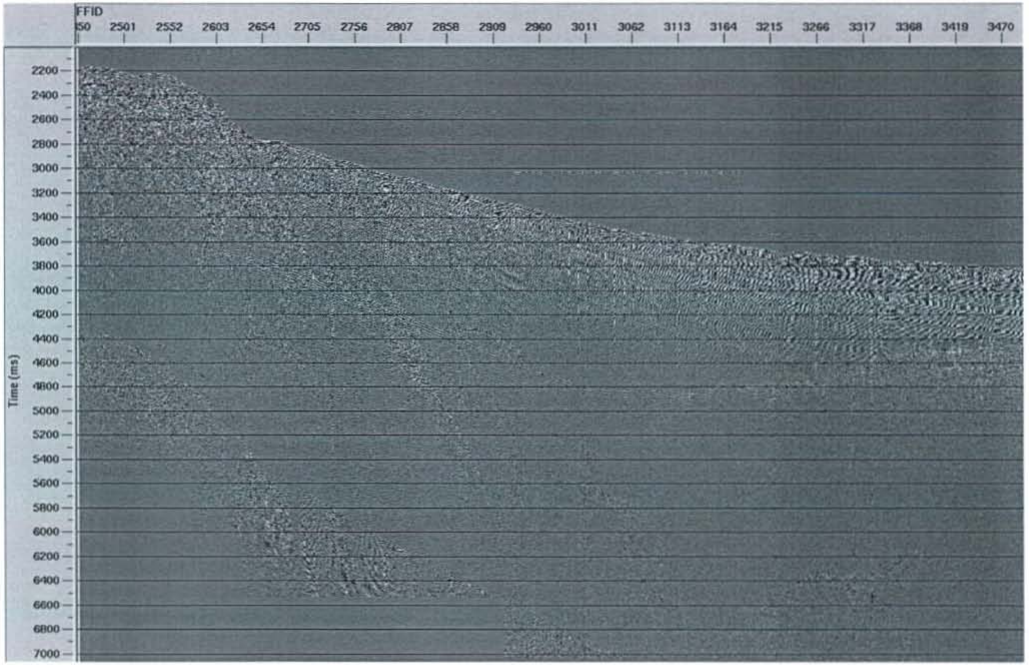

Figure 3.11 Trace display with no AGC applied. Notice that the maximum energy is retained around the first 1000 ms below the sea bed.

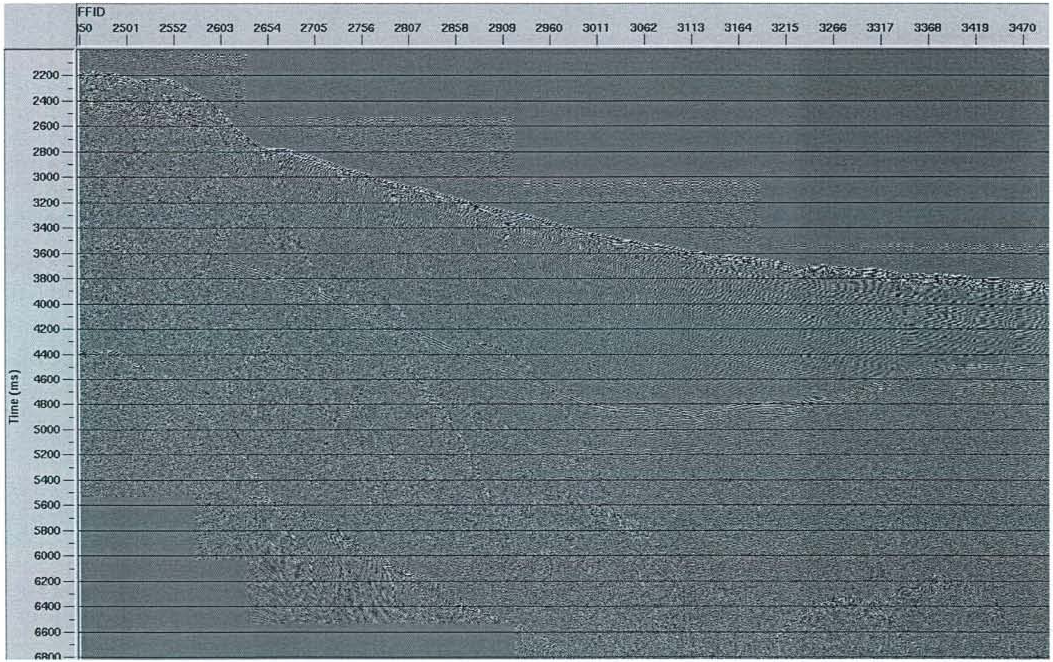

Figure 3.12 Trace display after the application of AGC. Notice that the amplitudes have been balanced down the section.

to the data the true amplitude of seismic events is altered. Therefore, the AGC function was not applied permanently to the data and was used for display purposes only. A scaling window of 500 ms was determined to be the most favourable.

3.2. Geometry and CMP Sorting

The geometry of the seismic spread contains pertinent information for further processing, such as, the velocity analysis and common midpoint (CMP) stacking. Therefore, before further processing could be carried out the shooting geometry for the 2007 survey was applied to the dataset. A simple geometry (straight line, constant shot point interval—usually 25 meters) was assumed and a 2D auto function is used to create a 2D marine geometry spreadsheet. Parameters such as the source and receiver interval, minimum and maximum offsets, the near and far channels, channel increment and the sail line azimuth were recorded and used to determine the source and receiver coordinates (Fig. 3.13).

By applying the correct geometry to the data set it was possible to create a binning spreadsheet which assigns each trace to a CMP. The CMP gathers created were further used to determine the staking velocities during the velocity analysis. After the shooting geometry was applied to the data it was necessary to do some trace quality control by carefully examining the final geometry spreadsheet to ensure that each channel corresponds to the correct CMP.

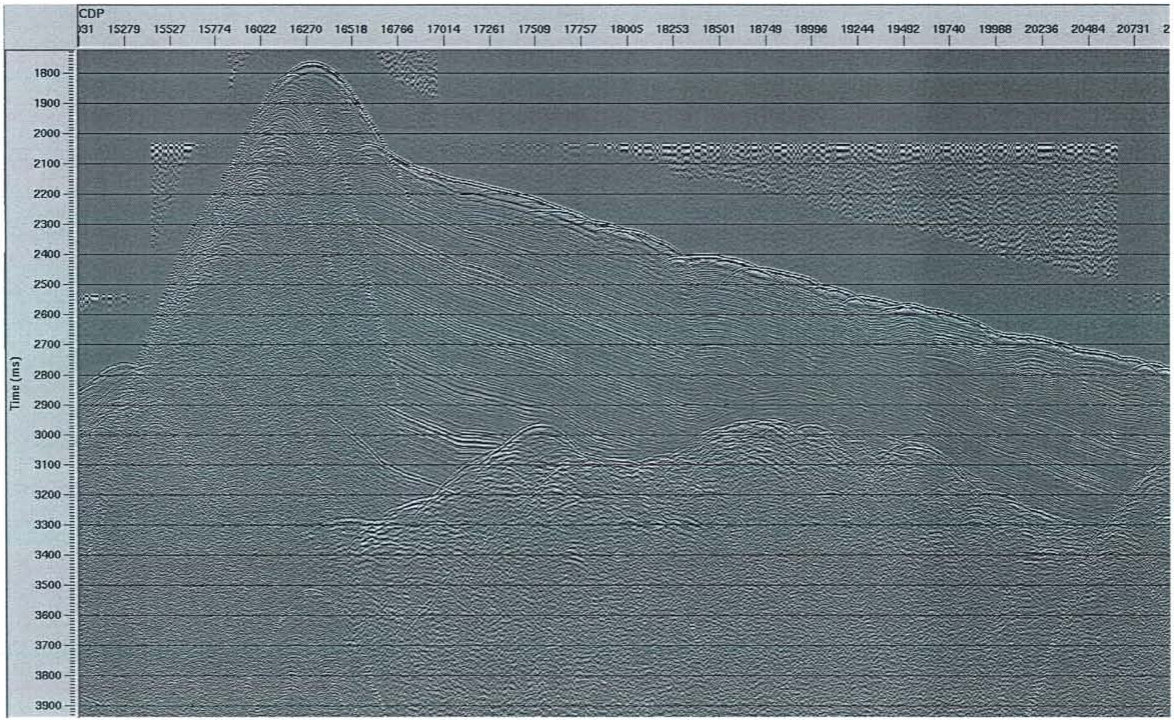

Figure 3.13 The data after the geometry has been applied. Notice that the data is now arranged by common mid point number and the signal quality has drastically increased, in comparison to the near trace gather (Fig. 3.10).

3.3 Velocity Analysis

3.3.1 Velocity Picking

Velocity analysis is one of the most important processes because successful NMO correction, stacking and migration require proper velocity information. In general, bad velocities produce poor final images (proMAX© Users Manual). Therefore, during processing it was important to spend a considerable amount of time on the velocity analysis of each profile. The velocity analysis was carried out using CMP supergathers (Figure 3.14) to determine the velocities that produce the best NMO correction.

The supergathers were created using the 2D supergather formation application in proMAX©. A supergather is created by summing together several adjacent CMPs, which increases the quality of the semblance spectra. In a CDP gather, traces can have different offsets (i.e., in every CDP group there are traces with offsets different than the traces immediately before and after a given trace). Therefore, the number of traces in the supergather is much greater than the maximum fold of the data, allowing a higher quality velocity analysis.

The supergathers provide the location and range of CMPs packed together into ensembles for the velocity analysis (proMAX© Users Manual). The 2D supergather formation process has the option to use a grid of values to pick the supergather CMPs. For example, it is possible to choose every 1000th CMP or every 500'th, forming a tighter grid where the geology is more complex. However, because the geology in the

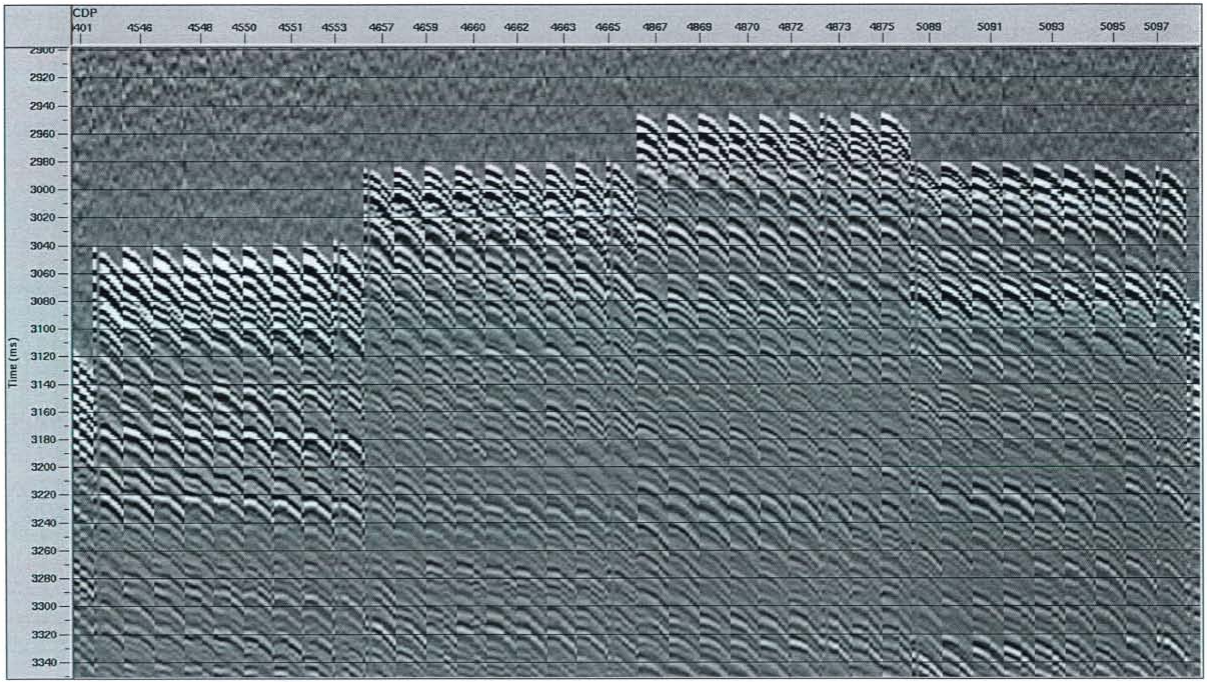

Figure 3.14 Supergathers used for the velocity analysis.

study area is very complicated with many steeply dipping structures it was beneficial to pick the CMP locations through visual inspection of a near trace garther annotated with CMP's (Figure 3.15) and type in the velocities. Furthermore, because NMO corrections are based on interpolation between points where velocity analysis are done, these points must picked where the seabed slope changes significantly.

An example of a possible velocity trend is delineated by the white dots located at the semblance peaks in Figure 3.16. The semblance window also has the option to use the interval velocity tool, shown as a black downward stepping line on the velocity spectra. Using the interval velocity function increases your confidence when picking, with the general assumption that velocity increases with depth (except possibly when Messinian deposits are present, see Chapters 4 and 5).

The semblance spectrum for the 2007 eastern Mediterranean data (Fig. 3.15a) is poorly constrained below 3500 ms. The poor constraints on velocity at depth are associated with the short streamer and comparatively large depth of reflectors in the area. The complex structures in the area can be relatively steeply dipping, producing very high stacking velocities. Also, the water depth in the study area is relatively deep with depths in most places >3000 ms and in many areas it can be impossible to distinguish between in- and out-of-plane reflections (Fig. 3.17).

The poor constraints on the velocities below 3500 ms decreases confidence for making good velocity picks at greater depths on the velocity colour spectrum but it was possible to integrate the semblance spectrum (Fig. 3.16a) with the CMP gathers (Fig.

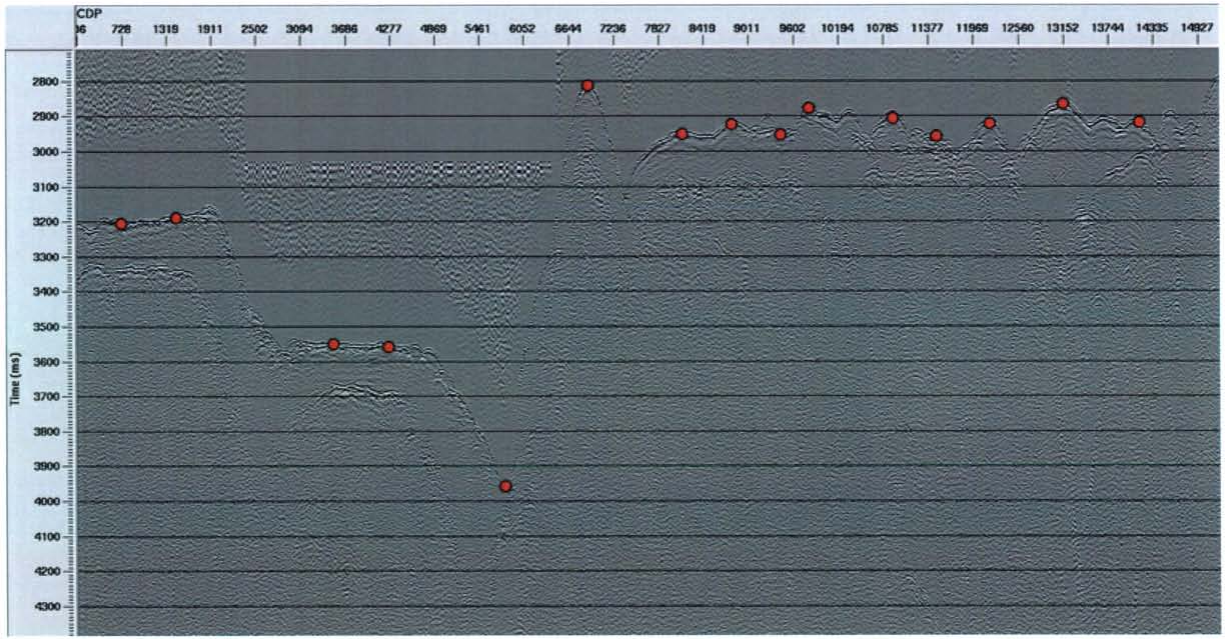

Figure 3.15 Near trace gather used to determine the optimal location for each velocity pick. The location of each velocity pick was marked with a red circle.

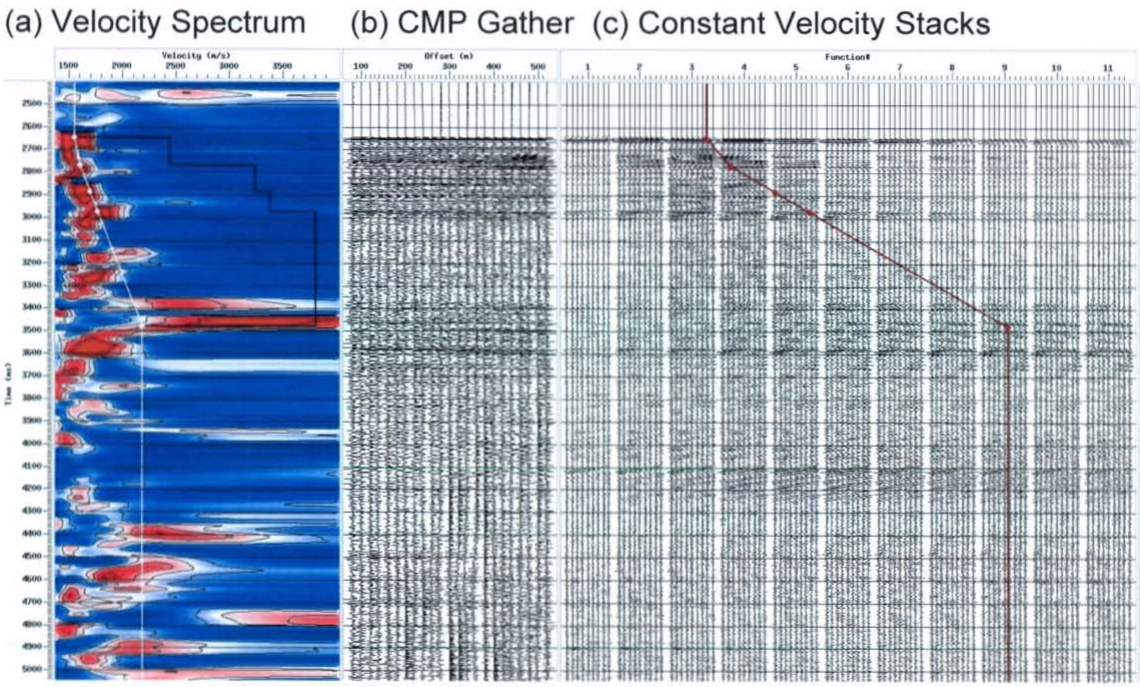

Figure 3.16 Velocity analysis showing **(a)** the velocity color spectrum, **(b)** CDP gather and **(c)** Constant velocity stacks used to determine stacking velocities.

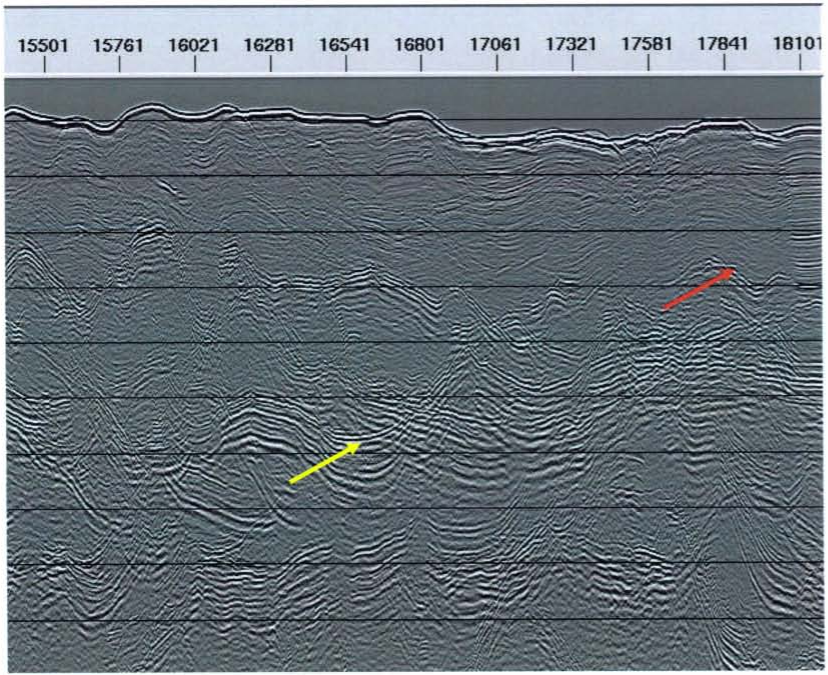

Figure 3.17 Trace display showing how in some areas it is not possible to distinguish between in and out of plane reflections. The red arrow and the yellow arrow point out the primary and secondary reflections, respectively.

3.16b) and constant velocity stacks (Fig. 3.16c) and use all three to make the best possible pick. As explained in Chapter 2, the CMP gather (e.g., Fig. 3.16b) displays the common offset stacked supergather for the specified CMPs. It was possible to see if each pick was under- or over-corrected for the NMO velocity by using the interactive NMO application to the CMP gather. When the velocity pick is too low and over-corrected for NMO the event will curve up (Fig. 3.18). If the pick is too high and is under-corrected for NMO the event will curve down (Fig. 3.19). Finally, when the NMO velocity is correct the given reflection in the gather will appear flat in time (Fig. 3.20).

The velocity range that worked best for the 2007 data was 1400-2400 m/s. The constant velocity stack images allow for visual identification of where the data is stacking in (Fig. 3.20c). The maximum stacked response in the velocity stacks is the best NMO velocity. Notice that when the velocity pick is incorrect (Figs. 3.18c, 3.19c) the data does not stack-in. These sections also show how well the reflections stack over a range of velocities. Although velocity functions were poorly constrained at greater depths, integrating the three velocity analysis methods significantly increased confidence when picking velocities.

3.3.2 Velocity Editing

After the velocity picking was complete it was necessary to display the output velocity field (Figure 3.21) and edit the function using the velocity viewer/point editor (Figure 3.22). The velocity viewer/point editor tool allows velocity picks to be manipulated and the new velocity function is output and saved. The velocity editing tool

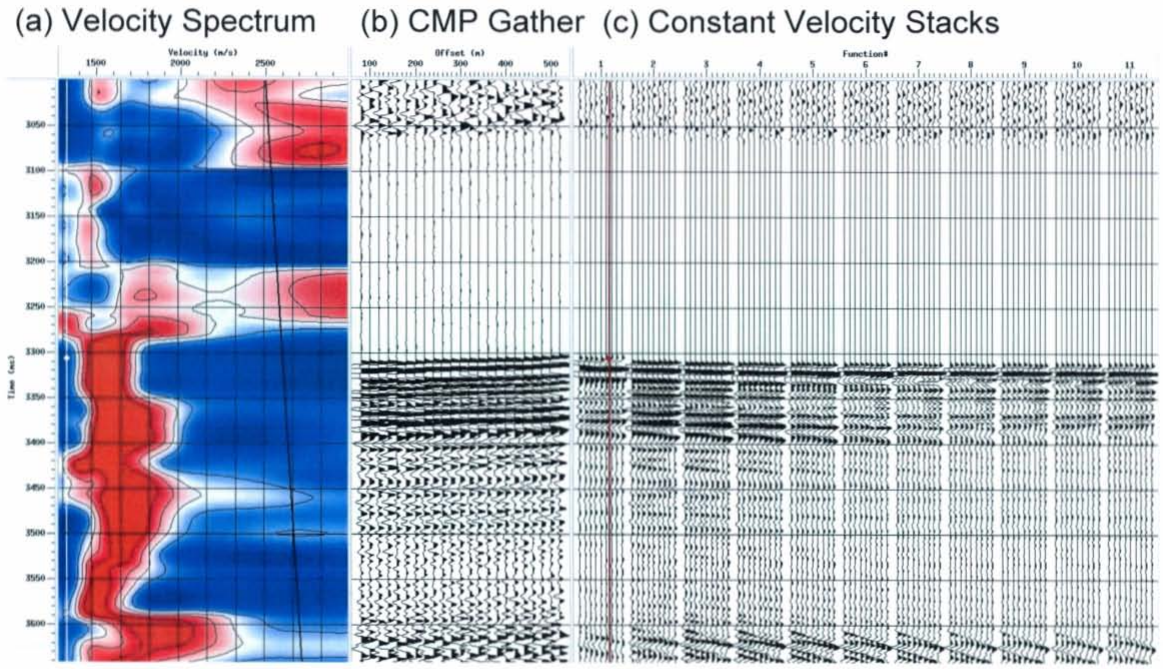

Figure 3.18 **(a)** Velocity semblance spectra showing a velocity pick where the velocity is too low **(b)** the normal move out is over- corrected on the common mid point gather, with events curving up and **(c)** the data is not stacking in on the constant velocity stacks.

((a) Velocity Spectrum (b) CMP Gather (c) Constant Velocity Stacks

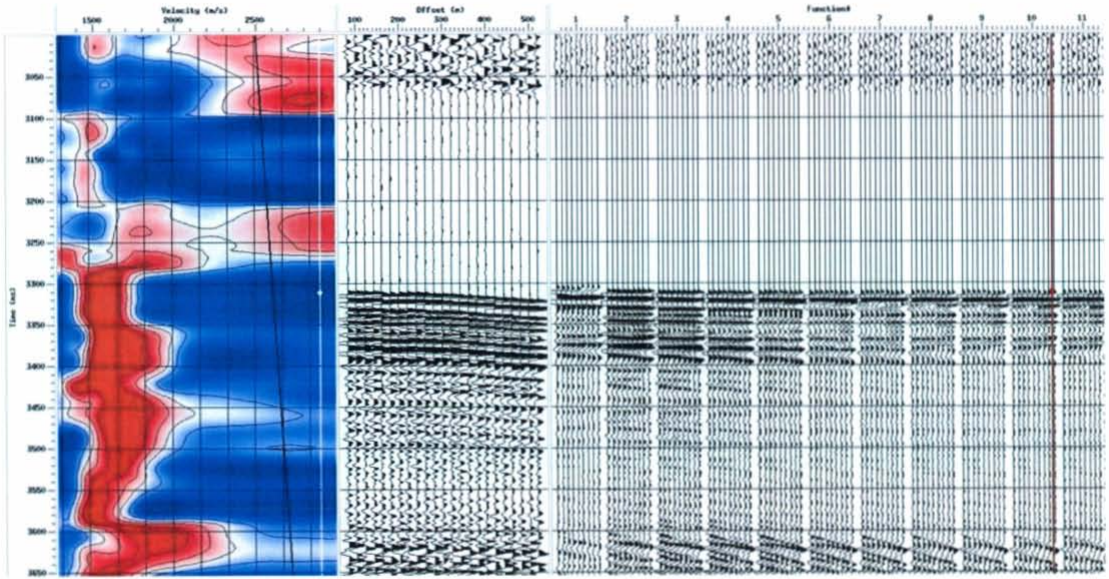

Figure 3.19 **(a)** Velocity semblance spectra showing a velocity pick where the velocity is too high **(b)** the normal move out is under-corrected on the common mid point Gather, with events curving down and **(c)** the data is not stacking in on the constant velocity stacks.

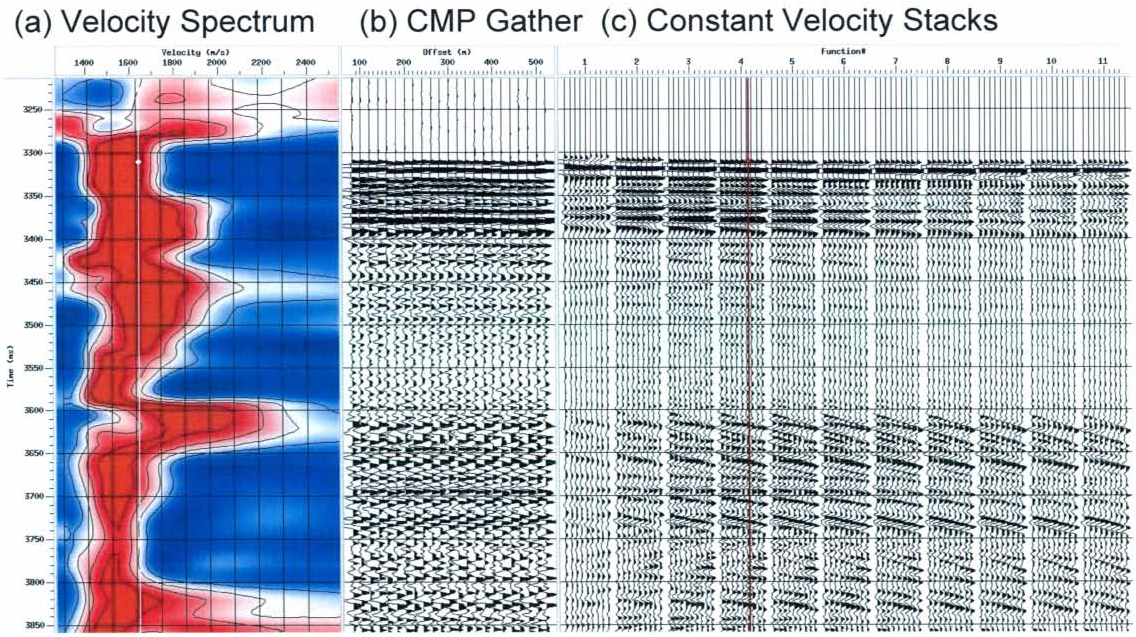

Figure 3.20 **(a)**Velocity spectrum showing a good velocity pick at a semblance peak on the velocity color spectrum, **(b)** the normal move out is corrected, with the events flattened on the common mid point gather and **(c)** the data is stacking in on the constant velocity stack.

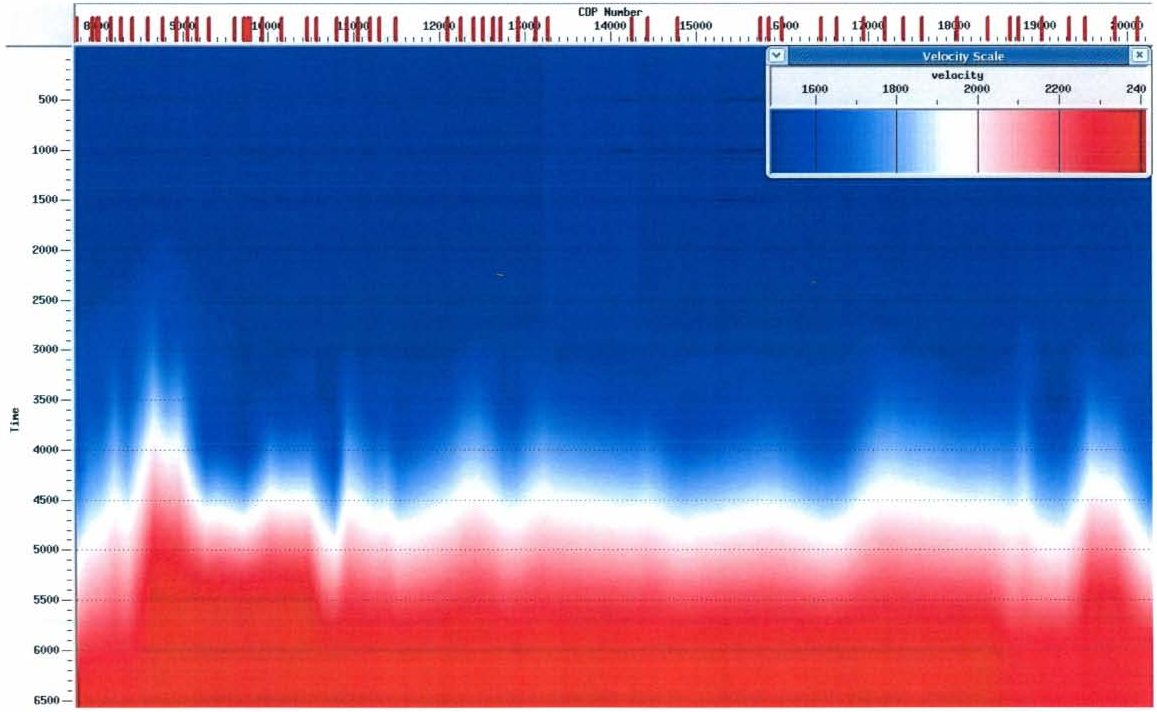

Figure 3.21 Output velocity function created from picking the NMO stacking velocities. Notice the sharp edges on the dipping Structures.

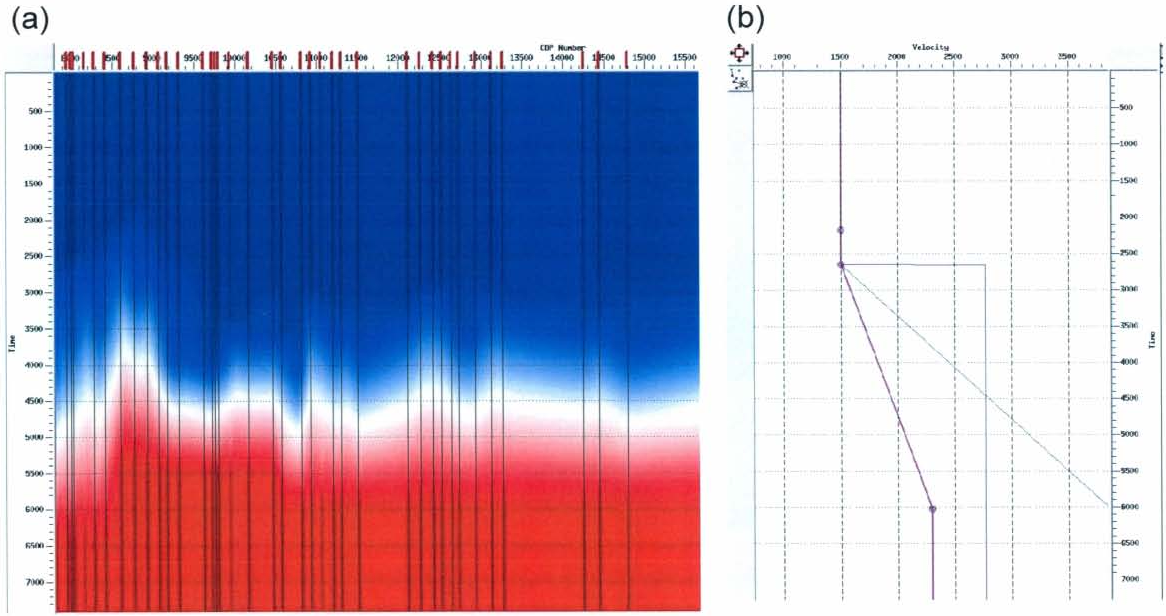

Figure 3.22 Velocity viewer/point editor tool used to edit the final velocity function for stacking. **(a)** shows the velocity function being edited and **(b)** is the velocity point editor tool.

was also used to delete unwanted CMPs from the velocity function and to do some minor smoothing where sharp edges occurred (Figure 3.23). Editing the velocity function for stacking was not critical because the water levels are relatively deep and the data stacked quite well over a large range of velocities. However, velocity editing was very important when choosing the correct velocities for migrations. Migration velocities will be discussed in greater detail, later in this chapter.

One important by-product of the velocity analysis is the information gathered on interval velocities. This is particularly critical when seismic reflection profiles are converted from time domain into depth domain.

3.4 Deconvolution

For the 2007 data the seabed reflection in most areas was close to, if not, a spike and did not require deconvolution. However, in some locations the seabed reflection has a slight reverberatory tail, illustrated as white troughs and black peak in Figure 3.24. Spiking deconvolution was attempted to compress the seismic wavelet and increase the temporal resolution of the data. The deconvolution design window was picked relative to the seabed and was chosen as ~20 ms relative to the seabed (Fig. 3.24). A stacked seismic section after the application of a minimum phase spiking deconvolution is shown in Figure 3.25. Notice that the seabed reflection is slightly compressed. However, the deconvolution introduced a significant amount of high frequency noise to the data. A zero phase deconvolution was also tested (Fig. 3.26). The zero phase deconvolution created slightly less high frequency noise than the minimum phase deconvolution

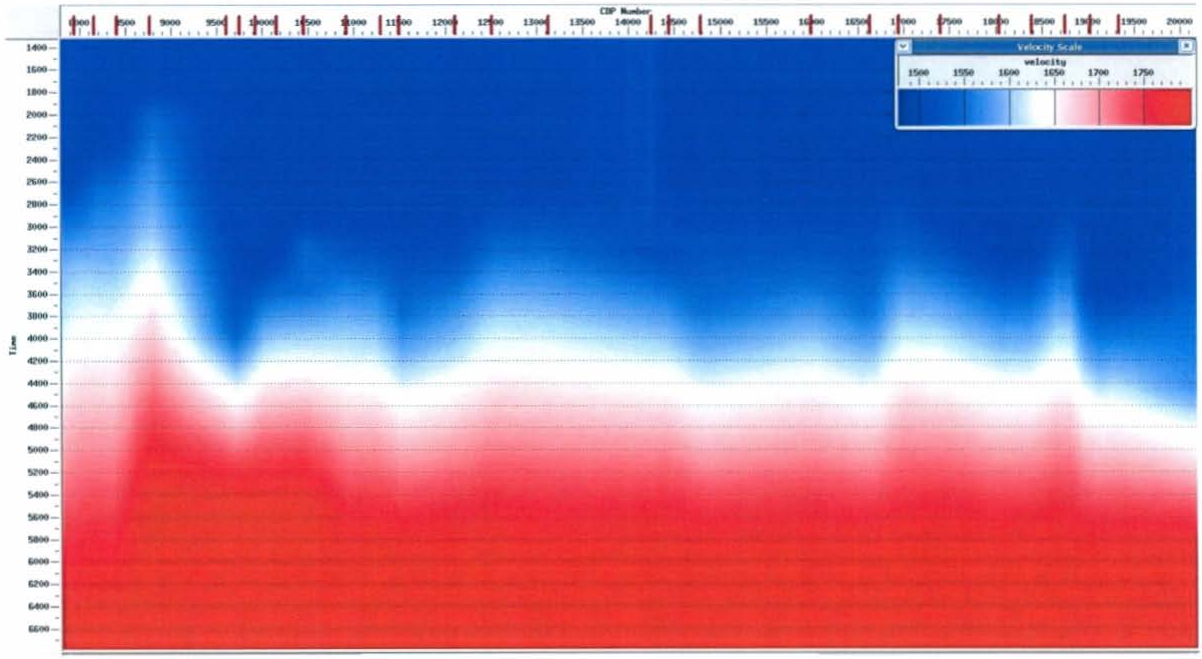

Figure 3.23 Velocity function post velocity editing. Notice how there are less CDP's and that the velocity function has been slightly smoothed in comparison to the original velocity function in Figure 3.21.

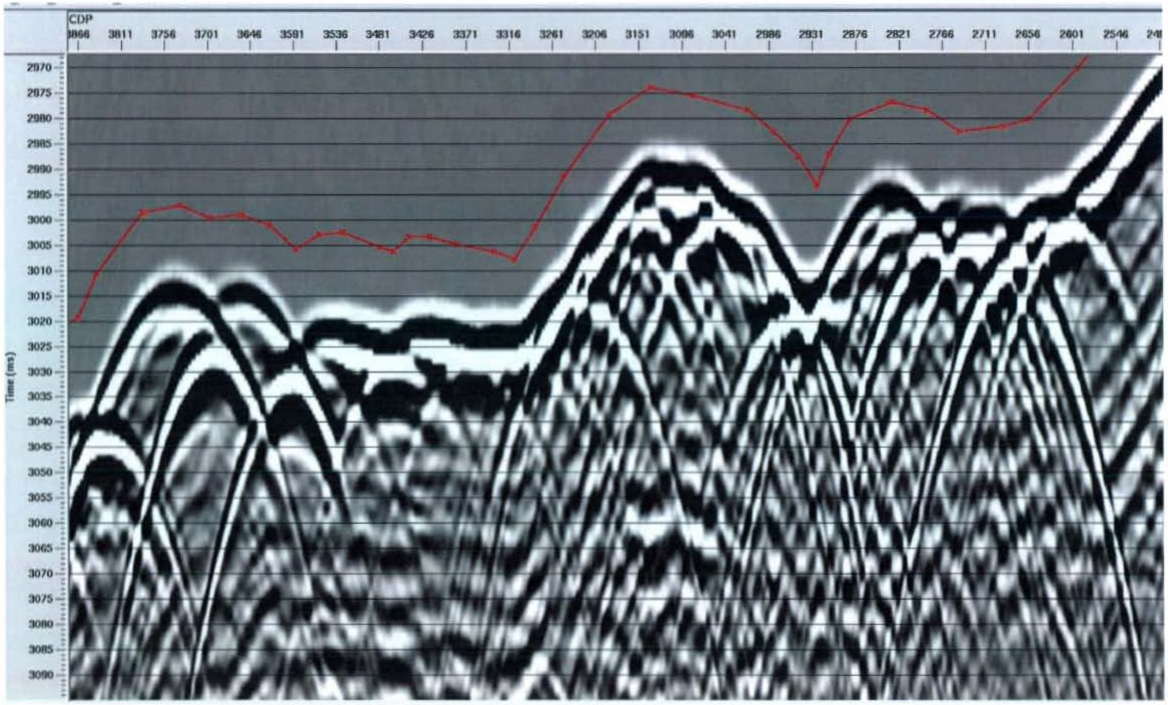

Figure 3.24 Trace display of a stacked section pre-deconvolution. The red line at ~20 ms above the seabed is the decon time gate, picked relative to the seabed.

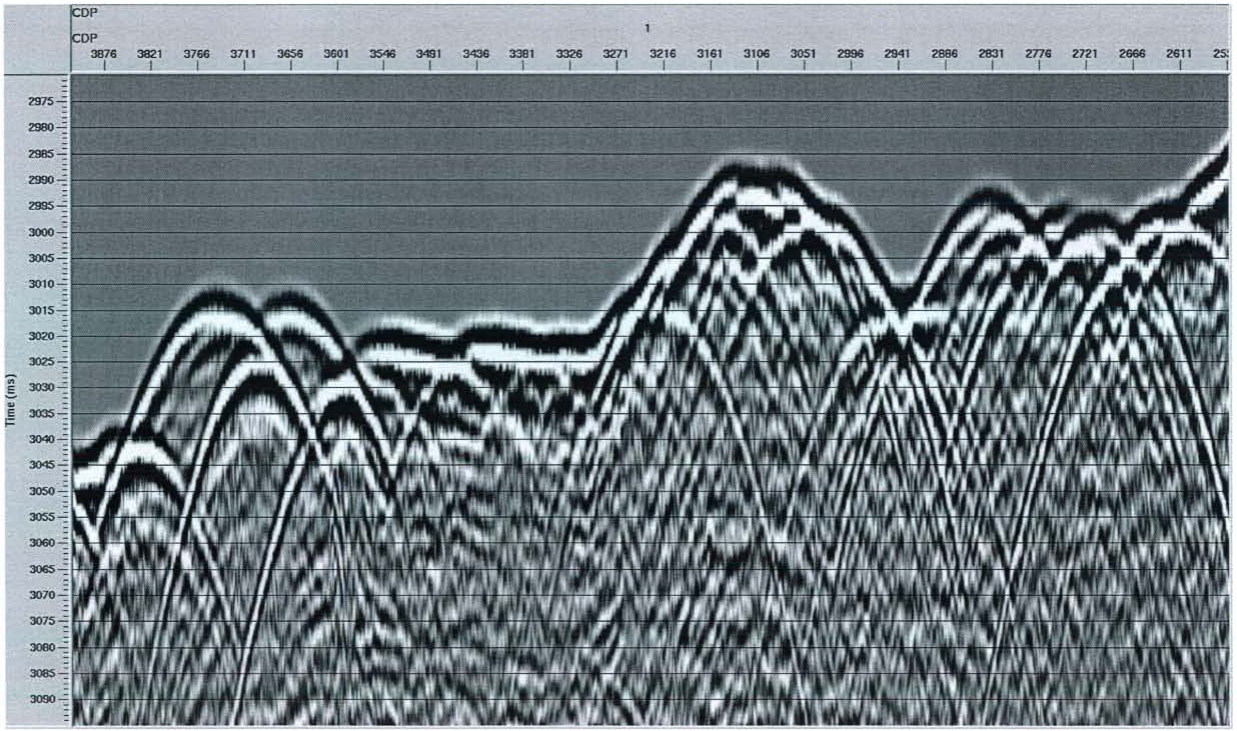

Figure 3.25 Trace display of a stacked section post-deconvolution using a minimum phase filter.

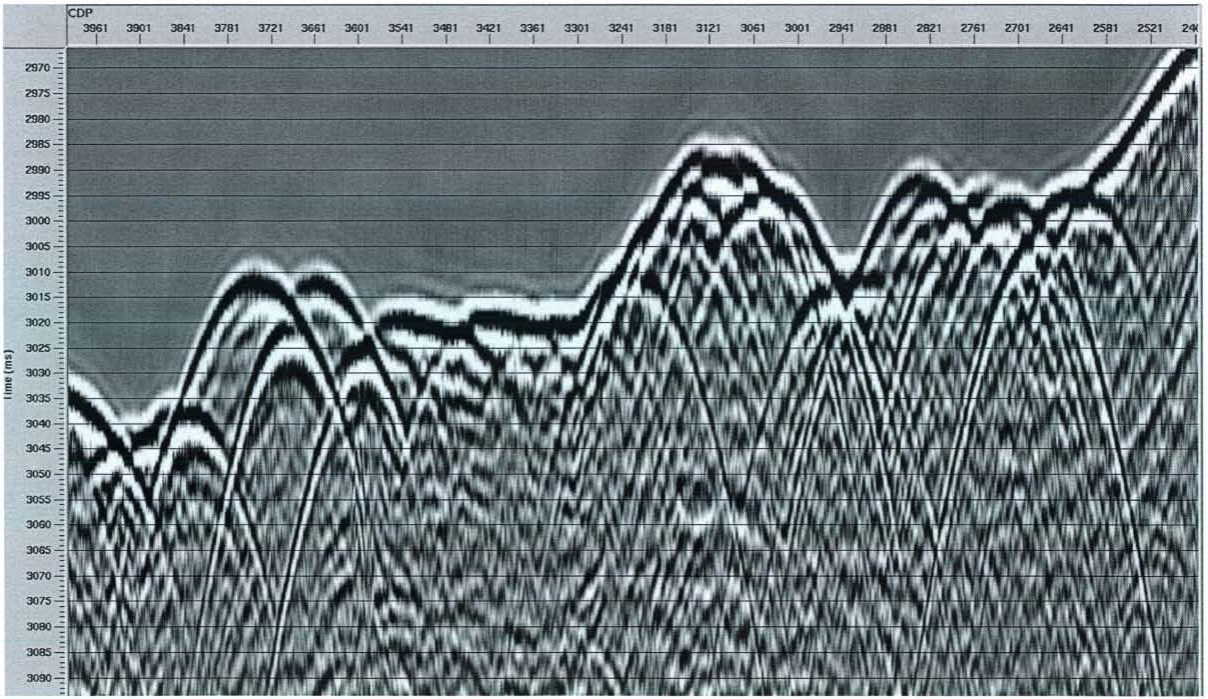

Figure 3.26 Trace display of a stacked section post-deconvolution using a zero phase filter.

operator, but produced unwanted ringing above the seabed (Fig. 3.26). Different filters were tested to attenuate the high frequency noise and ringing above the seabed introduced from the deconvolution, but all produced similar results. Filtering the data post deconvolution and steepening the filter slope parameters was somewhat successful in suppressing the high frequency noise; however, the signal to noise ratio of the deconvolved data was still lower than the original data.

It was useful to carry out the deconvolution process to develop a better understanding of the required parameters, but overall, spiking deconvolution did not prove to be beneficial for the 2007 data set. This is most likely because the assumptions required for deconvolution were not met, specifically, the source is probably not exactly minimum phase and the original information on the seismic wavelet is not well known.

3.5 NMO Correction and CMP Stacking

After some minor editing, the final velocity function (Fig. 3.23) is used to stack the data. The stacked seismic sections (Figs. 3.27, 3.28) show a significant increase in the signal to noise ratio, but the image is distorted by the diffraction hyperbolas and migration is required. This is because the CMP stacking method assumes hyperbolic move out from horizontal reflectors, but in areas such as the eastern Mediterranean Sea where the geology is extremely complicated, this assumption is violated and there is decreased move out on steeply dipping slopes. Therefore, in deep water where the geology is complex, stacking velocities will not equal the migration velocities. A

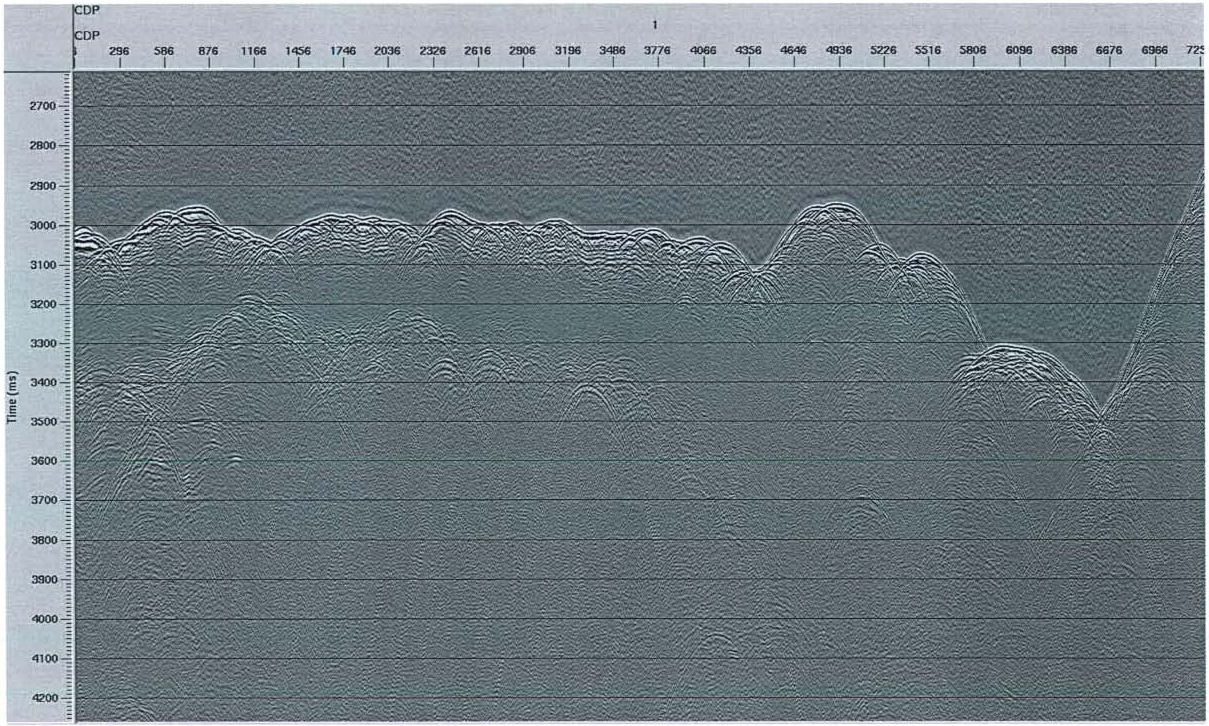

Figure 3.27 Trace display of a stacked seismic section.

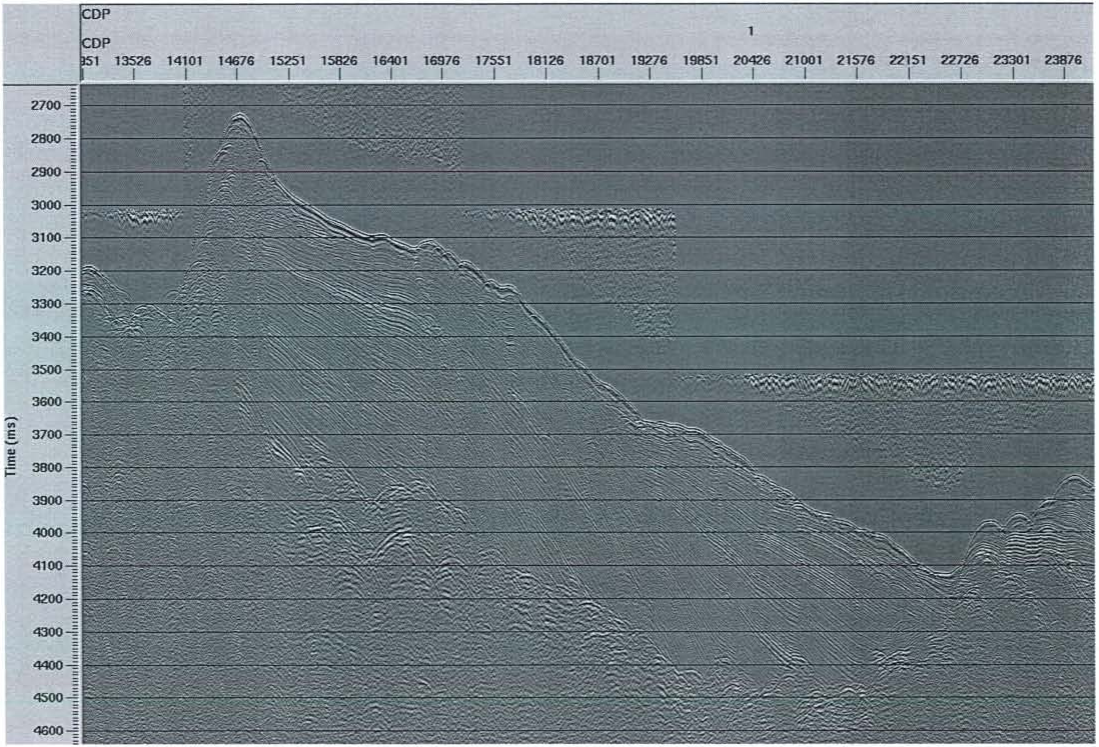

Figure 3.28 Trace display of a stacked seismic section.

significant amount of processing time was spent editing the velocity function for final migration of the seismic reflection profiles.

3.6 Migration

A number of migration techniques are used to process the 2007 seismic reflection data. All migrations attempted were post-stack and included both the Stolt (constant and variable velocity) and 2D Kirchhoff time migrations. The migration procedures used are described in detail in this section.

3.6.1 Stolt migration

The 2D Stolt migration was used because it is the fastest migration technique. The Stolt migrations processed very quickly and were used to identify areas were the migration velocities needed significant adjustments.

Stolt constant velocity migration

Stolt constant velocity migrations (using velocities of 1500, 1600 and 1700 m/s) were produced and compared for every line and output migrations were evaluated (Figs. 3.29-3.34). This was accomplished by printing each constant velocity migration and stacking each section one on top of each other, then marking in with arrows where the image is under-migrated (velocities are too low), producing migration frowns (Fig. 3.30) and over-migrated (velocities are too high), producing migration smiles (Figs. 3.34, 3.35). In areas where it was more difficult to constrain the velocities extra constant velocity migrations were run using very low (e.g., 1000 m/s) and high (2000 m/s)

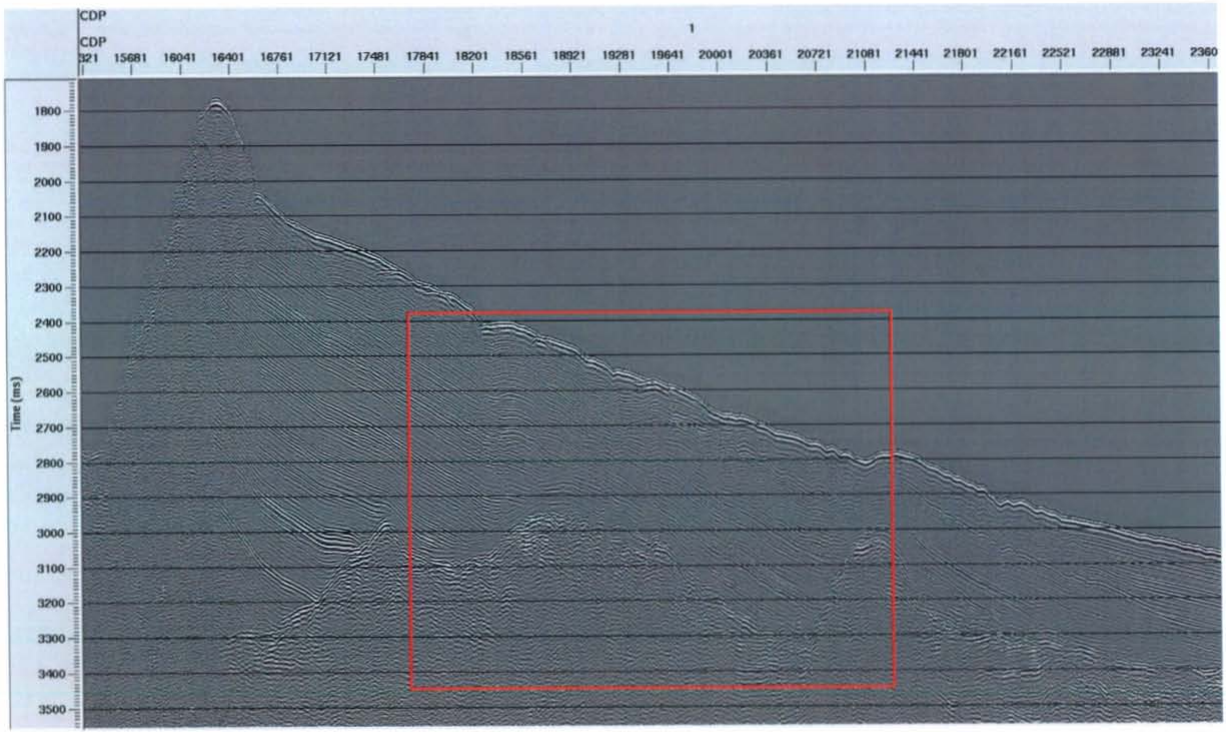

Figure 3.29 Stolt 1500 m/s constant velocity migration.

Figure 3.30 Zoom in on stolt 1500 m/s Constant velocity migration from Figure 3.29. The black arrows indicate where the migration velocities must be altered. Here the reflectors are under-migrated and migration frowns are visible.

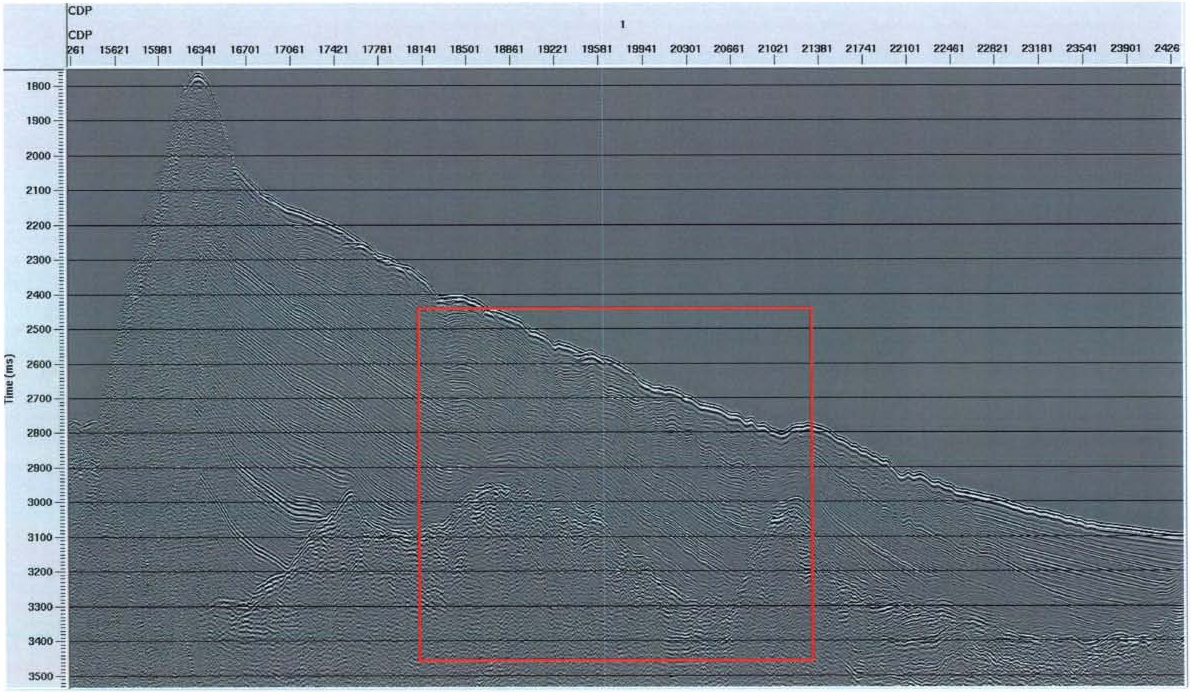

Figure 3.31 Stolt 1600 m/s constant velocity migration.

Figure 3.32 Zoom in on stolt 1600 m/s constant velocity migration from Figure 3.31. The black arrows indicate where the migration velocities must be altered.

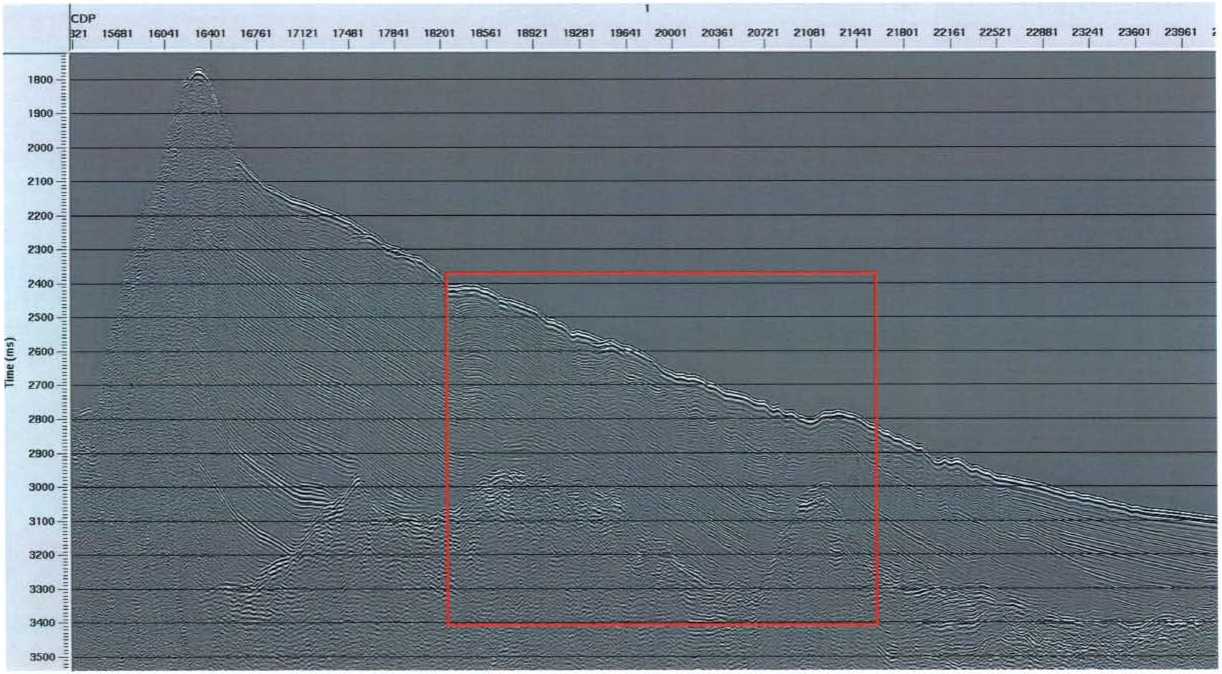

Figure 3.33 Stolt 1700 m/s constant velocity migration.

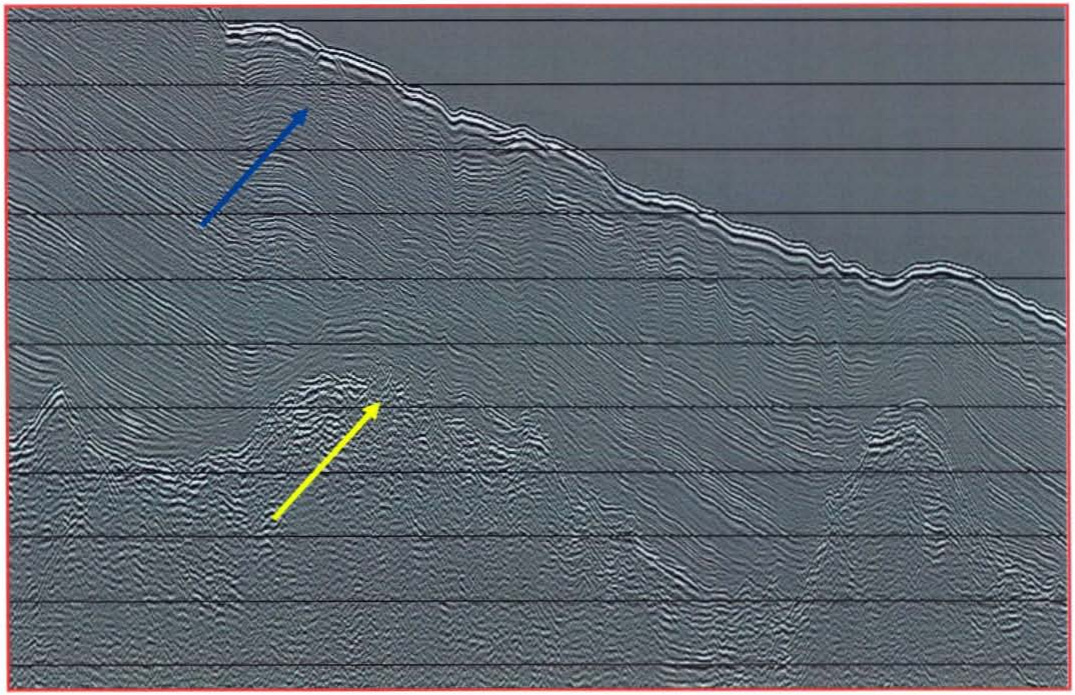

Figure 3.34 Zoom in on the red box in Figure 3.33. The blue arrow indicates where the migration velocities are too low and the reflectors curve down (i.e. migration frowns). The yellow arrow shows where the migration velocities are too high and the reflectors curve up (i.e. migration smiles).

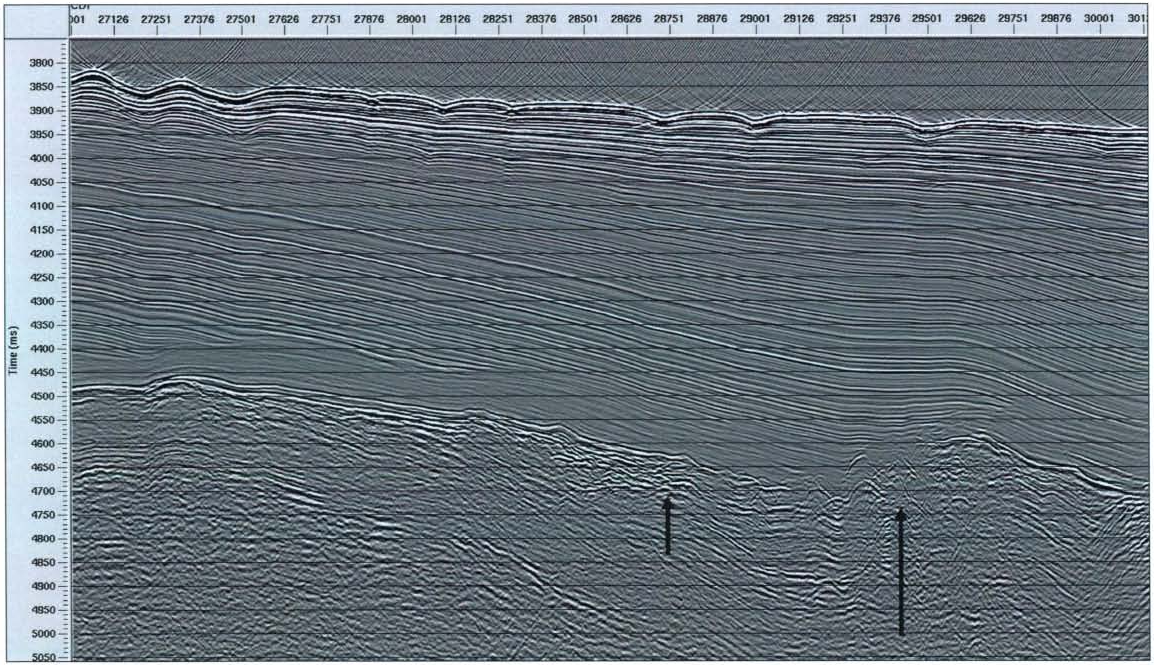

Figure 3.35 Stolt Variable migration used to adjust the final migration velocities. The black arrows indicate where the migrations should be adjusted.

velocities. This was helpful in areas with steeply dipping structures where migration velocities could be extremely high. Comparing each Stolt constant velocity migration was a quick and easy way to determine the general range of velocities that should be used for migration.

Stolt variable velocity migration

The constant velocity Stolt migration is the quickest migration technique and is useful to estimate the range of migration velocities but the constant migration does not handle complex structures and lateral variations in velocity well. Therefore, a variable velocity migration was required to develop final migration velocities. The Stolt variable velocity migration (Fig. 3.35) is also time efficient and was used to determine the optimal migration velocity function used for the final migration. By running a variable velocity migration it was possible to analyse the migrated section and determine where the velocity function needed to be changed. It was very common in the 2007 profiles for the data to be under migrated (frowning) at ~3000 ms and the over migrated (smiling) deeper down the section (Fig. 3.36). By analysing each Stolt variable velocity migration it was possible to edit the migration velocity function (using the velocity viewer/point editor discussed in the previous section) and output and save a new migration velocity function.

3.6.2 Kirchhoff time migration

One problem with the migration method is the amount of computing time required during processing. The Stolt migrations were used to estimate migration

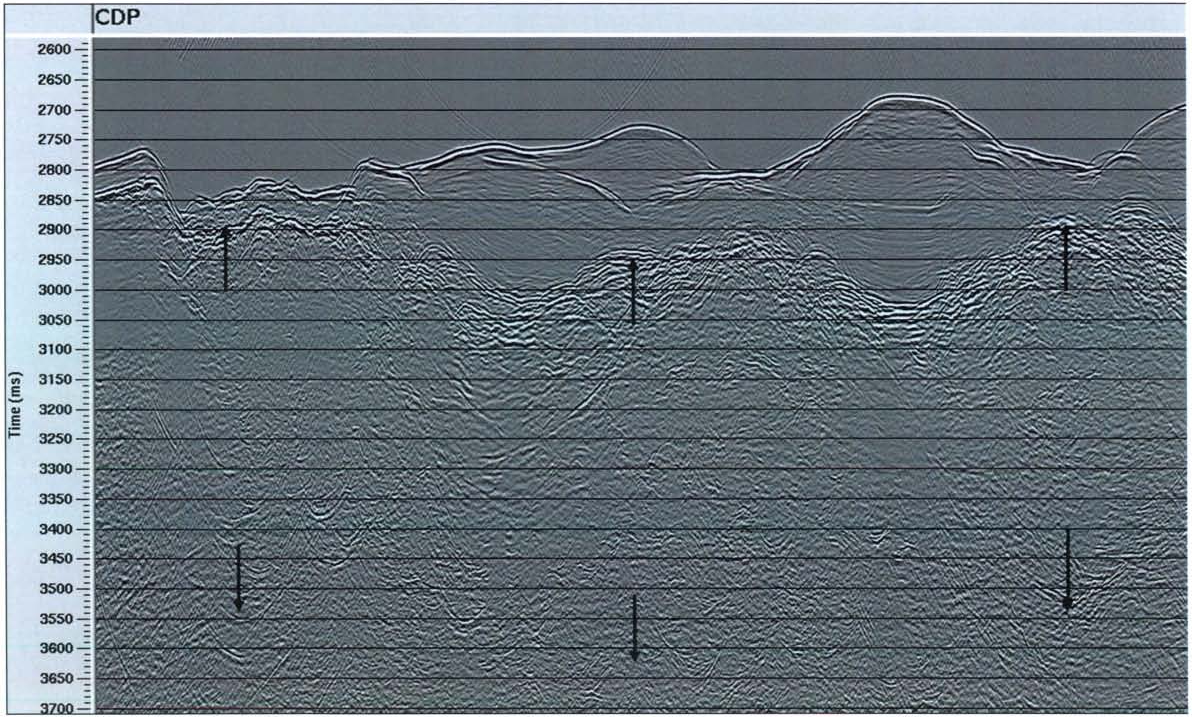

Figure3.36 Stolt variable migration used to adjust the final migration velocities. Notice that around 3000 ms the data is under-migrated but below 3300 ms the data is consistently over-migrated.

velocities because the algorithm is very time efficient. However, the Stolt migration does not handle complex geology and velocity variations well, therefore, the Kirchhoff time migration process was used for final migrations. The Kirchhoff migration method did a much better job at migrating steeply dipping structures because the algorithm can handle steep dips. An example of a velocity function used for a Kirchhoff migration is provided in Figure 3.37. Notice the significant difference between the velocity function used for migration and the velocity function used to stack the data (Fig 3.23).

The Kirchhoff migration algorithm is an integral solution to the scalar wave equation (Equation 3.1) and is therefore dependent on the wave propagation through the Earth (Yılmaz, 2001). This migration method is based on the following assumptions; (i) the medium consists of horizontal and flat layers, (ii) there are no lateral velocity variations and (iii) the stacked section represents the zero-offset section.

$$\frac{\partial^2 u}{\partial t^2} = c^2 \nabla^2 u \qquad 3.1$$

The Kirchhoff migration is carried out through a process known as diffraction summation. Amplitudes along a diffraction hyperbola are summed and the summed amplitude is at the apex of the hyperbola (Fig. 3.38). Figures 3.39-3.44 provide examples of stacked sections and their associated final Kirchhoff migration. Although the Kirchhoff time migration took longer, it proved to be much better when dealing with steeply dipping structures and velocity variations.

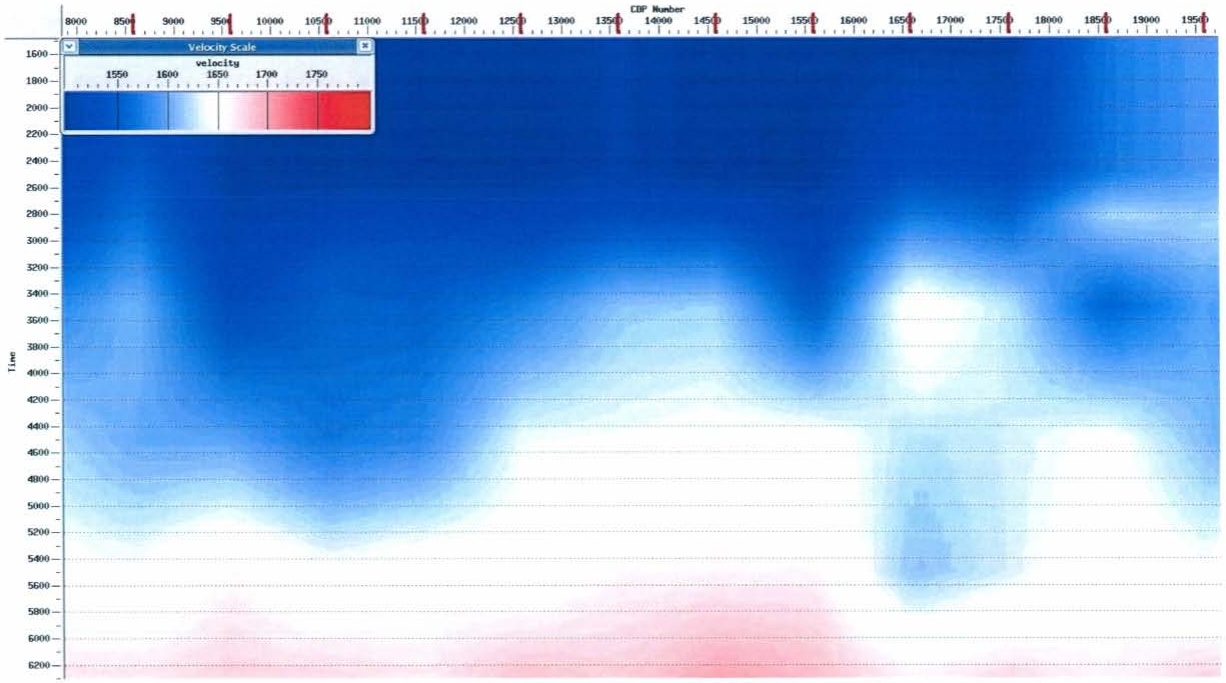

Figure 3.37 Final velocity function used for the Kirchhoff migration.

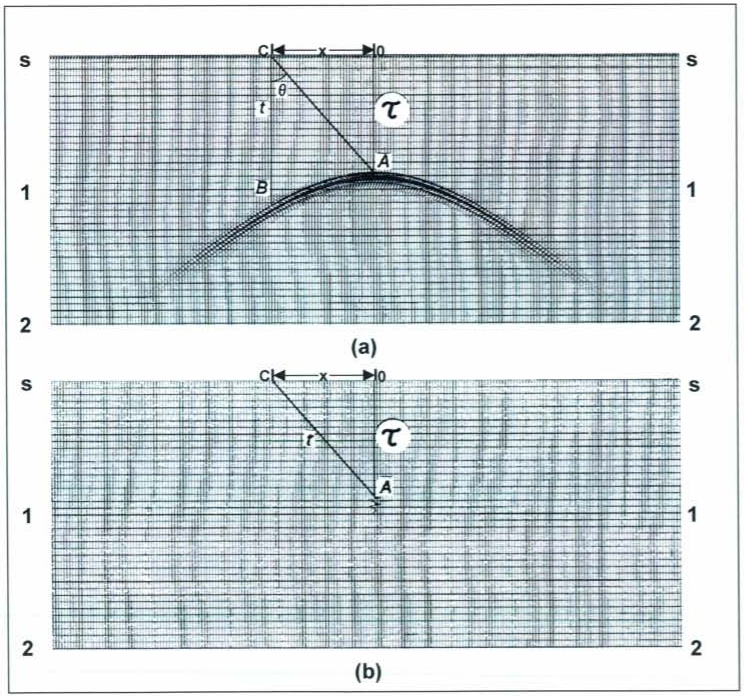

Figure 3.38 Principles of migration based on diffraction summation. (a) Zero-offset section (trace interval, 25 m; constant velocity, 2500 m/s), (b) A migration. The amplitude at input trace location B along the flank of the travel time hyperbola is mapped onto output trace location A at the apex of the hyperbola by equation (4-4) (Yılmaz, 2001).

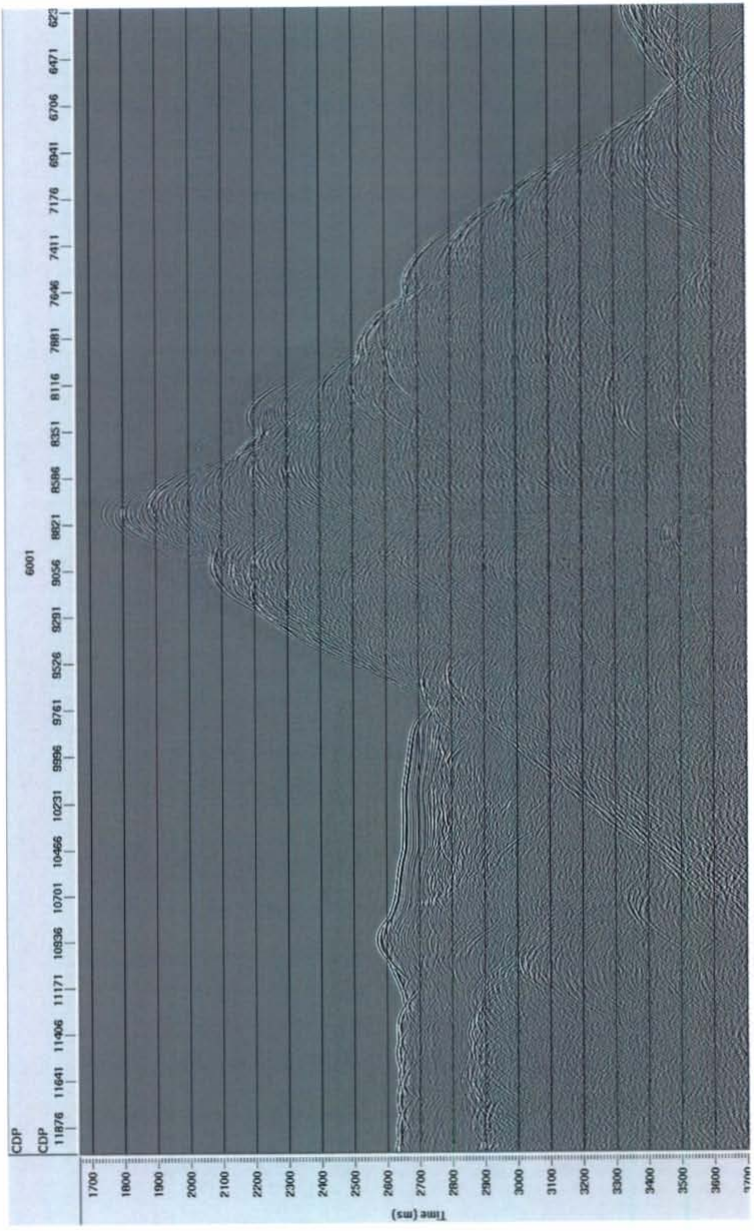

Figure 3.39 Stacked seismic section.

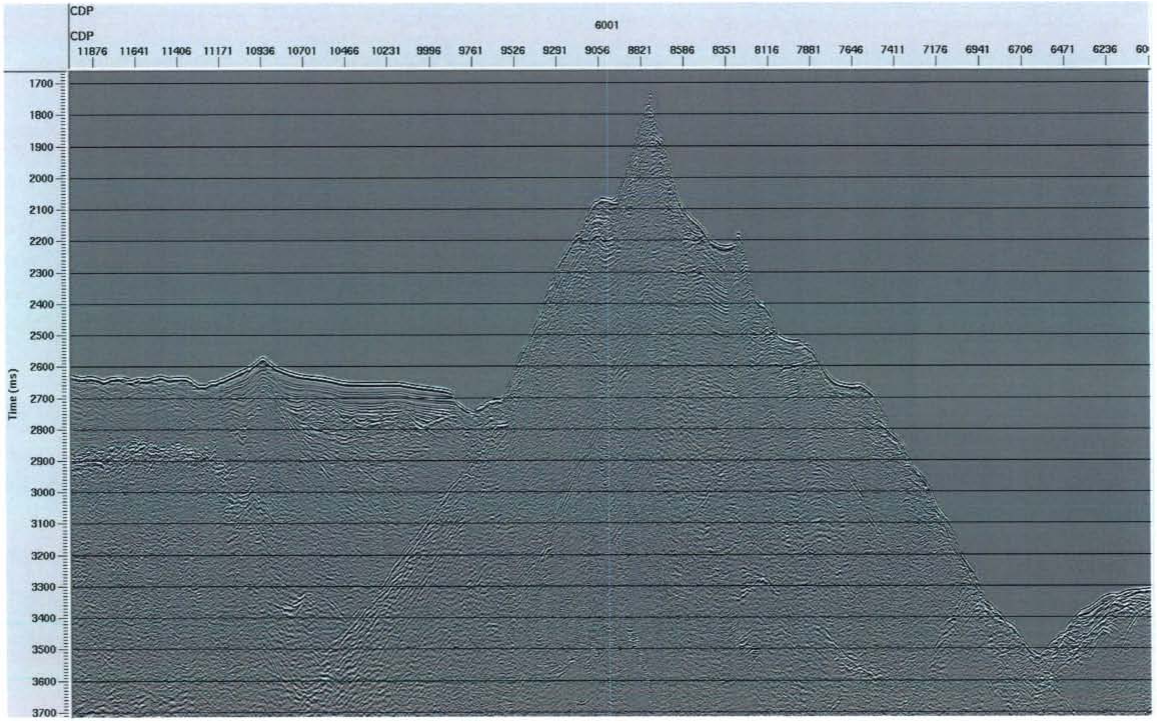

Figure 3.40 Kirchhoff time migration of the stacked seismic section in Figure 3.39.

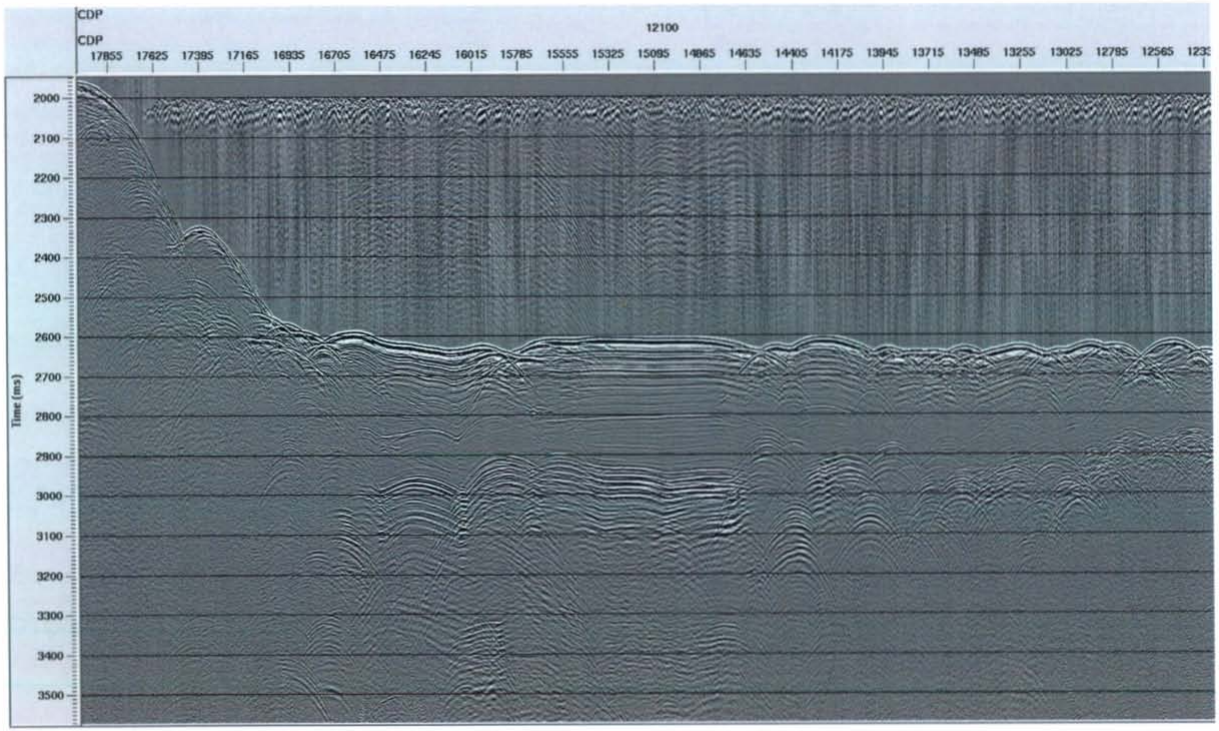

Figure 3.41 Stacked seismic section.

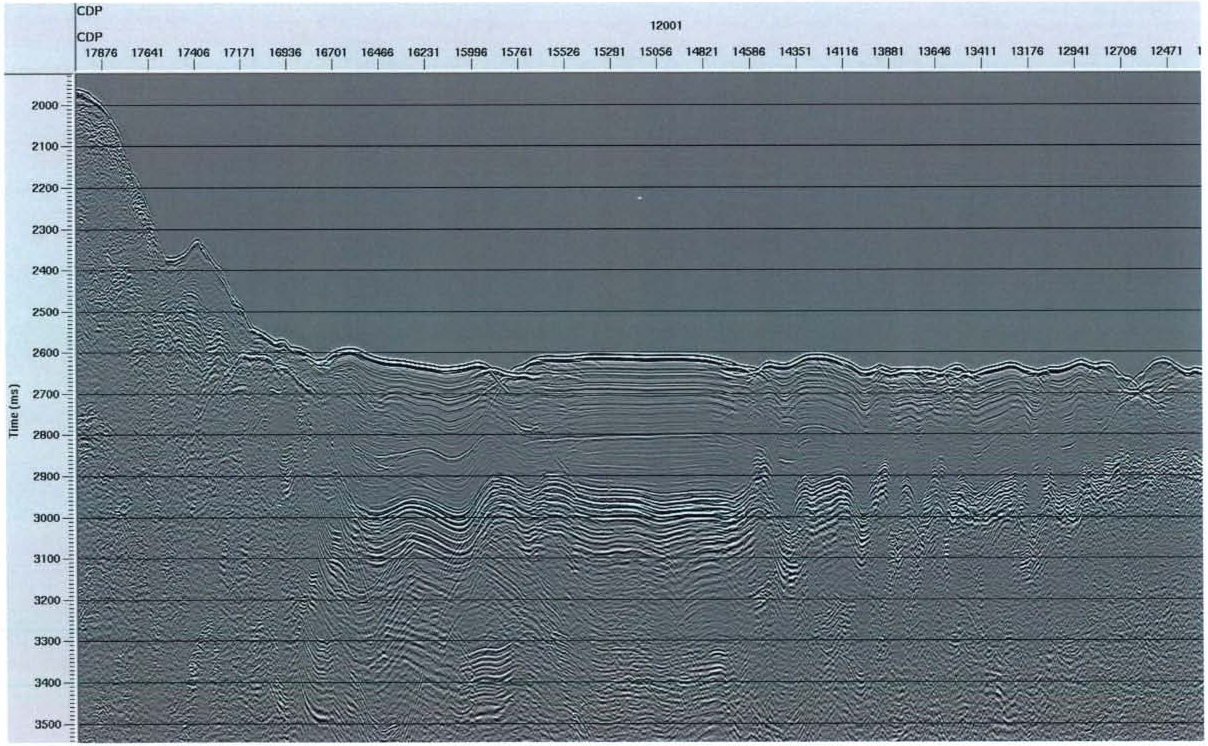

Figure 3.42 Kirchhoff time migration of the stacked seismic section in Figure 3.41.

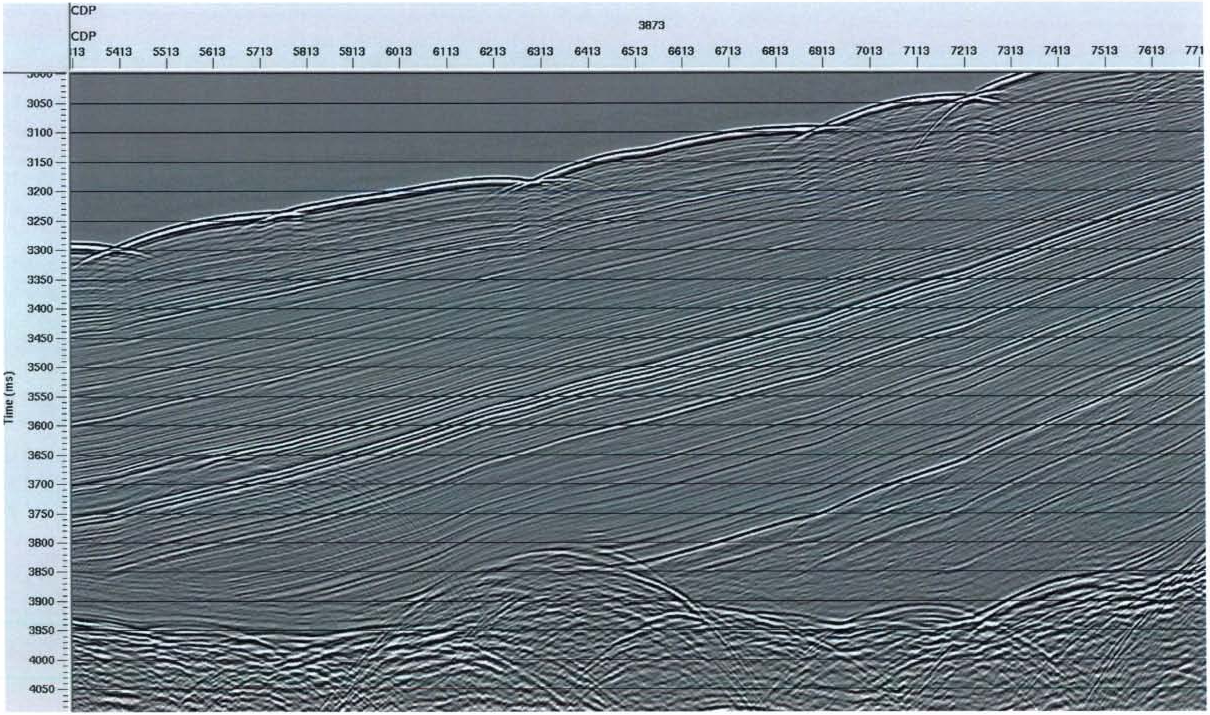

Figure 3.43 Stacked seismic section.

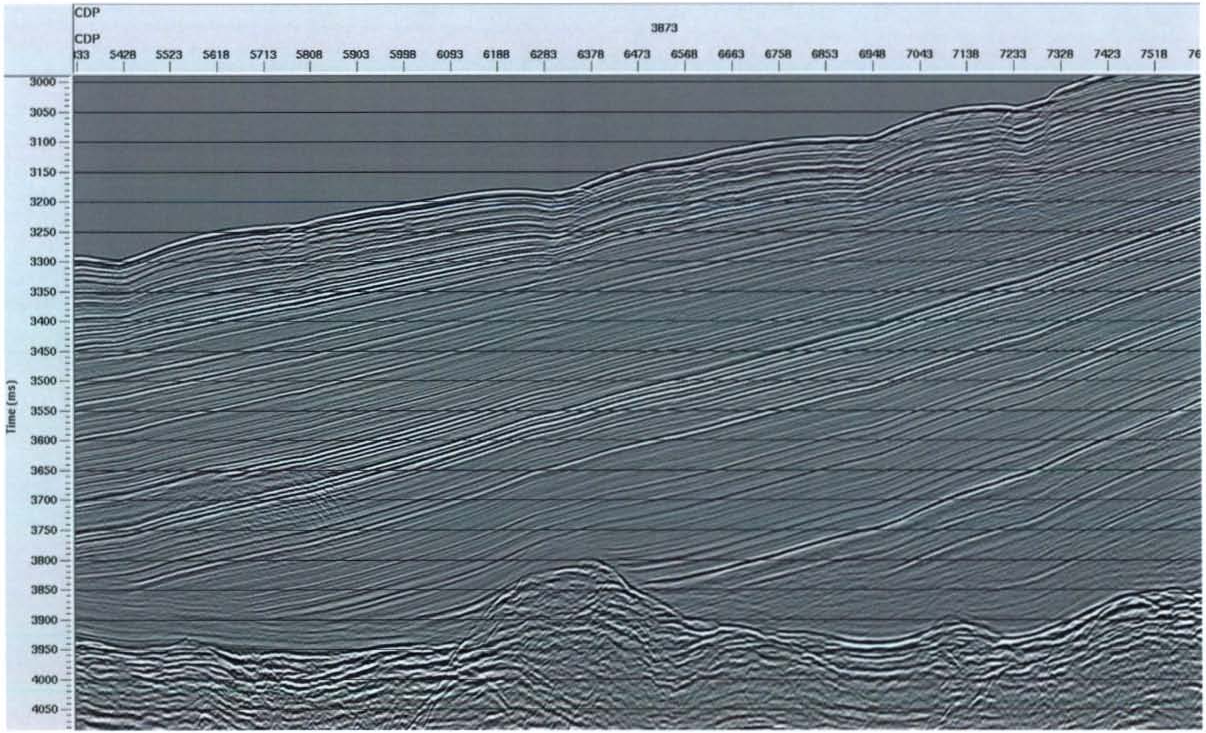

Figure 3.44 Kirchhoff time migration of the stacked seismic section in figure 3.43.

The migration process was one of the greatest challenges for this dataset because of the deep water environment, complicated sea floor morphology and significant lateral and vertical velocity variations in the area. A significant amount of time was spent altering migration velocities, trying to optimize the final image. One lesson learned from this process is that there may be no perfect migration, especially in 2D profiles of structures of varying orientations and it is that it is important to remember the balance between the time spent processing and what is actually gained in return.

3.7 Multiple Attenuation

Predictive deconvolution can be a useful data processing tool used to suppress/remove multiples. A predictive deconvolution filter is designed by analysing the autocorrelation for a given trace to determine the parameters required for deconvolution (Lines, 1996). These parameters include the prediction distance and the deconvolution operator length. The periodicity of the multiple is used to determine the prediction distance and the operator length is to cover the length of the seismic wavelet. With the correct parameters predictive deconvolution removes the predictable part of the wavelet (the multiples) and only primary reflectors are left behind (sepwww.stanford.edu).

The greater Anaximander Mountains are situated in relatively deep water, making multiple attenuation less of an issue in comparison to areas of very shallow water, where the attenuation of shallow water reverberations can be extremely difficult. For this study area the seabed reflection was the only multiple within the recorded time

window that needed to be attenuated. A number of multiple removal techniques, including predictive deconvolution and the application of a low velocity layer (LVL) in migration were attempted to try and diminish the effects of the seabed multiple.

Predictive deconvolution was tested on several lines to try to attenuate the seabed multiple. Figures 3.45 and 3.46 show stacked seismic sections pre- and post-deconvolution, respectively. Notice, there is very little, if any, difference between these two sections. The deconvolution application was ineffective at removing the sea bed multiple at ~5400 ms (Fig. 3.46). The failure of the deconvolution is most likely because the seabed multiple arrival time lacks the periodicity required to determine the prediction distance and the seabed reflection is complex where its curvature is high leading to bow-ties in stacked section. Throughout the study area the seabed reflection arrival time regularly occurs at ~3000 ms, with the exception of the three seamounts, reaching shallow depths less than 1000 ms. A multiple reflection occurs at 2x, 3x, 4x… the arrival time of a primary reflection, thus, the first seabed multiple in this study area will usually occur around 6000 ms. For example, in Figure 3.46 the seabed reflection occurs at ~2700 ms and the first seabed multiple is recorded at ~5400 ms. Thus, the second and subsequent multiples would occur at 8100 ms, 10800 ms and so on. The maximum time recorded for the 2007 data is 7500 ms, meaning that only the first multiple is recorded and all subsequent multiples would be beyond the range of the seismic record. Therefore, the 2007 data lack the periodicity of multiples required for Wiener predictive deconvolution. Furthermore, predictive deconvolution works best in areas where

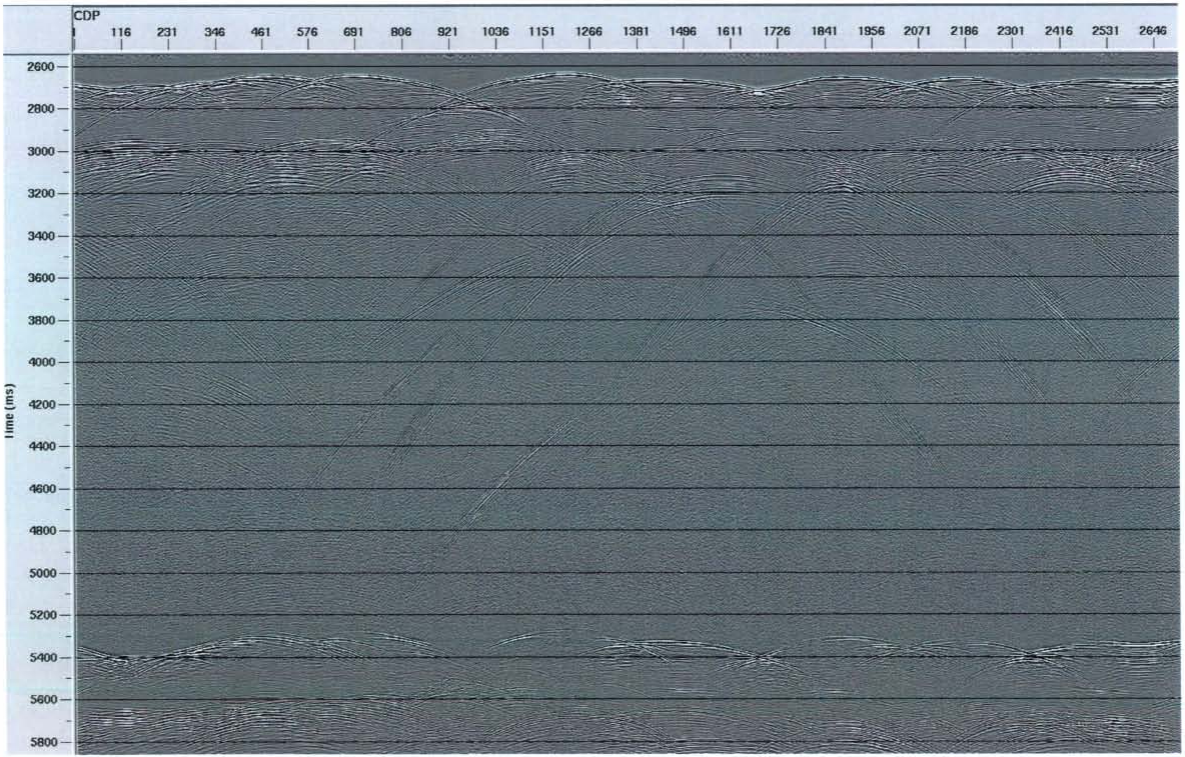

Figure 3.45 Stacked section with no predictive deconvolution applied.

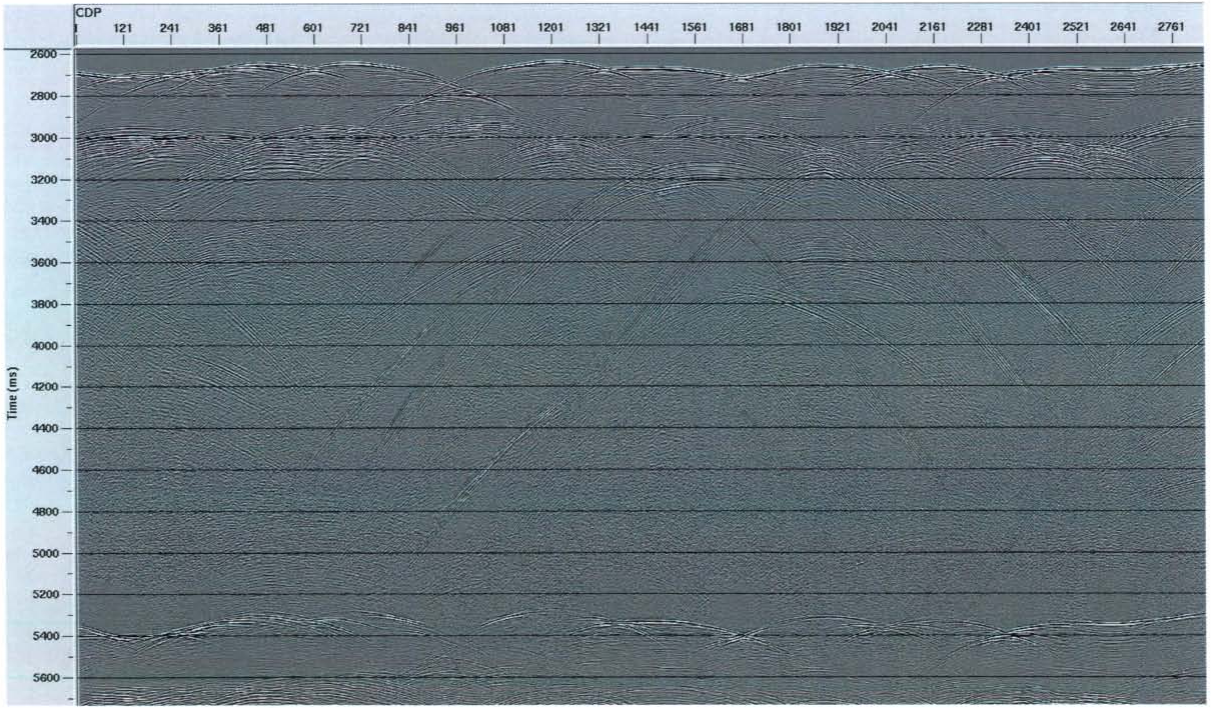

Figure 3.46 Stacked section after predictive deconvolution was applied.

reflectors are relatively horizontal and this assumption is violated by the complex seafloor morphology in the study area.

The inability to predict and attenuate the seabed multiple was not a concern, because the multiple arrival time is far down the section where very little primary energy is detectable. When possible, the seabed multiple was muted to avoid any distraction during interpretation. However, because the multiple velocity is significantly lower than the velocity of the primaries, after the data was migrated smiles from the over-migrated multiple would creep up through the section (Fig. 3.47), concealing primary reflections. Further attention was required to suppress the smiles coming off the seabed multiple.

After predictive deconvolution failed other multiple removal techniques including, adaptive deconvolution and f-k multiple removal were attempted, however, neither were beneficial. The adaptive deconvolution zeroed the multiple in areas leaving large holes in the dataset and in other areas where structures dipped more steeply the reflectors were not attenuated. The f-k multiple removal was tested, but did not show any improvement over the original data. This is probably because it was extremely difficult to distinguish between primary and multiple energy in the f-k spectrum.

In the end, applying a low velocity layer (Fig. 3.48) at the arrival time of the seabed multiple was the most beneficial method to suppress the migration smiles coming from the sea bed multiple. The velocity of the LVL changed for each line but ranged from 1000-1200 m/s. Figures 3.49 and 3.50 illustrate the data before the LVL is applied, whereas Figures 3.51 and 3.52 illustrate the data after the LVL is applied.

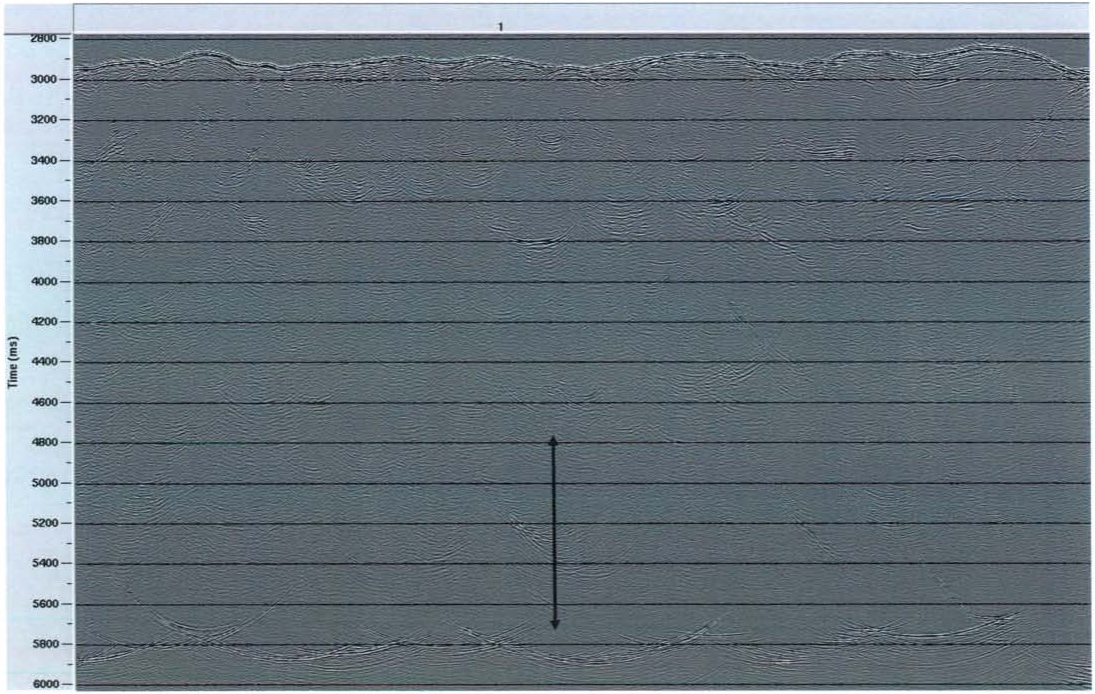

Figure 3.47 Migrated seismic section showing that the sea bed multiple at ~5800 ms is over migrated, causing smiles to creep up through the section. The black arrow marks some of the migration smiles.

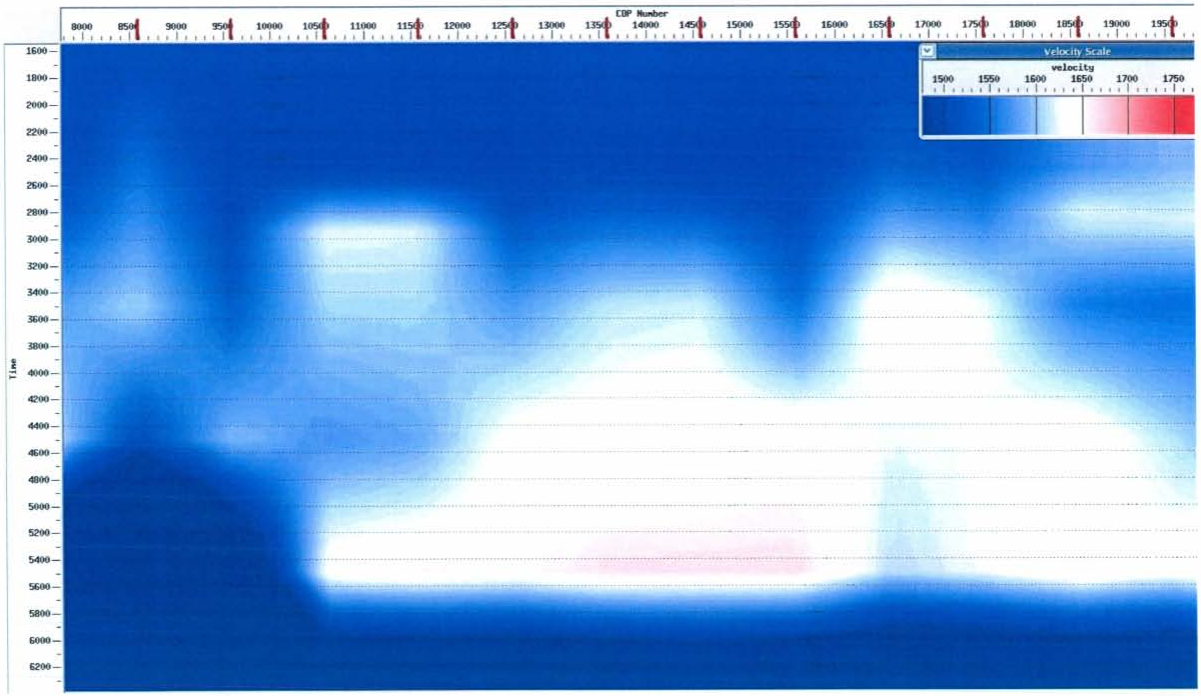

Figure 3.48 The velocity function used for migration, with the addition of a low velocity layer (i.e. the dark blue layer at ~4500-6400 ms). The low velocity layer is used to suppress the migration smiles from the over-migrated sea bed multiple.

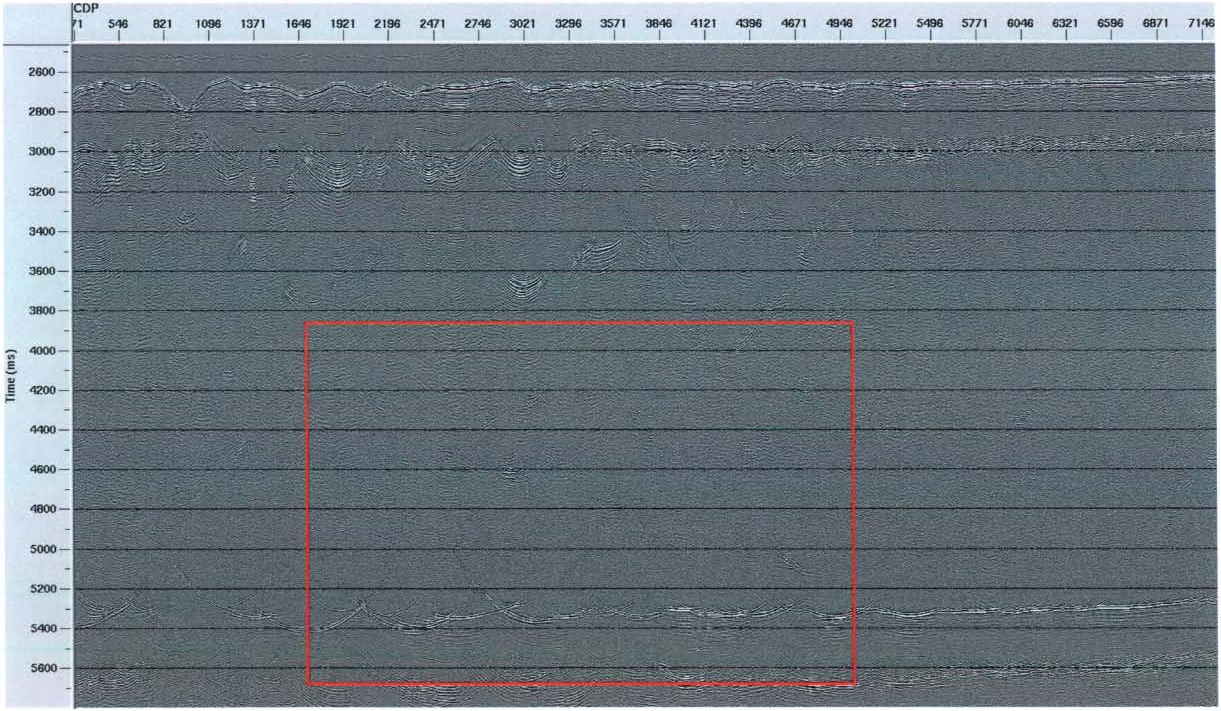

Figure 3.49 Trace display of a final migration with no low velocity layer.

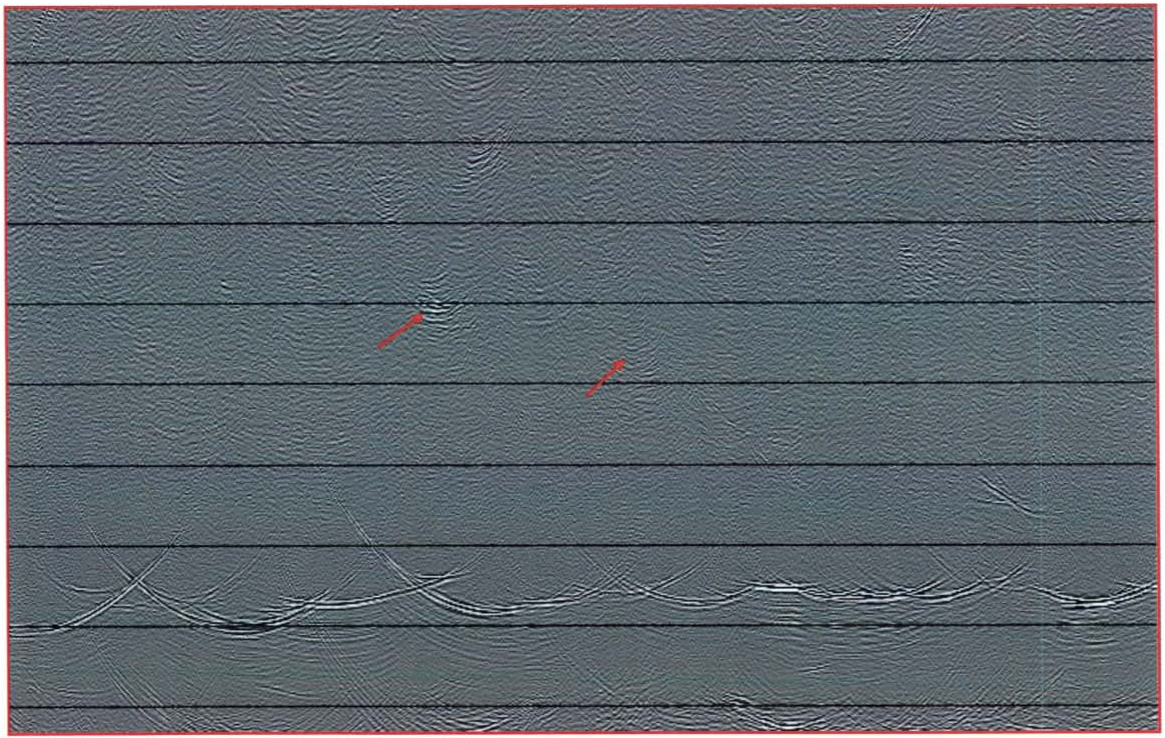

Figure 3.50 Zoom in on red box in Figure 3.49. The red arrows show where smiles from the multiple creep up through the section.

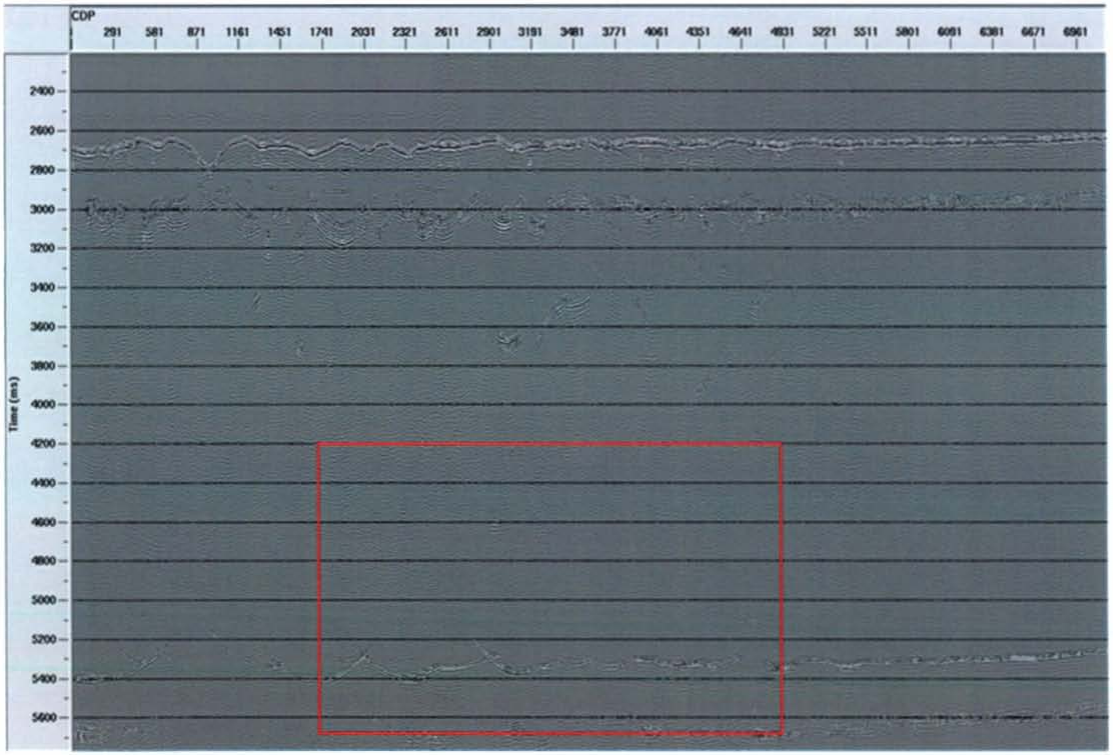

Figure 3.51 Final migration with the application of a low velocity layer.

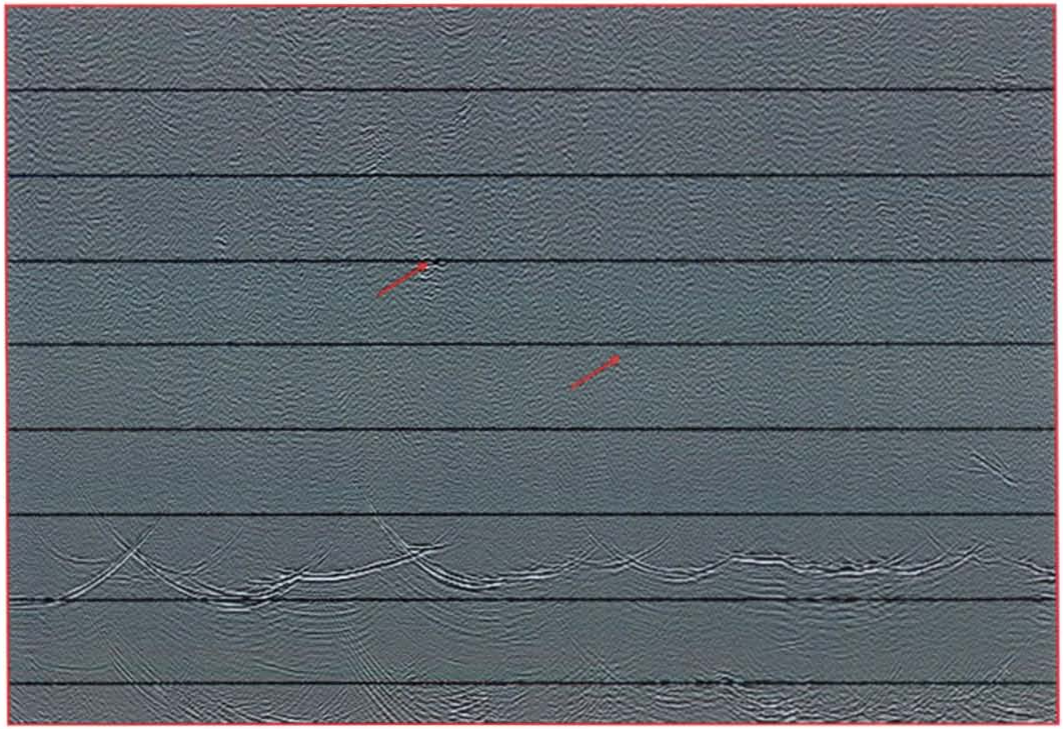

Figure 3.52 Zoom in on red box from figure 3.51. Notice the smiles from the multiple have been slightly reduced but the smiles that penetrate up through the section have been drastically reduced.

Following the addition of the LVL, the multiple is still over-migrated, but the smiles that penetrated up through the section have been drastically reduced (Fig. 3.49).

Applying trace mix to attenuate diffraction smiles from migration was also beneficial. A weighted trace mix of 5 (with weights of 1,1,1,1,1) did a good job at reducing the diffraction smiles. For each line a number of trace mixes were tested and some areas a greater mix of 7 or 9 was required.

3.8 Interval velocity determination for depth conversion

Accurate interval velocities are needed in order to carry out time – depth conversions. Although seismic reflection profiles are not depth-converted in this thesis, average interval velocity is calculated for the Pliocene-Quaternary succession to allow future conversions to be made (Table 3.1).

The red line in Figure 3.53 shows the location where the interval velocity was calculated. The trace display clearly shows that the seabed and the base of the upper unit (i.e., base Pliocene-Quaternary, see Chapter 4) are located at 3650 ms and 4800 ms, respectively. Initially the top and base of the succession were picked on the velocity semblance (Fig. 5.34). Then a closer look at the velocity semblance at the top (Fig. 3.55) and the base (Fig. 3.56) allowed for accurate determinations of the semblance peaks. As seen in Figures 3.55 and 3.56, the semblance peaks are not perfect bullseye targets, and that they could have been picked at slightly higher or lower velocities. To better

	TIME	V_RMS	V_INT
23891	3539	1562	2539
	4826	1873	
24515	3624	1569	2784
	4812	1941	
24642	3636	1558	2613
	4793	1868	
24729	3644	1510	2743
	4789	1880	
			avg=2670

V_RMS(high)	V_INT(high)
1558	2802
1933	
1510	2913
1940	

V_RMS(low)	V_INT(low)
1558	2413
1802	
1510	2479
1790	

Table 3.1 CDP location, time and root-mean-square (RMS) velocities used to determine the interval velocity for the Pliocene-Quaternary unit (discussed in Chapter 4).

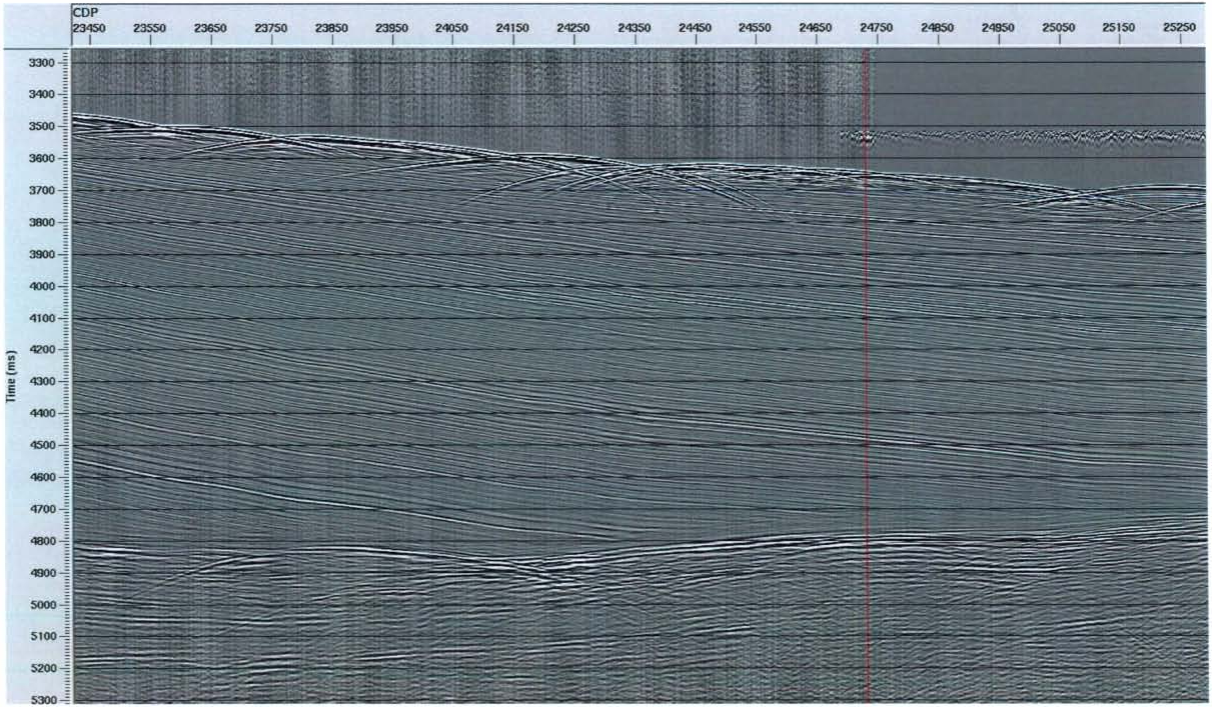

Figure 3.53 Trace display used to determine the optimal location (red line) for the calculation of the interval velocity for the Pliocene-Quaternary Unit 1 (discussed in Chapter 4).

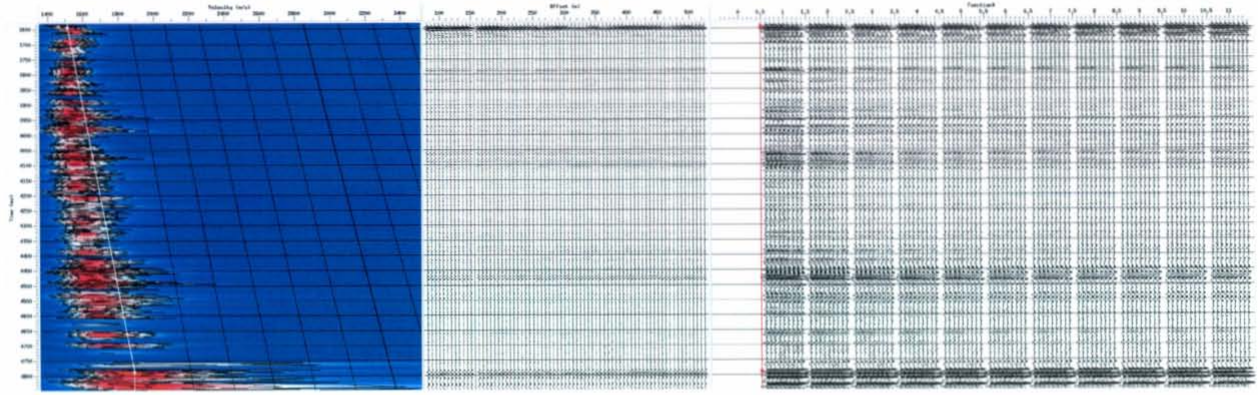

Figure 3.54 Velocity semblance stack and gather (from left to right) used to define a rough pick for the top and base of the Pliocene-Quaternary succession to determine the interval velocity.

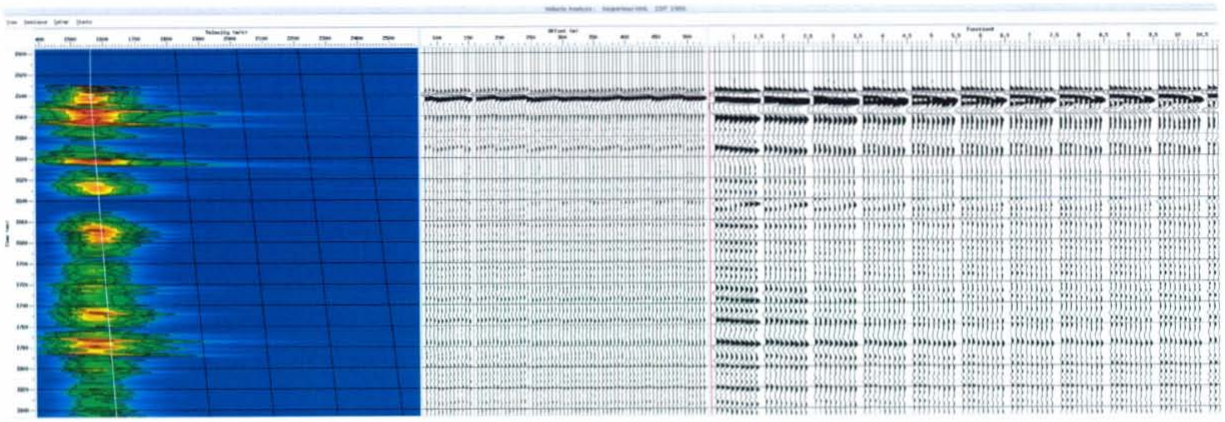

Figure 3.55 Velocity semblance stack and gather (from left to right) used to pick the top of the Pliocene-Quaternary succession.

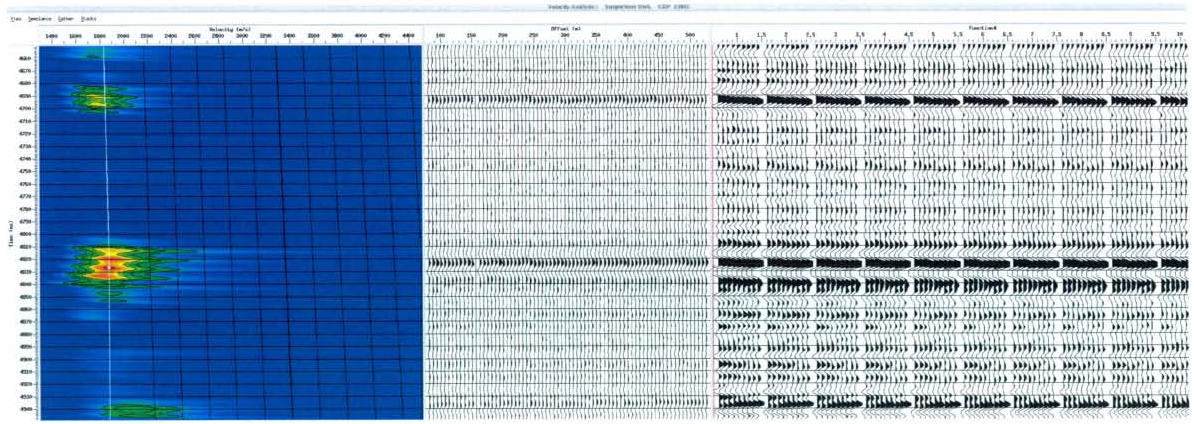

Figure 3.56 Velocity semblance, stack and gather (from left to right) used to pick the base of the Pliocene-Quaternary succession.

constrain the analysis, interval velocities were determined for higher and lower RMS velocities, which provided a more reliable average interval velocity (Table 3.1). Equation 3.2 is used to determine the final interval velocity.

$$V\_INT = \sqrt{((t_{base} * t_{base}^2) - (t_{top} * t_{top}^2) / (t_{base} - t_{top}))} \quad (3.2)$$

Chapter 4: Seismic Stratigraphy and Chronology

Seismic profiles from the Anaximander Mountains *(sensu lato)* show three distinct seismo-stratigraphic units (Unit 1, Unit 2 and Unit 3), separated from each other by prominent reflections that extend across the entire study area (Figs. 4.1). The locations of the seismic reflection profiles illustrated in this chapter are provided in Figure 4.2. Each unit is distinguished by its acoustic character, reflection strength and reflection continuity. In this chapter a detailed description of these stratigraphic units and their bounding surfaces is provided. Stratigraphic thickness is recorded in 2-way travel time and the dip amount is shown by the dip degree scale on seismic profiles. The chronology of the sedimentary successions imaged in seismic Units 1-3 in the study area is determined by integrating the principles of seismic stratigraphy with dredge samples, cores (Woodside et al., 1997), two boreholes drilled over the Florence Rise by the Deep Sea Drilling Project (Shipboard Scientific Party, 1978) and two exploration wells drilled in the onland Kasaba Basin (Şenel and Bölükbaşı, 1997). Lithological and age data from dredges and boreholes provide the information necessary to correlate seismic units across the study area and to determine the age and relationships of the different units.

4.1 Description of cores and dredges from the Anaximander Mountains

There are several short cores and dredge samples collected from the greater Anaximander Mountains region (Fig. 4.3; Woodside et al., 1997). Data from these samples in combination with the high-resolution seismic reflection profiles from the area provide a first order lithostratigraphy and chronology for seismic stratigraphic Units 1-3.

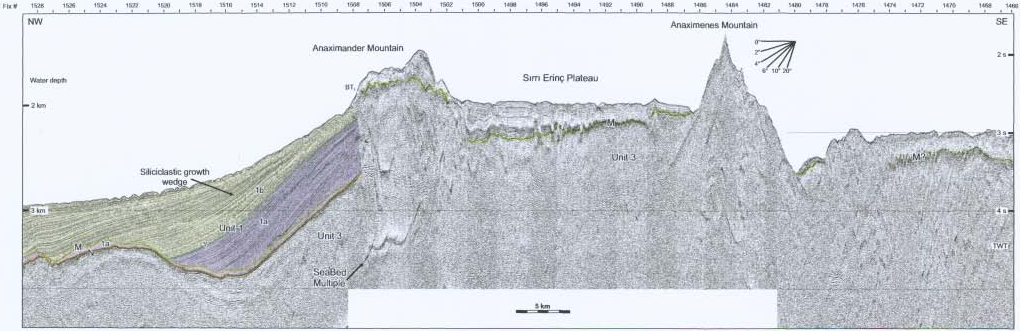

Figure 4.1 Multi Channel seismic reflection profile A showing stratigraphic Units 1-3, the M-reflector, N-reflector, γ-reflector, and subunits 1b discussed in text. Location is shown in figure 4.2.

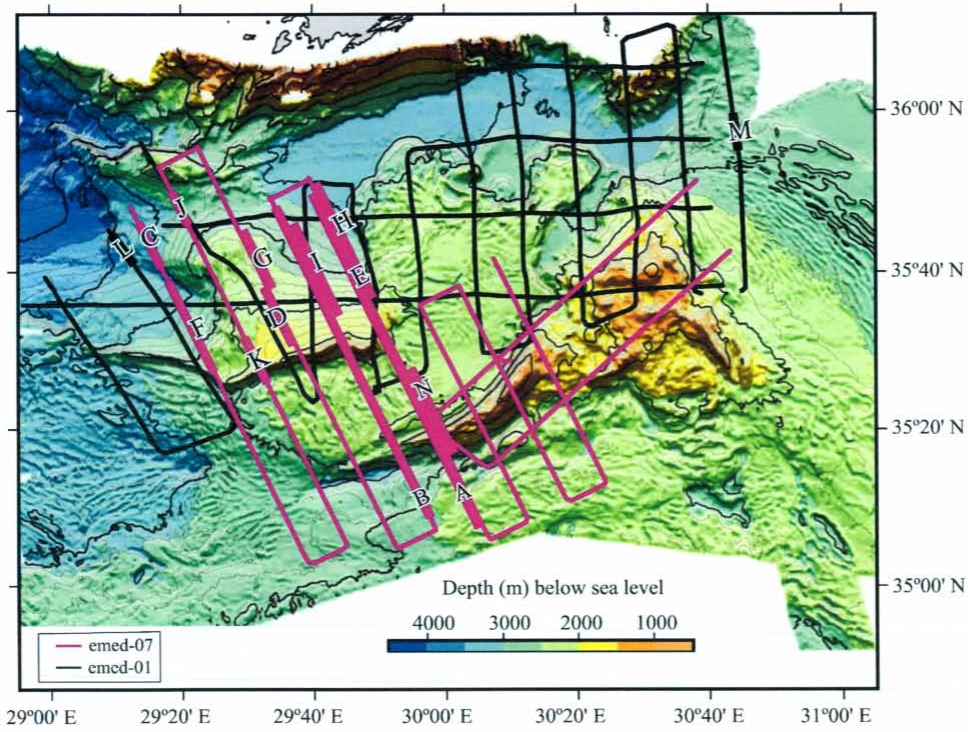

Figure 4.2 Map showing the locations of the seismic reflection profiles A-N illustrated in this Chapter.

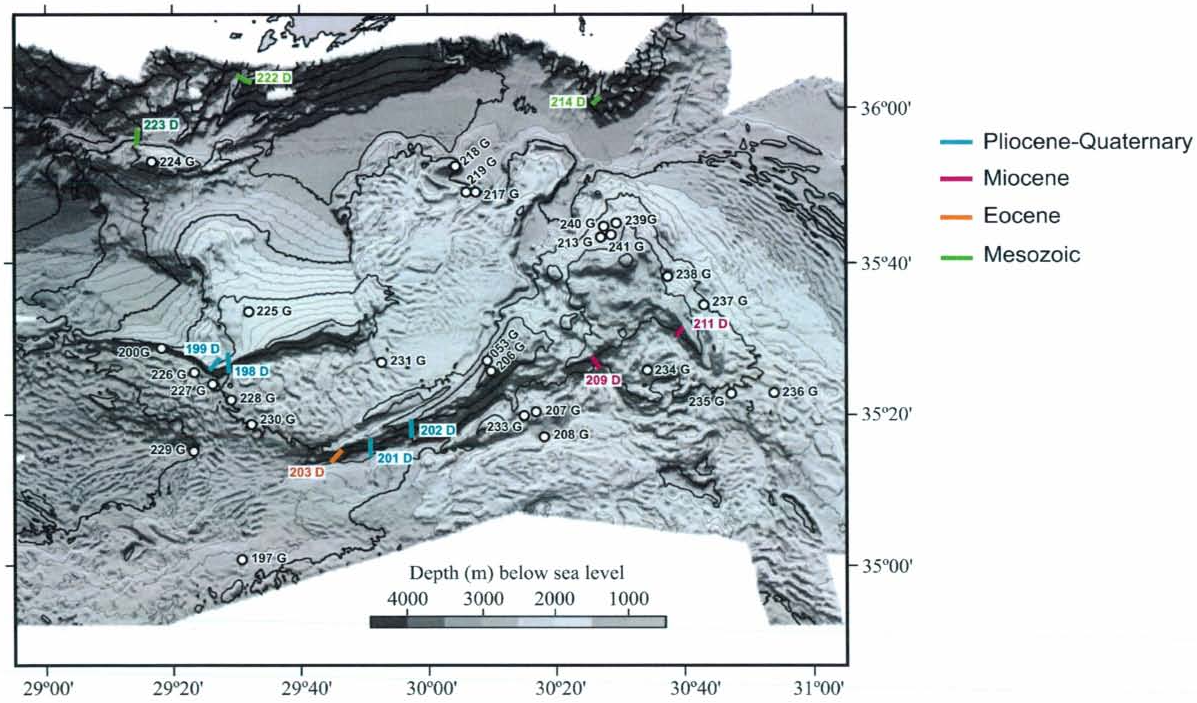

Figure 4.3 Map showing the locations of cores and dredge samples (data from Woodside et al., 1997).

4.1.1 Core samples

A total of 28 short soft-sediment cores are collected during the ANAXIPROBE/TTR-6 cruise from the Anaximander Mountains (*sensu lato*) (Fig. 4.3; Table 4.1). The coring results show that the entire study area is covered by variably thick Holocene-Pleistocene hemipelagic sediments, including bioturbated foraminifera- and nannofossil-rich muds and silty muds, sapropels and sapropellic muds, and tephra layers (Akhmanov et al., 1997).

4.1.2 Dredge samples

A total of 17 dredge samples was collected during the ANAXIPROBE/TTR-6 cruise from the Anaximander Mountains (Fig. 4.3; Table 4.2). The cruise report highlights that ~50% of the dredges were empty or contained few rock samples, while the remaining dredges recovered sufficient quantities of rock samples to establish the subsurface geology (Dumont and Woodside, 1997). Samples recovered in the dredges ranged from Eocene – early-mid Pliocene siliciclastic rocks, including claystones, siltstones, sandstones and conglomerates, to mid-Miocene flysch deposits, to Jurassic and Cretaceous sandstones, cherts and ophiolitic rocks. Close examination of the dredge results show that various types of ophiolitic rocks and flysch deposits mainly occur in the northern portion of the Anaxagoras Mountain, as well as along the Turkish continental slope (Table 4.2, Fig. 4.3).

Location	Cores	Lithology	Chronology	Description
Anaximander Mountain Şırrı Erinç Plateau?	224 229 230	slumped pelagic marls, clays, carbonate clays, with sapropel and tephra layers	Pleistocene-Holocene	The depositional environment of a weakly tilted plateau
Anaximenes Mountain	205 206	slumped sediments with marl, clay, carbonate pebbles and mud silty mud, silt, sapropel slump	Pleistocene-Holocene	Slope processes are prevalent
Anaxagoras Mountain	213 235 234	Mud breccia overlain by pelagic marl, ophiolitic rocks and cherts Pelagic marls with sapropel and tephra layers and mud breccia Mud breccia with hard rock clasts up to 7 cm and abundant shell fragments	Pleistocene-Holocene	Kula mud volcano- ophiolitic rocks and cherts imply a connection to the Antalya Napes Complex Complex Jurassic-Cretaceous macrofossils Mud is gas saturated and contains the first gas hydrates recovered from the Mediterranean Kazan Mud volcano Tuzlukush Mud volcano
Şırrı Erinç Plateau	231 219	Slumped breccia from slope, foram rich clays, marls with sapropel and tephra layers Foram and petropod rich marls, silty mud, clay and silt with clasts of sandstone	Pleistocene-Holocene	Evidence of reworked Eocene-Miocene strata

Table 4.1 Summary description of the core samples collected from the study area (from Woodside et al., 1997).

Location	Dredge	Lithology	Chronology	Description
Anaximander Mountain	199D 198D	clay, siltstone, sandstone	Pliocene-Pleistocene	Fault planes indicate contractional overlap
Anaximenes Mountain	201D 202D 203D	Siltstone, sandstone, limestone	Early-mid Pliocene Eocene, early-mid Miocene	Eocene-mid Miocene rocks are dominant on the southern margin
Anaxagoras Mountain	209D 211D	Siltstone, Flysch Sandstone, limestone	Mid Miocene	Miocene flysch present over a large portion of the area Reworked Eo-Miocene strata Slikinsides indicate compressive tectonics
West Turkish continental slope	223D 222D	Conglomeritic and fine grained "sandy limestone"	Early Pliocene and Mesozoic	Neritic limestone with rudests
East Turkish continental slope	214D	Ophiolitic rocks	Mesozoic	Suspected connection to the Antalya Napes complex

Table 4.2 Summary description of the dredge samples collected from the study area (from Woodside et al., 1997)

Dredge samples from the western Turkish continental slope (e.g., 222D, 223D in Fig. 4.3) consist of Mesozoic limestones and early Pliocene conglomeratic and fine-grained "sandy" limestones (Table 4.2). Dumont and Woodside (1997) suggested that these rocks were related to the Beydağları successions onland in southern Turkey. A single dredge sample from the eastern Turkish continental slope (e.g., 214D in Fig. 4.3) sampled ophiolitic rocks. Dumont and Woodside (1997) ascribed these rocks to be related to the Antalya Nappes Complex.

Two dredge samples (i.e., 198D, 199D; Fig. 4.3) from the Anaximander Mountain (*sensu stricto*) recovered Pliocene – Pleistocene claystones, siltstones and limestones (198D) and a Quaternary hard carbonate crust (199D). Two other dredge samples (i.e., 202D, 203D in Fig. 4.3) from the Anaximenes Mountain recovered mid-Miocene marls, lime-mudstones and Eocene greenstones, together with Pliocene-Pleistocene clays, siltstones and sandstones (Table 4.2).

A single dredge along the eastern segment of the Anaxagoras Mountain (211D, Fig. 4.3) recovered mid-Miocene limestones and undated sandstones. The cruise report indicates that the limestones are similar to those recovered from the Anaximenes Mountain dredge 202D (Dumont and Woodside, 1997).

4.2 Description DSDP 375 and 376 boreholes

Two deep boreholes were drilled on the Florence Rise by the Deep Sea Drilling Project: Sites 375 and 376 (Fig. 4.4). The sediments encountered in these boreholes are

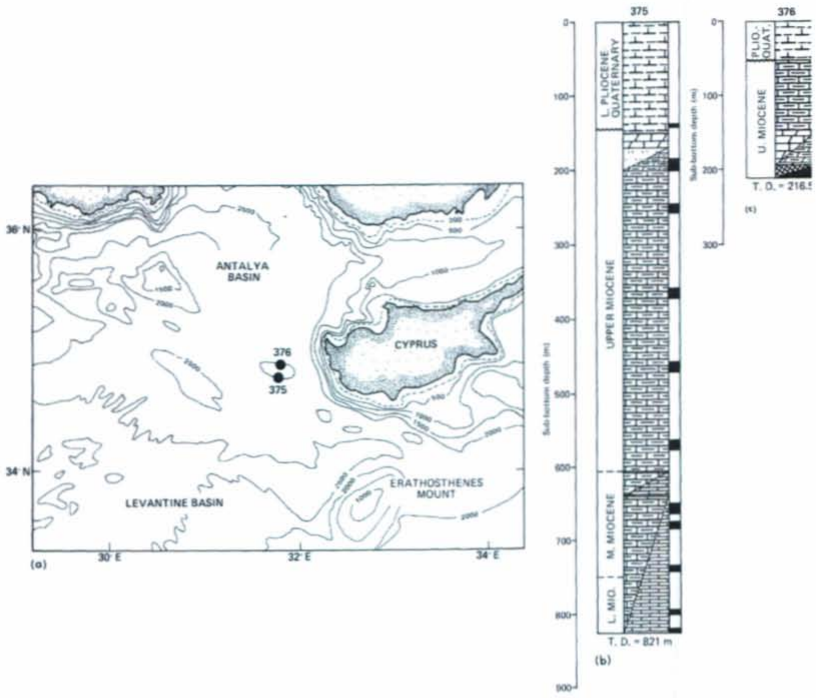

Figure 4.4 Map showing the locations of DSDP Sites 375 and 376 drilled over the Florence Rise, and the simplified lithostratigraphy of the drilled successions.

briefly described here to assist in the correlations between the lithostraigraphic units and the seismic reflection profiles used in this study (Shipboard Scientific Party, 1978). Site 375 was drilled to a depth of 821.5 m and a predominantly pre-evaporite succession was recovered. Site 376 was offset ~13 km to the north and was cored continuously into the Messinian evaporite succession. Eleven lithologic units have been distinguished at Sites 375 and 376: four units in the Pliocene-Quaternary pelagic succession, two in the late Miocene evaporite and post evaporite successions, a flysch-type unit in the Tortonian, and four units in the pre-Tortonian to Early-Middle Miocene sediments (Shipboard Scientific Party, 1978). These units are briefly described below:

- Unit I is a Quaternary hemipelagic sequence consisting of gray to brown unconsolidated nannofossil marls, whereas Unit II consists of Late Pliocene gray nannofossil and foraminifera-rich marls. Unit III is characterized by Early to Late Pliocene, brown to orange nannofossil marls. Units I, II and III also include minor thin interbeds of sapropelic marls and volcanic ash beds. Unit IV consists of light to medium gray Early Pliocene marls. It comprises two chaotically deformed subunits.

- Unit V consists of Late Miocene (Messinian) dolomitic marlstones and turbiditic sandstones and siltstones. It is subdivided into four subunits. Subunits Va and Vb are two successions of a slightly silty nannofossil dolomitic marlstone, with minor amounts of interbedded siltstones and sandstones. Subunit Vc contains thinly bedded inter-layered laminated siltstones and marlstones, probably of

turbiditic origin. Finally, Subunit Vd is characterized by abundant detrital gypsum, and greenish sandstones and siltstones.

- Unit VI is composed of gypsum, green dolomitic marlstone, anhydrite and halite which are Messinian in age. It is divided into two subunits. Subunit VIa underlies Unit V and contains olive grey to light grey gypsum. The subunit includes crudely layered and recrystallized gypsum, coarse selenitic gypsum crystals, coarse recrystallized gypsum with roughly equant and traced anhydrite and elongate selenitic "swallow-tail" gypsum crystals, set in a matrix of gypsiferous greenish-white marlstone. Subunit VIb is mainly composed of anhydrite and halite, and contains from top to base: (i) numerous small pieces of clear, coarsely crystalline halite with thin wavy interlayers of finely crystalline gypsum; (ii) larger fragments of white nodular anhydrite with large and small enter-oolitic folds and occasional chicken-wire structure with considerable amounts of gypsum; (iii) a fragment of banded anhydrite, in which thin dark brown, organic-rich laminae separate up to 1 cm thick bands of nodular anhydrite (iv) banded halite with 2 to 4 cm thick layers of clear coarsely crystalline halite separated by 0.5 cm thick, brown, fine-grained gypsum layers containing rare anhydrite.

- Unit VII consists of an upper Miocene (Tortonian) dark colored, partly dolomitic marlstone sequence. The sequence exhibits distinct cyclicity, with each cycle consisting of a fine-grained terrigeneous arenite subunit, which grades into a

structureless or finely-laminated dolomitic nannofossil marlstone subunit, which is overlain by a marlstone subunit.

- Unit VIII consists of Serravallian age variegated mudstones, nannofossil marlstones and foraminifera-nannofossil rich limestones. Unit IX also consists of Serravallian dark colored mudstones and nannofossil marlstones interlayered with lighter colored calcareous nannofossil marlstones. Unit X is composed of reddish-brown nannofossil marlstones with interbedded light grayish-blue green to greenish-gray nannofossil marlstones and foraminiferal limestones. The age of Unit X is Langhian. Unit XI is composed of dark green-gray limestones and marlstones of Burdigalian age.

4.3 Description of lithologies in of Kaş-1 and Demre-1 well

Turkish Petroleum Corporation drilled two exploration wells in the onland Kasaba Basin: Kaş-1 and Demre-1 (Fig. 4.5). The Kaş-1 well was drilled to a total depth of 5298 m. It recovered a 3375 m thick succession of predominantly limestone of Jurassic to Upper Cretaceous age, correlated with the Beydağları Formation (Fig. 4.5; Şenel and Bölükbaşı, 1997). From 3375 m to 5200 m, the well recovered an Upper Triassic dolomite, correlated with the Kuyubaşı Formation. At 5200 m the well encountered a major discontinuity, where the upper Triassic sediments were underlain by the lower Cretaceous limestones of the Beydağları Formation. This discontinuity is interpreted by Turkish Petroleum Corporation (unpublished data) and Şenel and Bölükbaşı (1997) as a major south-verging, north-dipping thrust (Fig. 4.5).

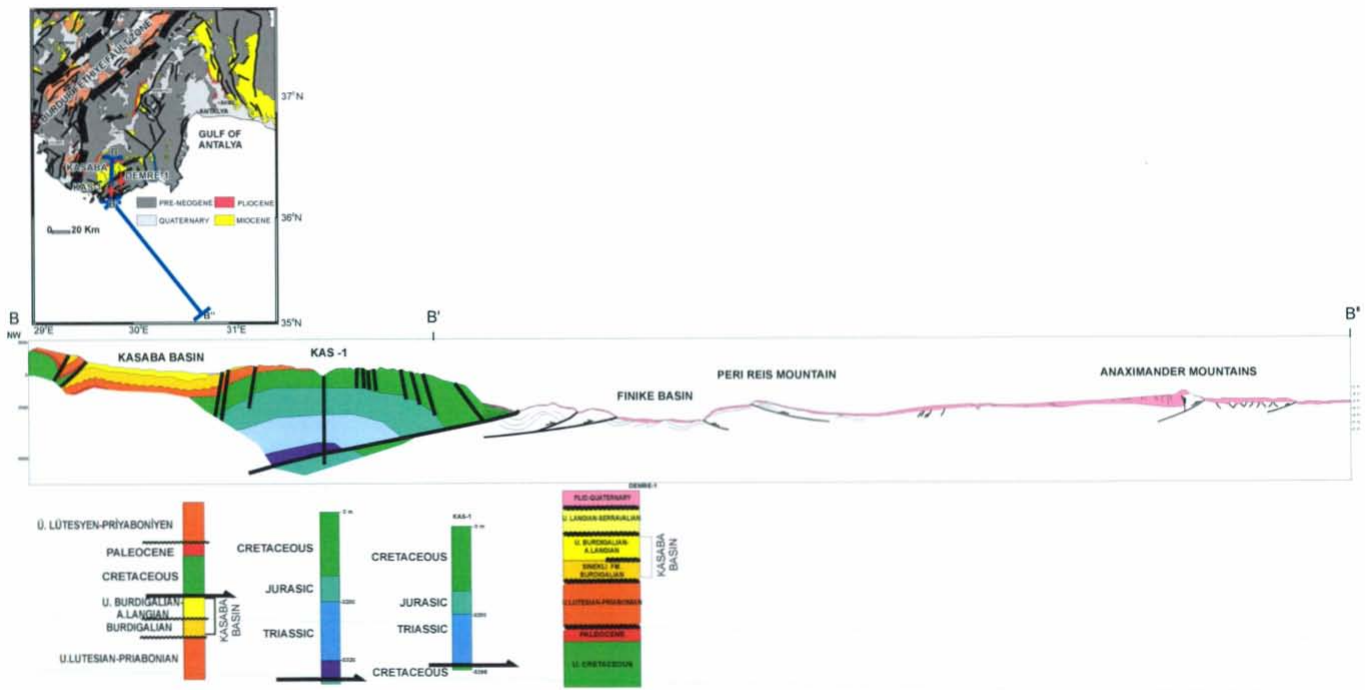

Figure 4.5. Cross section B-B' and B'-B" from SW Turkey to offshore Anaximander Mountains showing the linkage between thrusting observed in wells onshore in the Western Turide Mountains with that seen in the offshore (modified from Aksu et al., 2009).

The Demre-1 well is drilled to a total depth of 6110 m (Fig. 4.5). The well recovered 3200 m of Jurassic to upper Cretaceous neritic limestone succession of the Beydağları Formation (Şenel and Bölükbaşı, 1997). From 3200 m to 5356 m the well encountered a middle to upper Triassic dolomites of the Kuyubaşı Formation, followed by a 644 m thick lower Triassic. The well further recovered ~110 m of an undated domolitic succession.

The data from these two onland exploration wells, immediately north of the study area, show that the mid-late Miocene phase of deformation affected the Serravallian-Langhian sedimentary successions in the Kasaba Basin and the western Tauride Mountains (Şenel and Bölükbaşı, 1997). A significant thrust encountered in the Kaş-1 well and possibly in the Demre-1 well suggests the presence of a ~10° N-dipping, south verging major structure. This is in keeping with the fold-thrust geometries observed in the marine areas (discussed in Chapter 5).

4.4 Description of seismic stratigraphic units and their bounding surfaces

4.4.1 Unit 1: Pliocene-Quaternary

The youngest and uppermost stratigraphic unit in the Anaximander Mountains is a regularly reflective package with acoustically strong and highly continuous reflectors (Figs. 4.1, 4.6). Reflectors from this unit display the highest frequency content recorded on the seismic profiles. Well data from the Florence Rise, ~165-200 km southeast of the study area, show that this unit is Pliocene-Quaternary in age and is predominantly

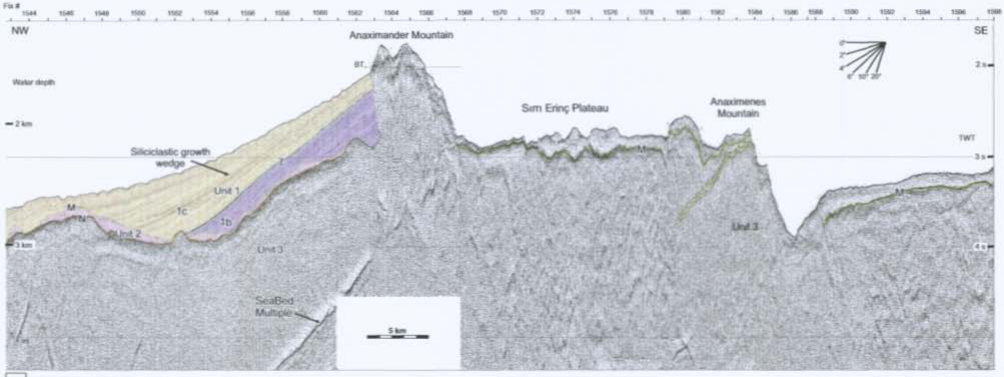

Figure 4.6 Multi channel seismic reflection profile B showing stratigraphic Units 1-3, the M-reflector, N-reflector, γ-reflector, and subunits 1a and 1b discussed in text. Location shown in Figure 4.2.

composed of siliciclastic sediments. The base of this unit is marked by the prominent M-reflector which can be correlated well beyond the immediate study area (discussed later in this chapter). Unit 1 occurs across the entire study area but shows considerable variations in sediment thickness (Fig. 4.7). The thickest Pliocene-Quaternary deposit is found in deep troughs to the northwest of the Anaximander Mountain *(sensu stricto)*, where sediment thickness reaches a maximum of 2200 ms in the Finike Basin (Fig. 4.7). Unit 1 dramatically thins over structural highs, where thinning is shown by the convergence of reflectors towards the high and onlap of reflectors onto other reflectors (Figs. 4.1, 4.6). These reflector configurations define a series of mild unconformities over the crest of structural highs but become conformable when traced toward the basin(s). This relationship is known as progressively stacked syntectonic unconformities and is the response to several periods of extended tectonic activity where sediments are deposited like a seesaw, rocking back and forth through time in the basin. This will be discussed further in Chapter 5. Unit 1 is thinner in the Sırrı Erinç Plateau, ranging in thickness from ~100-400 ms and the Anaximenes Mountain is starved of Pliocene-Quaternary sediment (Fig. 4.7). Regionally the Pliocene-Quaternary succession thickens southeast toward the Anaximander Mountain and here Unit 1 shows prominent north-directed growth strata wedges (Fig. 4.1).

The base of Unit 1 is marked by a prominent surface which is interpreted as a major unconformity because: (i) in many places, the gently (2-5°) landward dipping reflectors of the lower Unit 3 are erosionally truncated at this surface (Fig. 4.8), and (ii) in other places, the near-horizontal reflectors of the upper Unit 1 show progressive onlap

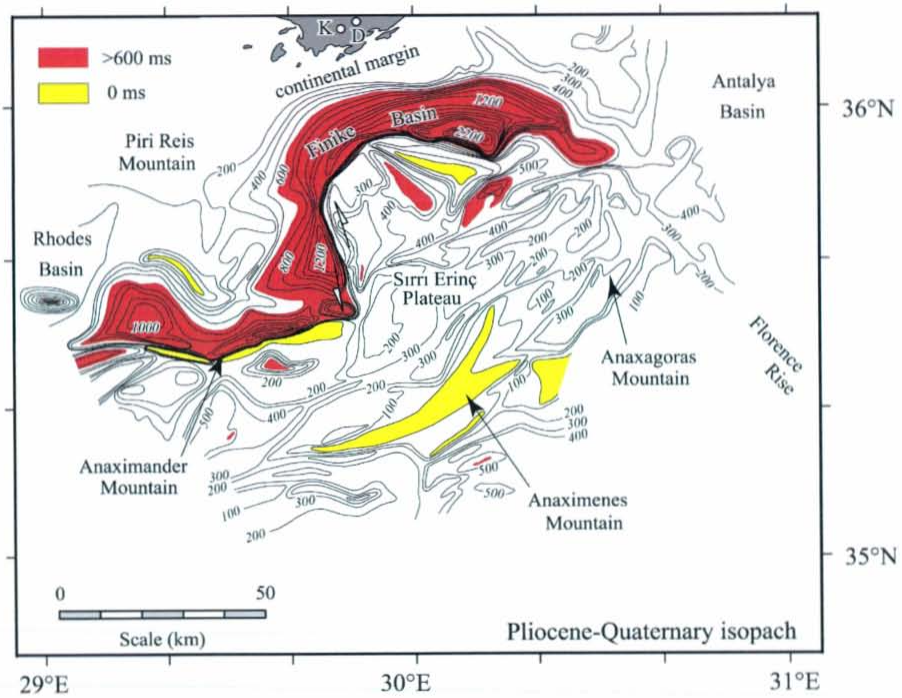

Figure 4.7 Isopach map of Unit 1, showing the thickness variations of the Pliocene-Quaternary sediments in the study area.

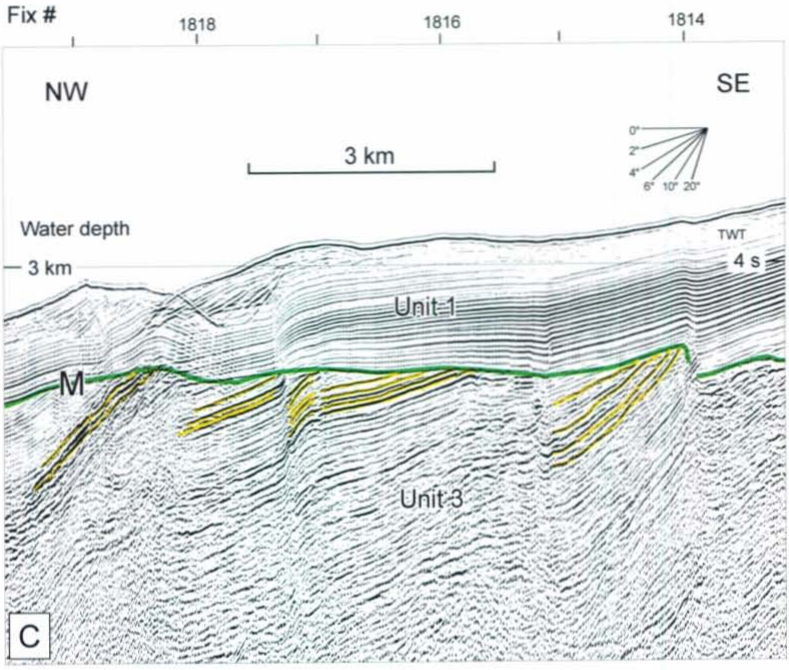

Figure 4.8 Seismic reflection profile C showing the erosional truncarion of the underlying Unit 3 at the M-reflector. Location shown in Figure 4.2.

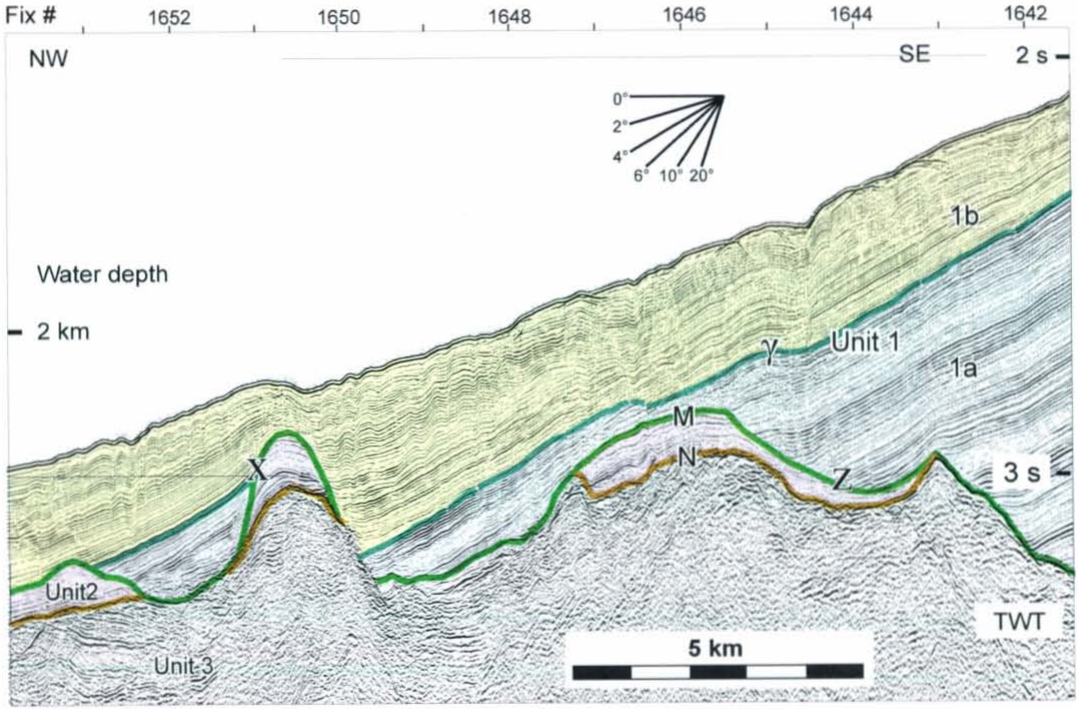

Figure 4.9 seismic reflection profile D showing the onlap (X) and down lap (Z) onto the M-reflector. Location is shown in figure 4.2.

and downlap onto this surface (Fig. 4.9). This unconformity resembles, in acoustic character and position in the seismic profiles, the "M-reflector" described by Ryan, (1969) as well as many subsequent studies such as Işler et al. (2005), Aksu et al. (2009), and Hall et al. (2009). Therefore, it is given the same name in this dissertation to be consistent with the previous publications. Unit 1 is further divided into two sub-units: Subunits 1a and 1b (Figs. 4.1, 4.6, 4.9), on the basis of internal architecture and external geometry of the package.

Subunit 1a

Subunit 1a is the lowermost unit of the Pliocene-Quaternary succession and is identified in the northwestern portion of the study area. It is characterized by acoustically strong, high amplitude reflectors that are very continuous. This subunit demonstrates onlap, downlap and truncation of surfaces (Fig. 4.8, 4.9, 4.10, 4.11). The thickness of this subunit varies significantly (i.e., from 0-1000 ms) over the backlimb of the Anaximander Mountain *(sensu stricto)*. These thickness variations are largely developed by north-directed apparent downlap observed on the northern slopes of the Mountain. Subunit 1a may be absent in the Sırrı Erinç Plateau and the Anaximenes Mountain and environs. The base of subunit 1a is marked by the M-reflector, while the top is shown by a highly reflective surface defined as the γ–reflector (Figs. 4.1, 4.6, 4.9, 4.10). The γ-reflector is interpreted as a mild unconformity because reflectors above onlap the γ-reflector, while reflectors below are truncated at the γ-reflector (Figs. 4.11, 4.12, 4.13, 4.14). It is correlated across the back of the Anaximander mountain *(sensu stricto),*

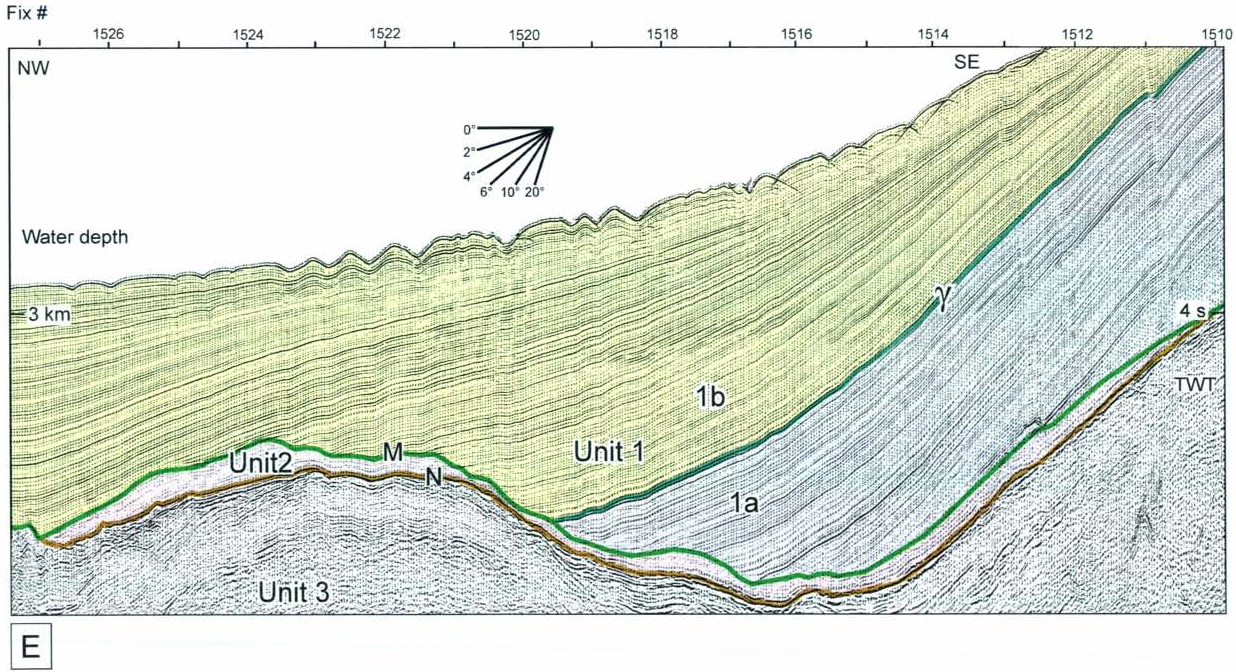

Figure 4.10 seismic reflection profile E showing the subdivisions in Unit 1, as well as the prominent down lap of reflectors over the M-reflector. Location shown in figure 4.2.

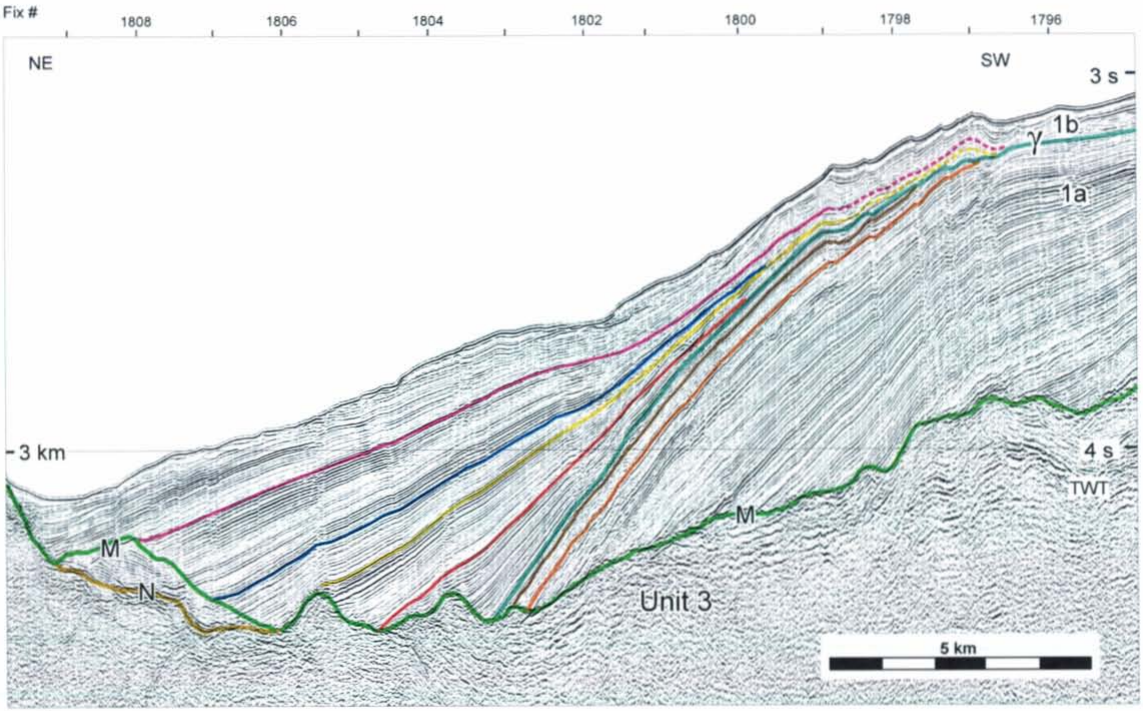

Figure 4.11 Seismic reflection profile F showing the growth strata wedges in subunit 1b above the γ-reflector. Note the onlap onto and truncation at the γ-reflector. Location shown in figure 4.2.

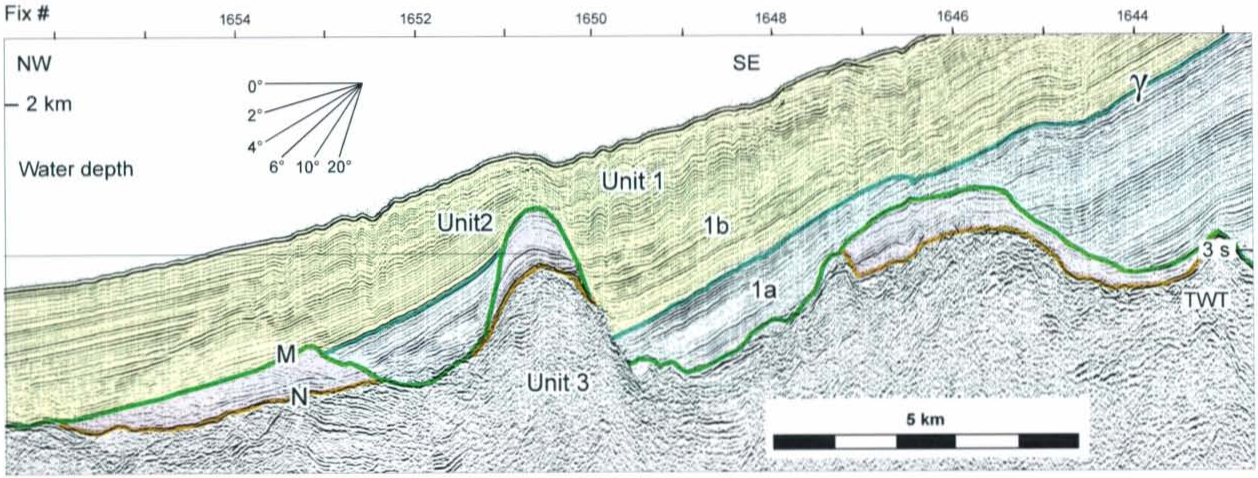

Figure 4.12 Seismic reflection profile G showing the prominent corrugation of the surface defined by the M-reflector. Note the onlap and downlap of the sediments in subunits 1a and 1b onto the M-reflector, and the truncation of the reflectors within Unit 3 at the level of the M-reflector. The inferred Messinian Unit 2 defines isolated pockets above the M-reflector. Location is shown in Figure 4.2.

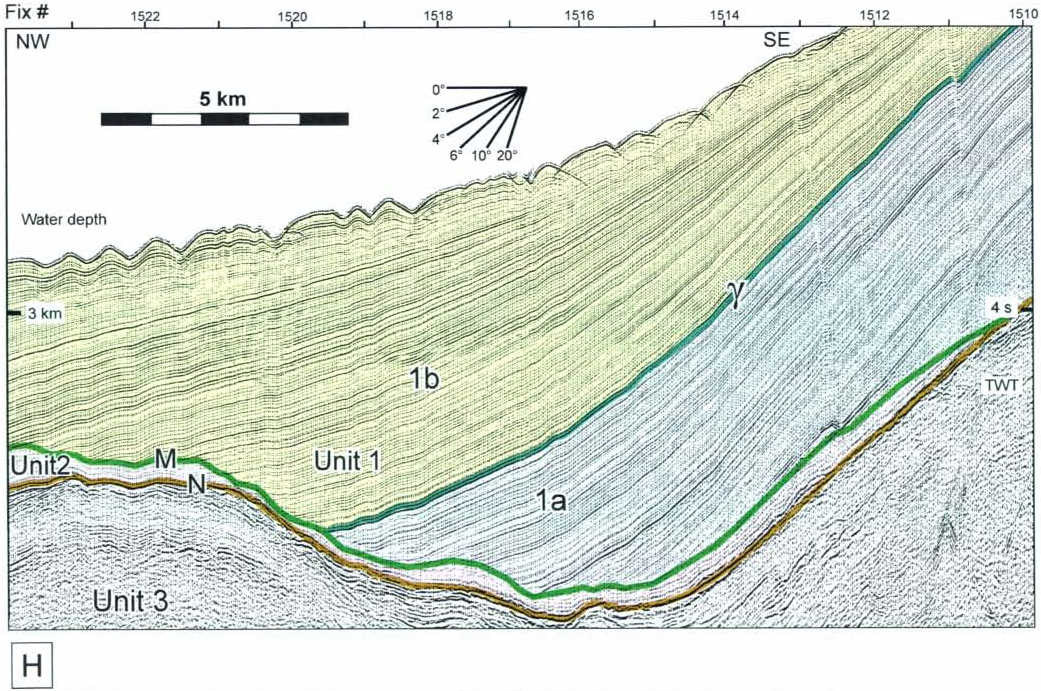

Figure 4.13 Seismic reflection profile H showing the growth strata wedges in subunit 1b above the γ-reflector. Note the near isopachous nature of subunit 1a. Location is shown in Figure 4.

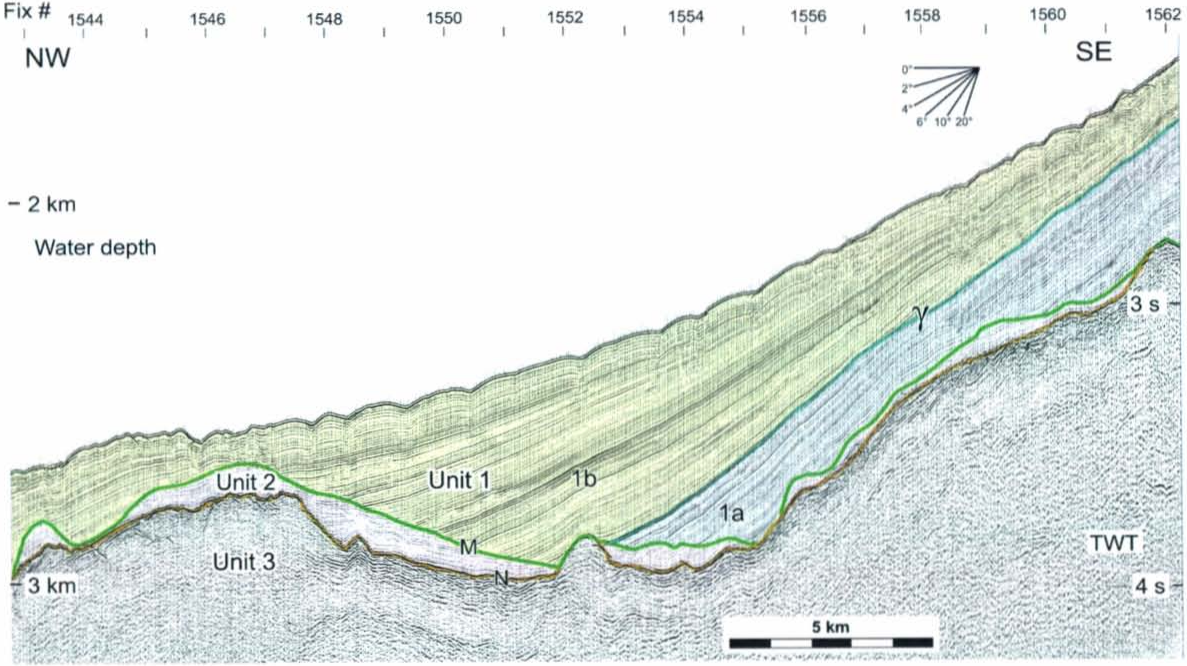

Figure 4.14 Seismic reflection profile I showing the growth strata wedges in subunit 1b above the γ-reflector. Note the onlap onto and truncation below the γ-reflector. Location is shown in Figure 4.2.

where sediments are thickest but, farther away from seismic crossover-points, confidence in correlation decreases. Subunit 1a shows little to no growth, thus reflectors below γ are interpreted to be deposited before deformation that occurred in the Pliocene-Quaternary (further discussed in Chapter 5).

Subunit 1b

Subunit 1b uncomformably overlies the γ-reflector and is the uppermost unit in the study area (Figs. 4.9-4.14). This package is acoustically very strong with moderately continuous reflectors, which have the highest frequency content observed in the study area. In some places, these reflectors are notably corrugated, yet in most places they are clearly flat (Figs. 4.9, 4.10). Subunit 1b is thickest (~1000 ms) in deep troughs northwest of the Anaximander Mountain *(sensu stricto)*, but thins over the Sırrı Erinç Plateau to ~100-400 ms. It is generally absent in the Anaximenes Mountain and environs. The subunit exhibits prominent northward-thickening growth strata wedges on the northern slopes of the Anaximander Mountain (Figs. 4.1, 4.6, 4.10, 4.11, 4.13, 4.14). Each wedge is about 200 ms thick immediately south of the Turkish continental slope, but drastically thins to ~0-10 ms toward the crest of the Anaximander Mountain *(sensu stricto)*. In the western portion of the study area where the Anaximander Mountain swings to assume a northwest-southeast trend (Fig. 4.2), subunit 1a is notably thick and forms a prominent paleo-topographic high (Fig. 4.11). Here the growth strata wedges developed in subunit 1b rapidly thin towards northern slopes of the high observed in subunit 1a, creating a series of stacked successions with the thickest pile of each successively younger wedge

migrating northward (e.g., Figs. 4.1, 4.6, 4.11). Traced from north to south, each wedge thins dramatically, with the lower two wedges clearly pinching out against the γ-reflector (Fig. 4.11). Progressively younger wedges thin towards the south, but overstep the high developed in subunit 1a (Fig. 4.11). Careful examination of seismic reflection profiles shows that each younger growth strata wedge is displaced further to the north, recording the growth history of the Anaximander Mountain. In many locations, reflectors within subunit 1b show near vertical offsets where the deformation clearly affects the seafloor morphology, creating small steps on the seabed, further discussed in Chapter 5 (Figs 4.13, 4.14). The successions in subunit 1b include occasional, internally acoustically-transparent lenses (Fig. 4.15). These lenticular bodies either show chaotic and discontinuous reflections, or very faint and discordant reflections. These lenses are interpreted as debris flow deposits because of their strong acoustic similarities with previously documented debris flow deposits (Aksu and Hiscott, 1989, Hiscott and Aksu, 1994).

4.4.2 Unit 2- Late Miocene (Messinian)

Unit 2 is an acoustically rather transparent package characterized by low reflectivity and discontinuous reflectors (Figs. 4.12-4.14). This unit is identified by its unconformable top, which defines the M reflector and its highly reflective base, the N-reflector (Figs. 4.1, 4.6, 4.12-4.14). Across most of the western portion of the study area (i.e., Anaximander Mountain *(sensu stricto)* and the Rhodes Basin) the unit is deposited as a very thin veneer of sediment (<267 ms) directly below the Pliocene-Quaternary Unit

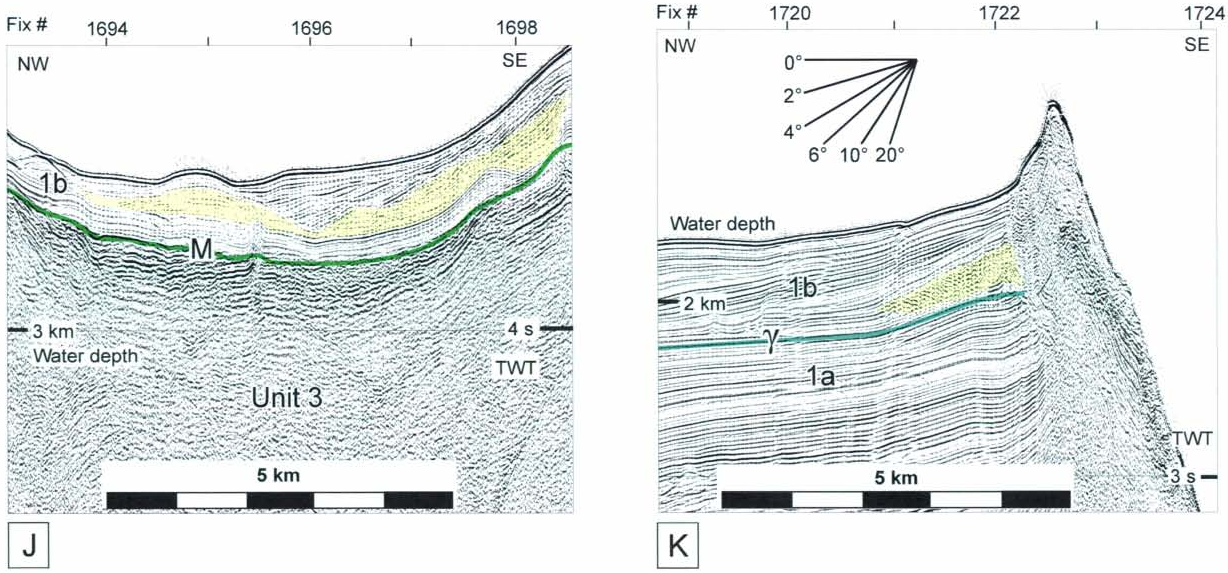

Figure 4.15 **(a)** Seismic reflection profile J and **(b)** Seismic reflection profile K showing debris flow deposits highlighted in yellow. Locations are shown in Figure 4.2.

1. It exhibits a restricted areal extent directly to the northwest of the Anaximander Mountain (Fig. 4.16).

Reflectors within Unit 2 are generally lower frequency then the overlying Pliocene-Quaternary Unit 1, and dip gently (~2°) towards the north. In some locations, such as the transition between the Anaximander Mountain and the Rhodes Basin, Unit 2 exhibits internal deformation that is disharmonious with the units above and below, and their bounding reflectors (Fig. 4.17).

In areas where Unit 2 is absent, the M-reflector is a strong horizon representing an erosional surface that defines a composite unconformity, which includes the M and N-reflector. In these regions, units above and below the M-reflector are interpreted as Pliocene-Quaternary and pre-Messinian, respectively (Figs. 4.8, 4.11).

Previous studies established the presence of a thick evaporite succession deposited almost everywhere in the eastern Mediterranean (Hsü et al., 1973; Cita et al., 1978; Unit 2 of Hall et al., 2005., Işler et al., 2005 and Aksu et al. 2009 and Hall et al., 2009). Most eastern Mediterranean basins, such as the Antalya Basin (Fig. 4.18) contain a thick evaporite sequence that was deposited during the Messinian (Işler et al., 2005). Unit 2 was deposited during the Messinian Salinity crisis (e.g., Cita et al., 1978) when the Mediterranean Sea was repeatedly desiccated to form the 1-2 km thick evaporite succession. Well data suggest that the Messinian evaporite deposits are composed of halite, alternating with lesser quantities of anhydrate and limestone (Shipboard Scientific Party, 1978). The Messinian evaporites are reported to be absent in the Anaximander

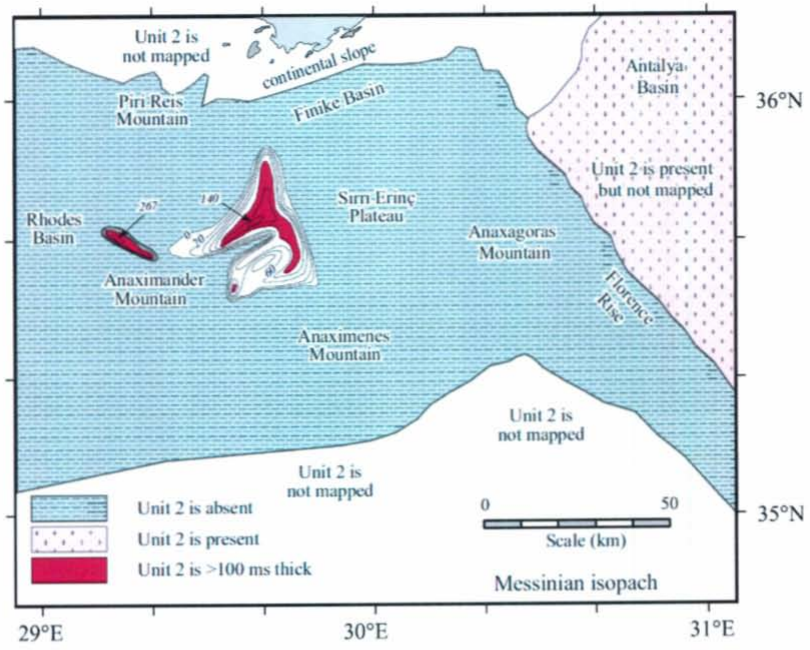

Figure 4.16 Map of the study area showing the regional distribution of Unit 2.

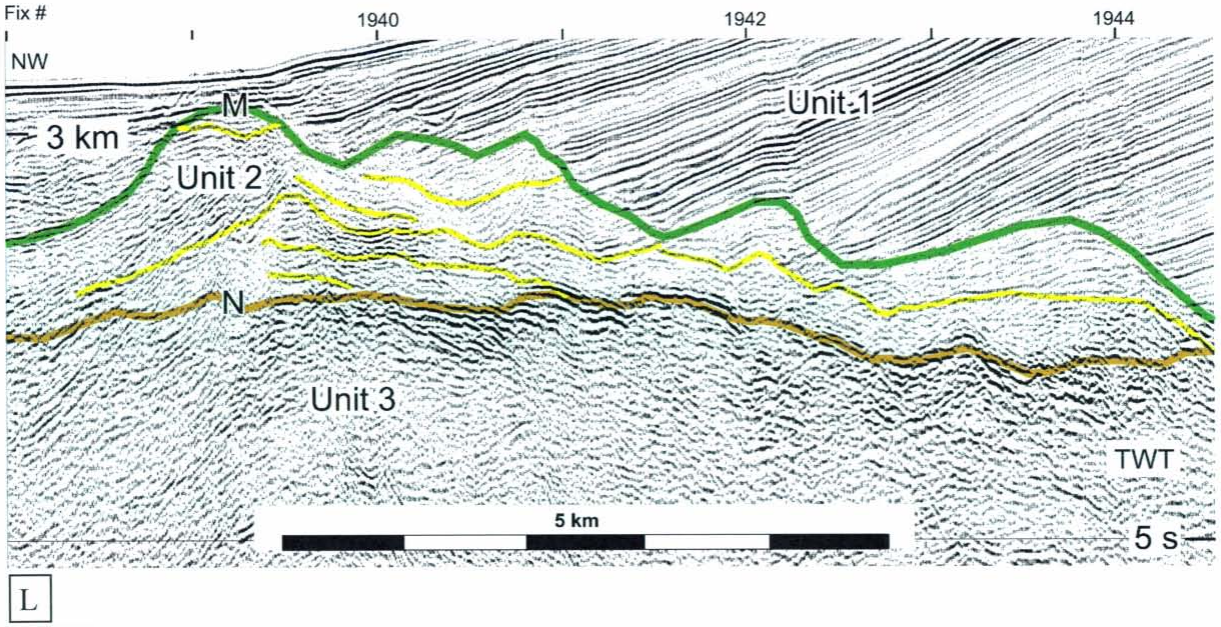

Figure 4.17 Seismic profile L showing the internal deformation in Unit 2. Location is shown in Figure 4.2

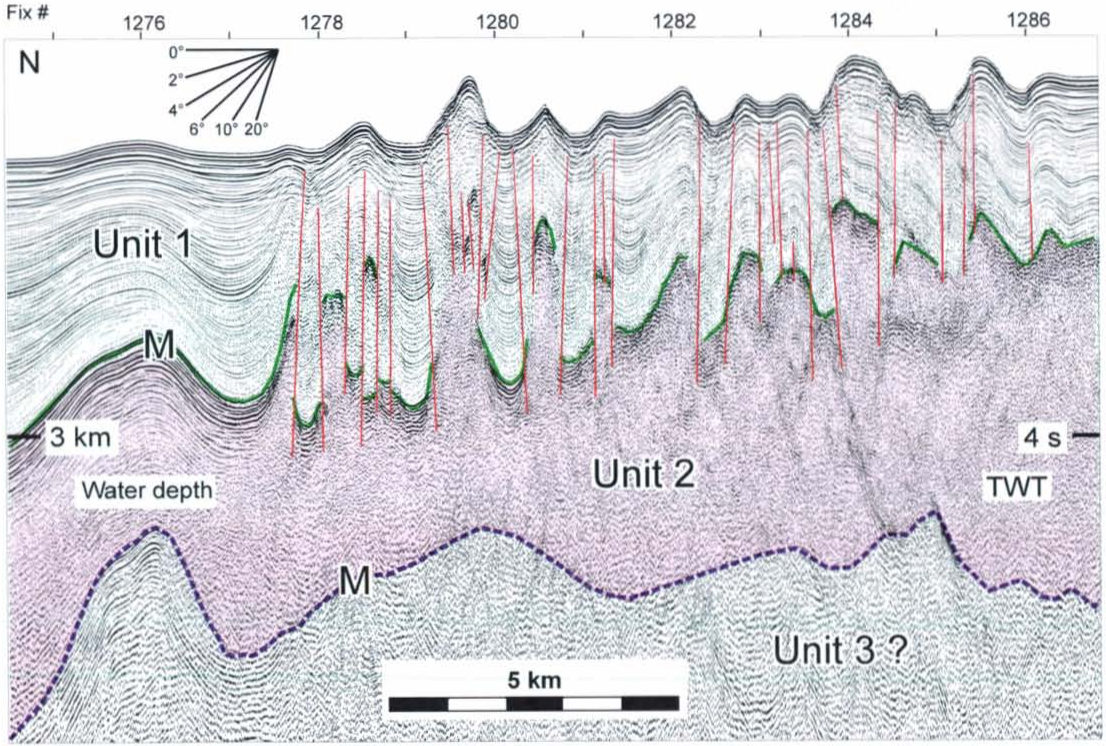

Figure 4.18 Seismic reflection profile M from the southwestern Antalya Basin showing the architecture of Unit 2. Location is shown in figure 4.2.

mountain region (Robertson et al, 2000, Aksu et al., 2009, Hall et al., 2009) in part because of the perceived absence of a strong M-reflector. However, this study is the first to report the possible presence of Messinian deposits from the Anaximander Mountain as well as the deep Rhodes Basin. Unit 2 described above is correlated with the Messinian evaporites based on internal reflectivity and the stratigraphic and structural relationship with the overlying Pliocene-Quaternary unit. It is possible that this unit could be associated with gypsiferous marls, and evaporitic successions intercalated with marls and chalks, such as the Kalavasos and Lapatza formations described from the Mesaoria Basin and Kyrenia Mountains (Gass, 1960, Moore, 1960, Robertson et al., 1991), and typical of thin, marginal facies of the evaporite basins.

4.4.3 Unit 3: Pre Messinian and Acoustic Basement

Unit 3 is the oldest and deepest unit in the study area. This package is acoustically weak with moderately continuous to discontinuous reflectors. As depth increases in seismic reflection profiles, the spatial and temporal resolution of the seismic data diminishes and the correlation of seismic horizons becomes increasingly difficult (Fig. 4.19). Seismic horizons from this unit are low frequency and often demonstrate broad folds, further described in Chapter 5. The top of Unit 3 is marked by the prominent M-reflector where Unit 2 is absent, and the N-reflector in regions where Unit 2 is present. The base of Unit 3 is not imaged in the survey area, and is therefore defined as the acoustic basement. Seismic reflections within Unit 3 are truncated by the M-reflector forming a clear angular unconformity (Fig. 4.8). The folded strata within Unit 3 mimic

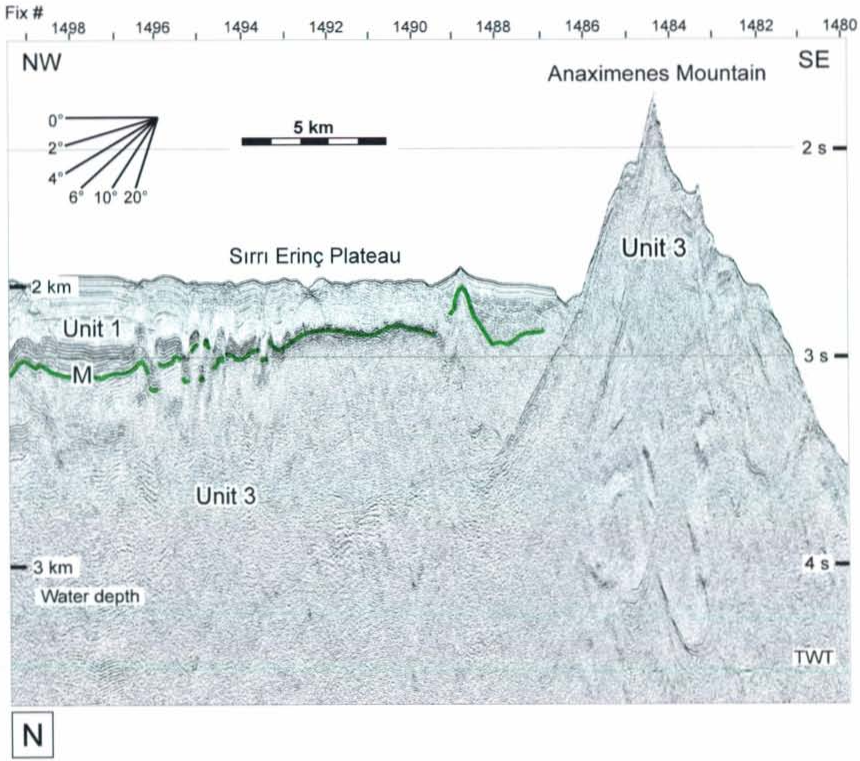

Figure 4.19 Seismic reflection profile N showing the architecture of Unit 3. Location is shown in figure 4.2.

the vertical variation of M-reflector (Fig. 4.12-4.14). Reflections below structural highs (i.e. Anaximander Mountain and Anaximenes Mountain) are correlated as Unit 3; however strata in these locations show a significant amount of internal deformation and reflector correlation is challenging (Figure 4.19). The lithology and chronology of Unit 3 has been investigated using core and dredge data collected during the ANAXIPROBE/TTR-6 cruise of the R/V *Gelendzhik*.

4.5 Chronostratigraphy of the seismic units

A long distance correlation of seismic profiles collected across the Florence Rise with those collected from the Anaximander Mountain region is provided in Figure 4.20.

The data described above provide the basis for a tentative chronology to be established for the seismic stratigraphic units identified in the study area (Fig. 4.21). Unit 1 is tentatively correlated with the Yenimahalle and Alakilise formations and the Antalya Tufa of the Aksu, Köprü, Manavgat and Antalya Basins. Unit 1 is further correlated with the Nikosia Athalassa formations and the Fanglomerate of the Mesaoria Basin and the Kyrenia Mountains of Cyprus. Unit 2 is correlated with the Taşlık and Gebiz formations of the Aksu, Köprü, Manavgat and Antalya Basins, as well as the Kalavasos and Lapatza formations of the Mesaoria Basin and the Kyrenia Mountains, respectively (Fig. 4.21).

Unit 3 contains a diverse group of lithologies of varying ages ranging from Mesozoic to pre-Messinian Miocene. It is broadly correlated with the Elekdağ, Kasaba

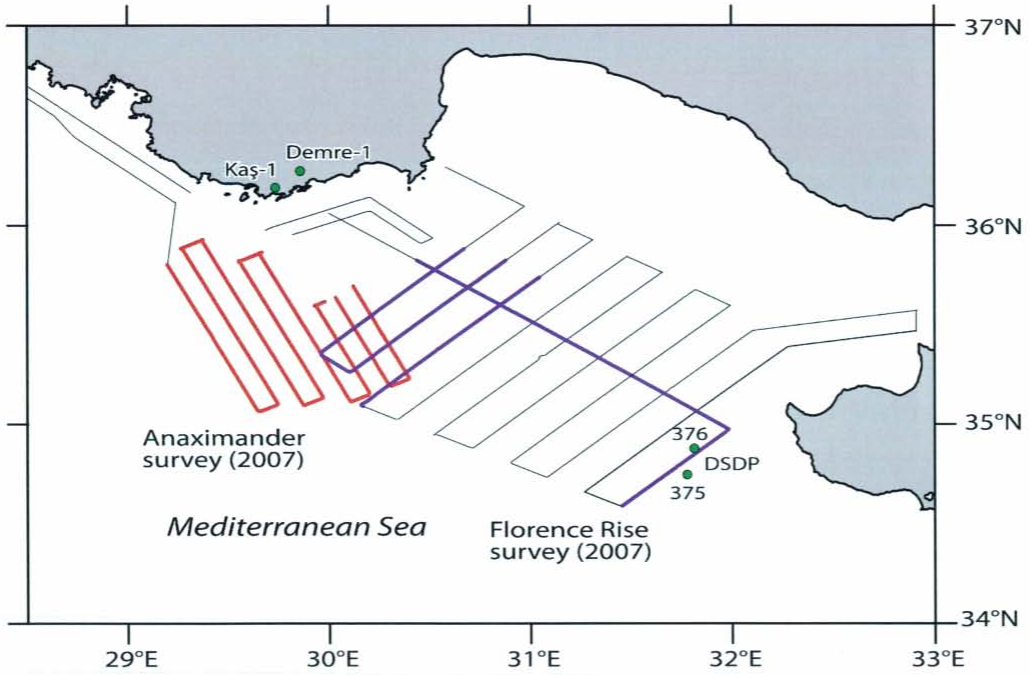

Figure 4.20 Map showing the long-distance correlation of DSDP boreholes over the Florence rise with the Anaximander Mountains. The location of the Kaş-1 and the Demre-1 are also shown.

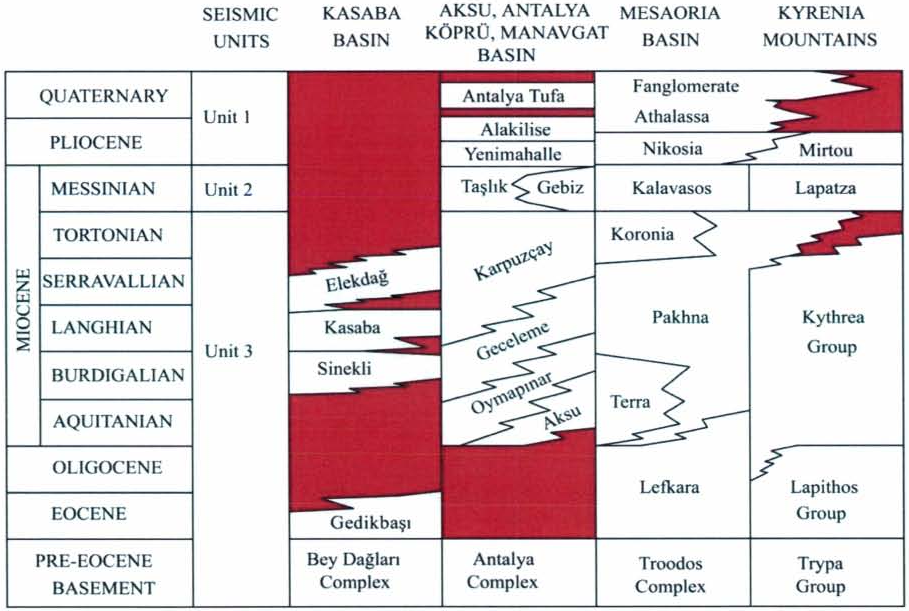

Figure 4.21 Chronostratigraphy of the Anaximander Mountains and the Finike Basin showing the correlations between seismic stratigraphic units 1–3 and the sedimentary successions of the on-land Kasaba Basin (Hayward, 1984; Şenel, 1997a,b; Şenel and Bölükbaşı, 1997); the marine Antalya Basin (Işler et al., 2005) the onland Aksu, Köprü and Manavgat Basins (Akay et al., 1985; Karabıyıkoğlu et al., 2000), and the onland Mesaoria Basin and the Kyrenia Mountains (Cleintaur et al., 1977; Robertson et al., 1995; Robertson et al., 1998).

and Sinekli formations of the onland Kasaba Basin. It is also correlated with the Aksu,Oymapınar, Geceleme and Karpuzçay formations of the Aksu, Köprü, Manavgat and Antalya Basins. It is further correlated with the Lefkara and Pakhna formations the Mesaoria Basin, including their Terra and Konoria Members as well as the Lapithos and Kythrea groups of the Kyrenia Mountains (Fig. 4.21). As the acoustic basement, Unit 3 could include the Beydağları and Antalya complexes of the western Tauride Mountain.

Chapter 5: Structural architecture

On the basis of seafloor morphology and the style and age of deformation the Late Miocene to Pliocene-Quaternary successions in the Anaximander Mountains (*sensu lato*) are divided into three morpho-tectonic domains: Domains 1-3 (Fig. 5.1). Each domain is developed during a specific time interval and comprises characteristic structural associations and stratigraphic architectures. Furthermore, each domain is confined to a specific geographic region within the study area. The multibeam map showing the seafloor morphology is shown in Figure 5.2, and the locations of seismic reflection profiles illustrated in this Chapter are shown in Figure 5.3.

5.1. Domain 1 – Anaximander Mountain (*sensu stricto*)

Domain 1 is situated in the western and northwestern portion of the study area, and includes the Anaximander Mountain and its northern slopes. It is bounded to the west by the deep Rhodes Basin, to the east and south by the Sırrı Erinç Plateau. In the north the domain extends toward the Piri Reis Mountain at the southern limits of the Turkish continental margin. Domain 1 developed during the post γ–reflector time interval in the mid-late Pliocene-Quaternary.

5.1.1 The southern margin of Domain 1: a pop-up structure

The multibeam bathymetry map shows that the southern edge of Domain 1 is marked by two distinct narrow escarpments (Fig. 5.2). These two escarpments define arcuate and convex-to-the-north lineaments that form a roughly E-W trending, V-shaped

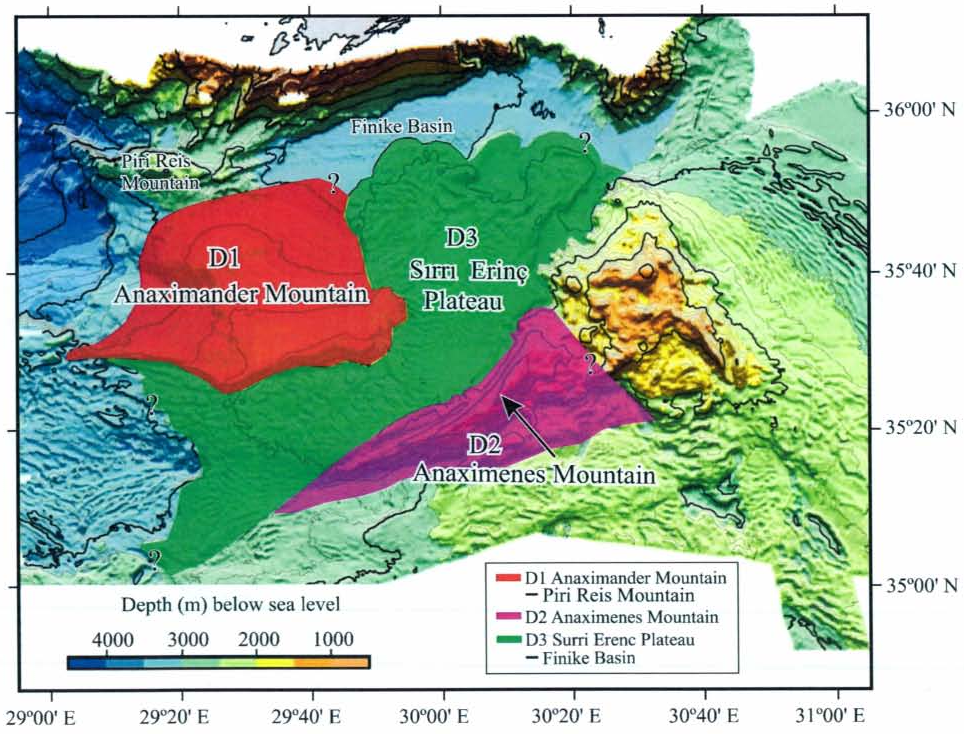

Figure 5.1 Map showing the regional distribution of morpho tectonic domains 1-3 in the study area.

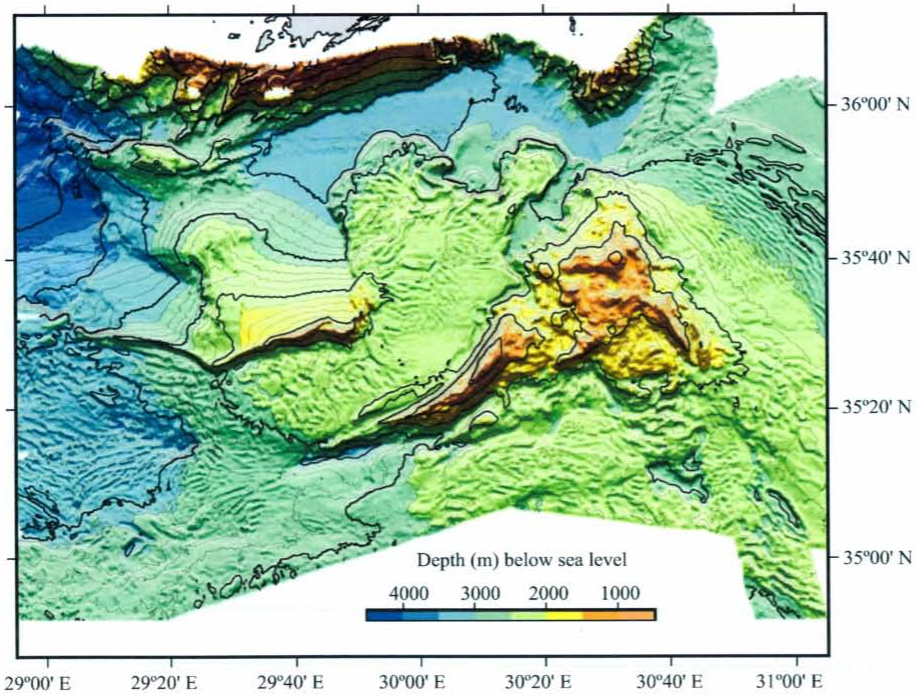

Figure5.2 Multibeam bathymetry map showing the seafloor morphology in the Anaximander Mountains and surrounding environs.

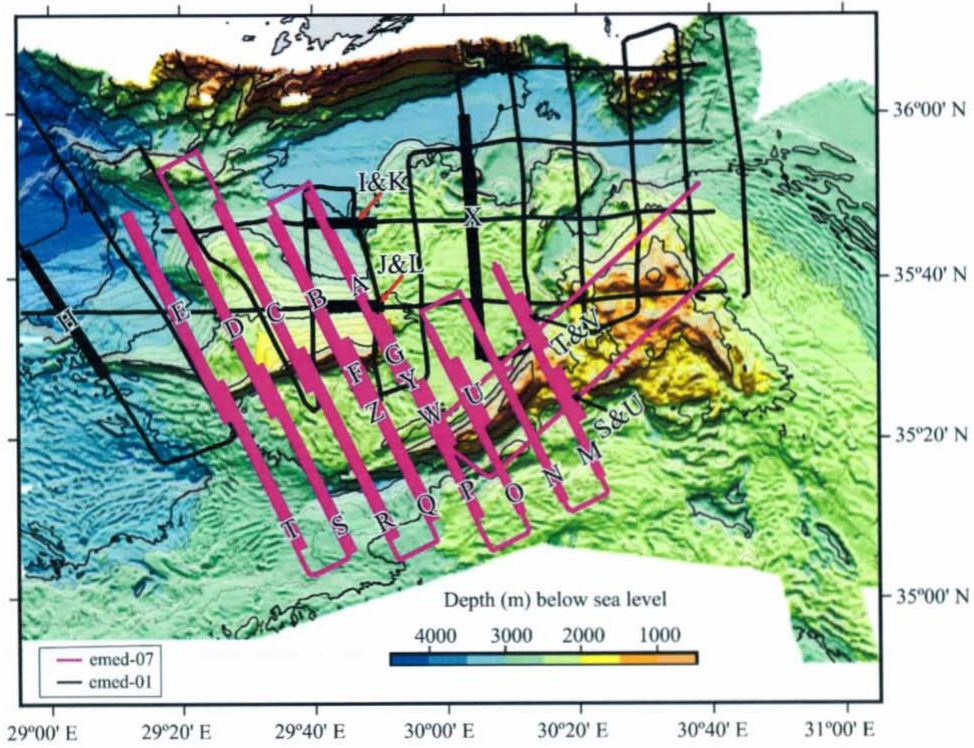

Figure 5.3 Map showing the location of seismic reflection profiles A-Z.

structure on the seafloor (Fig. 5.2). The escarpments dip very steeply to the south, with dip amounts ranging from 15°-20°, but the northern slopes of the Anaximander Mountain dip gently to the north ~2° to 10° (Fig. 5.2). Seismic reflection profiles across the southern margin of Domain 1 show that the two prominent escarpments are the seafloor expressions of the edge of a huge tilted block (Figs. 5.4 - 5.8). In the eastern portion of the Anaximander Mountain, the crest of the structure is ~8 km wide and displays one prominent peak at the southern edge of the structure (Fig. 5.4). Here the escarpment is ~3 km wide, dipping from ~2000 ms near the crest of the escarpment, reaching the floor of the Sırrı Erinç Plateau at ~2600 ms (Fig. 5.4). Seismic profile A (Fig. 5.4) shows that the escarpment has a rough surface morphology, with a minor peak on its southern slope. This secondary peak is associated with a small package consisting mainly of a thin veneer of Pliocene-Quaternary sediments, which show a sharp base and internally chaotic reflection configuration. This package is interpreted as a slide mass on the southern face of the Anaximander Mountain. Traced toward the west, the crest of the structure narrows from 8 km to 4 km, but two prominent peaks develop both rising ~300 ms (~225 m @ 1500 m/s) in elevation to ~1700 ms (Fig. 5.5). Further west, the crest dramatically narrows to 2 km and now only a single peak is visible (Fig. 5.6). Here the structure remains at approximately 1700-1800 ms (Fig. 5.6). The escarpment is steepest in this region with dips >20°. The crest of the structure continues to narrow moving west into the eastern Rhodes Basin reaching a minimum width of 1-2 km, but plunges from ~1700 ms to 2800 ms within a distance of ~20 km (Figs. 5.7, 5.8).

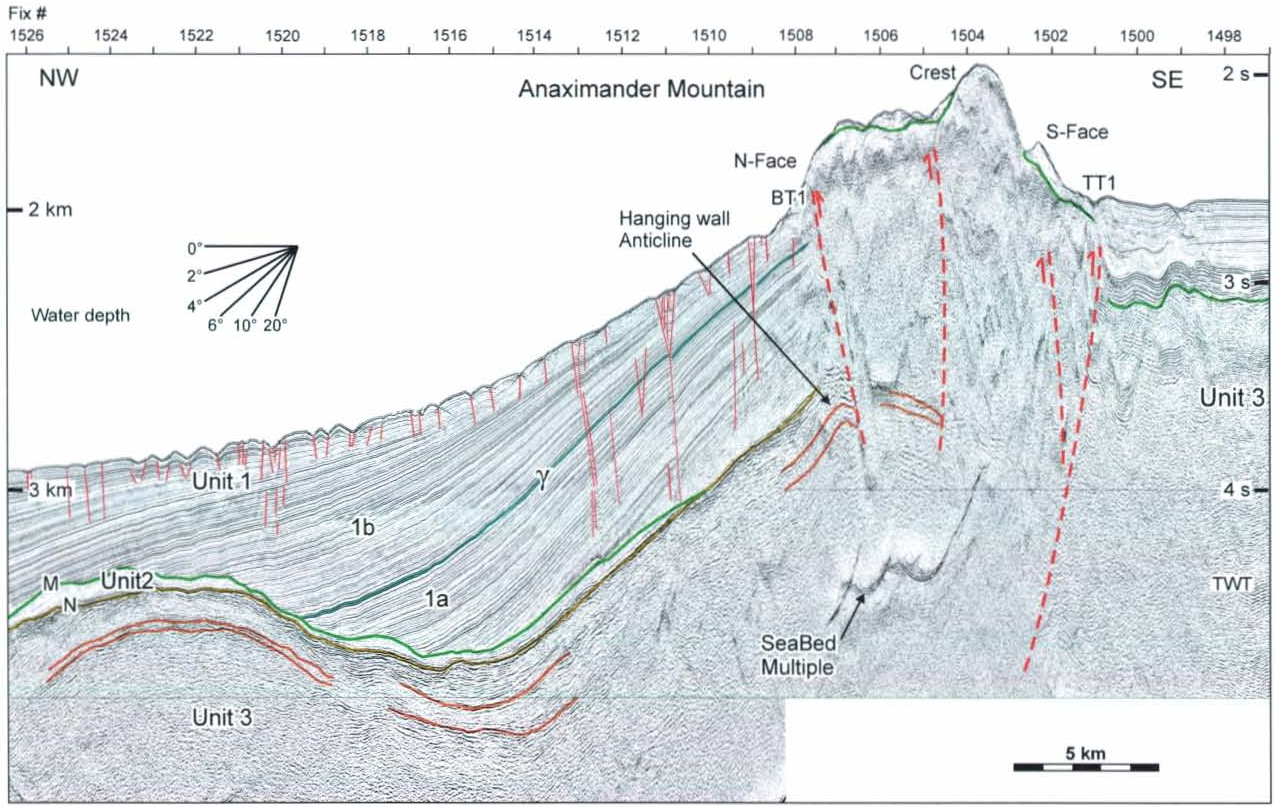

Figure 5.4 Seismic reflection profile A showing Domain 1 and the internal architecture of the large north dipping block created in the Pliocene-Quaternary successions that defines the core of the Anaximander Mountain. Location shown in Figure 5.3

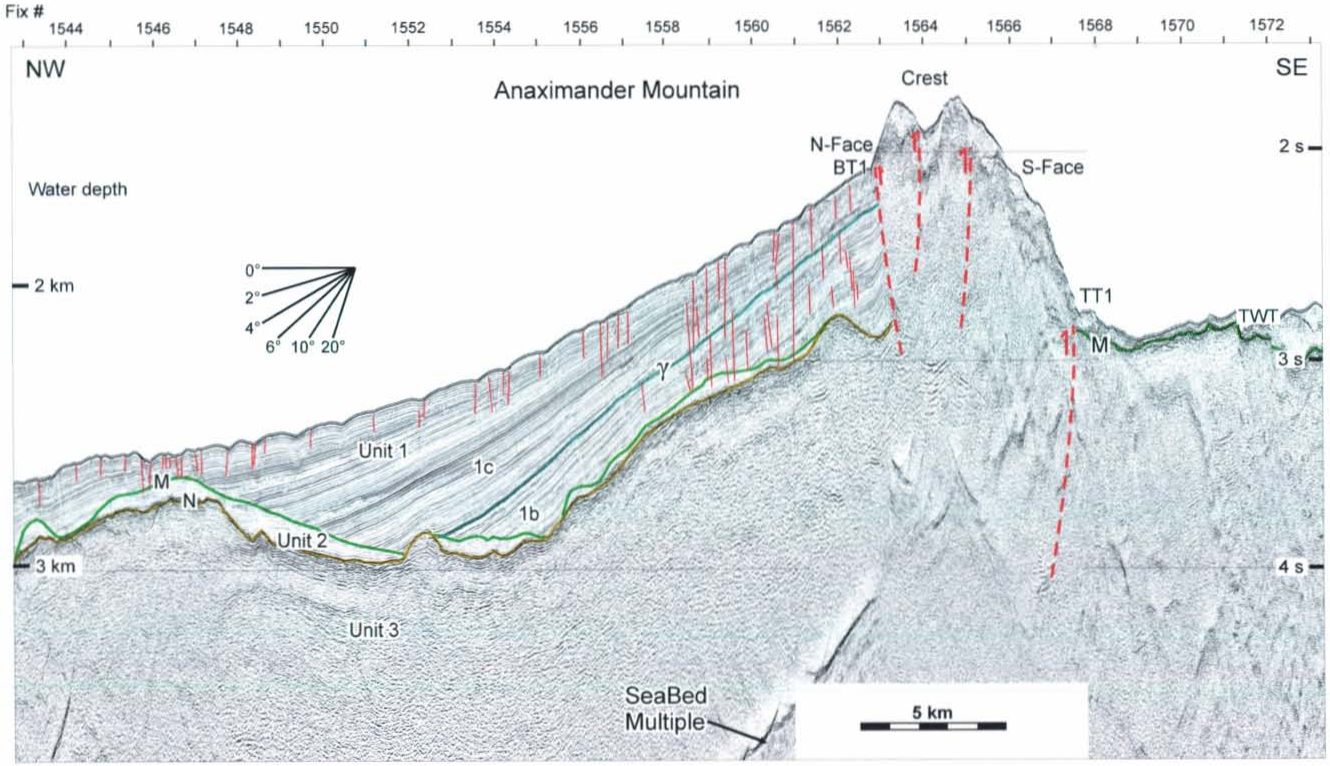

Figure 5.5 Seismic reflection profile B showing the growth strata on the backlimb of the Anaximander Mountain and thrust TT1 and back thrust BT1. Location shown in figure 5.3.

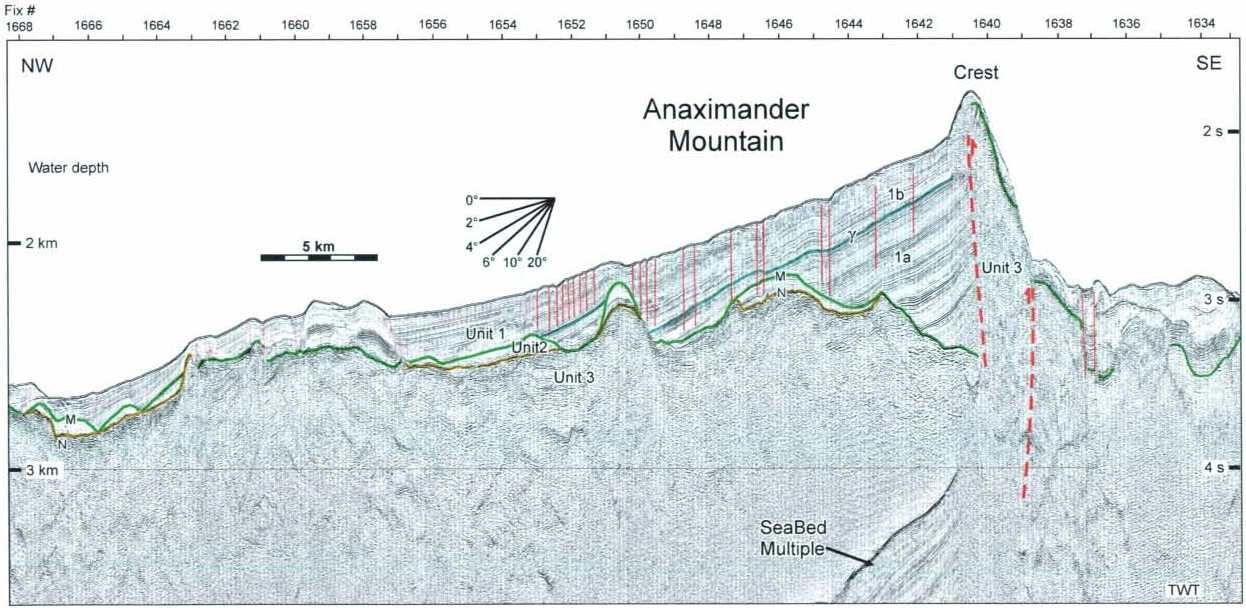

Figure5.6 Seismic reflection profile C showing thrusts TT1 and back thrust BT1 in the Anaximander Mountain. Location shown in figure 5.3

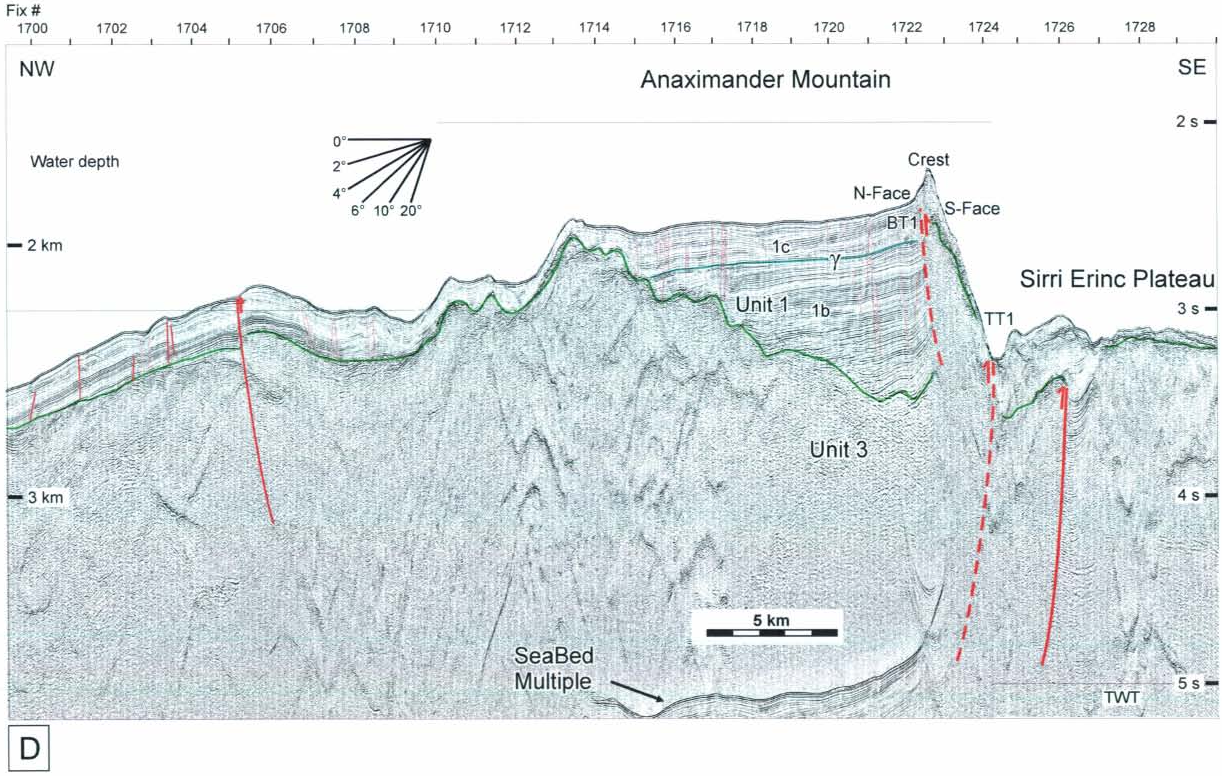

Figure 5.7 Seismic reflection profile D showing thrusts TT1 and back thrust BT1 in the Anaximander Mountain. Location shown in figure 5.3

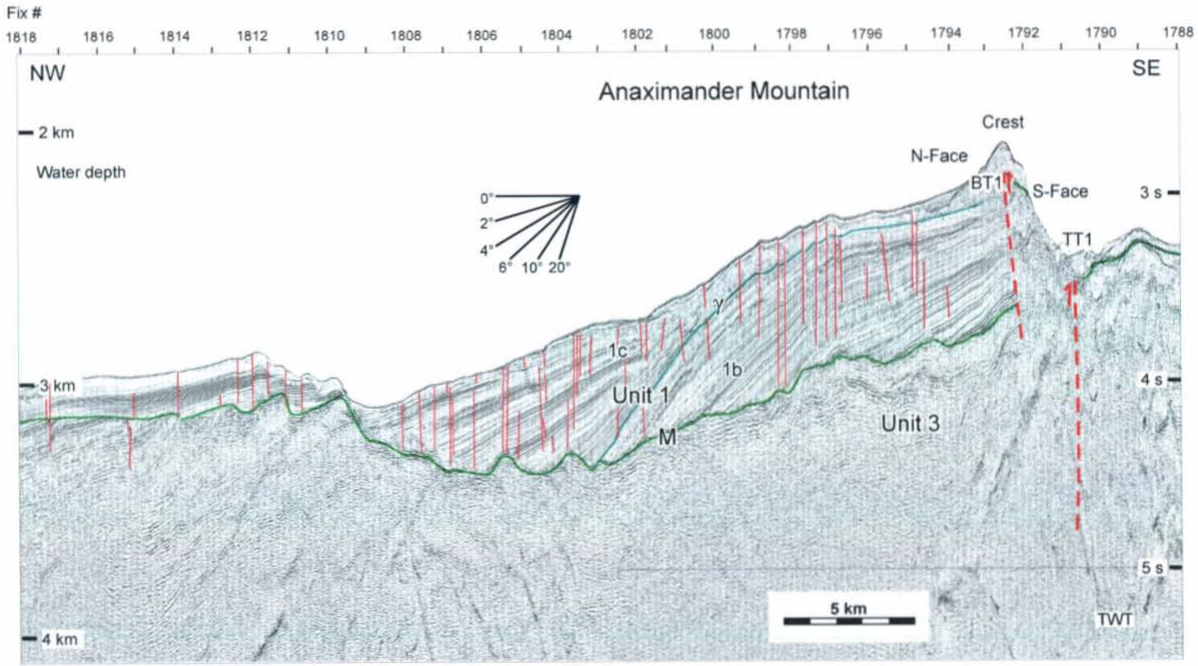

E

Figure 5.8 Seismic reflection profile E showing the growth in Subunit 1a and 1b and thrusts TT1 and BT2

Along the southern margin of the Anaximander Mountain, at the transition to Domain 3 (i.e., Sırrı Erinç Plateau), the M-reflector displays a very sharp vertical drop of ~1200-1500 ms over a less than 5 km-wide slope (Figs. 5.4-5.8). Comparison between the multibeam bathymetry and seismic reflection profiles indicates that this sharp vertical drop coincides with the prominent escarpment at the southernmost limit of the Anaximander Mountain (*sensu stricto*). This structure is interpreted as a north-dipping, south-verging major thrust (i.e., TT1), above which lies a hanging wall anticline visible in Unit 3 (Fig. 5.4). In seismic reflection profiles, the crest of the Anaximander Mountain is defined as a 1-5 km wide, broadly E-W trending zone, which is characterised by chaotic reflections, delineating a prominent narrow rim at the southern margin of the structure (Figs. 5.4-5.8).

The dense grid of high-resolution seismic reflection profiles with frequent cross overs (see Chapter 2), allows detailed mapping of large structures in the study area (Fig. 5.11). Careful mapping of the frontal portion of the Anaximander Mountain shows that TT1 very accurately traces the seafloor morphology of the Anaximander Mountain, with the projection of the TT1 fault trace at the seafloor coinciding with the base of the prominent southern escarpment.

There is also a minor escarpment developed on the northern face of the crest of the Anaximander Mountain, with similar steep dips ranging from 10°- >20° (Figs. 5.4-5.8). However, the height of this escarpment is considerably less than the southern escarpment. North of this second escarpment, the seafloor gently dips (2°-10°)

northward where the seafloor corresponds to the uppermost strata of the Pliocene-Quaternary succession (discussed below).

In the eastern portion of Domain 1, from north to south, the M-reflector gently rises from ~4000-4500 ms (~4000-4500 m @ 2000 m/s) in the western Finike Basin to ~3000 ms (~3000 m) at the northern face of the crest of the Anaximander Mountain (Figs. 5.4-5.5). Here, the M-reflector is sharply truncated by a fault (BT1) and is displaced ~1000 ms (Figs. 5.4-5.8). The geometric relationship between the footwall and hanging wall cutoffs show clear contractional overlap (Figs. 5.4-5.5), which is best illustrated in the 1:1 scaled profiles, which further document that this fault is a south-dipping, north-verging thrust (BT1), where the footwall of the structure is tilted and uplifted ~700-900 ms above the hanging wall (e.g., Figs. 5.9, 5.10). Regional geometric structural associations suggest that BT1 defines a major back thrust to thrust TT1 (further described and discussed later in this Chapter). The back thrust BT1 can also be accurately mapped and follows a parallel trajectory to major thrust TT1 (Figs. 5.4-5.8, 5.11).

Therefore, the frontal segment of the Anaximander Mountain can be interpreted as composed of two oppositely-verging thrusts, defining a pop-up structure (Figs. 5.4-5.8, 5.11). Seismic reflection profiles show that the core of this structure is composed of a sliver of Unit 3 (Figs. 5.4-5.8). The major thrust TT1 and its back-thrust BT1 are correlated toward the west into the Rhodes Basin (Fig. 5.11). Here these two thrusts also create a noticeable north-northwest tilt of the Pliocene-Quaternary

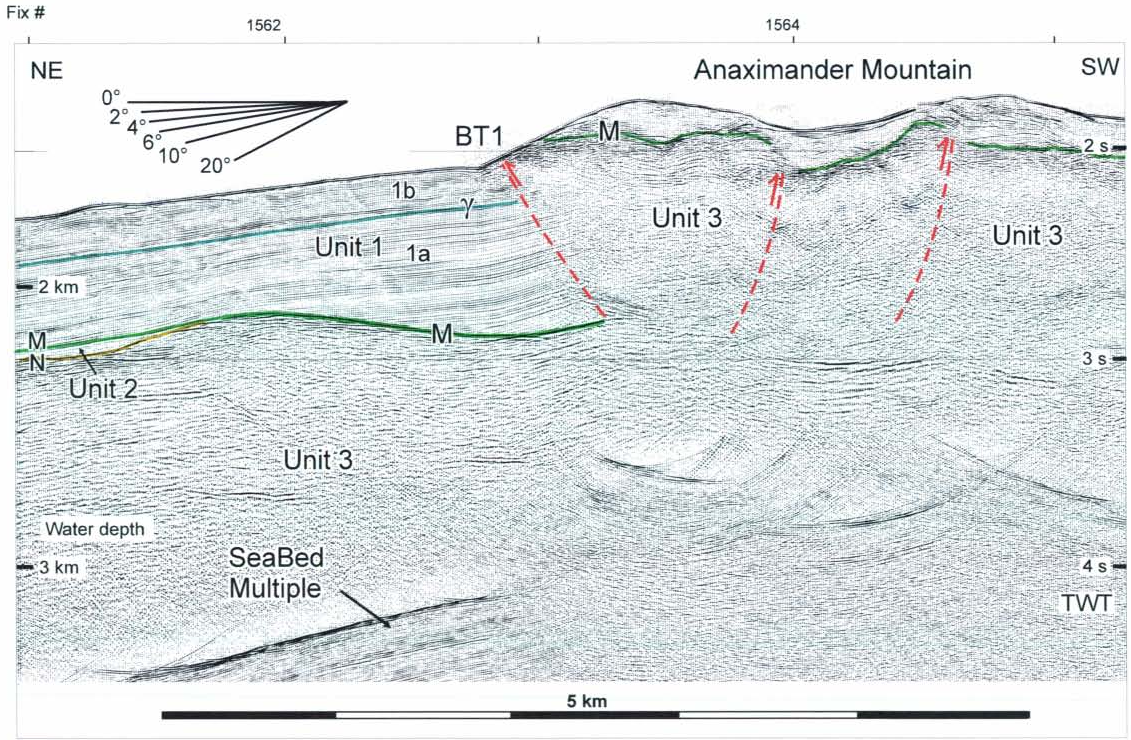

F

Figure 5.9 Seismic profile F at 1:1 scale showing the back thrust BT1 in the Anaximander Mountain. Location is shown in figure 5.3

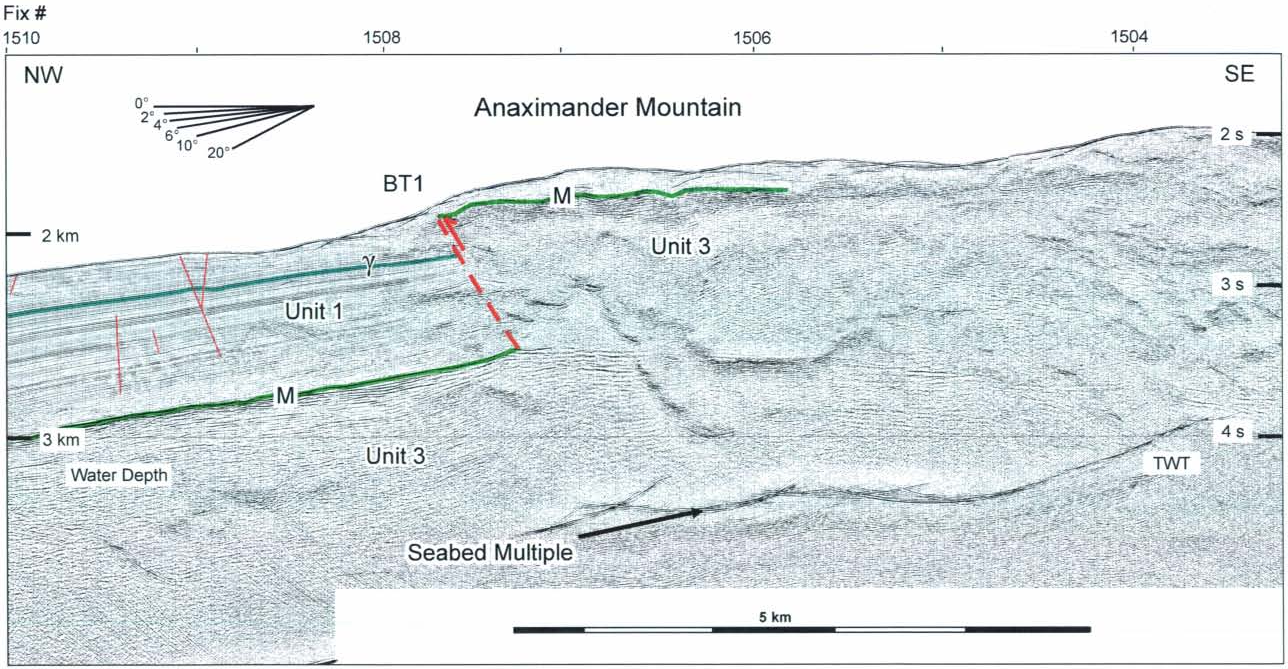

Figure 5.10 Seismic profile G at 1:1 scale showing the back thrust BT1 in the Anaximander Mountain. Location is shown in Figure 5.3

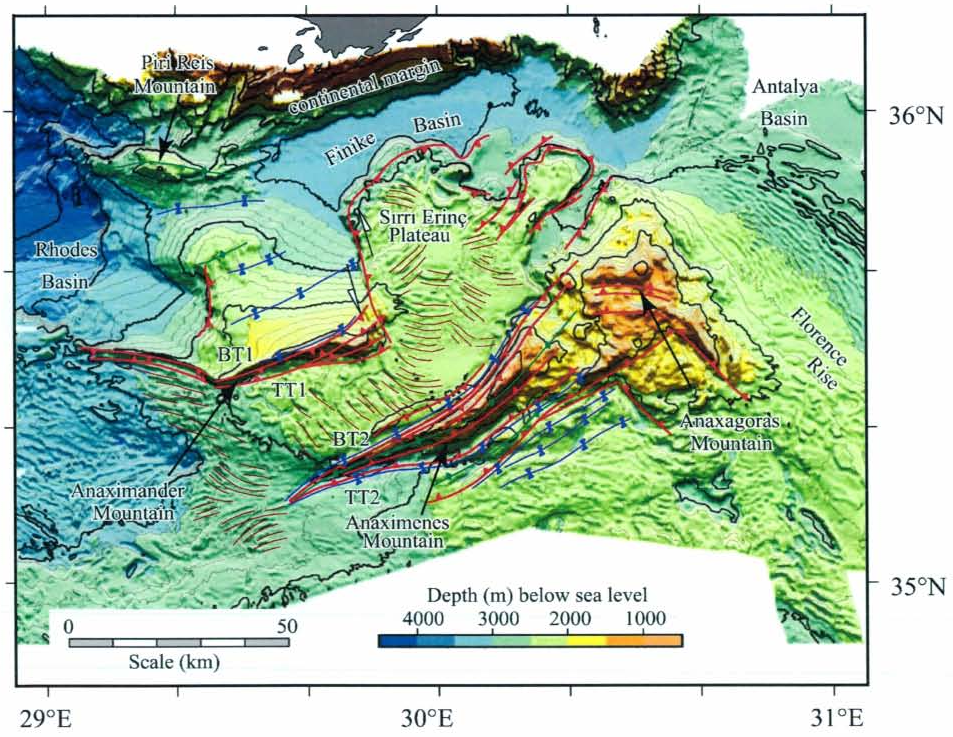

Figure 5.11 Structure Map of the Pliocene-Quaternary structures in the study area.

succession along the backlimb of the structure (Fig. 5.12). However, the west-directed plunge and attenuation of the crestal segment of the structure is a distinct difference between the eastern and western segments of the frontal portion of Domain 1.

5.1.2 The eastern margin of Domain 1: a strike-slip boundary

East-west trending seismic reflection profiles show that the north-dipping wedge north of the Anaximander Mountain, related to thrust TT1 and its back thrust BT1 abruptly terminate along a distinct boundary at ~29°50'E longitude (Figs. 5.13, 5.14). This boundary is clearly visible in the multibeam bathymetry map (Fig. 5.2). The M-reflector is a pronounced angular unconformity over the northern slopes of the Anaximander Mountain (e.g., Fig. 5.13). Here the unconformity lies at ~3400 ms, but gradually falls from 3400 ms to ~5000 ms toward the east. At the transition between the Anaximander Mountain and the Sırrı Erinç Plateau, the M-reflector is sharply truncated by a major north-south trending discontinuity and rises nearly vertically by >1100 ms (Figs. 5.13, 5.14; Aksu et al., 2009). These two E-W trending seismic reflection profiles show that an ~900-1200 ms-thick Pliocene-Quaternary succession sharply abuts reflections in Unit 3, along this nearly vertical face (Figs. 5.13, 5.14). In the Sırrı Erinç Plateau, Unit 3 displays footwall and hanging wall cutoffs which indicate the presence of an east-dipping, west-verging thrust, where the footwall of the structure is uplifted ~900-1100 ms above the hanging wall. The foot wall – hanging wall relationships are best imaged in the 1:1 scaled profiles (e.g., Figs. 5.15, 5.16). Aksu et al. (2009) pointed out the stratigraphic similarities between the Pliocene-Quaternary successions in the Finike

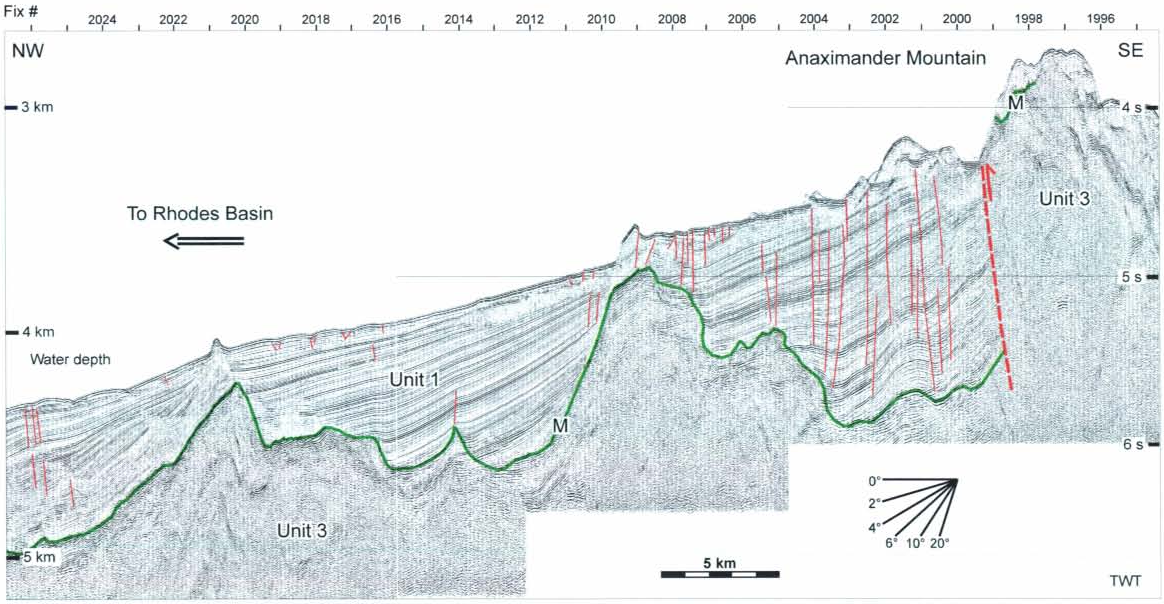

H

Figure 5.12 Seismic reflection profile F showing the architecture of the Pliocene- Quaternary succession on the backlimb of the Anixamander Mountain (*sensu stricto*) and the transition to the Rhodes Basin. Location is shown in Figure 5.3.

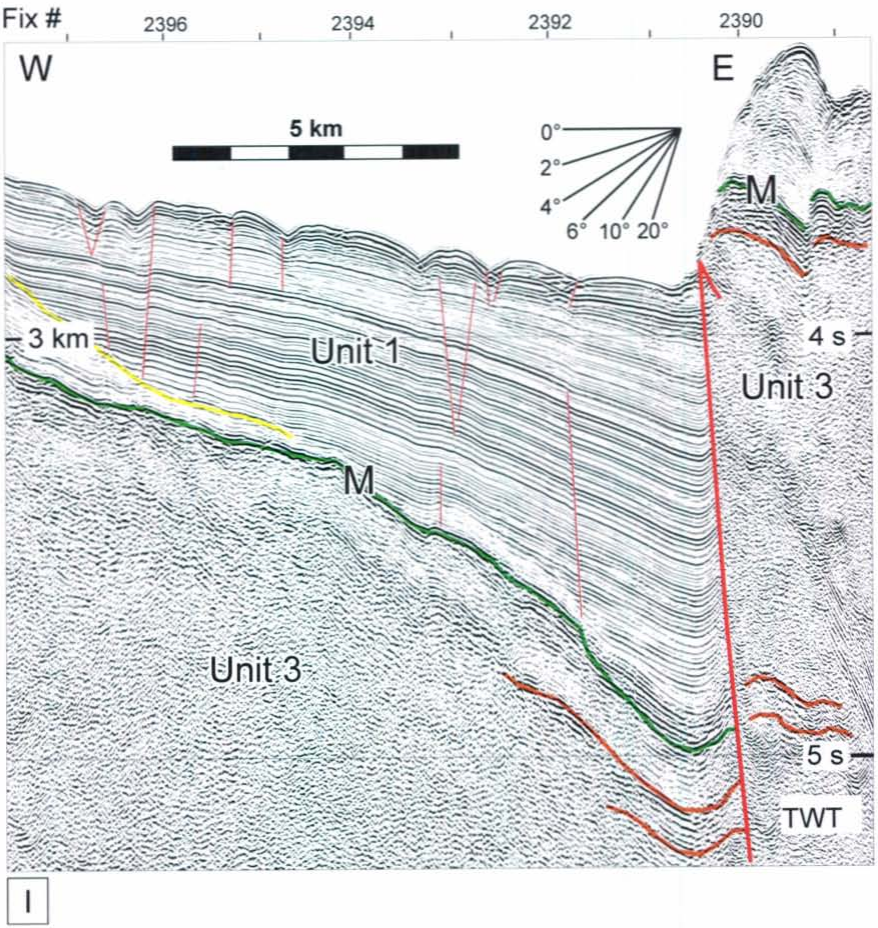

Figure 5.13 East-West trending seismic reflection profile I showing the architecture of the Pliocene-Quaternary succession on the backlimb of the Anaximander Mountain (*sensu stricto*) and the transition to the Sırrı Erinç Plateau. Location shown in figure 5.3.

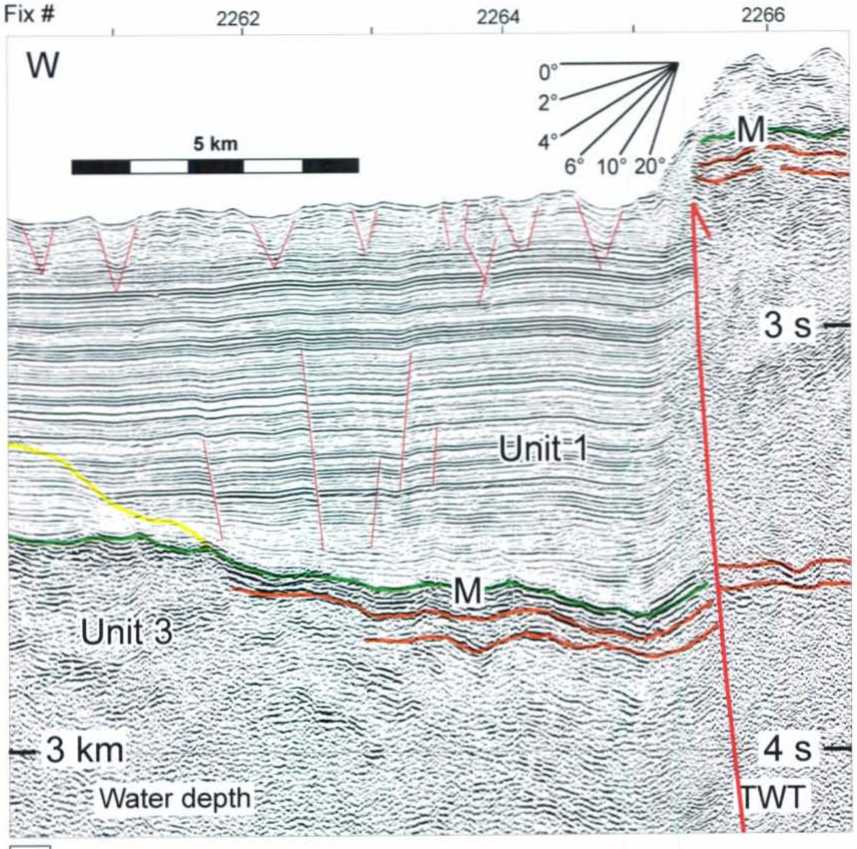

Figure 5.14 East-West trending seismic reflection profile J showing the architecture of the Pliocene-Quaternary succession on the backlimb of the Anaximander Mountain (*sensu stricto*) and the transition to the Sırrı Erinç Plateau. Location is shown in figure 5.3

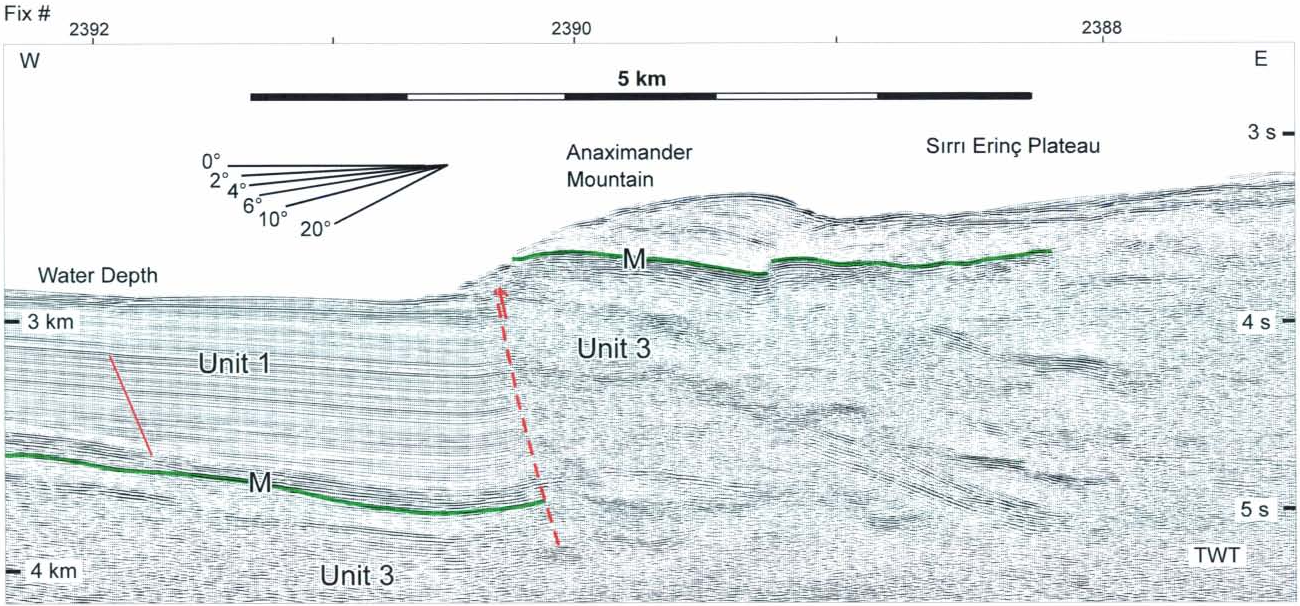

Figure 5.15 Seismic reflection profile K at 1:1 scale of seismic reflection profile G (Figure 5.13) showing the architecture of the Pliocene-Quaternary succession on the backlimb of the Anixamander Mountain and the transition to the Sırrı Erinç Plateau. Location is shown in Figure 5.3.

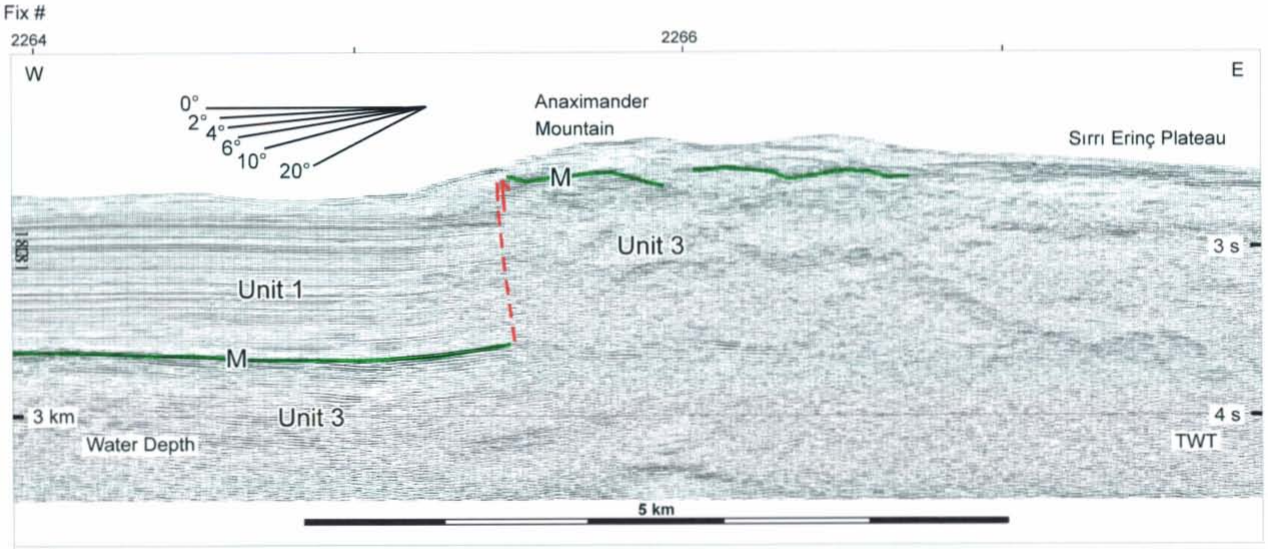

Figure 5.16 Seismic reflection profile L of seismic reflection profile H (Fig 5.14) showing the architecture of the Pliocene-Quaternary succession on the backlimb of the Anixamander Mountain (*sensu stricto*) and the transition to the Sırrı Erinç Plateau. Location shown in figure 5.3

Basin and the thick deposits nestled on the backlimb of the Anaximander Mountain: they referred to this as the Southern Anaximander Basin. They suggested that the large W-verging thrust at the boundary between Domains 1 and 3 must have a significant strike slip component, causing the abrupt eastward termination of the thrust TT1 and its back thrust BT1 at the boundary, and the displacement of the Finike Basin from the Southern Anaximander Basin. The new seismic profiles collected in 2007 support the interpretation that the north-south trending discontinuity is a major W-verging thrust (Figs. 5.15, 5.16). Additional east-west trending seismic profiles are needed to further constrain the strike-slip component of this boundary. Alternatively, this boundary could be a transfer zone separating the loci of deformation on the eastern and western sides.

5.1.3. Planar high-angle faults

In northern and eastern portions of the Anaximander Mountain (*sensu stricto*) there is a distinct set of planar, high-angle faults that show relatively small normal-sense dip separations, rarely exceeding 10 ms (Figs. 5.4-5.8). These faults largely affect the Pliocene-Quaternary succession. Many of these faults have tips lying close to the present-day seafloor, producing distinct small-scale corrugations. These faults invariably lack evidence for growth, and are therefore deemed younger than the middle to upper portion of the Pliocene-Quaternary succession. Aksu et al. (2009) also identified these high-angle planar faults, and determined that they show distinct northeast-southwest oriented corrugations on the seafloor.

5.1.4. Growth stratal architectures

The isopach map of the Pliocene-Quaternary succession in Domain 1 thickens both toward the east and south, creating a north-south trending depocentre (i.e., the eastern Anaximander Basin of Aksu et al., 2009) and an east-west trending narrow depocentre (i.e., the southern Anaximander Basin of Aksu et al., 2009) at the eastern and southern margins of the Anaximander Mountain, respectively (Fig. 5.17). Traced from west to east across the northern slope of the Anaximander Mountain, the Pliocene-Quaternary reflectors in subunit 1a show little to no sedimentary growth (Figs. 5.4-5.8). From west to east the reflectors in subunit 1a terminate at the large west-verging thrust, but progressively onlap westward (Figs. 5.4-5.8). From north to south, individual reflector packages in subunits 1a shows little to no sedimentary growth, indicating that subunit 1a represents pre-tectonic sedimentary deposition.

Above the γ-reflector, the Pliocene-Quaternary subunit 1b dramatically thins toward the south, and delineates several north-thickening growth stratal wedges over the backlimb of major thrust TT1 (Figs. 5.4-5.8). The axis of individual growth wedges progressively migrates northward in successively younger wedges, indicating a shift in the focal point of the Pliocene-Quaternary deposition. This stratigraphic architecture is the result of sedimentation associated with the development of the major structure that defines the core of Domain 1 (i.e., the Anaximander Mountain). Each growth strata wedge displays well-defined south-directed onlap, convergence of reflectors and minor erosion (Figs. 5.4-5.8; Chapter 4). Several minor unconformities are developed, which

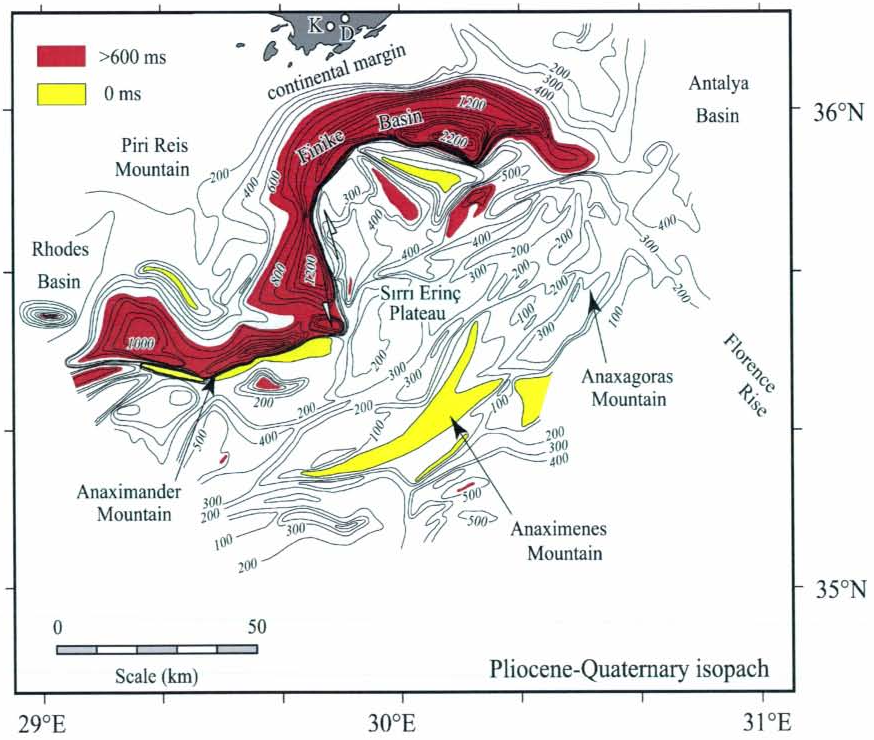

Figure 5.17 Isopach map of Unit 1, showing the variations of the Pliocene-Quaternary sediments in the study area.

are traced northward into the piggyback basin on the backlimb of the Anaximander Mountain. In the northeast area of Domain 1, immediately west of the Finike Basin, the reflectors defining these minor unconformities become conformable horizons within subunit 1b. The thickness of section lost to onlap and erosion ranges from 400-900 ms. This stratigraphic architecture is characteristic of progressive syntectonic unconformities developed in active foreland basins (Riba 1976).

In the northeastern portion of Domain 1, reflectors in subunit 1a as well as many growth strata wedges within subunit 1b show an apparent downlap relationship with the underlying M-reflector over a distance of 15-20 km (Figs. 5.4, 5.5, 5.6). Along the paleotopographic highs created at the level of the M-reflector, and within growth strata wedges developed in the mid-to-upper subunit 1b, the north-directed segments of downlapping reflections progressively curve upward to assume an onlap configuration (e.g., Figs. 5.5, 5.6). Further to the west, the growth strata packages in subunits 1a and 1b are nearly horizontal, and reflectors show a clear apparent onlap configuration over the M-reflector (Fig. 5.6). In the western profile running through the apex of the open V-shaped structure on multibeam data, the Pliocene-Quaternary Unit 1 displays a very strong apparent downlap relationship over the M-reflector, with minor apparent onlap on the southern flanks of paleotopographic highs (Fig. 5.8).

The occurrence of little to no growth in subunit 1a, and the development of prominent north-directed growth stratal wedges on the northern flank of the Anaximander Mountain collectively suggest that the apparent major downlap in the area cannot be an

original downlap deposition. The lack of any significant growth in subunit 1a indicates that the subunit was deposited nearly horizontal over the corrugated paleotopography of the M-reflector. Thus, the observed apparent downlap observed in the pre-γ sediments originally occurred as onlap deposition. The remarkable growth observed in the post-γ sediments and the progressive shift of the axis of younger wedges collectively suggests that the northern portion of Domain 1 experienced a major period of uplift and rotation during post-γ time. The presence of the major south-verging thrust TT1 at the southern limit of Domain 1 and its similarly-verging splays suggest that this structure is responsible for the observed uplift and rotation. The north-verging back thrust BT1 creates the narrow rim at the southern fringes of the domain.

5.2 Domain 2 – Anaximenes Mountain

Domain 2 is located southeast of the Domains 1 and 3, and comprises the Anaximenes Mountain. It is bounded to the northwest by the Sırrı Erinç Plateau and to the southeast by the Mediterranean Ridge, a broadly southwest-northeast trending prominent morphological feature associated with the convergence between the African and Eurasian Plates. In terms of seafloor morphology, the domain appears to be linked with the Anaxagoras Mountain to the northeast, but it is notably different in terms of stratigraphic and structural architecture.

The Anaximenes Mountain is a broadly northeast-southwest trending arcuate, concave to the northwest structure on the seafloor (Fig. 5.2). Toward the southwest the structure narrows dramatically to a point, whereas toward the northeast it widens to 15-20

km, and gradually merges with the similarly trending western segment of the Anaxagoras Mountain, defining a much broader lineament on the seafloor that extends northeast toward the Antalya Basin (Fig. 5.2). The eastern portion of the Anaxagoras Mountain has a northwest-southeast trend, and collectively these two mountains form a very prominent northward facing arrow head like structure on the seafloor.

The multibeam bathymetry map shows that the southeastern flank of the Anaximenes Mountain is marked by a prominent, but segmented escarpment (Fig. 5.2). In the easternmost portion of Domain 2, the escarpment is wider and displays complicated seafloor morphology. But, further to the southwest, the escarpment narrows and defines a prominent steep (15°-20°) scarp on the seafloor (Fig. 5.2). The escarpment defines a roughly arcuate and concave-to-the-northwest lineament: the southwestern portion of this lineament progressively swings to assume a more east-west trending orientation (Fig. 5.2). Multibeam bathymetry shows that the northern flank of the Anaximenens Mountain is also marked by a very prominent, arcuate and concave to the north escarpment, defining a smoother lineament on the seafloor. This escarpment dips very steeply to the northwest, with dip amounts ranging from 20° to 25°.

There are eight northwest-southeast oriented multi-channel seismic reflection profiles across the Anaximenes Mountain, which image the internal architecture of the mountain and its surrounding environs (Figs. 5.18-5.25). Seismic reflection profiles across Domain 2 show that these two escarpments are the seafloor expressions of a huge block elevated above the adjacent seafloor, where the escarpments represent the

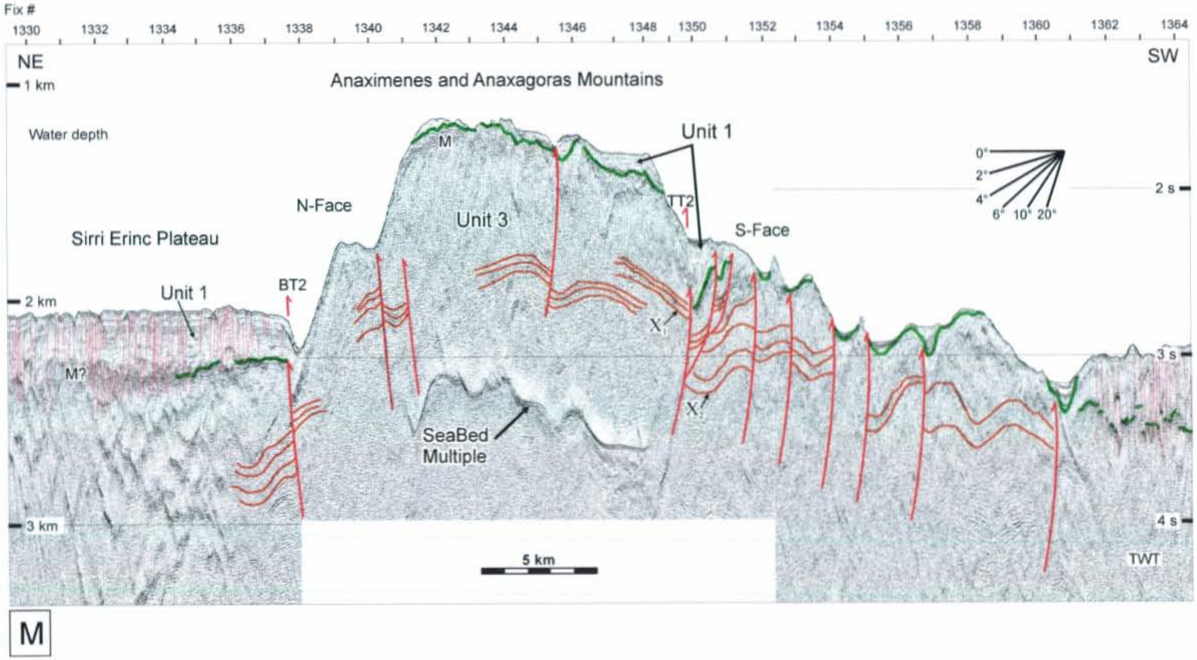

Figure 5.18 Seismic reflection profile M showing thrusts Tt2 and Bt2 in the Anaximenes Mountain. Location shown in figure 5.3

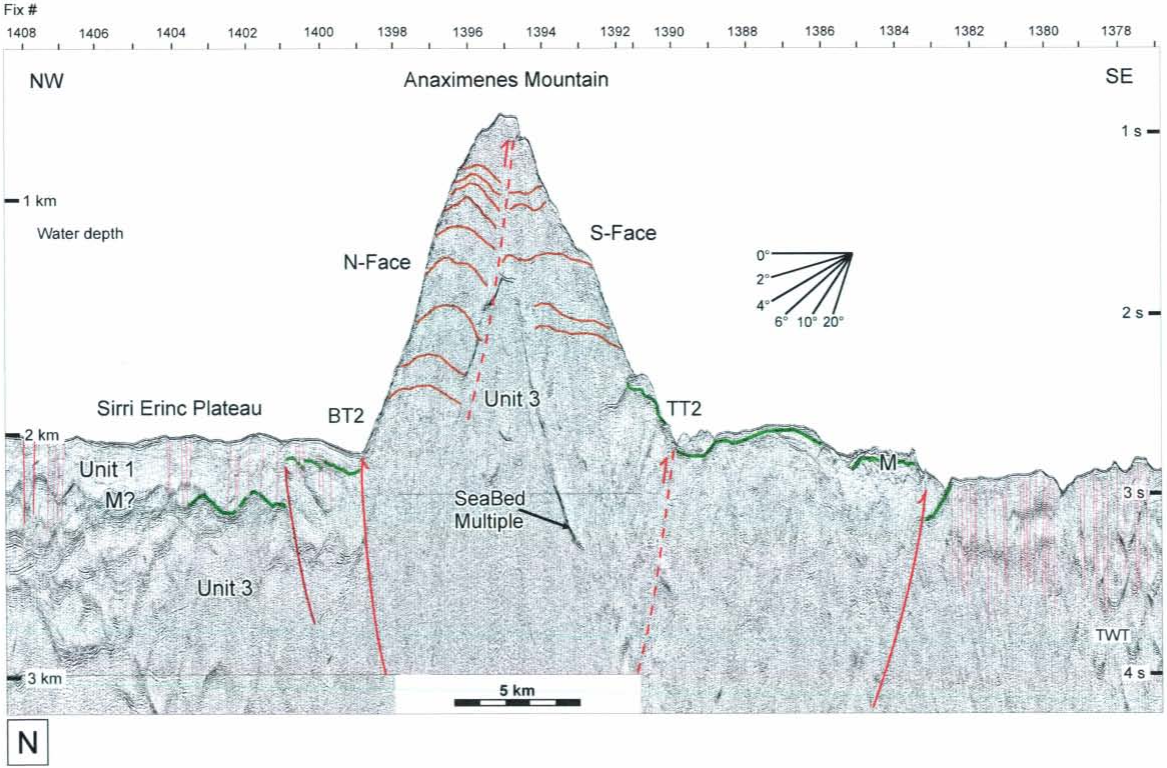

Figure 5.19Seismic reflection profile N showing thrusts TT2 and BT2 in the Anaximenes Mountian in the transition to the Sırrı Erinç Plateau. Location shown in figure 5.3.

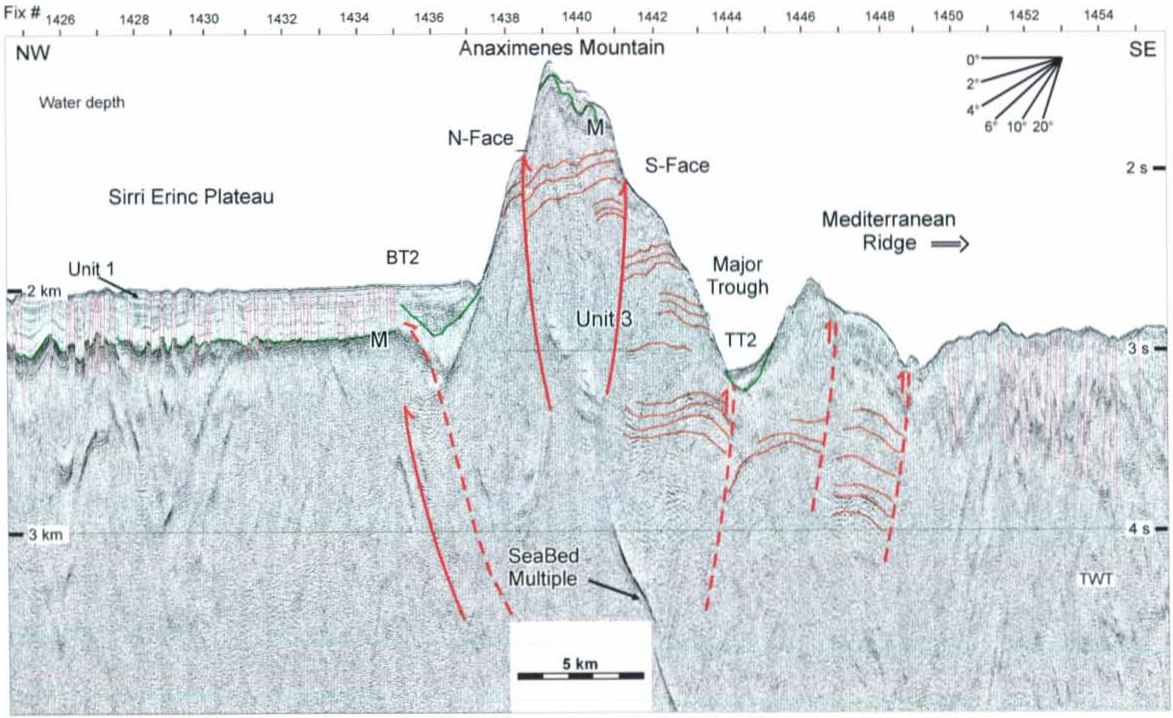

Figure 5.20 Seismic reflection profile O showing thrusts TT2 and BT2 in the Anaximenes mountain and the transition to the Sırrı Erinç Plateau. Location shown in figure 5.3.

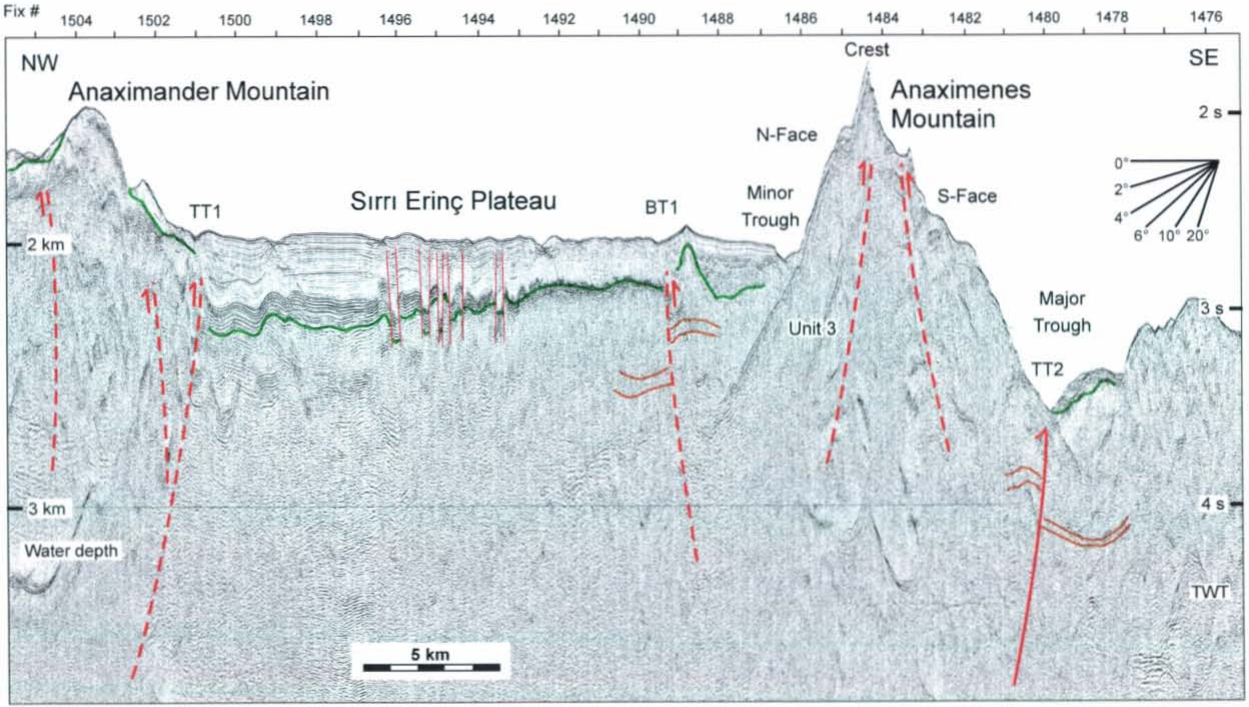

Figure 5.21 Seismic reflection profile P showing thrusts TT2 and BT2 and the internal architecture of the Anaximenes Mountain. Location shown in figure 5.3Figure 5.20 Seismic reflection profile O showing thrusts TT2 and BT2 in the Anaximenes mountain and the transition to the Sırrı Erinç Plateau. Location shown in figure 5.3.

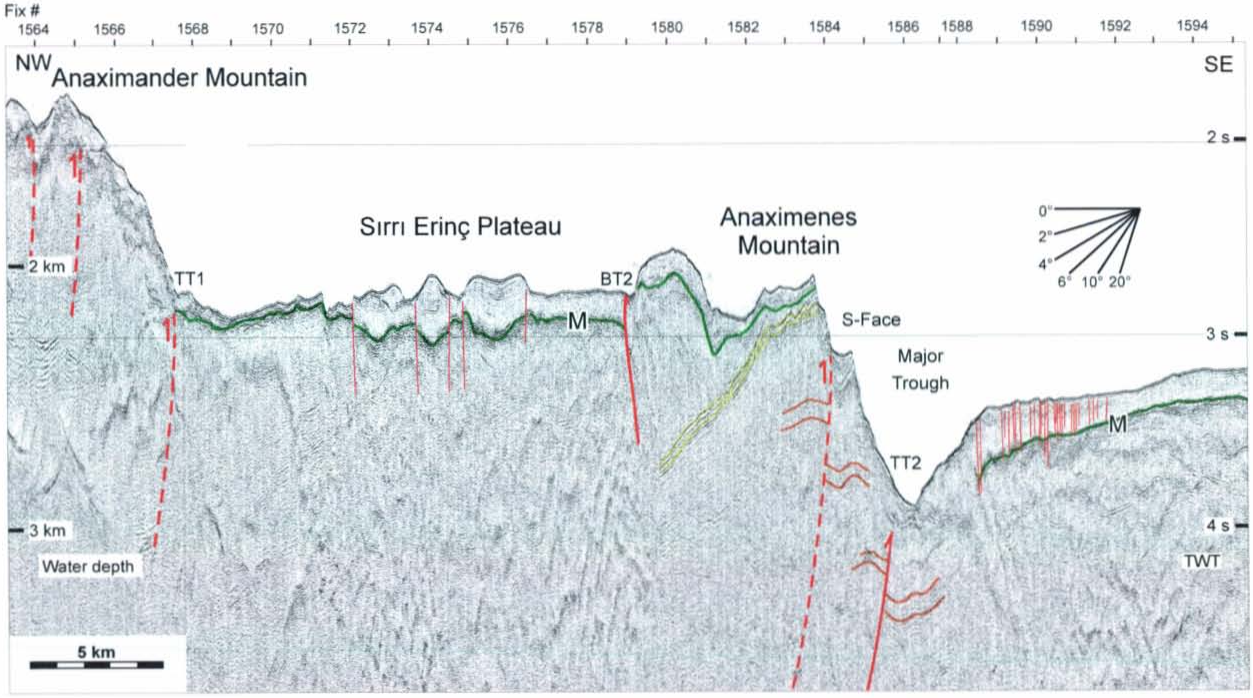

Q

Figure 5.22 Seismic reflection profile Q showing thrusts TT1 in the Anaximander Mountain and thrusts TT2 and BT2 in the Anaximenes mountain. Notice the Anaximenes mountain has plunged significantly. Location shown in figure 5.3.

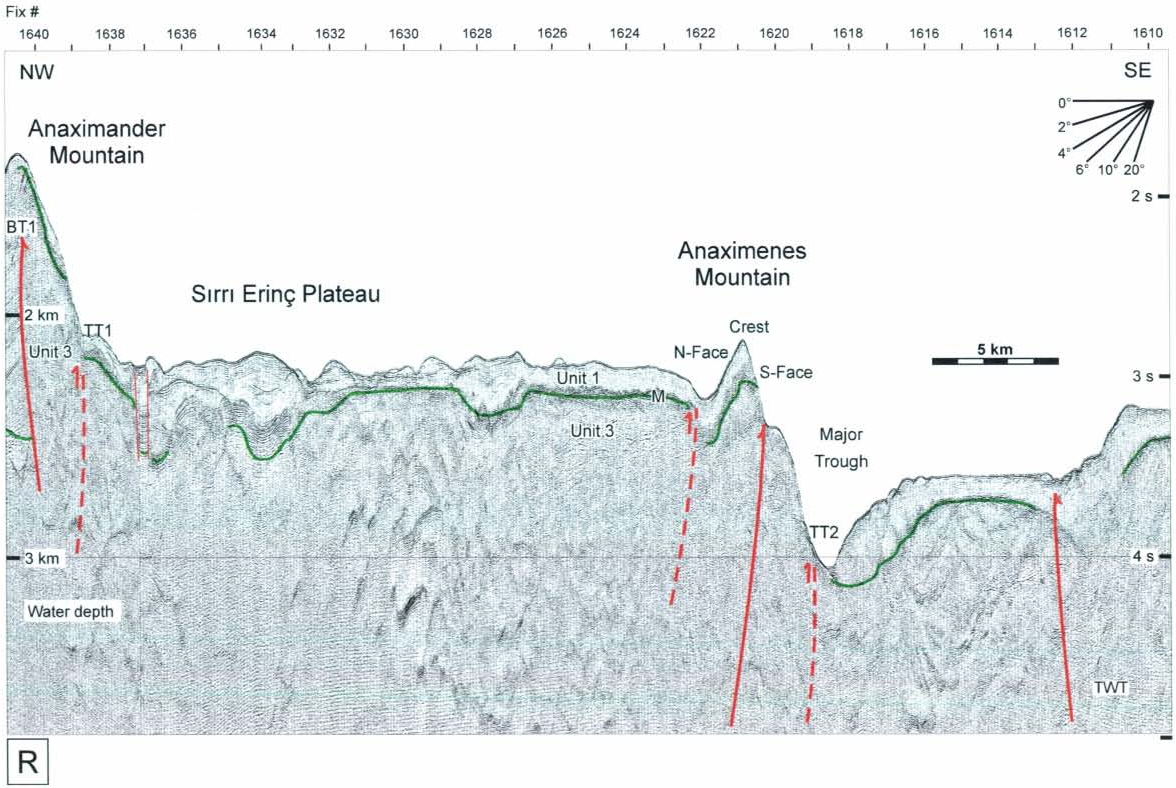

Figure 5.23 Seismic reflection profile R showing thrusts TT1 and BT1 in the Anaximander Mountain and thrust TT2 in the Anaximenes mountain. Location shown in figure 5.3.

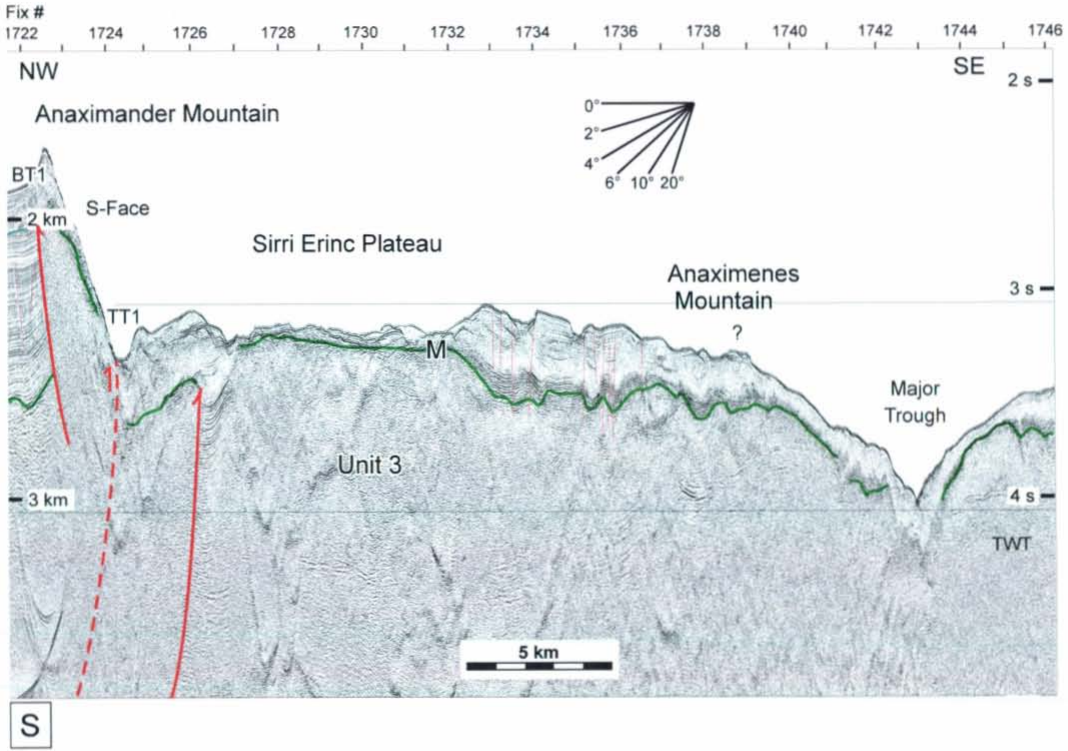

Figure 5.24 Seismic reflection profile S showing thrusts TT1 and BT1 in the Anaximander Mountain. Notice that the Anaximenes Mountain is no longer distinguishable. Location shown in figure 5.3.

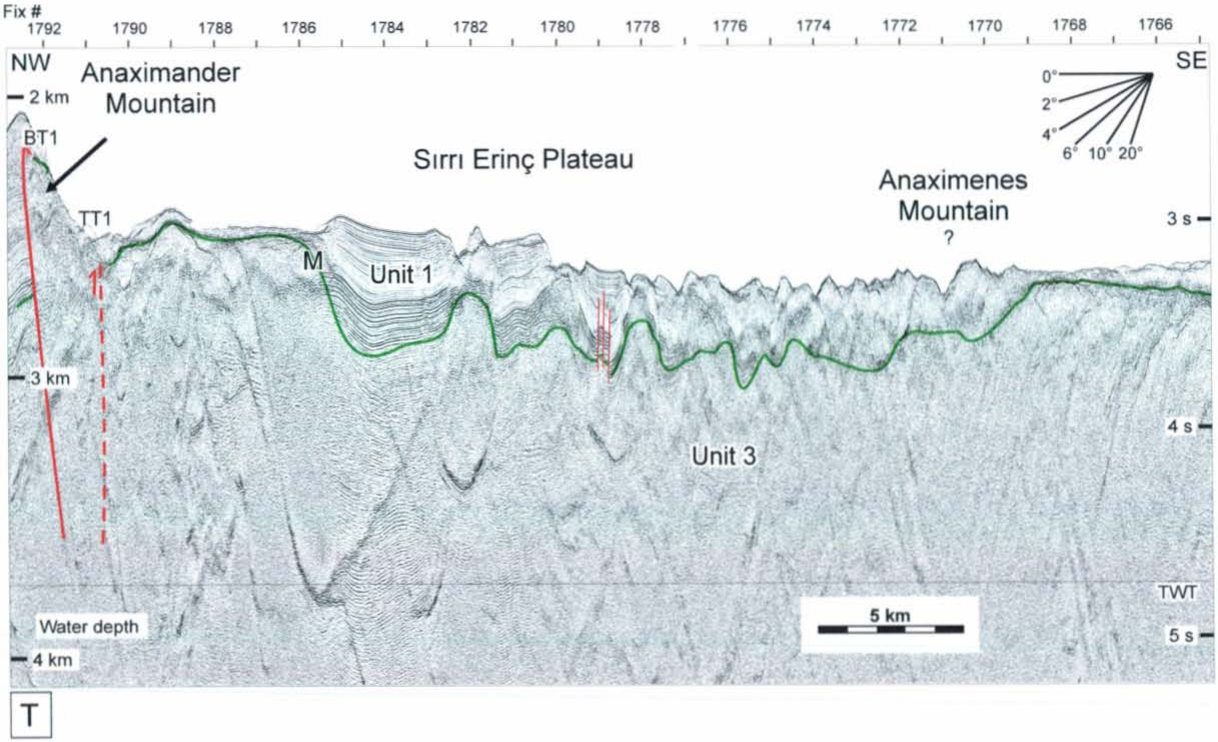

Figure 5.25 Seismic reflection profile T showing thrusts TT1 and BT1 in the Anaximander Mountain. The Anaximenes Mountain is no longer visible. Location shown in figure 5.3.

southern and northern edges of the block. The easternmost profile shows that the Amaximenes Mountain is a very wide- and flat-crested structure which is ~25 km wide and is elevated ~1000 ms above the adjacent seafloor (Fig. 5.18). Unlike the Anaximander Mountain (*sensu stricto*), which has a thick Pliocene-Quaternary succession on its backlimb, the Anaximenes Mountain is nearly barren of Pliocene-Quaternary sediments. In this area there are a few small depocentres, with ~200-250 ms thick Pliocene-Quaternary sediments nestled in the topographic depressions created within Unit 3, immediately below the M-reflector (Fig. 5.18). Careful examination of the seismic profile illustrated in Figure 5.18 shows the presence of a broadly folded internal structural fabric in Unit 3. These folds have wavelengths and amplitudes ranging from 2 to 6 km and 100 to 300 ms, respectively (Fig. 5.18). In many places, the folded geometry of Unit 3 displays major discontinuities, where the direction of dip reverses along a sharp boundary. These major discontinuities are interpreted as thrusts. Offsets in prominent marker horizons show footwall hanging wall relationships which show thrust vergence. For example, the reflectors highlighted as $\mathbf{X_1}$ and $\mathbf{X_2}$ in the easternmost seismic profile (i.e., Fig. 5.18) show footwall and hanging wall cutoffs across a major southeast verging northwest dipping thrust. This structure is labeled as TT2. The foot wall – hanging wall relationships are best imaged in the enlarged profile (e.g., Figs. 5.26). The small depocentres above this thrust display growth strata wedges within the Pliocene-Quaternary sediments, which suggest the presence of at least two smaller similarly verging splays of thrust TT2 (Figs. 5.18, 5.26). Further southeast toward the

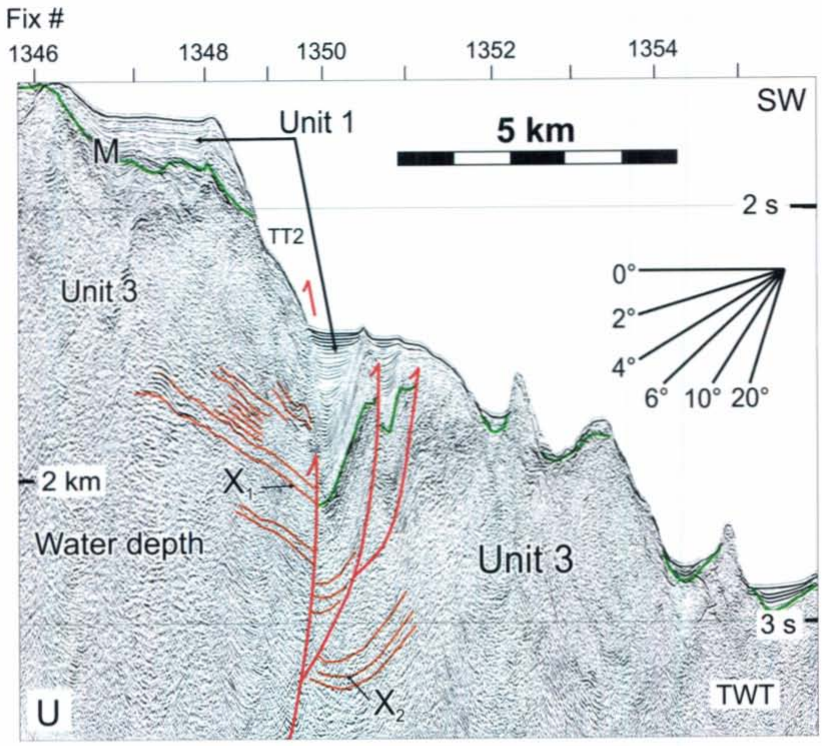

Figure 5.26 Seismic reflection segment U showing a blow up of the smaller splays of thrust TT2 (figure 5.18). Location shown in figure 5.3.

Mediterranean Ridge, the folded fabric of Unit 3 suggests the presence of several smaller similarly verging, and dipping thrusts (Figs. 5.11, 5.18).

Along the northwestern face in the easternmost portion of the Anaximenes Mountain the folded fabric of Unit 3 suggests the presence of a major northwest verging, southeast dipping thrust, labeled as BT2, where the M-reflector rises from ~3000 ms to 2300 ms within less than 2 km (Figs. 5.11, 5.18). The 1:1 profile here best illustrates the foot wall – hanging wall relationships of this thrust (Fig. 5.27). South of thrust BT2, there is another similarly verging and dipping thrust, where the M-reflector is offset once again from ~2300 ms to ~1500 ms at the crest of the Amaximenes Mountain (Fig. 5.18). Between these two thrusts, the seafloor occurs as a narrow flat-crested plateau.

Moving southwest, the morphology of the Anaximenes Mountain changes radically from a flat-crested broad structure in the northeast to a very narrow single crested high in the southwest (Figs. 5.19, 5.20). In this area, the Anaximenes Mountain is a prominent high, standing 1300-1800 ms above the adjacent seafloor. The Pliocene-Quaternary sediments of Unit 1 are very thin (>150 ms) in this area, and the M-reflector is located close to the seafloor. The southern face of the Anaximenes Mountain, has a rough morphology and dips toward the southeast ranging from 10°-15°, whereas the northern face of the mountain is much steeper (15°-25°). In this area (i.e., the central portion of the Anaximenes Mountain), the Unit 3 displays a very complexly folded and faulted internal architecture (Figs. 5.19, 5.20). Strong marker horizons in Unit 3 show footwall/hanging wall offsets which delineate the direction of thrusting. For example, a

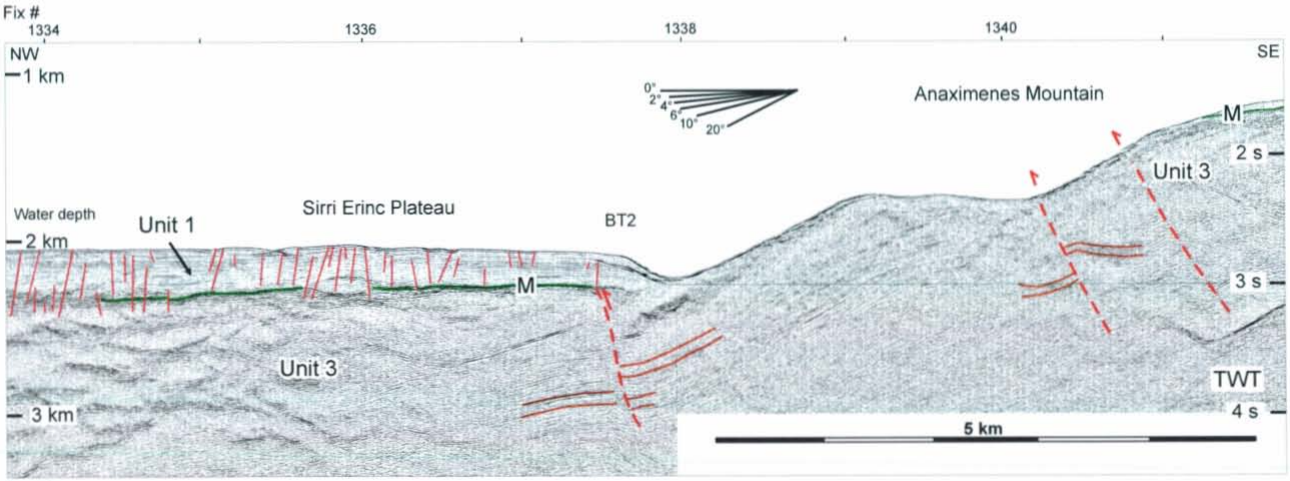

V

Figure 5.27 Seismic reflection segment V at a 1:1 scale showing BT2 (from figure 5.18) in the Anaximenes Mountain and the transition to the Sırrı Erinç Plateau. Location shown in figure 5.3.

reflector bundle highlighted as X_3 on the southern margin of Anaximenes Mountain show the presence of a southeast verging northwest dipping thrust (e.g., Fig. 5.20). Detailed mapping of structures indicates that this thrust correlates with TT2 described above (Figs. 5.11, 5.18-5.20). Similarly, the M-reflector at the northern margin of the Anaximenes Mountain (labeled as in Fig. 5.20) clearly displays contractional overlap. In this area, folded reflectors within Unit 3 also display footwall-hanging wall offsets, confirming the presence of a northwest verging, southeast dipping thrust. The 1:1 scaled profiles (e.g., Figs. 5.27, 5.28) illustrate the foot wall – hanging wall relationships of this thrust. The geometry of the thrust is peculiar in that it appears to cut continuous horizons at depth and flatten and disappear in a strange way upwards. This major thrust is correlated with BT2 thrust described above (Figs. 5.11, 5.18-20). Detailed examination of the seismic reflection profiles in this area shows that the core of the Anaximanes Mountain, north and south of its bounding faults, is also extensively and complexly deformed, showing the presence of secondary thrusts (e.g., Figs. 5.19, 5.20). In the core of the Anaximenes Mountain, the ~10 km spacing between adjacent seismic profiles and the 3-D nature of the structures make mapping of these thrusts with any degree of confidence difficult. South of major thrust TT2, there are several secondary southeast verging thrusts, that run roughly parallel to TT2 (Figs. 5.11, 5.19, 5.20).

Further west, the crest of the Anaximenes Mountain decreases in elevation from ~900 ms to ~1700 ms, within a distance of ~10 km (Fig. 5.2). The Pliocene-Quaternary sediments of Unit 1 are extremely thin (>100 ms) in this area, and the M-reflector is located close to the seafloor. Here, the structure becomes even narrower, with its crest

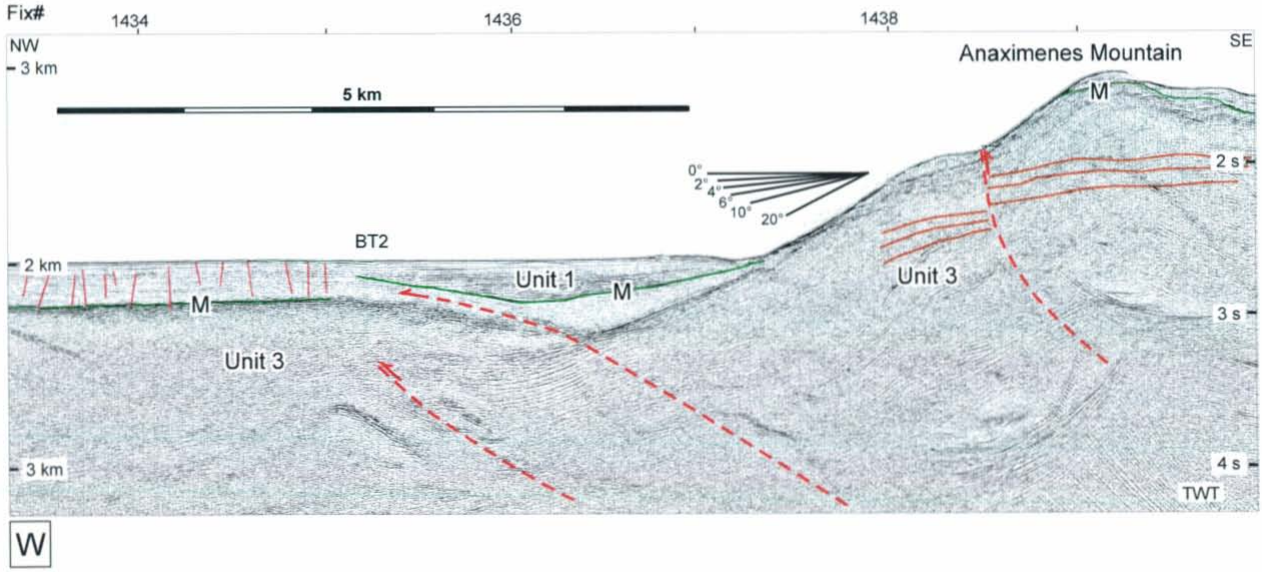

Figure 5.28 Seismic reflection profile W at a 1:1 scale showing trust BT2 (from figure 5.20) in the Anaximenes Mountain. Location is shown in figure 5.3.

<0.5 km wide (Figs. 5.21, 5.22). The major thrusts TT2 and BT2 that bound the Anaximenes Mountain can be readily identified by hanging wall – footwall relationships of markers in Unit 3 (Figs. 5.11, 5.21, 5.22). The core of the structure is equally intensely deformed as seen in the central segment of the domain, suggesting the presence of several secondary thrusts. A prominent trough is developed directly southeast of major thrust TT2 (e.g., Figs. 5.21-5.23). A similar, but much narrower and shallower through is also developed at the base of the northern escarpment (Figs. 5.21, 5.23).

The three southwestern seismic lines show that the Anaximenes Mountain continues to plunge progressively losing its morphological and tectonic characteristics (Figs. 5.23-5.25). The southern major trough is readily traced into this area. Here, the Anaximenes Mountain, which is located northwest of this trough, is only a small feature on the seafloor, barely rising ~300 ms above the northwestern seafloor (e.g., Fig. 5.23). In the two most southwesterly seismic profiles the Anaximenes Mountain can no longer be distinguished, and the region northwest of the trough resembles morphologically and structurally the Sırrı Erinç Plateau (Figs. 5.24, 5.25).

The seismic reflection data clearly show that the Anaximenes Mountain is imaged as two oppositely-verging thrusts, delineating a pop-up structure (Figs. 5.11). Similar to the Anaximander Mountain (*sensu stricto*) the core of the Anaxemenes Mountain is composed of slivers of Unit 3 (Figs. 5.18-5.25). The major thrust TT2 and its back-thrust BT2 are correlated toward the southwest into the Sırrı Erinç Plateau (Fig. 5.11). These two thrusts dramatically merge and plunge southwestward. West of

29°40′E longitude, the Anaximenes Mountain becomes undistinguishable from the seafloor corrugations of Domain 3 (Fig. 5.11).

5.3 Domain 3 – Sırrı Erinç Plateau

Domain 3 is an open V-shaped region of the seafloor with its open side facing northwest. It is situated between the Anaximander Mountain (*sensu strico*) in the west and northwest, the Anaximenes Mountain in the southeast and the Anaxagoras Mountain in the east (Fig. 5.2). It is bordered to the north by the deep Finike Basin. To the southwest, Domain 3 merges with morphologically and structurally similar portion of the southern Rhodes Basin (e.g., Winsor, 2004; Hall et al., 2009). Here the southern boundary of the domain is not well constrained.

Aksu et al. (2009) described the pre-Pliocene-Quaternary structural architecture of the northern portion of Domain 3. They showed that the region is characterized by a 20-30 km wide zone consisting of E-W trending, S-dipping and N-verging imbricate thrusts deforming Unit 3 strata (e.g., their Figure 14, replotted as Fig. 5.29). They further showed that the northernmost thrust panels sharply offset the M-reflector by >2500 ms and define the boundary between Domain 3 and the Finike Basin (Fig. 5.29). Aksu et al. (2009) also described the structural framework of the central portion of Domain 3, and showed that the region is delineated by a 20-40 km wide S-verging fold/thrust belt within Unit 3. They showed that the belt is characterized by 4-5 east-west trending, north-dipping, south-verging thrust sheets, with well-defined ramp-flat geometries (e.g., Fig. 5.29). The present data set also shows a similar set of tightly spaced, roughly north-

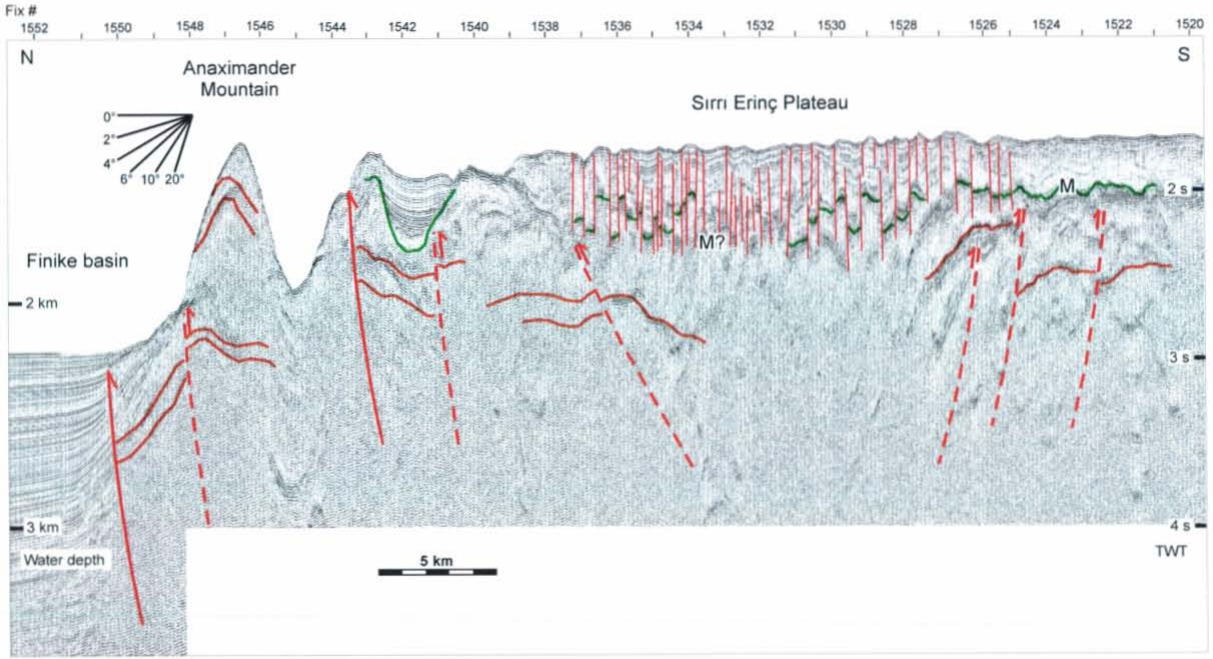

Figure 5.29 Mun-01 Seismic reflection profile X showing the transition from the Anaximander Mountain to the Sırrı Erinç Plateau and the Finiki Basin. Location shown in figure 5.3.

dipping, south-verging thrust sheets (Fig. 5.20). Sparse profiles in this area suggest a broadly east-west trend for these thrusts, but additional data are needed to better resolve the orientation of these structures.

The surface morphology of Domain 3 is characterized by distinct corrugations on the seafloor creating a series of troughs and peaks trending northwest-southeast in the southwestern portion of the domain, but gradually swing to assume a nearly east-west trend in the northern portion of the domain (Fig. 5.2). These corrugations are nearly orthogonal to the bounding structures of the domain, particularly the southern escarpment of the Anaximander Mountain and the northwestern margin of the Anaximenes Mountain, and along the north-south trending strike slip boundary between Domains 1 and 3 (Fig. 5.2). The swing of these corrugations closely follows the overall trend of the Sırrı Erinç Plateau.

Seismic reflection profiles across the domain show that the corrugated seafloor morphology is the reflection of the underlying structural fabric of the Pliocene-Quaternary successions of Unit 1 (Figs. 5.21-5.25, 5.29). The architecture of Unit 1 is characterised by a series of tightly-spaced upright anticlines and synclines (e.g., Figs. 5.20, 5.25, 5.29). The M-reflector is also corrugated across Domain 3, and is sharply segmented between adjacent synclines and anticlines, where faults bounding the structures create 50-250 ms offsets of the M-reflector extending into Unit 3. Seismic reflection profiles show that most, if not all, tip points of these faults lie at the seafloor, or within the uppermost portion of Unit 1. These seismic profiles reveal that a number of

faults show contractional offsets of marker horizons, yet others show extensional offsets (e.g., Figs. 5.20, 5.25, 5.29). Minor growth wedges observed in Unit 1 suggest that these faults developed during the deposition of the Pliocene-Quaternary strata. Lack of clear growth strata within Unit 3 suggest that the deformation occurred following the deposition of Unit 3.

One of the most notable attributes of these upright synclines and anticlines and their bounding faults is the reciprocal folding of the M-reflector and the seafloor (e.g., Fig. 5.30). That is, a syncline at the level of the M-reflector is turned into an anticline at the level of the seabed (e.g., Fig. 5.30). Here, the lower Pliocene-Quaternary reflectors mimic the trend of the M-reflector, whereas the upper Pliocene-Quaternary reflectors follow the trend of the seafloor. A prominent marker in mid-Pliocene-Quaternary level separates these two oppositely curved reflectors. Careful examination shows that this reflector displays mild truncation of the underlying reflectors, suggesting a switch in the polarity of deformation (further discussed in Chapter 6).

Multibeam bathymetry over Domain 3 shows that the seafloor corrugations have limited lateral extent, but they are mappable. There is a very strong correlation between the troughs and peaks observed on the multibeam bathymetry and the synclines and anticlines observed in the seismic reflection profiles. Therefore, the faults that bound these upright structures can be confidently mapped using the combination of multibeam traces of faults and the seismic reflection profiles. In the southern and southwestern portion of the domain these bounding faults have pronounced northwest-southeast trends,

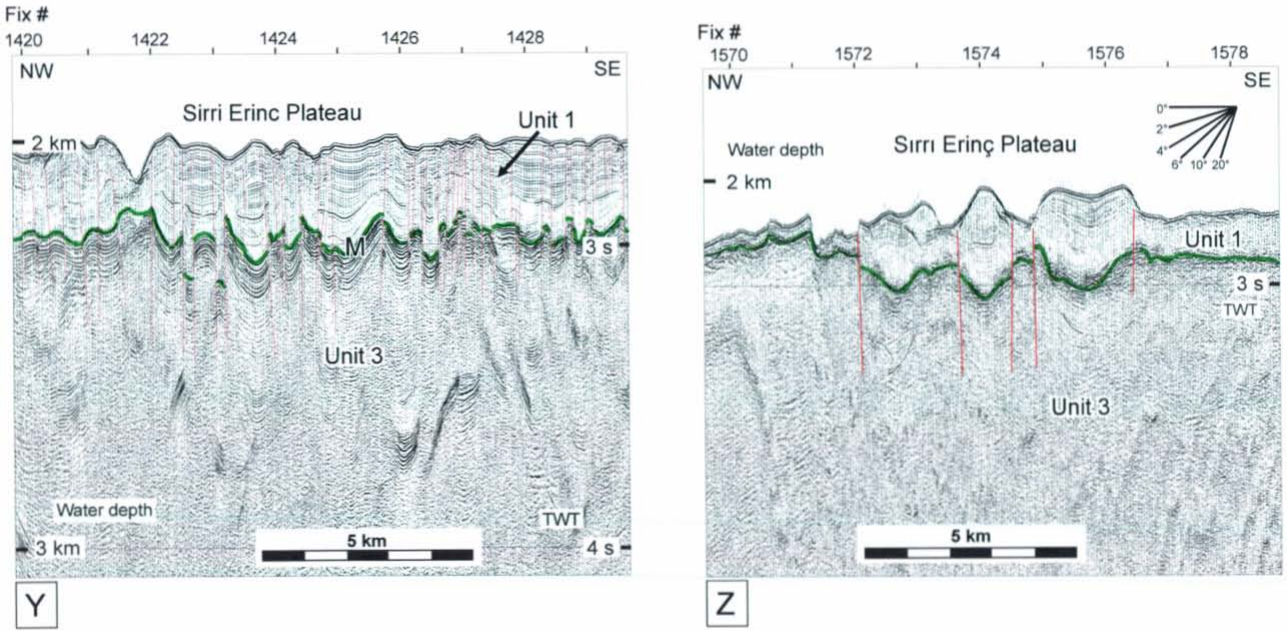

Figure 5.30 **(a)** seismic reflection profile Y and **(b)** seismic reflection profile Z from the Sırrı Erinç Plateau showing upright faults and inversion structures respectively. Location shown in figure 5.3.

and create 10-15 km long linear features on the seafloor. In the central portion of the domain the faults are ~5-10 km long and are dominantly in a northwest-southeast orientation. These faults progressively swing northward to assume an east-west trend (Fig. 5.11).

The seismic data clearly show that the Pliocene-Quaternary succession in Domain 3 is generally well stratified throughout, and is intensively faulted (e.g., Figs. 5.20, 5.25, 5.29). This domain is interpreted by Woodside and colleagues (e.g., Woodside et al., 1998, Zitter et al., 2003, ten Veen et al., 2004) as a massive gravitational slide mass: they referred to as the "Great Slide" (further discussed in Chapter 6). The seismic data presented in this thesis show well-bedded Pliocene-Quaternary succession across Domain 3, and lack any evidence of the chaotic internal architecture typically associated with slide masses.

Several observations suggest that the Sırrı Erinç Plateau experienced transtension and/or transpression throughout the Pliocene-Quaternary. These include: (i) the high degree of faulting, (ii) the reciprocal folding, (iii) the progressive rotation of the faults and seafloor corrugations, and (iv) the overall constant elevation of the M-reflector and the seabed. These points are further discussed in detail in Chapter 6.

In the Sırrı Erinç Plateau the corrugation of the sea bed and the M-reflector are out of phase (Fig. 5.30). This reciprocal folding maybe related to evaporite flow where the overburden is thin and less dense than the thicker evaporite, which is exactly what is expected of thin clastic sediments (< 1km) overlying an evaporite sequence if the

evaporite flow is syn-sedimentary (Jackson and Talbot, 1991). However, in the absence of distinctive evaporite structures such as salt rollers, walls and pillows within the Sırrı Erinç Plateau and the absence of a clear reflector signaling the presence of the N-reflector beneath the M-reflector preclude an unequivocal interpretation suggesting that evaporites may be present in this area.

Figure 5.31 schematically illustrates the evolution of the Pliocene-Quaternary and Messinian Units 1 and 2. Messinian evaporites of Unit 2 are deposited horizontally in isolated depressions across the Anaximander Mountains. The following period of desiccation of the eastern Mediterranean Sea associated with the so-called Messinian Salinity Crisis and minor uplift exposed Unit 2 to sub-areal erosion, creating the M-reflector. During the Pliocene-Quaternary a thick succession of siliciclastics were deposited over the uplifted limb of the Anaximander Mountain. Continued uplift associated with southward verging thrusting created a northward thickening wedge over the northern limb of the Anaximander Mountain (Fig. 5.31). The regional development of the Anaximander Mountains is further discussed in Chapter 6.

I. Unit 2 deposition

II. Erosion of Unit 2

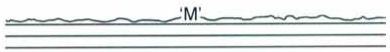

III. Uplift, tilting +/- folding

IV.

1a Unit 1a deposition

1b Enhanced growth, post γ

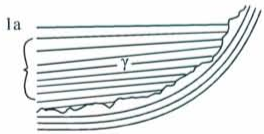

Figure 5.31 Schematic Structural Evolution of Units 1 and 2.

CHAPTER 6. Discussion

6.1 Previous work of the tectonic framework of the eastern Mediterranean Sea

There are only a limited number of studies that have been carried out in the Anaximander Mountains and environs (e.g., Woodside et al., 1998, Zitter et al., 2003, ten Veen et al., 2004, Aksu et. al., 2009). However, there are numerous studies addressing issues related to the structural and stratigraphic evolution of the eastern Mediterranean Sea and the surrounding landmass (e.g., Jongsma and Mascle, 1981, Anastasakis and Kelling, 1991, Papazachos and Papaioannou, 1999, Zitter et al., 2000, Woodside et al., 2000, 2002, ten Veen and Kleinspehn, 2002, Poisson et al., 2003, ten Veen, 2004, Savaşçın et al., 2005, van Hinsbergen et al., 2007). In this chapter a summary of the previous studies in the eastern Mediterranean region is provided. This summary provides the foundation for a detailed discussion of the evolution of the Anaximander Mountains and the surrounding environment.

In the early literature, most studies were concerned with the position and nature of the boundary between the African and Eurasian Plates. Woodside (1977) used seismic reflection profiles and gravity data to suggest that subduction probably ended within the last 5 million years with the disappearance of all oceanic crust between Turkish and African Plates. He pointed out that the morphological elements of the eastern Mediterranean Sea such as the character of the Florence Rise and Anaximander Mountains, the northward tilting and subsidence of the Antalya and Finike Basins, and the apparent continuation of the Strabo Trench south of the Florence Rise, suggesting

under-thrusting of the Turkish Plate by the African Plate. However, Woodside (1977) also noted the scarcity of seismicity between the African and Turkish Plates, the absence of an active volcanic arc, and the presence of a poorly-developed trench and concluded that active subduction must have ended. Jongsma and Mascle (1981) used seismic reflection data to conclude that the collision of the African continental margin with the Hellenic Arc is still in progress, causing the overriding of the Mediterranean Ridge along the southeastern branch of the Hellenic Trench system (Fig. 6.1). Anastasakis and Kelling (1991) used single-channel seismic reflection profiles to suggest that the Cyprus Trench displays evidence of underthrusting and morphostructural features typical of subduction zones, and that the Pytheus Trench (i.e., the western segment of the Cyprus Arc; Fig. 6.1) is associated with dextral strike-slip movement and connects the western end of the Cyprus Trench to the Strabo Trench sector of the Hellenic Trench system.

Papazachos and Papaioannou (1999) used locations of earthquakes recorded by seismographs and fault plane solutions of large recent earthquakes to define the plate boundaries and the pattern of plate motion in the eastern Mediterranean Sea, particularly south and west of Cyprus. They suggested that the distribution of shallow and intermediate depth earthquakes define a continuous boundary between the Eurasian and the African Plates. They show that this boundary consists of two arcuate, concave to the north structures (i.e., the Cyprus Arc in the east and the Florence Rise in the west), which are connected to each other by a north-northeast trending dextral transform fault, west of Cyprus (Fig. 6.1). They named this structure the Paphos Transform Fault. They further suggested that the western arc trends northwest following the Florence Rise and joins the

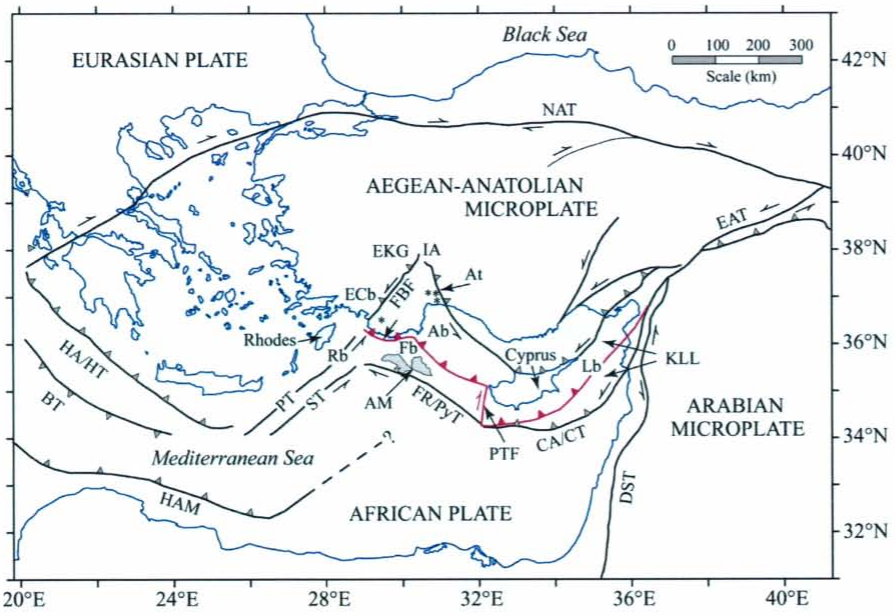

Figure 6.1 Locations-1 Map showing the location of Ab=Antalya Basin, AM=Anaximander Mountains At=Aksu Thrust, BT=Back thrust, CA/CT=Cyprus Arc/Cyprus Trench, DST=Dead Sea Transform fault, EAT=East Anatolian Transform fault, ECB= Esen Cay Basin, EKG= Egridir-Kovada Graben, FB=Finiki Basin, FBF=Fethiye-Burder Fault zone, FR/PyT=Florence Rise/Pytheus Trench, HA/HT=Hellenic Arc/Hellenic Trench, HAM=Hellenic Active Margin, KLL=Kyrenia/Larnaca/Latakia Ridges, LB=Latakia Basin, NAT=North Anatolian Transform fault, PT=Pliny Trench, PTF= Paphos Transform Fault, Rb=Rhodes Basin, Rt=Rhodes Thrust, ST-Strabo Trench.

Rhodes thrust fault (a previously undefined structure along the southern margin of the Turkish continental slope).

More detailed investigations of the eastern Mediterranean Sea were undertaken in the Training-Through-Research (The Floating University) program of UNESCO in 1991. A group of scientists from European universities used the former Soviet/Russian research vessel *Gelendzhik* to carry out numerous cruises in the Rhodes and Antalya Basins, Anaximander Mountains, Florence Rise and Pliny-Strabo Trenches (e.g., Woodside et al., 1997). The results of these expeditions are summarized below.

Woodside et al. (1998) were the first to document the occurrence of gas hydrates associated with mud volcanoes in the Anaximander Mountains. They used multibeam bathymetry to suggest that these mud volcanoes may be related to cross-cutting strike-slip faults defining individual blocks in the Anaximander Mountains, permitting over-pressured fluids from thrusts in the compression zone to be expelled at the surface. They showed evidence for the presence of gas in the sediments, such as pockmarks and mud volcanoes with carbonate crusts and benthic communities commonly found near gas seeps. They proposed that the region between the Anaximander Mountain and Anaximenes/Anaxagoras Mountains represents a massive gravitational slide, referred to as the "Great Slide" (Fig. 6.2). They suggested that the Great Slide started to gravitationally flow to the north and south during the Late Pliocene or Pleistocene. These authors indicated that the deformation in this region involved under-thrusting of the Anaximander Mountain by the Anaximenes Mountain and shortening between them.

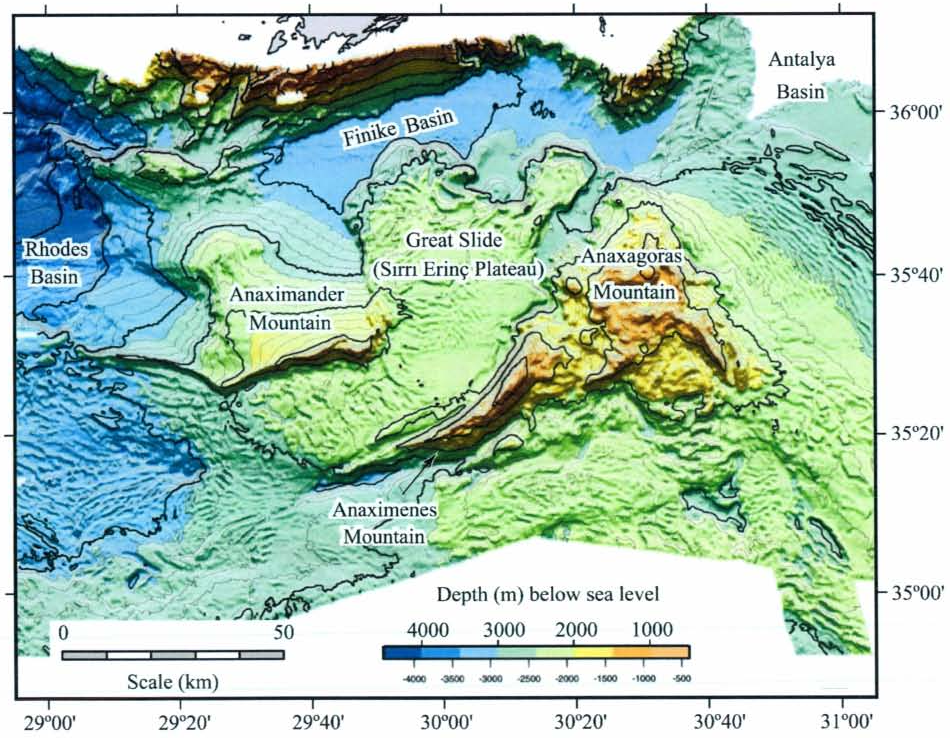

Figure 6.2 Map showing the location of the great slide of Woodside et al. (1998).

Here, the Anaximander Mountain was raised by the under-thrusting of the Anaximenes Mountain and the latter was tilted up toward the northwest. They envisaged that gas hydrates in poorly consolidated sediments with higher than normal water content may have triggered the flow in this tectonically active region. They suggested that sediment undergoing deformation within the compression zone began releasing gas from decomposing gas hydrates as it was elevated above the gas hydrate stability zone, thus the Great Slide.

Woodside et al. (2000) used swath bathymetry, seismic reflection profiles, gravity and magnetic data to show that the deep Rhodes Basin contains no Messinian evaporites and only a thin Pliocene–Quaternary sedimentary section overlying the acoustic basement. They indicated that the acoustic basement is probably composed of pre-Miocene rocks which may be related to the Hellenide–Tauride orogens. They suggested that reverse faulting, strike-slip faults, sedimentary nappe-formations and mass sliding are presently occurring in the Rhodes Basin, and that this basin is still evolving. They proposed that the Rhodes Basin developed as the result of a collapse of its brittle basement, in connection with the progressive development of transform motion along the eastern branch of the Hellenic Arc. They speculated that if this hypothesis is correct, the Rhodes Basin must be a post-Miocene foundered trough, somewhat similar to pull-apart basins developed along the transpressive branch of the Hellenic Arc (i.e., the Pliny Trench).

Zitter et al., 2000 and 2003 used high-speed seismic reflection, multibeam and gravity data collected during the ANAXIPROBE 95 and PRISMED II 98 surveys to show that there is no evidence for present-day thrusting along the Anaxagoras–Florence high. They described faulting along and across the Florence Rise to be characterized by anastomosing faults and pop-up structures. They suggested that most of the deformation in this area is the result of strike-slip faulting which developed as the reactivation of existing thrusts and normal faults. They described this deformation as a broad zone of northwest–southeast dextral wrenching and pointed out the similarities between the Hellenic and Cyprus Arcs, with sinistral faulting along their eastern segments such as the Strabo/Pliny versus Kyrenia/Larnaca/Latakia Ridges and dextral faulting along their western segments. They used multibeam data to suggest that the eastern Anaximander Mountains have affinity with the Florence Rise structure (western Cyprus Arc), but argued that the western Anaximander Mountains are directly related to the opening of the Rhodes and the Finike Basins, as transtension may have dominated in southwest Turkey since the Pliocene. The indicated that the connection with onshore Turkey is still unclear, but could be related to the Fethiye–Burdur Fault Zone that defines the western boundary of the complex Isparta Angle (Fig. 6.3). They concluded that the Anaximander Mountains and the Isparta Angle form together a tectonic accommodation zone between the active deformation in southwestern Turkey and the Aegean region and the tectonically quieter Cyprus region.

Woodside et al. (2002) used the PRISMED II data set which consisted of EM12D multibeam bathymetric data, high speed seismic refection profiles, and

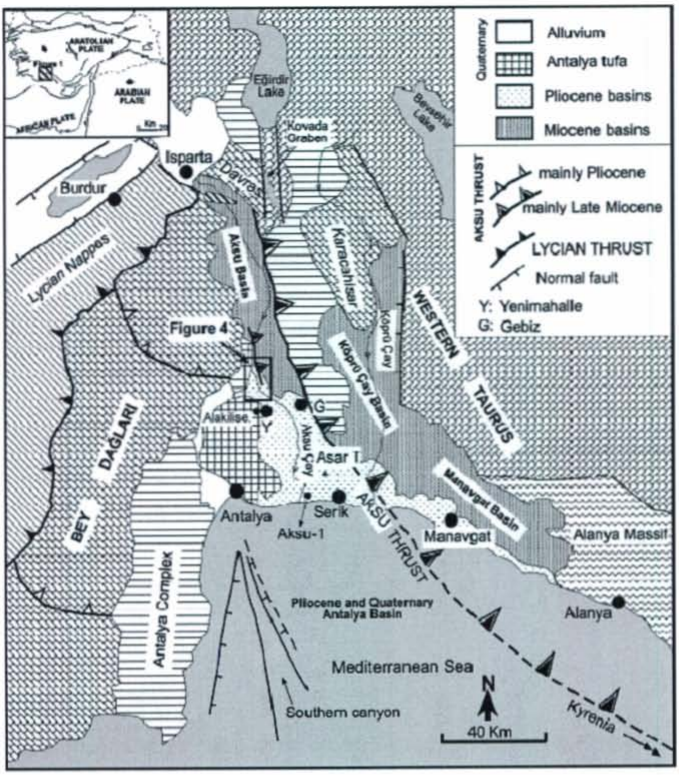

Figure 6.3 Structural sketch map of the Isparta Angle summarizing the Late Miocene and Pliocene basins and the main tectonic lineaments. Inset shows the figure location in the Eastern Mediterranean (from Poisson, 2003).

continuous gravity and magnetic data from the eastern Mediterranean Sea to study the tectonic evolution of the Florence Rise and Anaximander Mountains and environs. They suggested that the boundary between the Anatolian and African Plates is probably sutured, but that continuing deformation has resulted in the development of a broad dextral wrench zone extending across the Florence Rise toward the Anaximander Mountains. They further stated that "this tectonic deformation is related to the progressive adjustment along the Florence Rise of the collisional/compressional plate interaction between the westward moving Cyprus domain and the northeast moving African Plate". Woodside et al. (2002) ascribed a significant proportion of the current deformation to the passive superficial deformation caused by the invasion of thick sediments from the Herodotus Basin and Mediterranean Ridge into the area of the Florence Rise. They suggested that the subduction along the Cyprus Arc has probably ceased due to the presence of the Eratosthenes continental block at the subduction zone, and concluded that because of the geometrical constraints on a subducting slab descending at the Hellenic and Cyprus Arcs resulted in the tearing of the African Plate near the cusp between these two arcs.

ten Veen et al. (2004) used multibeam bathymetry, backscatter images, seismic reflection profiles and gravity and magnetic data to suggest that the western and eastern Anaximander Mountains are correlated with the Bey Dağları succession of southwest Turkey, and the Antalya Nappe Complex, respectively. They suggested that during the Serravallian–Tortonian, several graben developed extending from the southern Aegean to southwestern Turkey. During the Late Miocene differential subsidence resulted in the

formation of the Anaximander Mountains: this is reflected by an unconformity between the Lower–Middle Miocene and Pliocene–Quaternary successions. They also suggested that during the Messinian–Quaternary, the western part of the Anaximander Mountains was characterized by distributed sinistral shear parallel to N70°E, which was marked by the onset of an extension on N20°E-striking normal faults that formed long graben-like depressions. During the Pliocene, these basins were transected by N70°E-striking sinistral strike-slip faults, but continued crustal extension suggested that deformation was mainly transtensional. These authors suggested that the eastern part of the Anaximander Mountains is characterized by N150°E-striking normal and/or oblique normal faults, which lack significant evidence of strike-slip deformation.

There are several onland studies that provide critical insight for the understanding of the evolution of the Anaximander Mountains and surrounding environs (Yağmurlu et al., 1997, Savaşçın and Oyman, 1998, ten Veen and Kleinspehn, 2002, Poisson et al., 2003, ten Veen, 2004, Savaşçın et al., 2005, van Hinsbergen et al., 2007).

Yağmurlu et al. (1997) and Savaşçın and Oyman (1998) studied the volcanic successions of the Isparta Angle and the surrounding region. They documented that the volcanics in the Isparta Angle are alkaline and hyperalkaline in character, consisting of latitic and trachytic lavas, leucitic and lamproitic dikes, and pyroclastic constituents. They showed that alkaline volcanics are located on the west side of the Isparta Angle forming a north-south trend paralleling the Eğridir-Kovada graben (Fig. 6.1). The volcanics range in age from 15 to 4 Ma and get younger from north to south; their

arrangement along the north-south trending Eğridir depression indicates that the development of this volcanic activity is simultaneous with active tectonics during the late Miocene to early Pliocene. The volcanic centers are on the synthetic fault elements of the Eğridir-Kovada intra-continental rifting in connection to the northward movement of the African Plate.

Poisson et al. (2003a) showed that the tectonic history of the Isparta Angle region is poly-phased, with the main events in the Late Cretaceous (initiation of shortening), pre-Miocene (Antalya Nappe emplacement), and Late Miocene/Pliocene (Aksu thrusting). They showed that the Aksu phase of thrusting reactivated older thrusts, giving rise to the most prominent relief of the area, the Davras Dağ. Poisson et al. (2003b) showed that the mid-Pliocene successions are clearly involved in the Aksu Thrust phase. They documented that the Aksu Thrust is younger than previously believed (i.e., post-Late Pliocene), and suggested that the east-west compressional Aksu phase must be synchronous with the north-south sinistral strike-slip along the Dead Sea transform fault system, as well as the north-south compression and uplift which affected the Pliocene successions in north Cyprus.

ten Veen and Kleinspehn (2002) showed that five fault populations in the Apolakkia Basin on the southwestern portion of the Island of Rhodes record two neotectonic deformation phases separated by a kinematic change at ~4.5 Ma. They suggested that the Apolakkia Basin originated as a late Miocene fault wedge basin in response to syn-depositional southwest-northeast D1 extension with similar strain

patterns in the adjacent offshore Hellenic inner forearc zone. They attributed the kinematic change at ~4–5 Ma to a threshold of obliquity whereby the inner forearc started to experience sinistral-oblique divergence. They suggested that the Pliocene-Pleistocene D2 transtensional phase reoriented the basin and resulted in combined syn-depositional west-north – westeast-southeast extension and 070° sinistral shear. They further suggested that the principal shear zones offshore also occur consistently at ~070°, mimicking the D2 kinematic history of the Apolakkia Basin. They concluded that the upper crust of the expanding Aegean-Anatolian block behaved independently at its leading edge, and the Pliny trench constitutes a major boundary separating partitioned forearc slivers, a post-4.5 Ma partitioning recorded reliably by the Pliocene fill of the Apolakkia Basin.

ten Veen (2004) showed that during the late Pliocene the Eşen Çay Basin in southwestern Turkey experienced east-west extension resulting in the development of north-south normal faults. They further showed that during the Pleistocene 020° faults developed from a west-northwest – east-southeast extension, whereas the Holocene-Recent is characterized by a complex combination of faults with 070° sinistral strike-slip. They used fault-slip analysis to suggest that stresses evolved from simple tensional to transtensional over the Pliocene–Quaternary period.

van Hinsbergen et al. (2007) showed that the Island of Rhodes represents an uplifted block in the largely submerged southeastern Aegean forearc. They used palaeomagnetic data to document that the island experienced two phases of

counterclockwise rotation: a 9±6° rotation between 3.8 and 3.6 Ma, and a 17±6° rotation since 0.8 Ma. They showed that between these two phases of rotation, the Island of Rhodes tilted to the southeast, drowning the southeastern coast to a depth of 500–600 m between 2.5 and 1.8 Ma, then to the northwest, which resulted in the re-emergence of the drowned relief between 1.5 and 1.1 Ma. They suggested that these rotations are related to the formation of the south Aegean sinistral strike-slip system and the foundering of the Rhodes Basin.

Aksu et al. (2009) used multi-channel seismic reflection profiles to show that the Anaximander Mountains experienced a Miocene contractional tectonic phase characterised by an east-west trending and south-verging fold-thrust belt. They suggested that this tectonic phase ended in the latest Miocene and was replaced in the Pliocene by a tectonic regime dominated by transpression and rotation. They speculated that the Anaximander and the Anaximenes Mountains developed as the result of the reactivation, uplift and rotation of a linked, thick-skinned pre-Messinian imbricate thrust fan. They further speculated that the Anaximander and Anaximenes Mountains experienced a progressive counterclockwise rotation, while the Anaxagoras Mountain and the Florence Rise experienced a clockwise rotation. They interpreted the Sırrı Erinç Plateau as a major Pliocene-Quaternary transpressional fault system.

Hall et al. (2009) used multi-channel seismic reflection profiles to show that the evolution of the Rhodes Basin involved a period of Miocene convergence which resulted in the development of a south-southeast verging fold-thrust belt, which ended in the late

Miocene. They argued that the Messinian evaporites are absent in the Rhodes Basin, thus suggested that the region must have remained above the depositional base of marine evaporite environment during the Messinian. They further suggested that a second phase of deformation started in the middle Pliocene-Quaternary and that it is characterized by a northeast-southwest sinistral transpression, and rapid regional subsidence. These authors ascribed the evolution of the Rhodes Basin to subsidence associated with loading of the large imbricate thrust panels that carry the western Tauride Mountains in the north.

6.2 Latest Miocene of the Anaximander Mountains

The internal architecture of Unit 3 successions showing large open folds that are disharmonious with the morphology of the M-reflector and the architecture of the Pliocene-Quaternary successions suggests that a major contractional tectonic period dominated the Anaximander Mountains during the Miocene. This contractional phase and the resultant fold-thrust belt are described in detail by Aksu et al. (2009). The disharmonious nature between the architecture of the predominantly Miocene Unit 3 and the overlying Units 2 and 1 suggests that this contractional tectonic phase culminated in the latest Miocene. The morphology of the M-reflector showing a broadly corrugated erosional surface, further suggests that the remnants of the Miocene fold-thrust belt was exposed to erosion associated with the Messinian salinity crisis. The largely low level of internal deformation observed in Unit 2 compared to the underlying Unit 3 and the overlying Unit 1 strongly suggests the Messinian was tectonically less active interval.

This study is the first to image and describe a possible Messinian succession (i.e., Unit 2) in the Anaximander Mountains and the Rhodes Basin. Previous studies such as Woodside et al. (1998, 2000, 2002), Zitter et al. (2000, 2003), Aksu et al. (2009), Hall et al. (2009), all indicated that this region did not have the Messinian evaporites which are characteristic of the eastern Mediterranean Sea, and that the Pliocene-Quaternary was separated from the underlying Miocene and older deposits by the M-reflector. The thin Unit 2 described in this study situated immediately below the Pliocene-Quaternary Unit 1 is enveloped by the M- and N-reflectors and is clearly a sedimentary package older than Pliocene-Quaternary, but younger than the largely folded Miocene and older units. Unit 2 is interpreted to be a Messinian deposit, and it may represent a predominantly siliciclastic succession, such as that described in the Iskenderun Basin and inner Latakia Basin (e.g., Uffenorde, 1990). The distinct lack of acoustic impedance contrast across the Units 1 and 2 boundary and the absence of a strong velocity peak in the semblance analysis support the view that Unit 2 may not be an evaporite succession dominated by halite and anhydrite such as encountered in the DSDP Sites 375 and 376 (Hsü et al., 1978).

The unconformable nature of the M- and N-reflectors enveloping Unit 2 over the Anaximander Mountains suggests that the region was exposed and eroding prior to, and after, the deposition of Unit 2.

6.3 Pliocene-Quaternary evolution of the Anaximander Mountains

The tectonic framework of the greater Anaximander Mountains is characterized by two arcuate broadly northeast-southwest trending northward concave large southeast verging thrusts (TT1 and TT2), two similarly trending but oppositely verging backthrusts (BT1 and BT2), and the intervening ~30 km wide corrugated seafloor that shows extensively faulted internal architecture (i.e., the Sırrı Erinç Plateau). The TT1 and TT2 thrusts delineate the southeastern margins of the Anaximander and Anaximenes Mountains, respectively, whereas the BT1 and BT2 backthrusts define the northwestern margins of the Anaximander and Anaximenes Mountains, respectively (Fig. 6.4).

A quick examination of the structural and stratigraphic framework of the Anaximander and Anaximenes Mountains show some similarities but several obvious differences. For example, both Anaximander and Anaximenes Mountain show a similar underlying tectonic framework, with large southeast verging, deeply rooted thrusts, carrying the mountains and backthrusts creating distinct pop-ups across the crestal regions of the mountains (e.g., Fig. 6.4). Similarly, the core of these two mountains consists of Eocene-Miocene folded strata (Chapter 4). However, there are obvious differences between the Anaximander and Anaximenes Mountains. For example, there is a significant variation of the Pliocene-Quaternary sedimentary thickness (Fig. 5.17): the Anaximander Mountain contains a thick Pliocene-Quaternary wedge on its northern slope, but the Anaximenes Mountain is nearly devoid of Unit 1 sediments. The Anaximander Mountain is an asymmetric solitary structure, defined by a very narrow

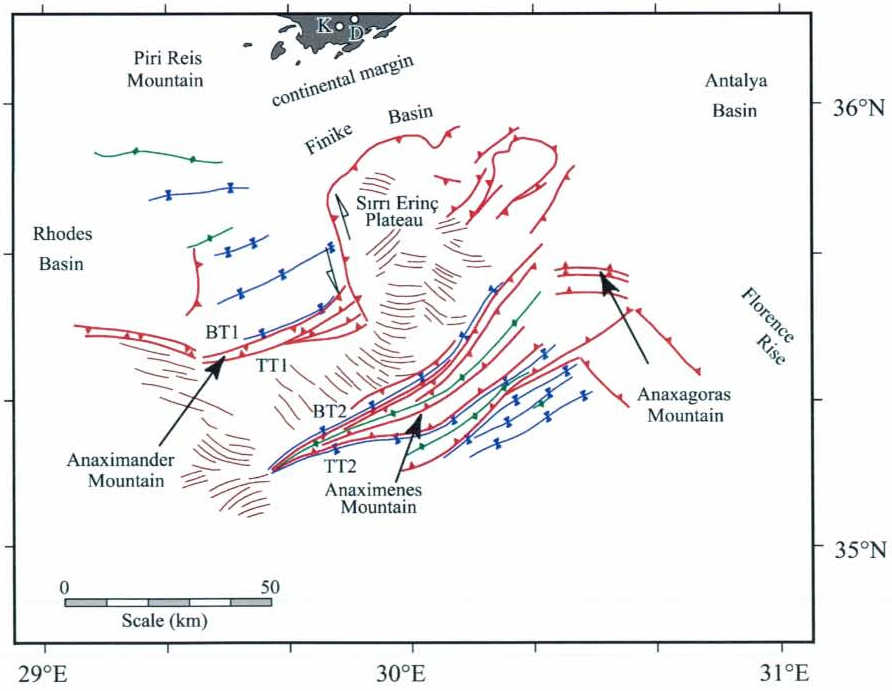

Figure 6.4 Map showing the Pliocene-Quaternary tectonic elements in the study area.

crest and gently northward dipping slopes, whereas, the Anaximenes Mountain has a more symmetrical shape and is narrow in its southwestern portion, but broadens to the northeast where it gradually merges with the Anaxagoras Mountain.

The stratigraphic and structural evaluation of the seismic reflection profiles (Chapters 4, 5) suggests that the TT1 thrust bounding the southern margin of the Anaximander Mountain is a reactivated thrust of the Miocene fold-thrust belt. The thick growth strata on the backlimb of the TT1 thrust provides evidence for the growth and development of the TT1 thrust and the Anaximander Mountain (*sensu stricto*). For example, the large north-thickening growth stratal wedges in subunit 1b above the γ reflector clearly document that the growth of the Anaximander Mountain occurred as the result of differential uplift in the Pliocene-Quaternary (e.g., Figs. 5.4-5.6, 5.8). The lack of growth in subunit 1a below the γ reflector clearly suggests that the reactivation of the TT1 must have occurred after the deposition of this lowermost Pliocene-Quaternary subunit. The backthrust BT1 is developed immediately north of the crest of the Anaximander Mountain. There is no distinct stratigraphic architecture of the Pliocene-Quaternary Unit 1 that can be readily attributed to the development of backthrust BT1: i.e. it is assumed to be a late feature.

The isopach map of the Pliocene-Quaternary sediments shows that there is a thick deposit which delineates an east-west trending basin immediately north of the crest of the Anaximander Mountain (Fig. 5.17). This basin merges with a north south trending basin that is developed immediately west of the boundary between the Anaximander

Mountain and the Sırrı Erinç Plateau. These two basins are also recognized by Aksu et al. (2009), and are referred as the Southern and Eastern Anaximander Basins by these authors. The north-south trending basin in turn, merges with another east-west trending Pliocene-Quaternary depocentre (i.e., the Finike Basin; Fig. 5.17). A comparison between the isopach map and seismic reflection profiles shows that the thick fill within these basins mainly consists of the lower Pliocene-Quaternary subunit 1a, with thinner deposits of subunit 1b. The data show that the east-west trending lower Pliocene-Quaternary basin on the backlimb of thrust TT1 has been progressively inverted during the late Pliocene-Quaternary. Aksu et al. (2009) postulated the presence of a sinistral strike slip fault at the boundary between the Anaximander Mountain and the Sırrı Erinç Plateau. They argued that the axes of the Finike Basin and the Southern Anaximander Basin (i.e., the east-west trending basin immediately north of the crest of the Anaximander Mountain) were probably aligned in the early Pliocene, and has experienced approximately 40 km of sinistral strike slip. However, this proposed offset is very large, encompassing a sizeable fraction of the length of the fault. It is possible that this fault represents a transfer zone with similar structures developing at different distances along the fault.

The TT2 thrust bounding the southern margin of the Anaximenes Mountain is interpreted as another deeply-rooted structure, running essentially parallel to the TT1 thrust described above. The very thin veneer of Unit 1 over the Anaximenes Mountain prevents a detailed evaluation of the timing of the development of TT2 and its backthrust BT2. However, the growth strata on the forelimb of the TT2 thrust, and its subsidiary

splays suggest that the thrust became reactivated during the Pliocene-Quaternary. Similarly, minor growth observed within the leading syncline along the southeastern margin of the Sırrı Erinç Plateau (i.e., on the footwall of BT2) suggest that BT2 was active during the deposition of Pliocene-Quaternary sediments (e.g., Figs. 5.19-5.21). Seismic reflection profiles show that the core of the Anaximenes Mountain is complexly folded and faulted and that the back limb of the culmination developed on the TT2 thrust is truncated by a prominent, steeply north-verging back thrust (i.e., BT2 in Figs. 5.18-5.20). This backthrust is deeply rooted within Unit 3. The resolution in the seismic profiles does not allow a detailed interpretation of the fault geometries across the Anaximenes Mountain. Therefore, the relationship between backthrust BT2 and the forethrust TT2 is not clearly imaged. Aksu et al. (2009) speculated that the backthrust probably branches from the forethrust at a depth >4000 ms. The growth strata within the small basins on the forelimb and backlimb of thrust TT2 and BT2 suggest that the timing for the development of TT2 and BT2 is post-Messinian (Chapter 5). Thus, the two oppositely verging thrust faults define a large pop-up structure over the crestal region of the Anaximenes Mountain.

The deep rooted nature of the trajectories of thrust TT1 and TT2 penetrating into 4-6 s in seismic reflection profiles (Chapter 5), suggests that these thrusts may be linked at depth to form a thick-skinned imbricate thrust system. The sole of this major south-verging thrust system and thus the linkage of these thrusts (i.e., TT1 and TT2) are not imaged in the seismic profiles. Deeper penetrating reflection profiles with a larger source and a longer receiver are necessary to image the deeper architecture of this thrust

system. A similarly south-verging major thrust is encountered deep in the Demre-1 and Kaş-1 wells in the Kasaba Basin (Chapter 4). Well data and geometric relationships of the rock successions drilled in these two wells show that this thrust is an approximately 10° north-dipping and south-verging structure (Aksu et al., 2009). This fold-thrust geometry is identical to what is observed in the marine areas. The southward projection of the thrust (i.e., that encountered in the Demre-1 and Kaş-1 wells) trajectory suggests that the fault should emerge at the base of the Turkish continental slope. This thrust is believed to carry the Western Taurus Mountains. The proposed imbricate thrust system TT1 and TT2 that carries the Anaximander and Anaximenes Mountains, respectively is believed to link at depth with the thrust that carries the Western Taurus Mountains, forming a crustal-scale linked thrust system, with TT1 and TT2 thrusts representing the leading thrust panels of this system. Woodside et al. (1998) suggested that the rise and tilt of the Anaximander Mountain (*sensu stricto*) and the linkage between the Anaximander Mountain and Anaximenes Mountain can best be explained by under-thrusting of the Anaximander Mountain by the Anaximenes Mountain, and the crustal shortening between these two mountains. The seismic reflection data presented in this thesis are not at odds with the under-thrusting model proposed by Woodside et al. (1998) but add significant detail and regional dimension to the story.

The northeastern limit of the study area is confined to the Anaximenes Mountain. The region of the Anaxagoras Mountain is beyond the scope of this thesis. However, it is noted that the major structural elements mapped across the Anaximenes Mountain, such as BT2 and TT2 extend toward the northeast, defining the northwestern

and southeastern margins of the Anaxagoras Mountain, respectively. Additional northwest-southeast trending high-resolution seismic reflection profiles are needed at the same line density as the current study to determine the kinematic history in Anaxagoras Mountain, and its linkage with the Anaximenes Mountains. Nonetheless, it is important to point out that the crustal-scale structures (i.e., BT2 and TT2) are not expected to die-out over very short distances. It is therefore, speculated that these structures must extend toward the northeast into the Antalya Basin, where they would form major basin-bounding elements.

ten Veen et al. (2004) suggested that during the Pliocene the western portion of the Anaximander Mountains was transected by a sinistral strike slip zone, characterized by normal faults that formed long graben-like depressions. However, they further suggested that the eastern portion of the Anaximander Mountains is characterized by a normal and/or oblique normal fault zone, and lacks evidence for strike-slip deformation. The seismic reflection data presented in this thesis and their interpretations radically differ from the interpretation of ten Veen et al. (2004). Except for small faults with negligible extensional offsets on the backlimb of the Anaximander Mountain, possible extensional faults in the Sırrı Erinç Plateau, and superficial extensional faults defining the bases of slide masses on very steep slopes, there is no evidence for normal faulting anywhere within the greater Anaximander Mountains region. The data presented in this thesis support a long-duration latest Miocene to Recent contractional to transpressional tectonic phase.

Aksu et al. (2009) showed that the large open folds within Unit 3 in the Sırrı Erinç Plateau are disharmonious with the tighter corrugations and structures delineated by the M-reflector. They suggested that these larger folds are invariably truncated by the M-reflector, and argued that the folded fabric in Unit 3 must have developed prior to the late Messinian erosional event. Aksu et al. (2009) further pointed out, from the thrust symmetry of the Miocene structures bounding it, that the Sırrı Erinç Plateau is probably a very large pop-up structure or a positive flower structure, the crest of which must have been exhumed and largely eroded during the development of the Messinian M-unconformity (e.g., Fig. 5.29).

The seafloor across Domain 3 is highly corrugated, and these corrugations are correlated with the high-angle faults that extend the depositional surface (Chapter 5). These seafloor corrugations together with the lobe-like boundary between the Finike Basin and the Sırrı Erinç Plateau may have contributed to the mis-interpretation of this region as a massive gravitational slide (i.e., the Great Slide of Woodside et al. (1998). However, as described in Chapter 5, seismic profiles presented in this thesis clearly show that the Pliocene-Quaternary successions within the Sırrı Erinç Plateau are well stratified and are cut by numerous high-angle faults. In a large slide mass the internal architecture of the slide mass would show little to no coherent reflections, and would image as a massive, internally structureless package. The data presented in this thesis do not show any evidence of the chaotic internal architecture that is expected in a massive gravitational slide. Therefore, the data are at odds with the interpretation that domain 3 is

a "Great Slide" as suggested by Woodside et al. (1998) and subsequently by Zitter et al. (2003) and ten Veen et al. (2004).

Instead, the Sırrı Erinç Plateau is interpreted as a 30-40 km wide broad shear zone between the Anaximander and Anaximenes Mountains. It is speculated that this zone is the linkage between the structures that define the southwestern margin of the Antalya Basin and the Anaximander Mountains (*sensu lato*). It is further speculated that that this shear zone could be a link between the northeastern continuation of the Pliny-Strabo Trench system and the western boundary of the Antalya Basin.

6.4 Comparison between the Isparta Angle and the Anaximander Mountains

The Isparta Angle is a large structure located in southwest Turkey, which separates the Bey Dağları block in the west and southwest, from the Western Taurus block in the east and northeast. The Isparta Angle is one of the most important tectonic elements of the eastern Mediterranean and is linked with the Kyrenia Range in northern Cyprus (i.e., the Aksu-Kyrenia Lineament of Işler et al. (2005)). The structure is developed as the result of the closure of the Pamphylian Basin in the Tertiary (Poisson et al., 2003), which originally separated the Bey Dağları and the Western Taurus platforms during the Mesozoic. Several hypotheses have been proposed for the evolution of the Isparta Angle (Robertson et al., 2003). These hypotheses all agree that the eastern limb of the Isparta Angle (i.e., the Anamas-Akseki Platform) experienced a 20-40° clockwise rotation since the Eocene (Kissel et al., 1993), while the western limb, including the Beydağları Platform, experienced a 30-40° counterclockwise rotation during the Miocene

(Kissel and Poisson, 1987). Thus, the Isparta Angle as a whole experienced a late Miocene phase of shortening, also known as the Aksu Phase, with coeval eastward and westward thrusting along the western and eastern limbs, respectively (e.g., Poisson et al., 2003). There is also agreement that this phase of deformation is accompanied by calc-alkaline volcanism along the north-south axis of the Isparta Angle between 21 and 4 Ma (Yağmurlu et al., 1997). Thus, the broad arrow-head-shaped structure is developed during the early Miocene-early Pliocene by the northward buckling of the western Tauride Mountains (Poisson et al., 2003). Aksu et al. (2009) indicated that when the western limb of the Isparta Angle (i.e., the Burdur Fethiye Fault zone) was rotated back clockwise by ~20° (i.e., its position during the middle-late Miocene), it assumed an east-northeast – west-southwest trend. They further indicated that during this time, the convergence vector between the African Plate and the Eurasian Plate was nearly orthogonal to this trend. The late Miocene – early-middle Pliocene-Quaternary counterclockwise rotation of the western Tauride Mountains and the Island of Rhodes are well documented in the literature (e.g., Kissel and Poisson, 1987, van Hinsbergen et al., 2007). This rotation changed the orientation of the plate margin and developed a sinistral shear zone (i.e., the 40-50 km wide Burdur-Fethiye Fault zone; Hall et al., 2009).

The Anaximander Mountains (*sensu lato*) and the Isparta Angle bear strong morphological resemblances. Both structures have a north-pointed arrow-shaped morphology, with a north-northeast – south-southwest trending western limb and a north-northwest – south-southeast trending eastern limb. Both structures are bounded by large crustal-scale thrusts.

Zitter et al., 2003 and Aksu et al. (2009) hypothesized that the Anaximander Mountains and Isparta Angle are genetically linked structures which evolved at different times. Aksu et al. (2009) remarked on the strong morphological resemblances between the Anaximander Mountains and Isparta Angle and showed that the northwest-southeast trending Sultan Dağ and Aksu Thrusts which bound the northeastern margin of the Isparta Angle are similar in strike, vergence and size to the two prominent thrusts that bound the northeastern limb of the Anaximenes and the Anaxagoras Mountains. They further suggested that the Sırrı Erinç Plateau is a 30-40 km wide sinistral transpressional belt extending through the Anaximander Mountains and is similar in orientation and width to the 40-50 km wide sinistral Burdur-Fethiye Fault zone that marks the western boundary of the Isparta Angle.

Block rotation is not an easy process to delineate in seismic reflection profiles. This is often done using detailed magnetostratigraphic work on carefully collected oriented samples. There are no deep drill holes in the study area where magnetostratigraphic studies can be carried out. Therefore, the similarities between the Isparta Angle and the Anaximander Mountains remain morphological and descriptive. If the conjecture of rotation of the arms of the Anaximander Mountains is correct, the amount of rotation required to form the present-day arrow head shaped structure can be estimated. This will require knowing the information regarding the orientation of the large fold-thrust structures that defined the tectonic framework of the Miocene tectonic environment. Numerous studies within the forearc basins of the eastern Mediterranean north of the subduction zone showed that the fold-thrust belt had a predominantly east-

west orientation (e.g., Calon et al., 2005a,b Aksu et al, 2005, Hall et al., 2005, Işler et al., 2005), including the Anaximander Mountains and the Rhodes Basin (e.g., Aksu et al., 2009, Hall et al., 2009). Assuming a broadly east-west trend for the Miocene fold-thrust belt, back-of-the-envelope calculations suggest that the Anaximander and Anaximenes Mountains must have experienced ~49° counterclockwise rotation whereas the Anaxagoras Mountain and Florence Rise to the east must have experienced a 53° clockwise rotation (Fig. 6.5). There are supporting data for block rotation from the landmass adjacent to the Anaximander Mountains. For example, the continuing rotation of the Island of Rhodes in the Quaternary suggests that the Island of Rhodes and the Rhodes Basin are also part of the rotation of the western limb of the Anaximander Mountains (van Hinsbergen et al., 2007).

The critical issues associated with block rotation are the determination of boundaries of rotating blocks and how the rotations are accommodated by regional strain variations. For example, when a block experiences ~40-50° rotation, the sedimentary pile along the margins of the rotating block will most likely deform in association with shear between the block and surrounding rigid mass. At depth the deformation along the rotating block is expected to be brittle. But in the near surface the unconsolidated sediments should also show signs of deformation, such as major strike-slip zones defined by corrugations associated with high-angle faults, delineating internally parallel zones, such as intensely transpressive regions with pup-ups, and/or long narrow and very deep linear depressions associated with zones of transtensions. How would these zones of lateral shear be reflected in the seismic reflection profiles? Can the boundary between be

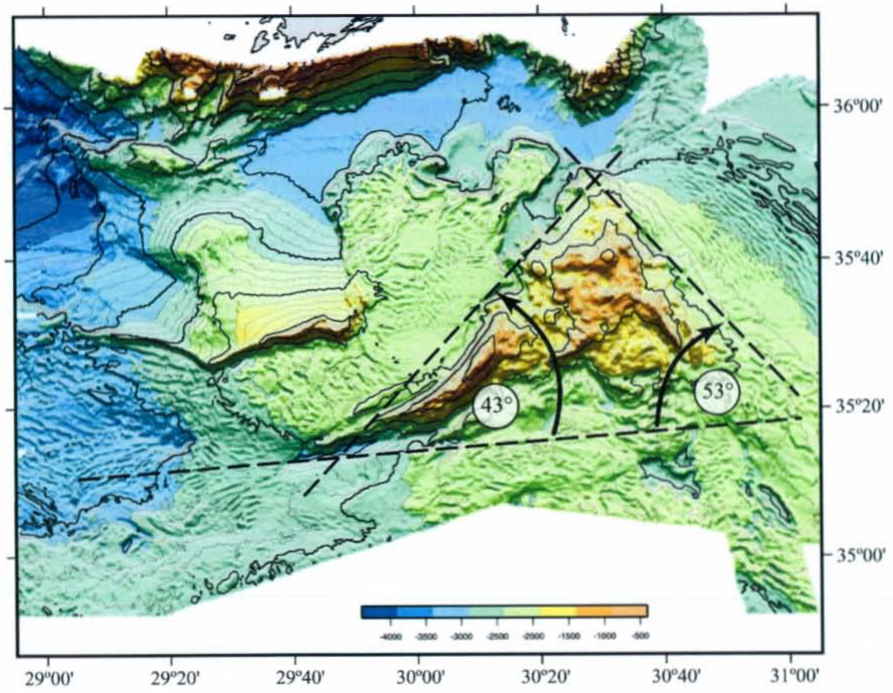

Figure 6.5 Map showing the 'back of the envelope' rotation calculations for the Anaximander Mountains.

incorporated into the arc-arc junction? If TT1 and TT2 are part of a linked thick-skinned imbricate fan, then they must represent the leading portion of the accretionary prism. Can the Anaximander Mountain and the Sırrı Erinç Plateau be viewed as a block rotation boundary? Is the Sırrı Erinç Plateau a major boundary between the clockwise rotating eastern Anaxagoras Mountain and Florence Rise and the counterclockwise rotatingAnaximander and Anaximenes Mountains? Is the Finike Basin a result of a transtensional depression associated with the counterclockwise rotation of the Anaximander block? These are questions that require further geodynamic modeling and palinspastic balanced section restoration.

There are further questions that arise from this thesis. For example, how does the southeastern margin of the Anaximenes Mountain relate to the Mediterranean Ridge further south? Is this region part of the accretionary prism associated with the subducting African Plate beneath the Aegean-Anatolian Microplate? If so, how does it relate to the Hellenic Active Margin? Could this region be part of the paleo-subduction zone, now incorporated into the arc-arc junction? If TT1 and TT2 are part of a linked thick-skinned imbricate fan, then they must represent the leading portion of the accretionary prism. The following might help answer some of these questions.

CHAPTER 7. Conclusions

This thesis work was built on preexisting data, but substantial new data further south of the 2001 survey lines significantly increased the spatial resolution, allowing detailed imaging and mapping of structures. The new data and mapping added significant detail to the Late Miocene to Pliocene-Quaternary evolution of the Anaximander Mountains (*sensu lato*). Consequently several new conclusions are drawn which are different from past interpretations. The following is a summary of these conclusions:

- Seismic reflection profiles examined in this thesis show that the tectonic framework of the Anaximander and Anaximenes Mountains is characterized by two arcuate broadly northeast-southwest trending large southeast verging thrusts (TT1 and TT2), and two similarly trending but oppositely verging backthrusts (BT1 and BT2). The fore-thrusts TT1 and TT2 delineate the southeastern margins of the Anaximander and Anaximenes Mountains, respectively, whereas the backthrusts BT1 and BT2 define the northwestern margins of the Anaximander and Anaximenes Mountains, respectively. Thrusts TT1 and TT2 were also proposed by Aksu et al. (2009); however, they did not have the seismic evidence for thrust TT2, and had limited data to map TT1.

- The deep rooted nature of the trajectories of thrust TT1 and TT2, suggests that these thrusts may be linked at depth to form a thick-skinned imbricate thrust system. A similarly south-verging major thrust is encountered deep in the Demre-

1 and Kaş-1 wells in the onland Kasaba Basin in SW Turkey, which is identical to what is observed in the marine areas. The southward projection of the thrust (i.e., that encountered in the Demre-1 and Kaş-1 wells) trajectory suggests that the fault should emerge at the base of the Turkish continental slope. This thrust is believed to carry the Western Taurus Mountains. The proposed imbricate thrust system TT1 and TT2 that carries the Anaximander and Anaximenes Mountains, respectively is believed to link at depth with the thrust that carries the Western Taurus Mountains, forming a crustal-scale linked imbricate thrust system, with TT1 and TT2 thrusts representing the leading thrust panels of this system.

- The stratigraphic and structural interpretation indicates that the TT1 thrust bounding the southern margin of the Anaximander Mountain is a reactivated old Miocene thrust. The lack of growth in subunit 1a below the γ-reflector suggests that the reactivation of the TT1 must have occurred after the deposition of the lowermost Pliocene-Quaternary. The large north-thickening growth stratal wedges in subunit 1b above the γ-reflector document that the growth of the Anaximander Mountain occurred during the Pliocene-Quaternary.

- Seismic reflection profiles show that the core of the Anaximenes Mountain is complexly folded and faulted. The back limb of a large thrust culmination developed on the TT2 thrust is truncated by a prominent, steeply north-verging backthrust BT2, which is deeply rooted within Unit 3. Growth strata on the forelimb of the TT2 thrust, and its subsidiary splays suggest that the TT2 thrust

also became reactivated during the Pliocene-Quaternary. Minor growth observed within the leading syncline on the footwall of BT2 backthrust along the southeastern margin of the Sırrı Erinç Plateau suggests that BT2 was also activated during the Pliocene-Quaternary. Aksu et al. (2009) speculated that the backthrust probably branches from the forethrust at a depth >4000 ms. However, this study is the first to provide detailed images and interpretations for the Anaximenes Mountain, including the TT2 thrust and the BT2 backthrust.

- The seafloor across the Sırrı Erinç Plateau is highly corrugated, and these corrugations are correlated with the high-angle faults that extend the depositional surface. The data presented in this thesis do not show any evidence of the chaotic internal architecture that is expected in a massive gravitational slide. Instead, the Sırrı Erinç Plateau is interpreted as a 30-40 km wide broad shear zone between the Anaximander and Anaximenes Mountains. It is speculated that this zone is the linkage between the structures that define the southwestern margin of the Antalya Basin and the Anaximander Mountains (*sensu lato*). It is further speculated that that this shear zone could be a link between the northeastern continuation of the Pliny-Strabo Trench system and the southwestern boundary of the Antalya Basin.

- Except for small faults with negligible extensional offsets on the backlimb of the Anaximander Mountain, possible extensional faults in the Sırrı Erinç Plateau, and superficial extensional faults defining the bases of slide masses on very steep slopes, there is no evidence for normal faulting anywhere within the greater

Anaximander Mountains region. The data presented in this thesis support a long-duration latest Miocene to Recent contractional to transpressional tectonic phase.

- At the transition between the Anaximander Mountain and the Sırrı Erinç Plateau, there is a prominent north-south trending zone where the M-reflector rises nearly vertically by >1100 ms and where an ~900-1200 ms-thick Pliocene-Quaternary succession sharply abuts reflections in Unit 3 along this nearly vertical face. This zone is interpreted as a strike slip fault linking the Anaximander Mountain and the Finike Basin.

- Within a geographically limited portion of the study area, there is a pre-kinematic unit below the M-reflector. This unit displays a distinctly transparent acoustic character, where there are few coherent reflections. Where present, these reflections are disharmoniously folded in relation to the overlying M-reflector and underlying N-reflector. This unit is interpreted to represent the Messinian succession in the study area. If correct, this is the first documentation of a Messinian succession within the greater Anaximander Mountains and Rhodes Basin areas. The thin transparent nature of the inferred Messinian succession may represent a predominantly siliciclastic sequence with evaporite interbeds.

- One of the ramifications of having a Messinian succession over the Anaximander Mountains and the Rhodes Basin is that the very high rate of Pliocene-Quaternary basin collapse envisaged by Hall et al. (2009) must be revised to reflect the inundation of the region during the Messinian. Hall et al. (2009) and Aksu et al.

(2009) suggested that the entire region must have been above the depositional base during the Messinian and that the subsidence leading to the present-day deep Rhodes and Finike Basins must have taken place during the Pliocene-Quaternary. However, if the region was already at or below the depositional base during the latest Miocene, the amount of subsidence required to bring the region to their present-day elevations would be much less.

CHAPTER 8. Future work

Additional seismic reflection profiles will help answer some of the questions proposed in the discussion.

- For data processing, pre-stack migrations could be attempted to better resolve the faults and steeply dipping structures.

- More high-resolution seismic reflection profiles are needed. For example, the existing data set lacks northwest-southeast trending profiles across the Anaximenes Mountain – Anaxagoras Mountain transition. Similarly, there is no data that cross the northeast-southwest trending profiles south of the Anaximander and Anaximenes Mountains.

- In order to image the stratigraphic relationships displayed in the data, the seismic profiles are often displayed with large vertical exaggeration (e.g., 1:7). Yet most structures such as, thrusts and halokinetic features are best imaged and interpreted at or close to 1:1 scale. Therefore, it is recommended to the next generation of graduate and undergraduate students that both 1:7 and 1:1 scale displays are printed and interpreted.

- The sole of the thick-skinned imbricate thrust fan (i.e., TT1 and TT2) is never imaged in the seismic reflection data. Therefore, additional seismic profiles collected using a larger source and longer streamer would be essential to resolve the roots of this system.

- The best method of determining block rotations is to measure pole positions of oriented samples recovered from rotating blocks and their surroundings. If funds were unlimited, paleomagnetic data from four oriented geotechnical boreholes drilled to the M-reflector on the backlimb of the Anaximander Mountain, Sırrı Erinç Plateau, the forelimb of the Anaximenes Mountain and the northern Anaxagoras Mountain would provide the much needed confirmation for large scale block rotation.

References:

Akhmanov, G.G., Akhmetjanov, A.M., Ivanov, M.K., Mazzini, A., van der Bosch, H., Kleeven, T.P., Korkin, A.V., Ivanova, E.K., Kozlova, E.V., Gablina, S.S., Yu Belen'kaya I., van der Schans, E., Stadnitskaya, A.N. and Sautkin, A.P., 1997. Coring Results. *In*: Woodside, J.M., Ivanov, M.K. and Limonov, A.F., ŞEds.) Neotectonics and fluid flow through seafloor sediments in the Eastern Mediterranean and Black Seas. Part 1: Eastern Mediterranean Sea. Intergovernmental Oceanographic Commission Technical Series, 48: 72-120, 128 pp.

Aksu, A.E., and Hiscott, R.N., 1989. Slides and debris flows on the high-latitude continental slopes of Baffin Bay. Geology, 17: 885-888.

Aksu, A.E., Hall, J. and Yaltırak, C., 2005a. Editorial - Miocene to Recent tectonic evolution of the eastern Mediterranean: new pieces of the old Mediterranean puzzle. Marine Geology, 221: 1-13.

Aksu, A.E., Calon, T.J., Hall, J., Mansfield, S., and Yaşar, D., 2005b. The Cilicia–Adana Basin complex, Eastern Mediterranean: Neogene evolution of an active fore arc basin in an obliquely convergent margin. Marine Geology, 221: 121–159.

Aksu A.E., J. Hall, and Yaltırak, C., 2009. Neogene evolution of the Anaximander Mountains and Finike Basin at the Junction of Hellenic and Cyprus Arcs, Eastern Mediterranean. Marine Geology, 258: 24-47.

Bridge, C., Calon, T.J., Hall, J. and Aksu, A.E., 2005. Salt tectonics in two convergent margin basins of the Cyprus Arc, northeastern Mediterranean. Marine Geology 221: 223-259.

Burton-Ferguson, R., Aksu, A.E., Calon, T.J., and Hall, J., 2005. Seismic stratigraphy and structural evolution of the Adana Basin, Eastern Mediterranean. Marine Geology, 221: 189-222.

Calon, T.J., Hall, J. and Aksu, A.E., 2005. The Oligocene-Recent evolution of the Mesaoria Basin (Cyprus) and its western marine extension, Eastern Mediterranean. Marine Geology, 221: 95-120.

Calon, T.J., Aksu, A.E. and Hall, J., 2005. The Neogene evolution of the Outer Latakia Basin and its extension into the Eastern Mesaoria Basin (Cyprus), Eastern Mediterranean. Marine Geology, 221: 61-94.

Cita, M.B., Wright, R.C., Ryan, W.B.F. and Longinelli, A., 1978. Messinian Paleoenvironments. In: K. Hsü, L. Montadert et al., Initial Reports of the Deep Sea Drilling Project XLII, Part I, p. 1003-1035. U.S. Government Printing Office, Washington.

Cranshaw, J., Aksu, A., Hall, J., Çifçi, G., Dondurur, D., Yaltırak, C., 2009. The junction of Hellenic and Cyprus arcs: a detailed study of the morphology and Neogene tectonic evolution of the Anaximander Mountains. EGU 2009, TS6.6/G27/GD21/SM3.1, Halls X/Y.

Dumont, J.F., and Woodside, J.M., 1997. Dredging Results. *In*: Woodside, J.M., Ivanov, M.K. and Limonov, A.F., ŞEds.) Neotectonics and fluid flow through seafloor

sediments in the Eastern Mediterranean and Black Seas. Part 1: Eastern Mediterranean Sea. Intergovernmental Oceanographic Commission Technical Series, 48: 65-71, 128pp.

Gass, I.G., 1960. The geology and mineral resources of the Dhali Area. Memoir No: 4, Geological Survey Department, Cyprus.

Hall, J., Aksu, A.E., Calon T.J., Yaşar, D, 2005a. Varying tectonic control on basin development at an active microplate margin: Latakia Basin Eastern Mediterranean. Marine Geology, 221: 15-60.

Hall, J., Calon, T.J., Aksu, A.E., and Meade, S.R., 2005b. Structural evolution of the Latakia Ridge and Cyprus Basin at the front of the Cyprus Arc, Eastern Mediterranean Sea. Marine Geology 221: 261-297.

Hall, J., Aksu, A.E., Yaltırak, C., Winsor, J.D., 2009. Structural architecture of the Rhodes Basin: a deep depocentre that evolved since the Pliocene at the junction of Hellenic and Cyprus Arcs, eastern Mediterranean. Marine Geology, 258: 1-23.

Hiscott, R.N., and Aksu, A.E., 1994. Submarine debris flows and continental slope evolution in front of Quaternary ice sheets, Baffin Bay, Canadian Arctic. American Association of Petroleum Geologists Bulletin, 78 (3): 445-460.

Hsü, K.J., Cita, M.B. and Ryan, W.B.F., 1973. The origin of the Mediterranean evaporites. In: W.B.F. Ryan, K. Hsü, et al., Initial Reports of the Deep Sea Drilling Project 13 Ş1), p. 1203-1231. U.S. Government Printing Office, Washington.

Işler, F.I., 2004. Miocene to Recent stratigraphy, structural architecture and tectonic evolution of the Antalya Basin, eastern Mediterranean Sea. Unpublished MSc thesis, Department of Earth Sciences, Memorial University of Newfoundland, 248 pp.

Işler, F.I., Aksu, A.E., Hall, J., Calon T.J, and Yaşar, D., 2005. Neogene development of the Antalya Basin, Eastern Mediterranean: an active fore-arc basin adjacent to an arc junction. Marine Geology, 221: 299-330.

Jackson, M.P.A., and Talbot C.J., 1991. A Glossary of Salt Tectonics. Bureau of Economic Geology. University of Texas at Austin, Austin, Texas, 78713-7508, Geological Circular 91-4, 44 pp.

Krebes, E.S., and Hearn, D.J., 1985. On the geometrical spreading of viscoelastic waves. Bulletin of the Seismological Society of America, 75: 391-396.

Krebes, E.S., 1989. Seismic Theory and Methods: Geophysics 551 course notes, University of Calgary, 4.1 - 4.18.

McClusky, S., Balassanian, S., Barka, A., C. Demir, S. Ergintav, I. Georgiev, O. Gurkan, M. Hamburger, K. Hurst, H.-G. Hans-Gert, K. Karstens, G. Kekelidze, R. King, V. Kotzev, O. Lenk, S. Mahmoud, A. Mishin, M. Nadariya, A. Ouzounis, D. Paradissis, Y. Peter, M. Prilepin, R. Relinger, I. Sanli, H. Seeger, A. Tealeb, M.N. Toksaz, G. Veis, 2000. Global positioning system constraints on plate kinematics and dynamics in the eastern Mediterranean and Caucasus. Journal of Geophysical Research, 105, 5695-5719.

Mitchum, M. R., Jr., Vail, P. R. and Sangree, J. B., 1977a. Seismic stratigraphy and global changes of sea level, Part 6: Stratigraphic interpretation of seismic reflection patterns in depositional sequences. *In*: C. E. Payton (Editor), Seismic Stratigraphy Applications to Hydrocarbon Exploration. Memoir of the American Association of Petroleum Geologists, 26: 117-135.

Mitchum, R.A.Jr., Vail, P.R. and Thompson III, S., 1977b. Seismic stratigraphy and global change of sea level. Part 2: The depositional sequence as a basic unit for stratigraphic analysis. *In*: C.E. Payton (Editor), Seismic Stratigraphy Applications to Hydrocarbon Exploration. American Association of Petroleum Geologists. Memoir, 25: 53-62.

Moore, T.A., 1960. The geology and mineral resources of the Astromeritis-Kormakiti area. Memoir No: 6, Geological Survey Department, Cyprus.

Moores, E.M., Robertson, P.T., Malpas, J., Xenophontos, C., 1984. Model for the origin of the Troodos massif, Cyprus and other Mideast ophiolites. Geology 12, 223-226.

Myers, K.J. and Milton, N.J., 1996. Concepts and principles of sequence stratigraphy. *In*: D. Emery and K.J. Myers (Eds.), Sequence Stratigraphy. Blackwell Science, p. 11-44, 297 pp.

Poisson, A., Yağmurlu, F., Bozcu, M., Şentürk, M., 2003. New insight on the tectonic setting and evolution around the apex of the Isparta Angle, SW Turkey). Geological Journal, 38: 257-282.

Poisson, A., Wernli, R. Sağular, E.K. and Temiz, H., 2003. New data concerning the Age of the Aksu thrust in the south of the Aksu valley, Isparta Angle (SW Turkey): consequences for the Antalya Basin and the eastern Mediterranean. Geological Journal, 38: 311-327.

Riba, O., 1976. Syntectonic unconformities of the Alto Cardener, Spanish Pyrenees: a genetic interpretation. Sedimentary Geology, 15: 213-233.

Robertson, A.H.F., 1998. Mesozoic-Tertiary tectonic evolution of the easternmost Mediterranean area: integration of marine and land evidence. *In*: A.H.F Robertson, K.C. Emeis, C. Richter, A. Camerlenghi (Eds.), Proceeding of the Ocean Drilling Program, Scientific Results, 160: 723-782.

Robertson, A.H.F., 2000. Mesozoic-Tertiary tectonic-sedimentary evolution of a south Tethyan oceanic basin and its margin in southern Turkey. *In*: E. Bozkurt, J.AQ. Winchester and J.D. Piper (Eds.) Tectonics and Magmatism in Turkey and the Surrounding Area. Geological Society, London, Special Publications, 173: 43-82.

Robertson, A.H.F., Eaton, S., Follows, E.J. and McCallum, J.E., 1991. Role of local tectonics versus global sealevel change in the Neogene evolution of Cyprus. *In*: D.I.M. MacDonald (Ed.), Sealevel Changes at Active Plate Margins: Processes and Products: Oxford, Blackwell Scientific Publications, International Association of Sedimentologists Special Publication, 12: 331-369.

Robertson, A.H.F. and Dixon, J.E., 1984. Introduction: aspects of the geological evolution of the Eastern Mediterranean. In: The Geological Evolution of the Eastern Mediterranean, J.E. Dixon and A.H.F. Robertson ŞEds), Blackwell

Scientific Publications, Oxford, Geological Society Special Publication 17: 1-74, 824 pp.

Robertson, A.H.F., Eaton, S., Follows, E.J., Payne, A.S., 1995. Depositional processes and basin analysis of Messinian evaporites in Cyprus. Terra Nova 7, 233–253.

Ryan, W.B.F., 1969. The floor of the Mediterranean Sea. PhD Thesis, Columbia University, New York, 236 pp.

Şengör, A.M.C., Yılmaz, Y., 1981. Tethyan evolution of Turkey: a plate tectonic approach. Tectonophysics 75: 181-241.

Şengör, A.M.C., Görür, N. and Şaroğlu, F., 1985. Strike-slip faulting and related basin formation in zones of tectonic escape: Turkey as a case study. Society of Economic Paleontologists and Mineralogists, Special Publication 37: 227-264.

Şenel, M., 1997a. Geological Map of Fethiye, L8 quadrangle, No:2, 1:100,000 General Directorate of Mineral Research and Exploration, Ankara, Turkey, 22 pp.

Şenel, M., 1997b. Geological Map of Fethiye, M8 quadrangle, No:4, 1:100,000 General Directorate of Mineral Research and Exploration, Ankara, Turkey, 15 pp.

Şenel, M., Bölükbaşı, A.S., 1997a. Geological Map of Fethiye, M9 quadrangle, No:5, 1:100,000 General Directorate of Mineral Research and Exploration, Ankara, Turkey, 11 pp.

Şenel, M. and Bölükbaşı, A.S., 1997b. Geological Map of Turkey, Fethiye – M9 Sheet, 1:100,000 scale. General Directorate of Mineral Research and Exploration ŞMTA), Jeoloji Etütler Dairesi, Ankara.

Shipboard Scientific Party, 1978. Sites 375 and 376, Florence Rise. *In*: K. Hsü, L. Montadert et al., Initial Reports of the Deep Sea Drilling Project 42 §1), p. 219-304. U.S. Government Printing Office, Washington.

ten Veen, J.H., Kleinspehn, K.L., 2002. Geodynamics along an increasingly curved convergent plate margin: late Miocene–Pleistocene Rhodes, Greece. Tectonics 21 (3) 21 pp. (10.1029/2001TC001287).

ten Veen, J.H., Woodside, M., Zitter, T.A.C., Dumont, J.F., Mascle, J., Volkonskaia, A., 2004. Neotectonic evolution of the Anaximander Mountains at the junction of the Hellenic and Cyprus Arcs. Tectonophysics, 391: 35-65.

Winsor, J., 2004. Seismic stratigraphy and structural evolution of the Rhodes Basin, eastern Mediterranean Sea. Unpublished MSc thesis, Department of Earth Sciences, Memorial University of Newfoundland, 318 pp.

Woodside, J.M., Ivanov, M.K. and Limonov, A.F., 1997. Neotectonics and fluid flow through seafloor sediments in the Eastern Mediterranean and Black Seas. Part 1: Eastern Mediterranean Sea. Intergovernmental Oceanographic Commission Technical Series, 48.

Woodside, J., Ivanov, M.K., Limanov, A.F., 1998. Shallow gas and gas hydrates in the Anaximander Mountains region, eastern Mediterranean Sea. *In*: Henriet, J.-P., Mienert, J. (Eds.), Gas Hydrates: Relevance to World Margin Stability and Climate Change. Geological Society, London, Special Publications, 137: 177–193.

Woodside, J., Mascle, J., Huguen, C., Volkonskaia, A., 2000. The Rhodes Basin, a post-Miocene tectonic trough. Marine Geology, 165, 1–12.

Woodside, J., Mascle, J., Zitter, T., Limonov, A., Ergün, M., Volkonskaia, A., 2002. The Florence Rise, the Western Bend of the Cyprus Arc. Marine Geology 185, 175–194.

Yılmaz, Ö., 2001. Seismic Data Analysis: Processing, Inversion and Interpretation of Seismic Data (2 Volumes). Investigations in Geophysics No: 10. Society of Exploration Geophysicists.

Zitter, T., Woodside, J., Mascle, J., 2003. The Anaximander Mountains: a clue to the tectonics of southwest Anatolia. Geological Journal, 38, 375-394.